AD-A040 378 ARCON CORP WAKEFIELD MASS F/G 12/1
INTERACTIVE MATH MODELING.(U)
FEB 77 S WOOLF, J V O'BRIEN, E COHEN, D BAKER F19628-74-C-0049
UNCLASSIFIED RADC-TR-77-86 NL

1 OF 3
AD
A040378

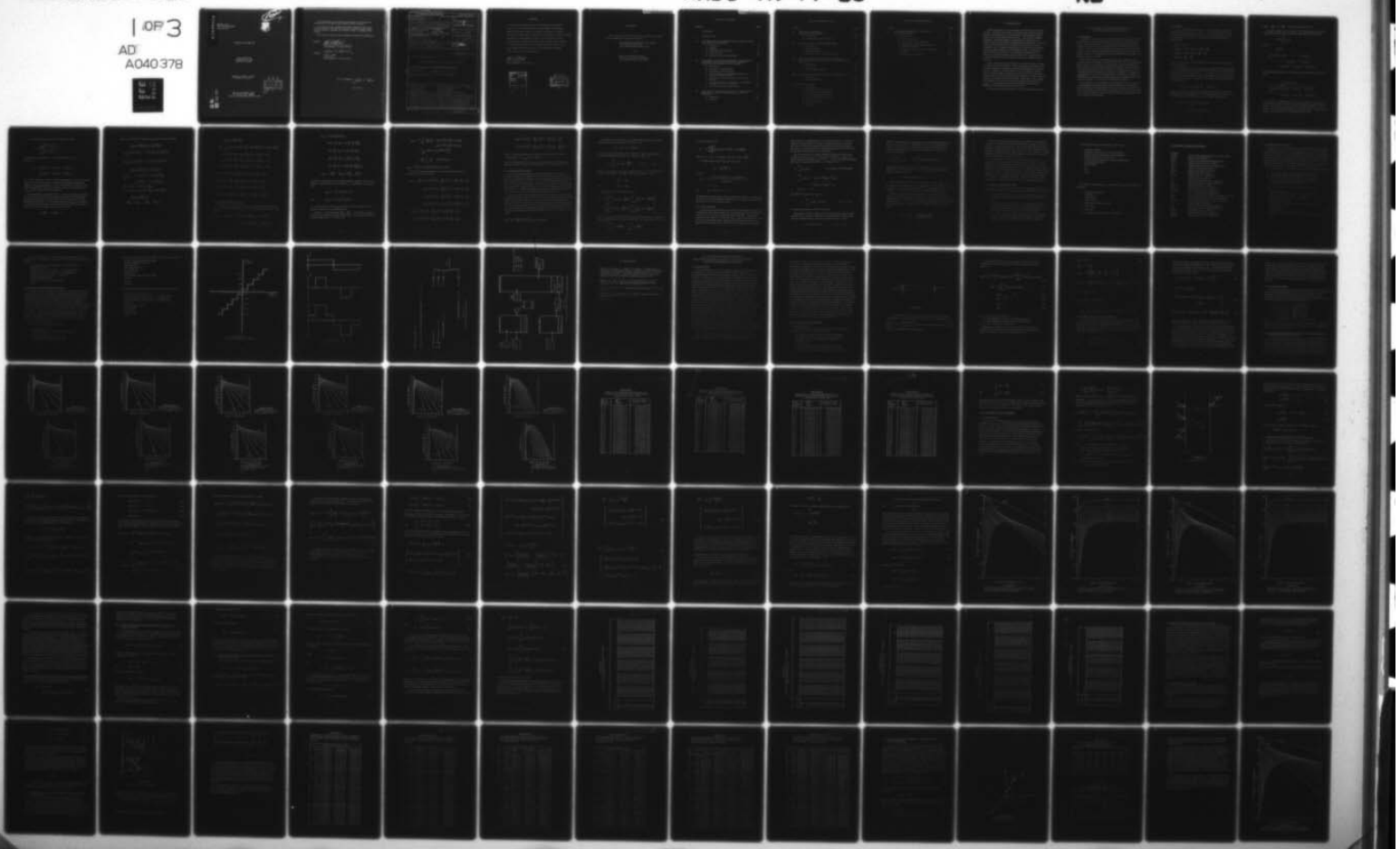

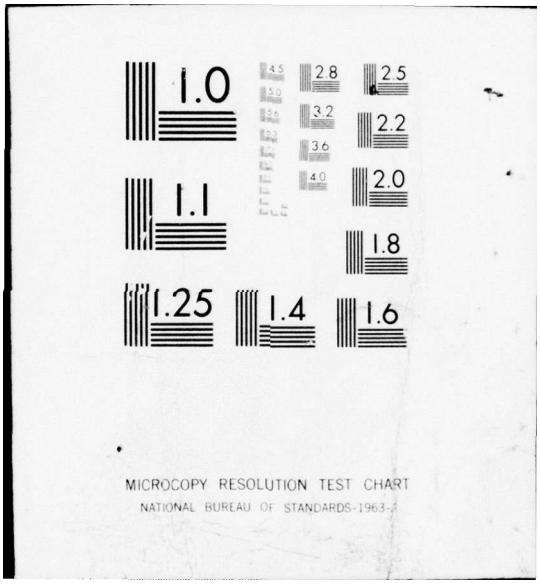
1.0
1.1
1.25
1.4
1.6
1.8
2.0
2.2
2.5
2.8
3.2
3.6
4.0
4.5
5.0
5.6
MICROCOPY RESOLUTION TEST CHART
NATIONAL BUREAU OF STANDARDS-1963-A

AD A040378

RADC-TR-77-86
Final Technical Report
February 1977

INTERACTIVE MATH MODELING

Arcon Corporation
Lakeside Office Park
Wakefield, MA 01880

Approved for public release;
distribution unlimited.

DDC
RECEIVED
JUN 9 1977
D

ROME AIR DEVELOPMENT CENTER
AIR FORCE SYSTEMS COMMAND
GRIFFISS AIR FORCE BASE, NEW YORK 13441

AD No.
DDC FILE COPY

Dr. Stanley Woolf is the Principal Investigator for this contract. John Pustaver is the RADC Project Engineer (Contract Monitor).

This report has been reviewed by the RADC Information Office (OI) and is releasable to the National Technical Information Service (NTIS). At NTIS it will be releasable to the general public, including foreign natiojns.

This technical report has been reviewed and approved for publication.

APPROVED:

JOHN A. PUSTAVER, JR
Microwave Detection Techniques Br.
Electromagnetic Sciences Division

APPROVED:

ALLAN C. SCHELL
Acting Chief
Electromagnetic Sciences Division

FOR THE COMMANDER:

Plans Office

Unclassified

SECURITY CLASSIFICATION OF THIS PAGE (When Data Entered)

REPORT DOCUMENTATION PAGE	READ INSTRUCTIONS BEFORE COMPLETING FORM
1. REPORT NUMBER: RADC-TR-77-86	2. GOVT ACCESSION NO.	3. RECIPIENT'S CATALOG NUMBER
4. TITLE (and Subtitle): DEVELOPMENT OF MATHEMATICAL MODELS AND STATISTICAL ANALYSIS TECHNIQUES AS APPLIED TO THE DIGITAL PROCESSING OF SIGNALS AND THE DESCRIPTION OF OTHER PHYSICAL SYSTEMS.	5. TYPE OF REPORT & PERIOD COVERED: Final Report, 1 Oct 73 to 1 Sep 76; 6. PERFORMING ORG. REPORT NUMBER
7. AUTHOR(s): Stanley Woolf, John V. O'Brien, Edward Cohen, David Baker, Jean Hsiung, Elihu J. Tichovolsky, William Rosenfeld	8. CONTRACT OR GRANT NUMBER(s): F19628-74-C-0049
9. PERFORMING ORGANIZATION NAME AND ADDRESS: ARCON Corporation, 18 Lakeside Office Park, Wakefield, Massachusetts 01880	10. PROGRAM ELEMENT, PROJECT, TASK AREA & WORK UNIT NUMBERS: N/A; 270 p.
11. CONTROLLING OFFICE NAME AND ADDRESS: Deputy for Electronic Technology/(RADC/ETEP), Hanscom AFB, Massachusetts 01731, Contract Monitor: John Pustaver/ETEP	12. REPORT DATE: February 1977; 13. NUMBER OF PAGES: 272
14. MONITORING AGENCY NAME & ADDRESS (if different from Controlling Office)	15. SECURITY CLASS. (of this report): Unclassified; 15a. DECLASSIFICATION/DOWNGRADING SCHEDULE

16. DISTRIBUTION STATEMENT (of this Report)

Approved for Public Release; distribution unlimited.

17. DISTRIBUTION STATEMENT (of the abstract entered in Block 20, if different from Report)

Interactive Math Modeling.

18. SUPPLEMENTARY NOTES

19. KEY WORDS (Continue on reverse side if necessary and identify by block number)

Statistical Analysis
Harmonic Analysis
Gravity Waves
Correlation Analysis
Electron Transport
Speech Processing
Monte Carlo Calculations
Boltzmann Equation
Radar Simulation
Surface Acoustic Wave Filters
Loran Integral Equation

20. ABSTRACT (Continue on reverse side if necessary and identify by block number)

In this report, we will describe the techniques and computer programs developed to analyze various problems. The scope of our work extended into a variety of technical areas. A program was written to design a filter for analog-to-digital converted radar signals. The problem of low energy electron transport in irradiated solids was studied via four independent approaches: 1) an orders-of-scattering invariant imbedding calculation of transmitted and reflected scattered particle currents; 2) an iterative numerical solution for the one-dimensional Boltzmann equation for isotropic scattering.

DD FORM 1 JAN 73 1473 EDITION OF 1 NOV 65 IS OBSOLETE

403 370

Unclassified

SECURITY CLASSIFICATION OF THIS PAGE (When Data Entered)

EVALUATION

1. This is the Final Report on the contract which over the period from 1 Oct 73 to 30 Sep 76 worked on the development of mathematical models and statistical analysis techniques as applied to the digital processing of signals and the description of other physical systems including low energy electron transport, surface acoustic wave filter design, reflection from an idealized atmospheric wave and long range navigation.

2. The above work was of value in supporting research projects at Air Force Cambridge Research Laboratories and the Rome Air Development Center, Electronic Technology Deputate.

JOHN A. PUSTAVER, JR.
Contract Monitor
Electromagnetic Sciences Division

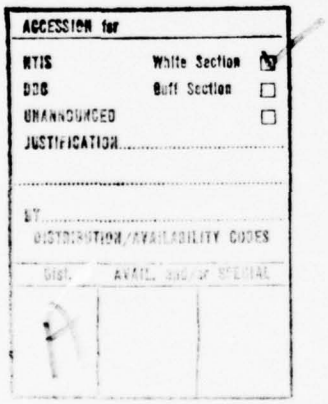

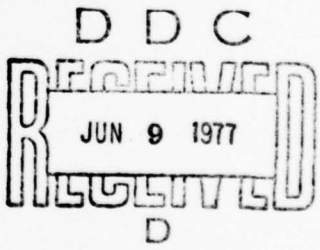

PRECEDING PAGE BLANK-NOT FILMED

FOREWORD

The computer programs and results discussed herein are the result of analytical research performed for:

The Analysis and Simulation Section (SUYA)
AFGL Computation Branch
L. G. Hanscom AFB, Mass. 01731

and

Rome Air Development Center
Deputy for Electronic Technology
L. G. Hanscom AFB, Mass. 01731

PRECEDING PAGE BLANK-NOT FILMED

TABLE OF CONTENTS

TABLE OF CONTENTS (Cont'd)

TABLE OF CONTENTS (Cont'd.)

I. INTRODUCTION

During the past year, we have worked on several tasks in a variety of areas. Programs were written to implement matched filtering techniques for the enhancement of simulated A/D converted radar signals immersed in a background of ground clutter. The problem of particle transport in scattering media was studied from the standpoint of an orders-of-scattering invariant imbedding analysis and through a numerical solution of the integral form of the Boltzmann equation for isotropic scattering. Also, a numerical technique for the study of the low energy electron transport problem was developed by means of a perturbative approach to the solution of the time-dependent Boltzmann equation. High energy electron transport was also studied with a program written to solve the Spencer-Lewis equation by means of the method of characteristics.

In other technical areas, programs were written to aid in the design of surface acoustic wave filters. Another program was prepared to aid in the processing and analysis of the output of atmospheric measurement devices. In addition, more development work was done on computer codes to analyze Doppler-shifted radar reflections from the ionosphere. Finally, in the area of speech processing technology, a realtime computer program was written for speech bandwidth compression. This program was designed to run on a minicomputer developed specifically for this purpose. A multipurpose monitoring program for loading realtime programs into the minicomputer was also written.

The above tasks will be described in detail in the following sections.

II. FILTERING OF A/D CONVERTED SIGNALS AND CLUTTER IN A SIMULATION PROGRAM

A. Introduction

The purpose of this effort was to extend the signal processing capabilities of a program to simulate radar signals backscattered by a field of moving objects imbedded in clutter.[1] By employing matched filtering techniques to enhance deterministic radar signals immersed in additive ground clutter returns, a filter was to be designed that would operate on the total received signal, after the signal had undergone front-end conversion by a finite word length A/D device. The predetection problem addressed in this chapter is of the sure-signal-in-noise type.

Since A/D conversion is a nonlinear process, there appears to be no reason to assume that weakly stationary clutter will remain weakly stationary after conversion. This leads one to expect that a maximized signal/noise ratio criterion, which is usually applied to the design of a filter working on a covariance stationary time series, may not be strictly optimal for the A/D converted process investigated in this study. Nevertheless, it appears to be a nearly optimal criterion in the sense that the deviations from wide-sense stationarity in the total noise covariance matrix are negligibly small in many practical situations, as will become evident from the analysis.

The asymptotic results obtained in the derivation were used as the basis for an algorithm to design predetection filter weights for the simulation program that had been written under the previous contract, No. F19628-74-C-0049. It should be mentioned that when the higher order terms in the signal/noise ratio are neglected, results are obtained which are in agreement with work reported in the literature.

B.1. Analysis

Let $\{s_m\}$ and $\{c_m^{(j)}\}$ be deterministic signals and clutter, respectively, sampled at times $t_m = m\Delta t$ ($m = 0, \pm 1, \pm 2, \ldots$) just prior to being received. Assume the signals are additively immersed in the clutter whose real (R) and imaginary (I) parts have zero means and are wide-sense stationary. It follows that

$$E\{c_m^R\} = E\{c_m^I\} = 0 \quad ,$$

$$E\{c_n^R c_m^R\} = C^{RR}(|n\Delta t - m\Delta t|) = C_{nm}^{RR} = C_{mn}^{RR} \quad ,$$

$$E\{c_n^I c_m^I\} = C^{II}(|n\Delta t - m\Delta t|) = C_{nm}^{II} = C_{mn}^{II} \quad ,$$

$$E\{c_n^R c_m^I\} = C_{nm}^{RI} = C_{mn}^{IR} \quad ,$$

where $E\{\cdot\}$ is the statistical expectation operator, and the member index (j) has been suppressed.

Upon being received the real and imaginary components of the total signal, $s_m + c_m$, are individually subjected to a front-end conversion as depicted by the A/D characteristic of figure II. B. 1: the quantizer is without a dead zone. For the non saturated situation, the staircase function can be resolved into a straight line and sawtooth component such that after the A/D transformation, $s_m + c_m$ becomes

$$y_m = s_m + c_m + g[s_m^R + c_m^R] + i\, g[s_m^I + c_m^I] \quad ,$$

where $g[\cdot]$ signifies the nonlinear transformation induced by the sawtooth component of the A/D mapping. $g[\cdot]$ can be approximated by a Fourier sine series leading to a total instantaneous A/D converted signal given by

$$y_m = s_m + c_m + \sum_{n=1}^{\infty} b_n \sin \beta_n (s_m^R + c_m^R)$$

$$+ i \sum_{n=1}^{\infty} b_n \sin \beta_n (s_m^I + c_m^I) \quad ,$$

with $b_n = \frac{q}{\pi n}$, $\beta_n = \frac{2\pi n}{q}$, and q = the quantization level.

If complex weights, w_m, are applied to the converted signal, the instantaneous filtered output from N consecutive input data points is given by

$$z(N\Delta t) = \sum_{m=0}^{N-1} w_m y_m \quad ,$$

so that

$$E\left\{|z|^2\right\} =$$

$$\sum_{m,m'} w_m w_{m'}^* \left[s_m s_{m'}^* + 0 + s_m E\left\{g_{m'}^*\right\} \right.$$

$$+ 0 + E\left\{c_m c_{m'}^*\right\} + E\left\{c_m g_{m'}^*\right\}$$

$$\left. + E\left\{g_m\right\} s_{m'}^* + E\left\{g_m c_{m'}^*\right\} + E\left\{g_m g_{m'}^*\right\} \right] \quad .$$

For predetection purposes it is of interest to seek weights that maximize the ratio

$$\eta = \frac{\sum_{m,m'} w_m w_{m'}^* \; s_m s_{m'}^*}{\sum_{m,m'} w_m w_{m'}^* \left[s_m E\left\{g_{m'}^*\right\} + E\left\{c_m c_{m'}^*\right\} + E\left\{c_m g_{m'}^*\right\} \right.}$$

$$\left. + E\left\{g_m\right\} s_{m'}^* + E\left\{g_m c_{m'}^*\right\} + E\left\{g_m g_{m'}^*\right\} \right] \quad .$$

η is not strictly a signal/noise ratio, because in the absence of clutter not all terms in the denominator vanish: terms corresponding to signal distortion remain. The g-terms are small, but time-varying contributions. Nevertheless for $c \neq 0$ the denominator contains noise and these other "unwanted" terms, and the criterion appears to be useful for design purposes.

η can be expressed as the ratio of two quadratic forms:

$$\eta = \frac{\sum_{m,m'} w^*_{m'} A_{m'm} w_m}{\sum_{m,m'} w^*_{m'} B_{m'm} w_m}$$

Following Cheng and Tseng[2], η is maximized when $\underline{w} = \underline{\underline{B}}^{-1}\underline{s}$. Obviously

$$B_{m'm} = E\{g^*_{m'}\} s_m + E\{c^*_{m'} c_m\} + E\{g^*_{m'} c_m\}$$

$$+ s^*_{m'} E\{g_m\} + E\{c^*_{m'} g_m\} + E\{g^*_{m'} g_m\} .$$

$\underline{\underline{B}}$ is not only Hermitian, but to an excellent approximation it is also a Toeplitz matrix, the inversion of which is readily effected; and the Toeplitz form signifies covariance stationarity. In view of the lengthy task involved in the formal manipulations to effect the ensemble averages in the expression for $B_{m'm}$ only the results will be presented here.

By expressing the sine functions of $g[\cdot]$ in terms of complex exponentials, the statistical averages lead to expressions composed of the characteristic functions and the derivatives of the characteristic functions of the clutter probability distributions. For an explicit evaluation of $B_{m'm}$ an assumption as to the statistical properties of the clutter must be made. The situation of interest to us involved complex Gaussian clutter having

$$E\{(c^R_m)^2\} = E\{(c^I_m)^2\} = \sigma^2 \quad .$$

In this case, the terms comprising $B_{m'm}$ evaluate to the following:

$$\underline{\Gamma_{m'm} \equiv E\left\{g^*_{m'}\right\} s_m + s^*_{m'} E\left\{g_m\right\}}$$

$$= s_m \sum_{n=1}^{\infty} b_n \left[\sin \beta_n s^R_{m'} - i \sin \beta_n s^I_{m'}\right] \exp\left(-\beta_n^2 \sigma^2/2\right)$$

$$+ s^*_{m'} \sum_{n=1}^{\infty} b_n \left[\sin \beta_n s^R_m + i \sin \beta_n s^I_m\right] \exp\left(-\beta_n^2 \sigma^2/2\right) \quad ,$$

$$\underline{\Psi_{m'm} \equiv E\left\{c^*_{m'} g_m\right\} + E\left\{g^*_{m'} c_m\right\}}$$

$$= \sum_{n=1}^{\infty} b_n \beta_n \left\{ \left[\cos \beta_n s^R_{m'} + \cos \beta_n s^R_m\right] C^{RR}_{m'm} \right.$$

$$+ \left[\cos \beta_n s^I_{m'} + \cos \beta_n s^I_m\right] C^{II}_{m'm}$$

$$- i \left[\left(\cos \beta_n s^R_m + \cos \beta_n s^I_{m'}\right) C^{IR}_{m'm}\right.$$

$$\left.\left. - \left(\cos \beta_n s^I_m + \cos \beta_n s^R_{m'}\right) C^{RI}_{m'm}\right]\right\} \exp\left(-\beta_n^2 \sigma^2/2\right) \quad ,$$

$$\underline{C_{m'm} \equiv E\left\{c^*_{m'} c_m\right\}}$$

$$= C^{RR}_{m'm} + C^{II}_{m'm} + i\left[C^{RI}_{m'm} - C^{IR}_{m'm}\right]$$

$$\underline{G_{m'm} \equiv E\{g^*_{m'}\, g_m\}}$$

$$= 1/2 \sum_{n=1}^{\infty} \sum_{\varkappa=1}^{\infty} b_n b_\varkappa \Big[\exp\Big(-\big(\sigma^2\beta_n^2 + \sigma^2\beta_\varkappa^2 - 2\beta_n\beta_\varkappa C^{RR}_{m'm}\big)/2\Big) \cos\big(\beta_n s^R_{m'} - \beta_\varkappa s^R_m\big)$$

$$- \exp\Big(-\big(\sigma^2\beta_n^2 + \sigma^2\beta_\varkappa^2 + 2\beta_n\beta_\varkappa C^{RR}_{m'm}\big)/2\Big) \cos\big(\beta_n s^R_{m'} + \beta_\varkappa s^R_m\big)$$

$$+ \exp\Big(-\big(\sigma^2\beta_n^2 + \sigma^2\beta_\varkappa^2 - 2\beta_n\beta_\varkappa C^{II}_{m'm}\big)/2\Big) \cos\big(\beta_n s^I_{m'} - \beta_\varkappa s^I_m\big)$$

$$- \exp\Big(-\big(\sigma^2\beta_n^2 + \sigma^2\beta_\varkappa^2 + 2\beta_n\beta_\varkappa C^{II}_{m'm}\big)/2\Big) \cos\big(\beta_n s^I_{m'} + \beta_\varkappa s^I_m\big)$$

$$+ i\Big\{\exp\Big(-\big(\sigma^2\beta_n^2 + \sigma^2\beta_\varkappa^2 - 2\beta_n\beta_\varkappa C^{RI}_{m'm}\big)/2\Big) \cos\big(\beta_n s^R_{m'} - \beta_\varkappa s^I_m\big)$$

$$- \exp\Big(-\big(\sigma^2\beta_\varkappa^2 + \sigma^2\beta_\varkappa^2 + 2\beta_n\beta_\varkappa C^{RI}_{m'm}\big)/2\Big) \cos\big(\beta_n s^R_{m'} + \beta_\varkappa s^I_m\big)$$

$$- \exp\Big(-\big(\sigma^2\beta_n^2 + \sigma^2\beta_\varkappa^2 - 2\beta_n\beta_\varkappa C^{IR}_{m'm}\big)/2\Big) \cos\big(\beta_n s^I_{m'} - \beta_\varkappa s^R_m\big)$$

$$+ \exp\Big(-\big(\sigma^2\beta_n^2 + \sigma^2\beta_\varkappa^2 + 2\beta_n\beta_\varkappa C^{IR}_{m'm}\big)/2\Big) \cos\big(\beta_n s^I_{m'} + \beta_\varkappa s^R_m\big)\Big\}\Big] \quad .$$

B.2 Asymptotic Expansion of $B_{m'm}$

In most applications of interest $(\sigma/q) > 1$, so that the first terms of $\Gamma_{m'm}$ and $\Psi_{m'm}$ dominate the expansions, and even they are small relative to $C_{m'm}$. Thus,

$$\Gamma_{m'm} \sim \frac{q}{\pi} \exp\big(-2\pi^2\sigma^2/q^2\big)\Big\{s_m\Big(\sin\frac{2\pi}{q}\, s^R_{m'} - i \sin\frac{2\pi}{q}\, s^I_{m'}\Big)$$

$$+ s^*_{m'}\Big(\sin\frac{2\pi}{q}\, s^R_m + i \sin\frac{2\pi}{q}\, s^I_m\Big)\Big\} \quad ,$$

$$\psi_{m'm} \sim 2\exp\left(-2\pi^2\sigma^2/q^2\right) \cdot$$

$$\cdot\left\{\left(\cos\frac{2\pi}{q}\, s^R_{m'} + \cos\frac{2\pi}{q}\, s^R_m\right) C^{RR}_{m'm}\right.$$

$$+\left(\cos\frac{2\pi}{q}\, s^I_{m'} + \cos\frac{2\pi}{q}\, s^I_m\right) C^{II}_{m'm}$$

$$-i\left[\left(\cos\frac{2\pi}{q}\, s^R_m + \cos\frac{2\pi}{q}\, s^I_{m'}\right) C^{IR}_{m'm}\right.$$

$$\left.\left. - \left(\cos\frac{2\pi}{q}\, s^I_m + \cos\frac{2\pi}{q}\, s^R_{m'}\right) C^{RI}_{m'm}\right]\right\} \quad ,$$

$$C_{m'm} = C^{RR}_{m'm} + C^{II}_{m'm} + i\left[C^{RI}_{m'm} - C^{IR}_{m'm}\right] \quad .$$

It should be noted that the above formulas hold for arbitrary deterministic signals. Specializing to the case where $s_m = A\exp(i\omega m\Delta t)$, it is apparent that

$$|\Gamma_{m'm}| < \frac{Aq}{\pi}\exp\left[-2\pi^2(\sigma/q)^2\right] \quad ,$$

and

$$|\psi_{m'm}| < 2\sigma^2\exp\left[-2\pi^2(\sigma/q)^2\right] \quad .$$

$C_{m'm}$ can be left as is, but $G_{m'm}$ requires careful consideration. The diagonal elements will be determined first.

Setting $m' = m$ and noting that $C^{RI}_{mm} = C^{IR}_{mm} = 0$ for clutter components that are uncorrelated at the same instant of time, the exponentials drop off rapidly except when $n = k$. In this case,

$$G_{m'm'} \sim 1/2 \sum_{n=1}^{\infty} \frac{q^2}{\pi^2 n^2} \left[2 - \exp\left[-2\pi^2 n^2 (\sigma/q)^2\right] \cos 2\beta_n s^R_{m'} \right.$$

$$- \exp\left[-2\pi^2 n^2 (\sigma/q)^2\right] \cos 2\beta_n s^I_{m'}$$

$$\left. + i \sum_{n \neq \kappa} \text{terms} \leq \exp\left[-4\pi^2 (\sigma/q)^2\right] \right] ,$$

$$\sim \frac{q^2}{\pi^2} \sum_{n=1}^{\infty} \frac{1}{n^2} \qquad \text{which evaluates to}$$

$G_{m'm} \sim \frac{q^2}{6}$ for an arbitrary deterministic signal.

For the off-diagonal elements it can be shown that the term n= k=1 dominates the expansion so that

$$G_{m' \neq m} \sim \frac{q^2}{2\pi^2} \left\{ \exp\left[-4\pi^2 (\sigma/q)^2 \left(1 - C^{RR}_{m'm}/\sigma^2\right)\right] \cdot \cos \frac{2\pi}{q} \left(s^R_{m'} - s^R_m\right) \right.$$

$$- \exp\left[-4\pi^2 (\sigma/q)^2 \left(1 + C^{RR}_{m'm}/\sigma^2\right)\right] \cdot \cos \frac{2\pi}{q} \left(s^R_{m'} + s^R_m\right)$$

$$+ \exp\left[-4\pi^2 (\sigma/q)^2 \left(1 - C^{II}_{m'm}/\sigma^2\right)\right] \cdot \cos \frac{2\pi}{q} \left(s^I_{m'} - s^I_m\right)$$

$$- \exp\left[-4\pi^2 (\sigma/q)^2 \left(1 + C^{II}_{m'm}/\sigma^2\right)\right] \cdot \cos \frac{2\pi}{q} \left(s^I_{m'} + s^I_m\right)$$

$$+ i \left(\exp\left[-4\pi^2 (\sigma/q)^2 \left(1 - C^{RI}_{m'm}/\sigma^2\right)\right] \cdot \cos \frac{2\pi}{q} \left(s^R_{m'} - s^I_m\right) \right.$$

$$\left. - \exp\left[-4\pi^2 (\sigma/q)^2 \left(1 + C^{RI}_{m'm}/\sigma^2\right)\right] \cdot \cos \frac{2\pi}{q} \left(s^R_{m'} + s^I_m\right) \right)$$

$$- \exp\left[-4\pi^2\left(\sigma/q\right)^2\left(1 - C^{IR}_{m'm}/\sigma^2\right)\right] \cdot \cos\frac{2\pi}{q}\left(s^I_{m'} - s^R_m\right)$$

$$+ \exp\left[-4\pi^2\left(\sigma/q\right)^2\left(1 + C^{IR}_{m'm}/\sigma^2\right)\right] \cdot \cos\frac{2\pi}{q}\left(s^I_{m'} + s^R_m\right)\Big]\Big)\Big\} \quad .$$

Clearly, the diagonal elements dominate for many situations of interest.

When $\left(\sigma/q\right) \gg 1$, $B_{mm} \approx \left(2\sigma^2 + q^2/6\right) + \ldots$

For pure real functions, others (reference 3) have found that the total noise power goes as $\left(\sigma^2 + q^2/12\right)$, a result equivalent to the one obtained above.

C.1 Validation of the A/D Logic

In the course of putting together the simulation program for the EAI 8400/8800 computer, the addition of the A/D logic patch led to CRT displays that were often difficult to interpret when the simulated wordlength was small—of the order of 6 bits/word or less. It was not clear whether the difficulty resulted from small mismatching errors between the frequency of the aircraft signal and the FFT output harmonics, as caused by the actual wordlength of the EAI computer, or whether the problem lay elsewhere: there might have been an error in the A/D logic patch that had escaped our notice, etc.

A concise version of the simulation program was written for the CDC-6600 computer, built upon the same A/D logic. Page plots of the amplitude spectrum showed very complex structures, and in the end it was decided that it was necessary to check the correctness of the A/D logic by running a test case for which the answer was known. A nontrivial and analytically tractable example was devised in which the instantaneous amplitude of the (harmonic) aircraft signal was quantized to assume values of either $\pm q/2$ or $\pm 3q/2$ after A/D conversion.

Note: DFT stands for discrete Fourier transform.

A comparison between $|DFT(y_m)|$ obtained from the simulation program with results derived analytically was needed. Let

$$\Gamma_p = C_p + i\, S_p \equiv DFT(y_m) \quad .$$

It is convenient to determine S_p first, and then to exploit the properties of the DFT of shifted functions to get C_p. With $y_m = y_m^R + i\, y_m^I$,

$$S_p = \sum_{m=0}^{N-1} y_m^I \exp\left[-i \frac{2\pi mp}{N}\right] \quad , \qquad p = 0, 1, \ldots, N-1 \quad .$$

Figure II. C. 1 shows how y_m^I can be expressed as the sum of two rectangular functions, $f_m^{(1)}$ and $f_m^{(2)}$. Both $f_m^{(1)}$ and $f_m^{(2)}$ are odd functions so that

$$f_m^{(1)} = - f_{N-m}^{(1)} \quad ,$$

and

$$f_m^{(2)} = - f_{N-m}^{(2)} \quad .$$

Substituting into the formula for S_p gives

$$S_p = \frac{q}{2}\left[\sum_{m=0}^{N/2-1} f_m^{(1)} \exp\left[-i \frac{2\pi mp}{N}\right] - \sum_{m=N/2}^{N-1} f_{N-m}^{(1)} \exp\left[-i \frac{2\pi mp}{N}\right]\right]$$

$$+ q\left[\sum_{m=a_1}^{a_2} f_m^{(2)} \exp\left[-i \frac{2\pi mp}{N}\right] - \sum_{m=N/2+a_1}^{N/2+a_2} f_{N-m}^{(2)} \exp\left[-i \frac{2\pi mp}{N}\right]\right] \quad .$$

Let $m' = N-m$ in the 2nd and 4th sums, and rearrange the order of summation. Since the amplitudes are zero at $m=0$ and $m=N/2$, and noting that $(N/2)-a_1 = a_2$, this leads to

$$S_p = -iq\left[\sum_{m=1}^{(N/2)-1} \sin\left(\frac{2\pi mp}{N}\right) + 2 \sum_{m=a_1}^{a_2} \sin\left(\frac{2\pi mp}{N}\right)\right] \quad .$$

The sums evaluate to[4].

$$S_p = i\,q\,\frac{\sin\left(\frac{p\pi}{2}\right)}{\sin\left(\frac{p\pi}{N}\right)}\left[\sin\left(N/2-1\right)\frac{\pi p}{N} + 2\sin\left(\frac{\mu\pi p}{N}\right)\right] \quad ,$$

where $\mu = a_1 - a_2 + 1 = \#$ of points in one of the pulses of $f_m^{(2)}$.

A 90 degree phase shift of y_m^I yields y_m^R so that

$$C_p = \exp\left[i\,\frac{\pi p}{2}\right] S_p \quad .$$

Finally

$$\Gamma_{4p+1} = 2q\,\frac{\left[\sin\,(N/2-1)\,\frac{\pi}{N}\,(4p+1) + 2\sin\frac{\mu\pi}{N}(4p+1)\right]}{\sin\frac{\pi}{N}\,(4p+1)} \quad ,$$

$$p = 0,\ 1,\ 2,\ \ldots \quad ,$$

and $\Gamma_p = 0$ for $p \neq 1,\ 5,\ 9,\ \ldots$.

Excellent agreement between Γ_p and the simulation program was obtained on the CDC system, and the Hybrid computer gave reasonable results when the parameters were very carefully chosen.

D.1 "Zoom" Filtering

A signal processing technique was sought for the simulation package that would provide good clutter suppression, and Doppler spectrum resolution that could be altered by varying a parameter in the algorithm. Changing the parameter was to lead to a "zoom" lens effect in the frequency domain. This was to be accomplished using a relatively low-order DFT routine having a fixed number of output points, similar to one that might provide frequency

domain output to a small display screen aboard an aircraft. To achieve th objectives, trade-offs had to be made: A rather large initial input data string was required, and magnified aliasing effects had to be tolerated in this scheme. The basic spectral resolution property of the zoom filter will become evident from the discussion that follows.

The A/D conversion of a signal composed of target and clutter terms results in a time series, y_m, as discussed in section B. 1. Applying the clutter suppression weights $\{w_m: m=0,1,2, \ldots Q-1\}$ to partially overlapping data strings yields filtered outputs, z_j. See figure II. D. 1.

$$z_j = \sum_{m=0}^{Q-1} y_{m+j\delta}\, w_m \qquad (\delta = \text{overlap or shift parameter})$$

$$= \sum_{m=0}^{Q-1} \left\{ s_{m+j\delta} + c_{m+j\delta} + g\left[s^R_{m+j\delta} + c^R_{m+j\delta} \right] + i\, g\left[s^I_{m+j\delta} + c^I_{m+j\delta} \right] \right\} w_m \quad ,$$

with $j=0,1, \ldots S-1$.

The DFT of S values of z_j is given by

$$a_\ell = \sum_{j=0}^{S-1} z_j \exp\left[-i\, 2\pi \ell j/S \right] \quad , \qquad \ell = 0,1,\ldots,S-1 \quad .$$

The displayed quantities would be 20 log $|a_\ell|$.

The spectral resolution behavior of the zoom filtering scheme becomes apparent if one considers a signal due to a target having a constant radial velocity component relative to an airborne radar receiver. Then,

$$s_m = A \exp[2\pi i\, m\, L^*/Q] \qquad m=0, 1, \ldots Q-1 \quad ,$$

where L^* is the harmonic corresponding to the aircraft Doppler frequency, for a Q-point data string[5]. Neglecting the A/D conversion and clutter effects, so that the salient features of the spectral resolution are not obfuscated by the mathematics, and substituting s_m into a_ℓ leads to an expression of the form:

$$a_\ell = A \sum_{m=0}^{Q-1} w_m \exp\left[2\pi i\, m\, L^*/Q\right] \sum_{j=0}^{S-1} \exp\left[2\pi i\, j \left(L^*\delta/Q - \ell/S\right)\right] \quad .$$

The spectrum peaks at $\ell = S\delta(L^*/Q)$. For a target at $L^* + \Delta L^*$, the peak would occur at $\ell = S\delta(L^* + \Delta L^*)/Q$. The separation in the zoom frequency domain is therefore given by

$$\Delta\ell = \text{MODULO}[S\delta(\Delta L^*)/Q,\ S]$$

The magnification effected by the zoom process is given by $\frac{\Delta\ell}{\Delta L^*} = S\delta/Q$. Increasing the magnification is done at the expense of greater aliasing. Also, as figure II.D.1 suggests, the total number of y_m data points required to produce S points of $|a_\ell|$ is $Q + (S-1)\delta$, which can be substantially larger than Q.

It might be noted that in the expression for a_ℓ, the m-sum is related to the DFT of the clutter suppression weights, w_m. To be consistent with the notation adopted in this study, if w_m and W_p are DFT pairs, then the m-sum evaluates to $W_{p=-L^*}$, which acts as a constant amplitude factor in the ℓ-domain for a given value of L^*. Summing over j and taking the absolute magnitude leads to

$$|a_\ell| = |W_{-L^*}| \quad \frac{\sin \pi(L^*\delta/Q - \ell/S)S}{\sin \pi(L^*\delta/Q - \ell/S)} \quad .$$

This does not complete the discussion on the presence and resolution of two or more targets, as might be determined by an observer sitting at a scope and viewing the display of a_ℓ. The relative scattering amplitudes of the targets, the line shapes on the screen, the frequency mismatch between the target signals and the FFT output frequencies, etc. contribute to whether an observer will decide if one or more targets are present. But, the zoom filtering scheme does "spread out" the picture.

An important feature of the simulation program is that it permits one to perform simulations involving accelerating targets, letting one judge how many targets are present and with what speeds they are moving, without resorting to rather sophisticated analyses that in the end do not tell what will be decided by an observer viewing a screen. With finite wordlength and clutter entering the picture, simulation experiments in this context should provide additional knowledge about resolution and parameter estimation problems. As the program is currently constituted, a sequence of frequency-plane "snapshots" are printed out showing the time varying spectral signatures.

E. Simulation Program Input/Output

Figure II. E. 1 illustrates the configuration of programs and I/O serving the simulation program. Three sources of input are needed for its execution:

1) NAMELIST data cards must be provided (by the user) which select the various target and noise parameters as well as the filtering options.

2) A clutter time series that has been tailored according to a particular spectral profile must be read in by the simulation package. The clutter corresponds to antenna modulated environmental noise in which the aircraft and target signals will be immersed.

3) Data cards containing the clutter suppression filter weights must be inserted immediately after the NAMELIST cards. The clutter weights originate as punched data from the WNOPT-program.

The simulation deck uses the following control cards:

```
VSN(MFN=CC0030)
REQUEST, MFN, MF, E, HY.(CC0030/COHEN)
LABEL(TAPE9, R, M=MFN, L=CLUTTERB100975)
FTN(R=3, OPT=1, SL, PL=7000, B=SM)
ATTACH(FOURT, FFTFOURT4334, ID=COHEN, MR=1)
LDSET(PRESET=ZERO)
LOAD(FOURT)
SH.
EXIT.
EXIT.
```

The output of a simulation run is composed of a listing with the following information:

1. Processing constraints
   Signal data
   Target #1 data
   Target #2 data
2. NAMELIST parameter variables
3. w_m^{opt} array
4. 20 log $|W_p|$
5. Page plots of 20 log $|a_1|$ for t = 0 (ΔT) TMAX

E.1 NAMELIST Variables and Definitions

$PARAM	
NWNDO	SIZE OF FFT WINDOW (without the ZOOM option)
NSKIP	SIZE OF SHIFT WINDOW
SPRD	SPREAD OF WINDOW TRANSITION BAND
TCA	TIME OF START OF FFT WINDOW
TMAX	FINAL TIME OF LAST POINT PROCESSED
VA	AIRCRAFT SPEED (MACH NO.)
S2NDB	SIGNAL/CLUTTER RATIO (DB)
BITS	SIMULATED WORD LENGTH
FTOL	NUMBER OF S.D. TOLERANCE
T1	INITIAL TIME (TARGET 1)
T1A	TIME OF MAXIMUM SPEED (TARGET 1)
T1B	END TIME OF MAX. SPEED (TARGET 1)
V1MAX	MAXIMUM SPEED (TARGET 1)
ALP1	PROFILE DECAY RATE (TARGET 1)
SGM1DB	CROSS SECTION (DB - TARGET 1)
NS	NO. ZOOM FFT POINTS DISPLAYED
NDEL	OVERLAP OR DISPLACEMENT PARAMETER (ZOOM)
NQ	DATA STRING LENGTH FOR ZOOM PROCESS.
LZOOM	ZOOM OPTION SWITCH (0 = bypass, 1 = process)
T2	INITIAL TIME (TARGET 2)
T2A	TIME OF MAXIMUM SPEED (TARGET 2)
T2B	END TIME OF MAX. SPEED (TARGET 2)
V2MAX	MAXIMUM SPEED (TARGET 2)
ALP2	PROFILE DECAY RATE (TARGET 2)
SGM2DB	CROSS SECTION (DB - TARGET 2)
$	

E.2 Synthesis of Clutter Series

Program FILT III reads the Gaussian variates stored on file GAUSSFILE of a multifile labelled tape, CC0030, and filters them in a manner controlled by the user through his choice of the NAMELIST parameter set. A particular set of values will define one filter configuration, and the time series emerging from the filter will be stored on disk. The clutter can be accessed from the disk permanent file or transferred back to CC0030 where a new file is created for longer term storage. The simulation program can then access the type of clutter of interest to the user by means of the appropriate control cards.

In the course of its execution, FILT III prints out the following information:

1. The transfer function of the filter used to shape the clutter.
2. A header that identifies the filter that shaped the clutter.
3. The mean, variance, standard deviation, autocovariance function, and histograms of the real part, imaginary part, amplitude, and phase of the complex clutter.

FILT III in its deck form employs the following control cards:

```
VSN (MFN = CC0030)
REQUEST, MFN, MF, E, RING, HY.  (CC0030/COHEN)
LABEL (TAPE6, R, M = MFN, L = GAUSSFILE)
FTN (B = SH, R = 3, OPT = 1, SL, PL = 7000)
REQUEST (TAPE7, *PF)
ATTACH (FOURT, FFTFOURT4334, ID = COHEN, MR = 1)
LDSET (PRESET = ZERO)
LOAD (FOURT)
SH (INPUT, OUTPUT, TAPE6, TAPE7)
CATALOG (TAPE7, CLUTTERX4334, ID = COHEN, MR = 1, RP = 999)
EXIT.
```

Program PF2TAPE moves the Butterworth filtered clutter from the permanent file CLUTTERX4334 to a file on CC0030 using the following control cards:

```
ATTACH (TAPE7, CLUTTERX4334, ID = COHEN, MR = 1)
VSN (MFN = CC0030)
REQUEST, MFN, MF, E, RING, HY. (CC0030/COHEN)
LABEL (TAPE9, W, M = MFN, L = CLUTTERB100975)
FTN (SL, PL = 7000, B = SH, R = 3, OPT = 1)
LDSET (PRESET = ZERO)
SH (INPUT, OUTPUT, TAPE7, TAPE9)
EXIT.
```

E.3 Generation of Clutter Suppression Weights

The clutter reduction weights are created by running program WNOPT. The user makes use of, or supplies, a subroutine which defines the complex covariance matrix, $\underline{\underline{C}}$ and the program subsequently forms the matrices $\underline{\underline{G}}$ and $\underline{\underline{B}}$ using the formulas derived in section B.2. $\underline{\underline{B}}$ is then inverted with a Toeplitz inversion code and the resulting matrix is used to multiply the (complex conjugate of the) harmonic signal vector under consideration. The vector produced by this matrix-vector multiplication operation has components which form the set of optimum weights for the signal which is to be detected in the clutter. A signal having a frequency other than the one for which the weights were designed will lead to a lower signal-clutter-ratio. This 'mismatched' signal-clutter-ratio is page-plotted by WNOPT for the user's edification. Finally, the program punches out the weights onto cards according to the FORMAT(8(1X, F9.5)).

WNOPT prints out the following information:

NAMELIST variables
Frequency harmonic at which the aircraft signal peaks
Covariance matrix, $\underline{\underline{C}}$
Input vector of normalized first row of $\underline{\underline{B}}$
Complex conjugate of input signal vector, $\underline{s}$

The output of the Toeplitz routine consists of listings and page-plots of

$\underline{w}$ values (clutter suppression weights)
Absolute maximum value of $\underline{w}$
Magnitude of w_m
DB - magnitude of w_m
20 log DFT(w_m)
Phase of w_m
Mis-matched signal/noise ratio in DB
$\underline{\underline{C}}$ matrix
$\underline{\underline{G}}$ matrix
$\underline{\underline{B}}$ matrix

The control cards required by the WNOPT deck are specified below.

```
FTN, R=3, OPT=1, SL, PL=7000.
ATTACH (FOURT, FFTFOURT4334, ID=COHEN, MR=1)
ATTACH (BESJ, JNOFXARCX4334, ID=COHEN, MR=1)
ATTACH (HTOEP, TOEPLITZX4334, ID=COHEN, MR=1)
MAP (ON)
LDSET (PRESET=ZERO)
LOAD (FOURT)
LOAD (BESJ)
LOAD (HTOEP)
LGO.
```

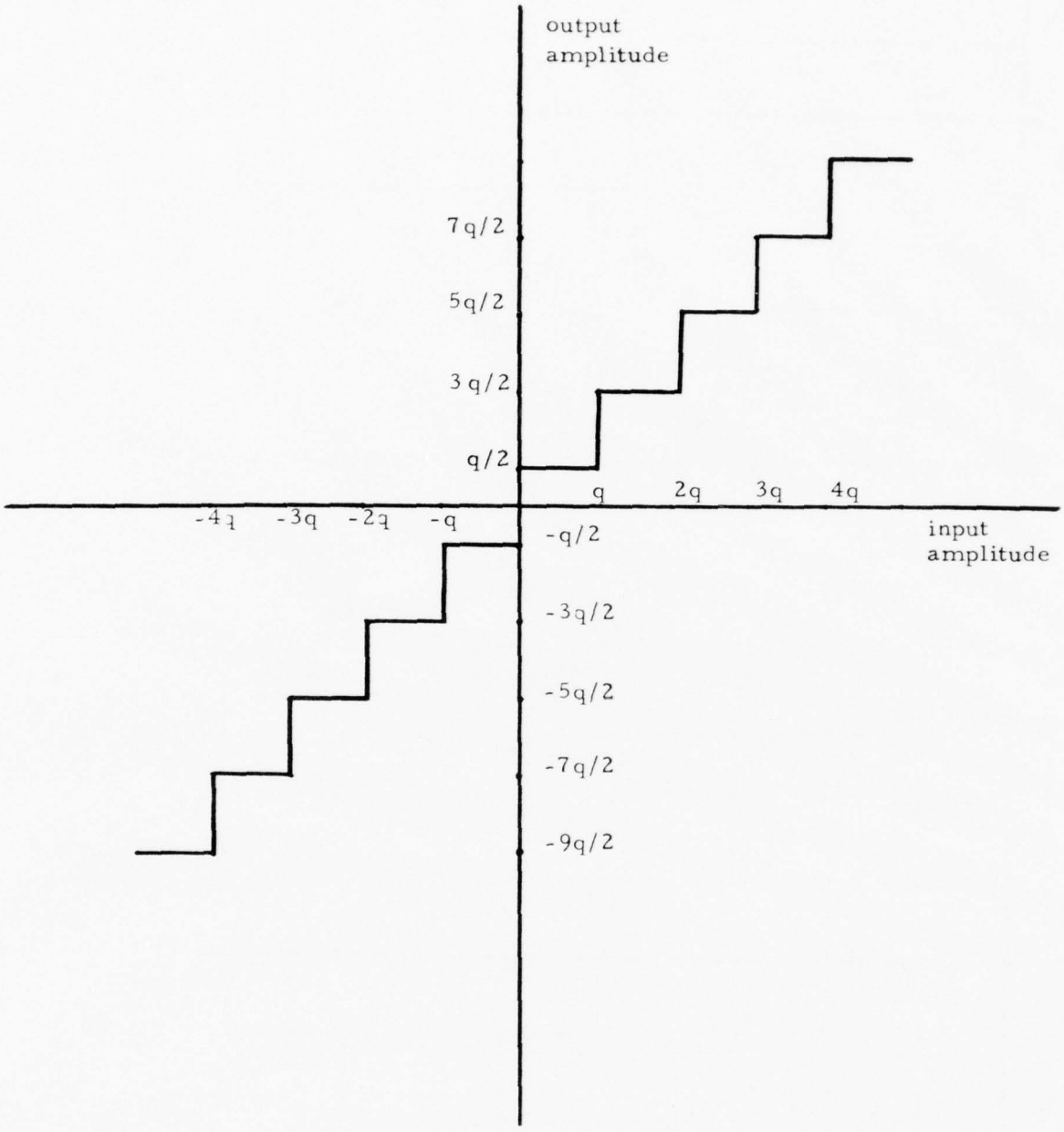

Figure II.B.1
A/D TRANSFER CHARACTERISTIC

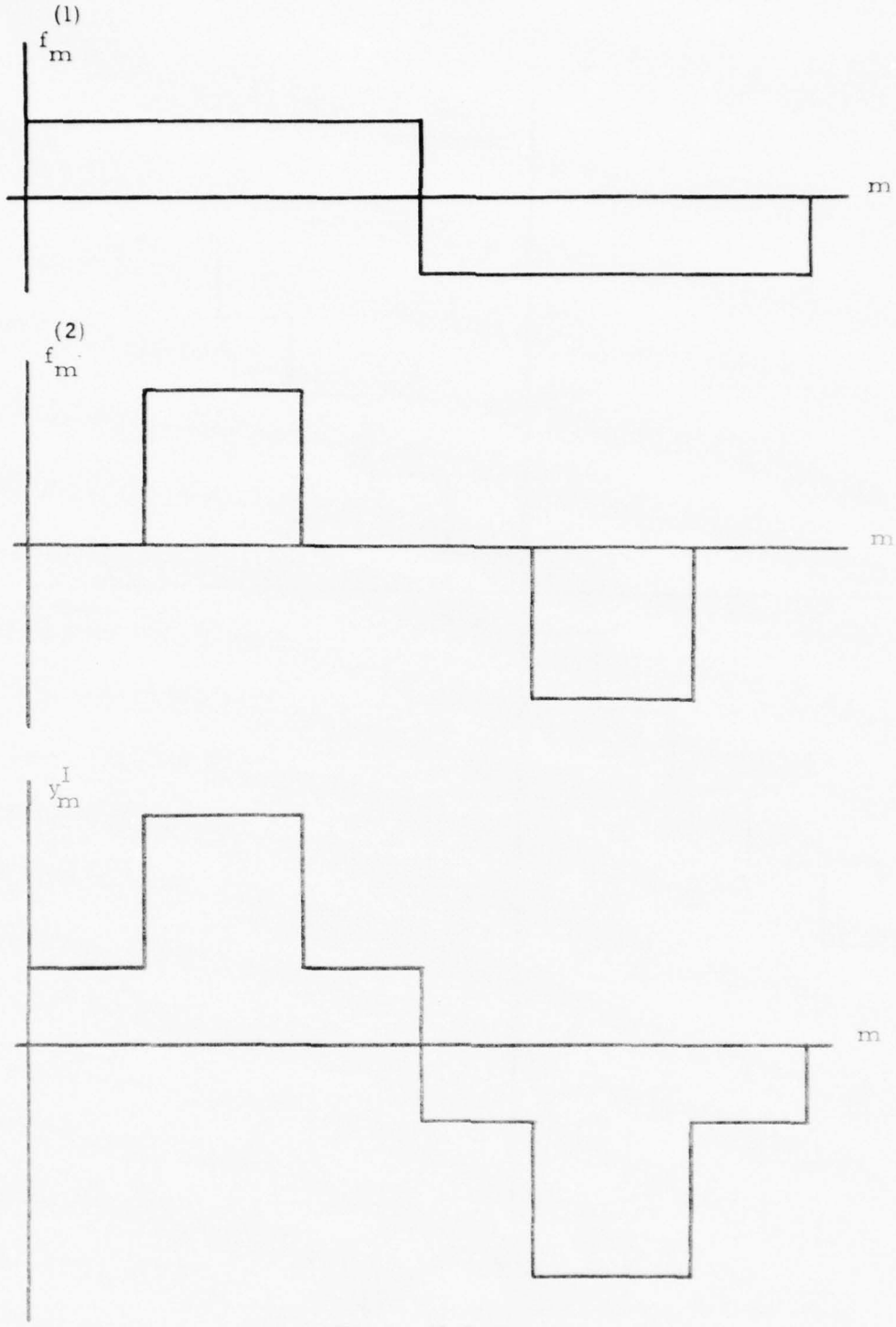

Figure II.C.1
RECTANGULAR PULSE FUNCTIONS

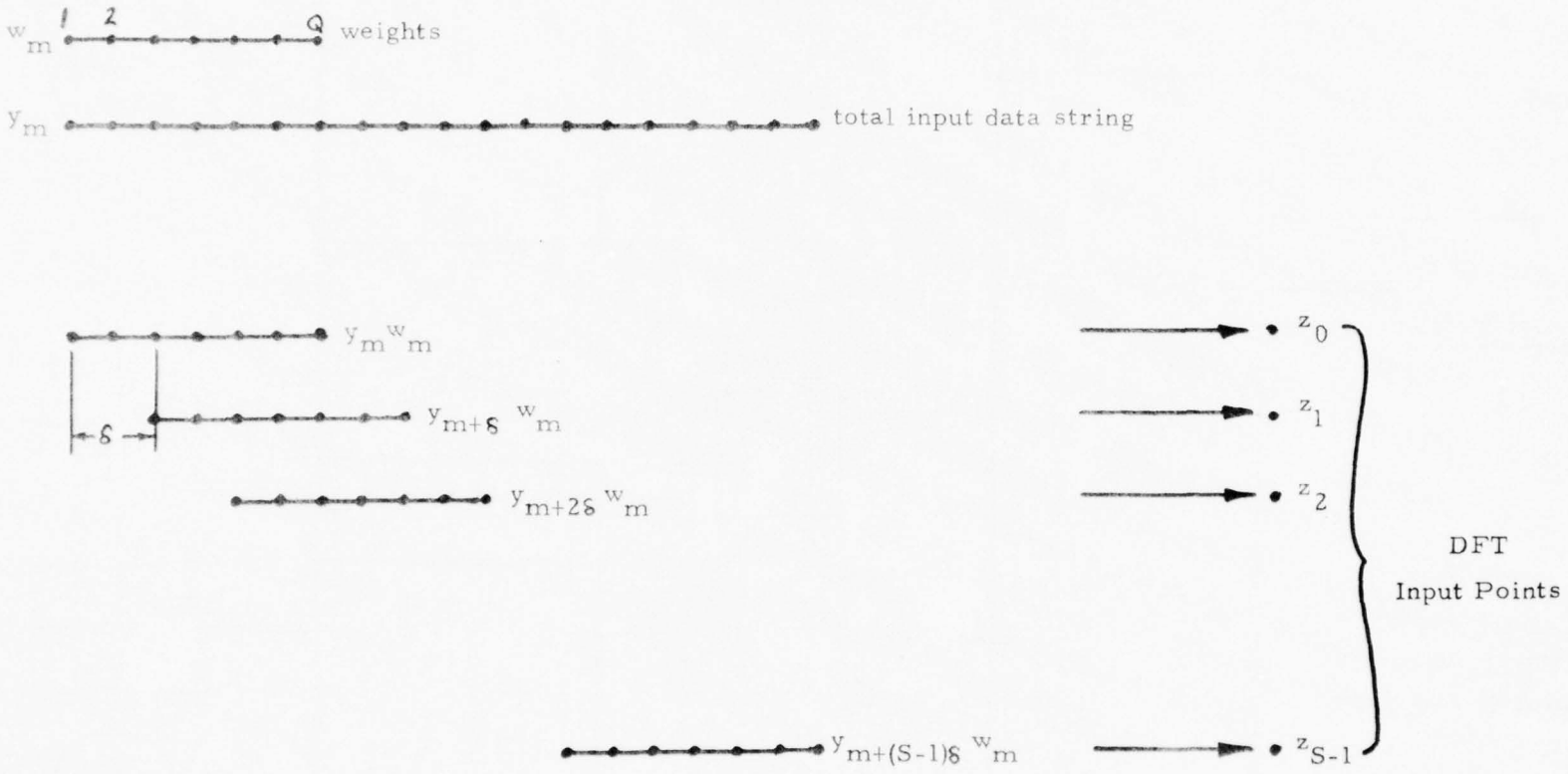

Figure II.D.1
ZOOM FILTERING QUANTITIES

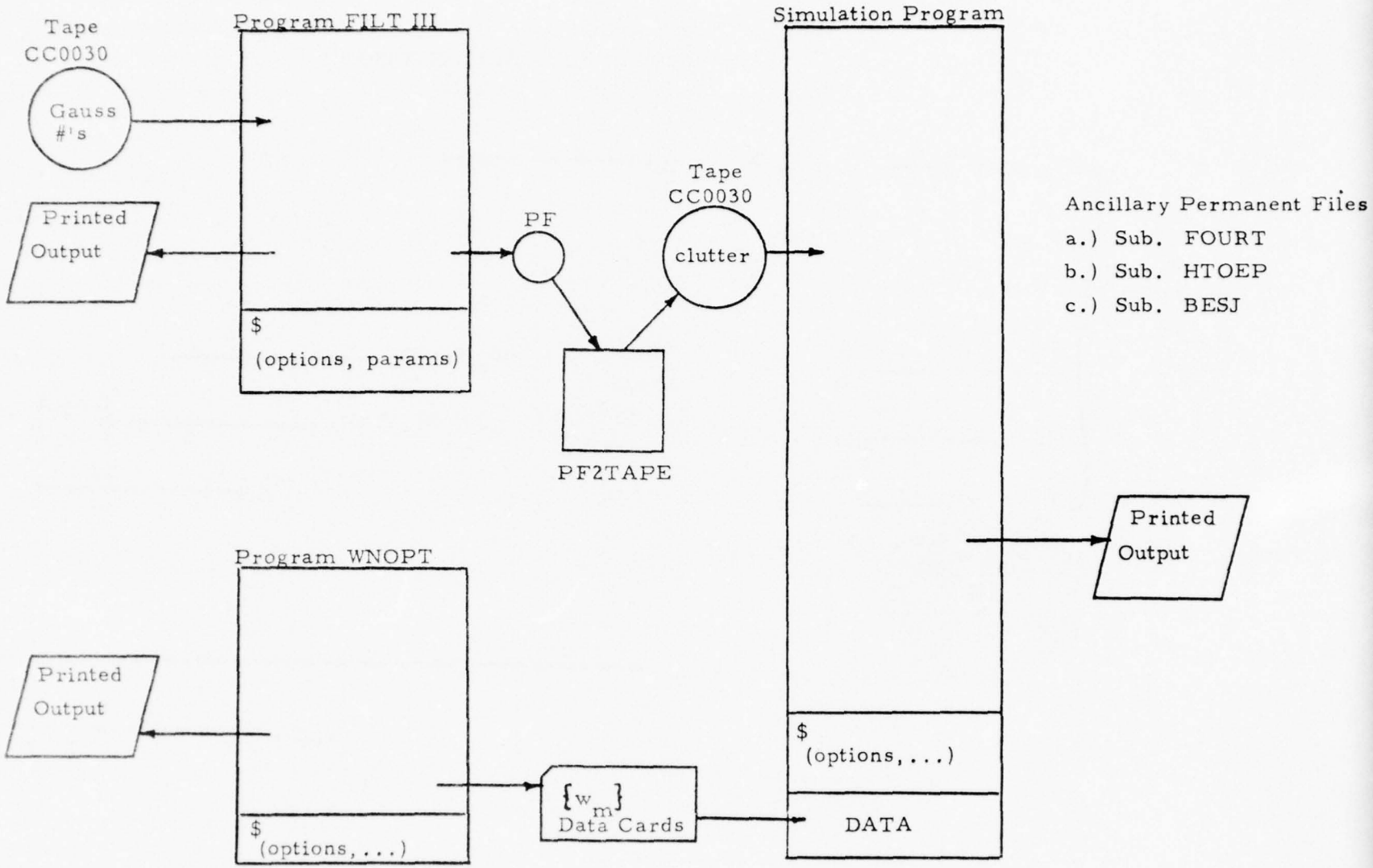

Figure II.E.1
OVERVIEW OF SIMULATION HARDWARE/SOFTWARE

II. REFERENCES

1. Woolf, S., O'Brien, J.V., Cohen, E., Hsiung, J., Tichovolsky, E.J. Development of Mathematical Models and Statistical Analysis Techniques as Applied to the Digital Processing of Signals and the Description of Other Physical Systems. ARCON Corporation, Scientific Report No. 1, AFCRL Contract No. F19628-74-C-0049, February 28, 1975.

2. Cheng, D.K., and Tseng, F.L., "Gain Optimization for Arbitrary Antenna and Arrays, "IEEE Trans. on Antennas and Propagation, November, 1965, Vol. AP-13, No. 6, pp. 973, 974.

3. Gold, B., and Rader, C.M., Digital Processing of Signals, McGraw-Hill, 1969, Ch. 4.

4. Gradshteyn, I.S., and Ryzhik, I.M., Tables of Integrals, Series, and Products, Academic Press, 1965, p. 29.

5. Ibid (1), p. 34.

III. LOW ENERGY ELECTRON TRANSPORT— AN INVARIANT IMBEDDING ANALYSIS OF PARTICLE TRANSPORT INCORPORATING ORDERS-OF-SCATTERING

A. INTRODUCTION

Invariant Imbedding theory has been applied extensively to particle transport problems, especially in nuclear particle shielding calculations. A principal advantage of the invariant imbedding approach is that it is a direct calculation of particle current emergent from a scattering medium and does not require the calculation of the particle flux at all points within the medium. Conventional invariant imbedding calculations have the disadvantage that they often prove to be computationally burdensome, hence their practicality has been somewhat limited. The word "conventional" is applied here to denote the class of calculations which at once include all orders of scattering, zero to infinity, and for which the dependent variable, the particle current, is an explicit function of the particle energy, position and direction of motion. For this reason invariant imbedding has not been extensively applied to such problems as slowing down of neutrons and electrons in scattering media. This has not proven to be a serious handicap at high energies where continuous slowing down theory can be applied. However, at low energies the success achieved by alternative methods is not nearly as formidable. Prominent among these alternatives are methods spanning the wide range of sophistication from the direct solution of the Boltzmann Equation to Monte Carlo calculations. The Boltzmann approach consists of a flux calculation, which for even the case of isotropic scattering is not trivial. For scattering other than isotropic, spherical harmonic expansions can be performed on either the differential or integral form of the Boltzmann equation. This approach becomes impractical when the scattering anisotropy extends beyond first order. At the other extreme, Monte Carlo calculations while providing a relatively certain means of achieving the solution in most cases, can be costly when high accuracy is required.

A class of particle transport problems exists for which a variation of the invariant imbedding method seems most appropriate, those instances where the average energy of a particle can be related to the number of collisions it

has undergone in the course of transport through a scattering medium. For these cases a method for calculating emergent n-th scattered particle currents from scattering media has been developed which combines an orders-of-scattering formulation with the familiar invariant imbedding method. The equations for the transmitted and reflected current are evolved through the consideration of the dependence of the n-th scattered current on the lower order scattered currents. The final expressions for these currents assume the form of coupled integral recursion relations expressing the interdependence of the currents of the various scattering orders. In the sections that follow, these invariant imbedding recursion relations will first be presented for the simple one-dimensional case or rod model, and then for the case of angle-dependent particle transport in a slab geometry. In the former case comparisons are made with the exact analytic result for the total transmitted and reflected currents obtained from the classical rod model, and for the case of scattering in a slab geometry, the results are compared with those obtained by two independent methods, the solution of the one-dimensional Boltzmann equation for isotropic scattering and a Monte Carlo calculation. The application of the orders-of-scattering invariant imbedding method, henceforth to be referred to as OOSII to anisotropic scattering situations is then demonstrated for two cases, anisotropy such as encountered in the elastic scatter of neutrons from hydrogen, and the scattering of low energy electrons (hot) by phonons, a process for which a screened Rutherford cross-section has been proposed on the basis of empirical observations.[1]

B. SCATTERING IN ONE DIMENSION

B.1. Current Equations

Consideration of the one-dimensional geometry is advantageous for several reasons, the most notable of which are:

1) the geometric simplification allows for the development of the basic equations without the complicating presence of angular variables which would tend to obscure the fundamental logic.

2) the results obtained can be compared with well-known analytical results, thus providing verification of both the basic equations and the numerical means for their solution.

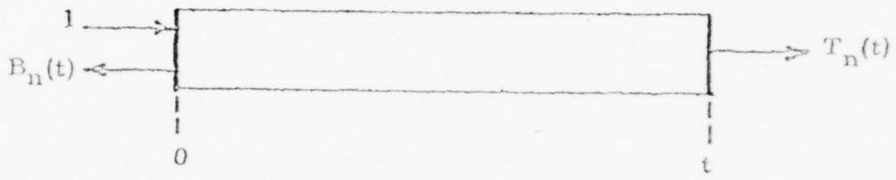

Figure III. B. 1

If a unit particle current is injected into the left end of a rod of length t (figure III. B. 1), then the quantities $T_n(t)$ and $B_n(t)$ can be defined such that $\begin{Bmatrix} T_n(t) \\ B_n(t) \end{Bmatrix}$ is the $\begin{Bmatrix} \text{transmitted} \\ \text{reflected} \end{Bmatrix}$ particle current emerging from the $\begin{Bmatrix} \text{right} \\ \text{left} \end{Bmatrix}$ end of the rod of length t after n interactions.

Expressions[2] for these currents are given by the following set of coupled integral recursion relations, with their accompanying initial conditions.

$$T_n(t) = \frac{f}{\lambda} e^{-t/\lambda} \int_o^t e^{x/\lambda} T_{n-1}(x)dx + \frac{b}{\lambda} e^{-t/\lambda} \sum_{m=1}^{n-1} \int_o^t e^{x/\lambda} B_m(x) T_{n-m-1}(x)\, dx \,, \tag{1}$$

$$B_n(t) = \frac{b}{\lambda} \sum_{m=0}^{n-1} \int_o^t T_{n-m-1}(x)\; T_m(x)\, dx \quad , \tag{2}$$

$$T_n(0) = 0 \quad , \quad n \geq 1 \tag{3a}$$

$$T_o(t) = e^{-t/\lambda} \quad , \tag{3b}$$

$$B_o(0) = 0 \quad , \tag{4a}$$

$$B_o(t) = 0 \quad . \tag{4b}$$

Here x is a point in the rod interior,

f is the probability of scatter in the forward direction,

b is the probability of scatter in the backward direction,

and λ is the scattering mean-free-path.

Although it is possible to obtain exact solutions for all orders of scattering, such an analytical approach becomes impractical beyond n-3. The expressions for T_n and B_n are listed below for $n \leq 3$.

$$T_o(t) = e^{-t/\lambda} \quad , \tag{5a}$$

$$T_1(t) = e^{-t/\lambda} f \frac{t}{\lambda} \quad , \tag{5b}$$

$$T_2(t) = e^{-t/\lambda}\left[\frac{f^2t^2}{2\lambda^2} + \frac{b^2t}{2\lambda} - \frac{b^2}{4}\left(1 - e^{-2t/\lambda}\right)\right] \tag{5c}$$

$$T_3(t) = e^{-t/\lambda}\frac{f^3t^3}{6\lambda^3} + \frac{fb^2}{2}\left(t^2/\lambda^2 + t/2\lambda - 1\right) + \frac{fb^2}{2}\left(1 - \frac{3}{2}\frac{t}{\lambda}\right)e^{-2t/\lambda} \quad , \tag{5d}$$

$$B_1(t) = \frac{b}{2}\left[1 - e^{-2t/\lambda}\right] \quad , \tag{6a}$$

$$B_2(t) = \frac{fb}{2}\left[1 - \left(1 + 2t/\lambda\right)e^{-2t/\lambda}\right] \tag{6b}$$

$$B_3(t) = \frac{f^2b}{2} - \frac{f^2b}{2}\left(2\frac{t^2}{\lambda^2} + 2\frac{t}{\lambda} + 1\right)e^{-\frac{2t}{\lambda}} + \frac{b^3}{8}\frac{t}{\lambda}e^{-\frac{2t}{\lambda}} + \frac{b^3}{8}\left(1 - e^{-\frac{4t}{\lambda}}\right), \tag{6c}$$

B.2. Numerical Solution of Current Equations

Numerical solutions for equations (1) and (2) were obtained for values of n up to 40 by means of a semi-analytical method based on the assumption that the T_n and B_n could be considered piecewise linear. If an appropriate integration interval (t_1, t_2) could be found over which the approximation holds, then integrals of the type occurring in (1) and (2) could be readily evaluated. The linearity assumptions are

$$T_n(x) \doteq m_T^n x + b_T^n \qquad \left(t_1 \leq x \leq t_2\right) \tag{7a}$$

and

$$B_n(x) \doteq m_B^n x + b_B^n \tag{7b}$$

where m_T^n and m_B^n are the slopes over the interval (t_1, t_2) for the n-th scattered transmitted and reflected currents respectively, and b_T^n and b_B^n are the corresponding intercepts at x_1, $x=t_1$. There are three distinct integral forms present in (1) and (2) which under the above assumptions, are readily evaluated. That is

$$\int_{t_1}^{t_2} e^{x/\lambda}\, T_\ell(x)\, dx \doteq \lambda e^{x/\lambda}\left[m_T^\ell\,(x-\lambda) + b_T^\ell\right]\Bigg|_{t_1}^{t_2} \tag{8a}$$

$$\int_{t_1}^{t_2} e^{x/\lambda}\, T_\ell(x)\, B_k(x)\, dx \doteq$$

$$\lambda e^{x/\lambda}\left[m_T^\ell\, m_B^k\left(x^2 - 2\lambda x + 2\lambda^2\right) + \left(m_B^k\, b_T^\ell + m_T^\ell\, b_B^k\right)(x-\lambda) + b_T^\ell\, b_B^k\right]\Bigg|_{t_1}^{t_2}, \tag{8b}$$

$$\int_{t_1}^{t_2} T_\ell(x)\, T_k(x)\, dx \doteq \left[m_T^\ell\, m_T^k\,\frac{x^3}{3} + \left(m_T^\ell b_T^k + m_T^k b_T^\ell\right)\frac{x^2}{2} + b_T^\ell b_T^k\, x\right]\Bigg|_{t_1}^{t_2}. \tag{8c}$$

Since exact expressions were available for $T_n(t)$ and $B_n(t)$ up to n=3, the approximate method of solution was employed only for values of $n \geq 4$.

A computer code was written to solve the system of recursion relations. Slopes and intercepts for the first three orders of scattering were readily available from the exact expressions. The computer program was written in such a way as to compute the currents for all orders of scattering, up to n=40, in one pass for each increment of rod length. Computations were made of T_n and B_n for 51 values of rod length ranging from t = 0.0 to t = 10.0 mean-free-paths in steps of 0.2 mfp. It was found that an integration interval of 0.004 mfp proved adequate to satisfy the piecewise linearity assumption. This was verified by a comparison of the computational results for the case

where f = 1, b = 0 with exact answers obtained by evaluation of the Poisson distribution. Additional verification was obtained by comparison of the current totals for other values of f and b over the first 40 orders of scattering with exact expressions obtained for the totals over all orders by the "classical" method of solution for the rod model. The values of the three integral forms (8) were accumulated from one step in t to the next, eliminating the necessity to start the integration from t = 0 for each rod length of interest.

B.3 Computational Results

Plots of the computational results are given in figures III. B. 2 through III. B. 7. The transmission and reflection current curves are plotted vs. order of scattering for rods ranging in length from 1 to 10 mfp in steps of 1 mfp (the scattering mean-free-path was assumed constant for all collision orders) and for the following values of scattering probability:

1) f = 0.5, b = 0.5 --- figures III. B. 2a, b
2) f = 0.6, b = 0.4 --- figures III. B. 3a, b
3) f = 0.7, b = 0.3 --- figures III. B. 4a, b
4) f = 0.8, b = 0.2 --- figures III. B. 5a, b
5) f = 0.9, b = 0.1 --- figures III. B. 6a, b
6) f = 1.0, b = 0.0 --- figure III. B. 7a

and 7) Poisson distribution curves --- figure III. B. 7b.

The last set (figures III. B. 7a, b) are included for the purposes of comparison. Only cases of conservative scattering were considered (f + b = 1), although this was not a necessary restriction.

B.4 Comparison of One-Dimensional Results with those Obtained Using the Classical Treatment of the Rod Model

An independent means of testing the validity of the orders-of-scattering results can be found in the classical treatment of the rod model. Simple expressions for the total (infinite order) transmitted and reflected currents can be readily obtained which when evaluated should yield results which agree closely with the totals of the orders-of-scattering currents up to 40 orders, at least for the shorter rod lengths. Determination of the total currents to infinite order according to the classical treatment[3] are given as follows:

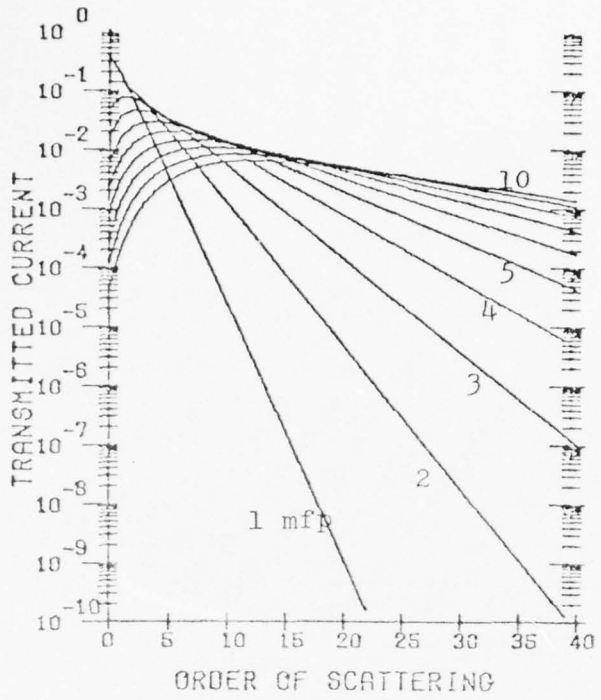

Figure III. B. 2a
Transmitted current vs. order of scattering for 10 rod lengths: f=0.5

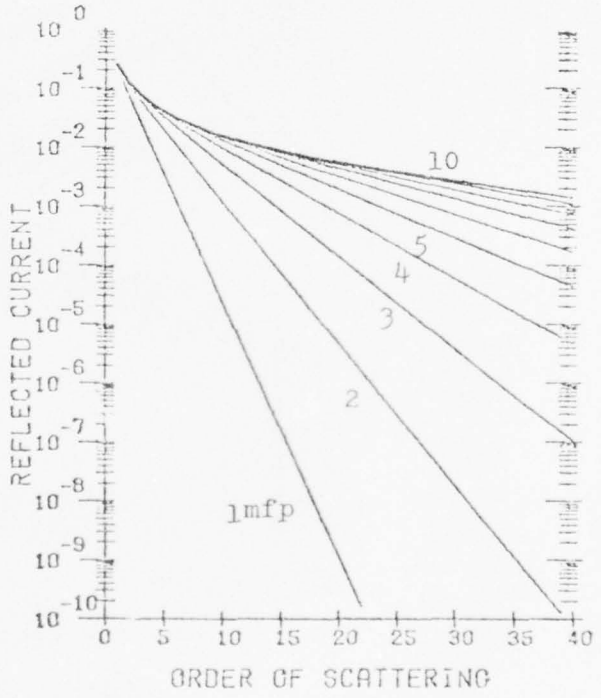

Figure III. B. 2b
Reflected current vs. order of scattering for 10 rod lengths: f=0.5

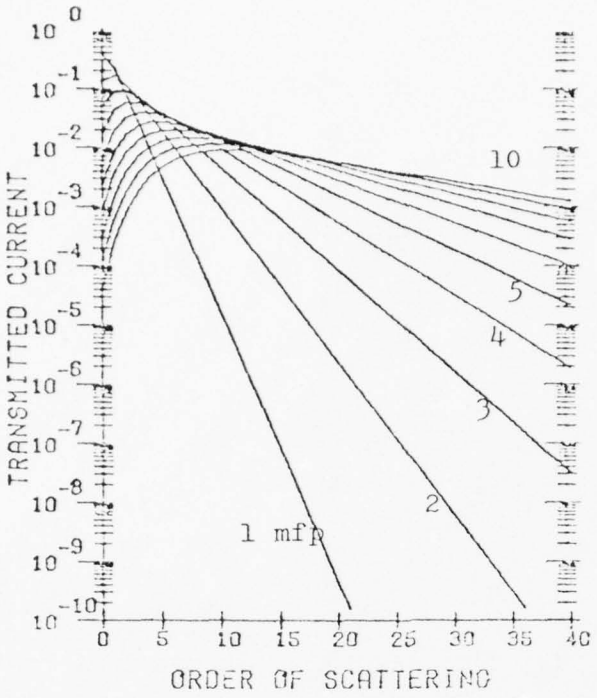

Figure III. B. 3a
Transmitted current vs. order of scattering for 10 rod lengths: f=0.6

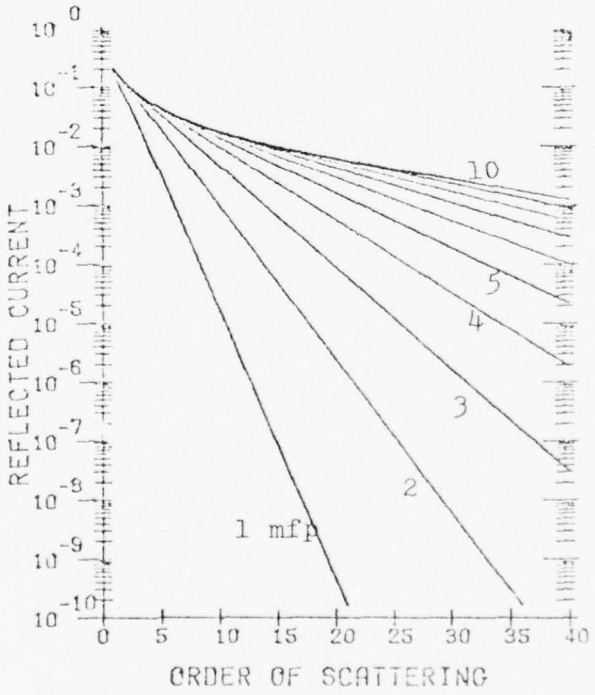

Figure III. B. 3b
Reflected current vs. order of scattering for 10 rod lengths: f=0.6

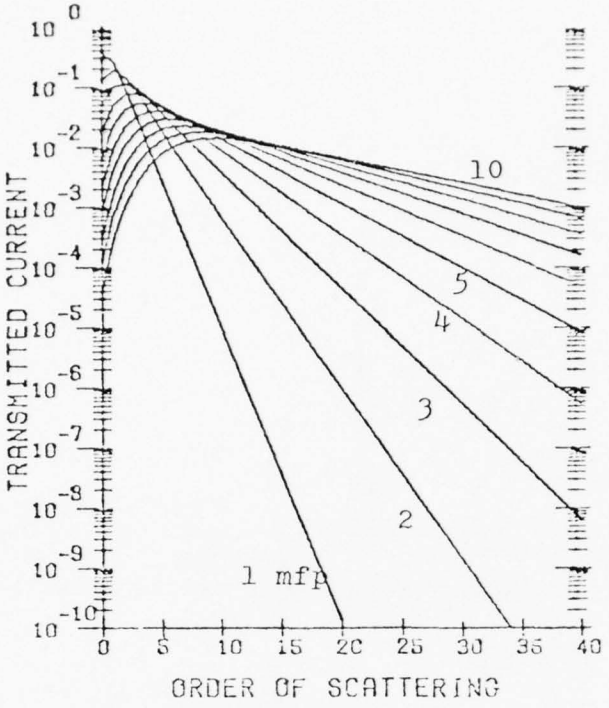

Figure III. B. 4a
Transmitted current vs. order of scattering for 10 rod lengths: f=0.7

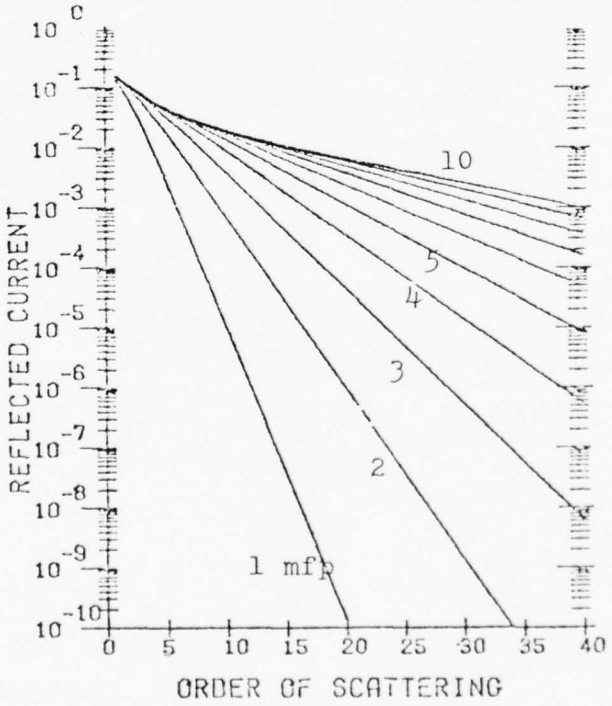

Figure III. B. 4b
Reflected current vs. order of scattering for 10 rod lengths: f=0.7

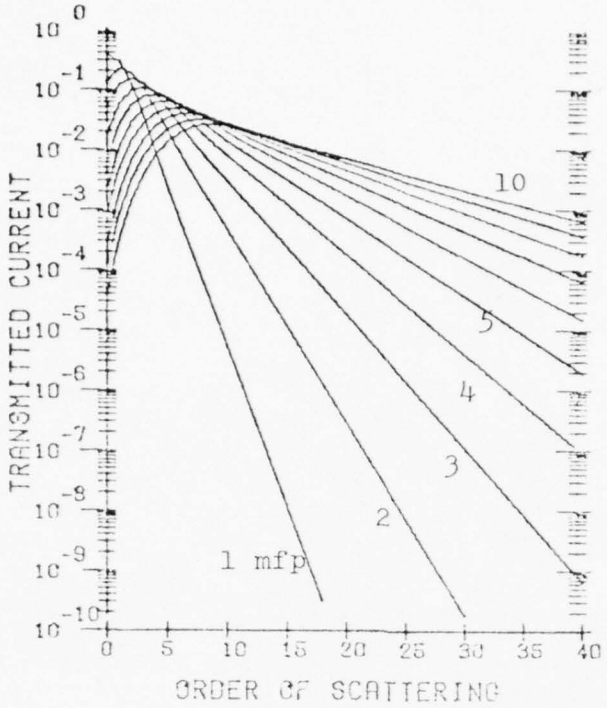

Figure III.B.5a
Transmitted current vs. order of scattering for 10 rod lengths: f=0.8

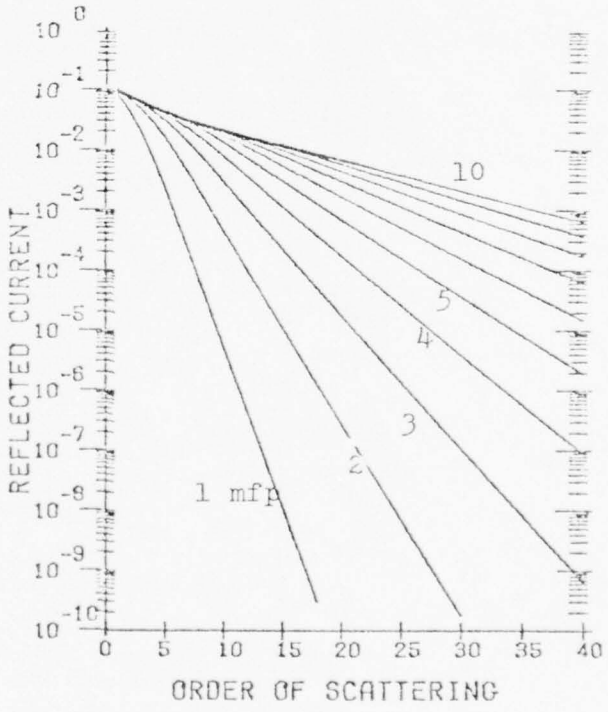

Figure III.B.5b
Reflected current vs. order of scattering for 10 rod lengths: f=0.8

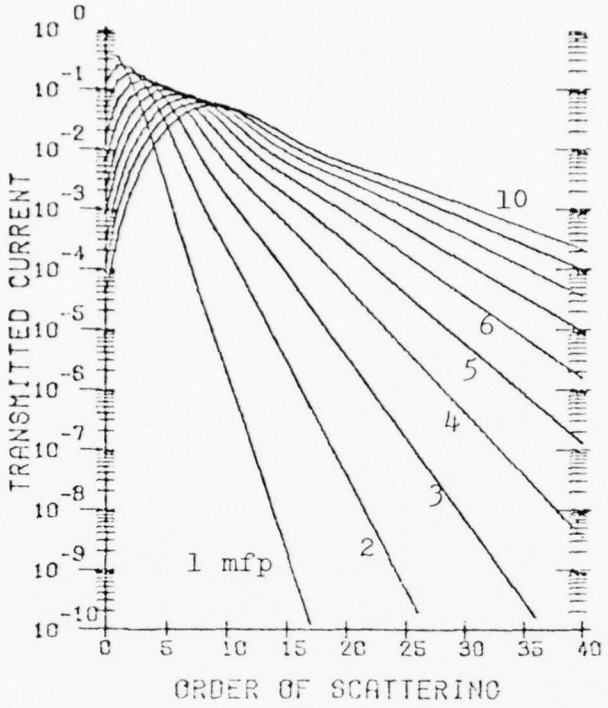

Figure III.B.6a
Transmitted current vs. order of scattering for 10 rod lengths: f=0.9

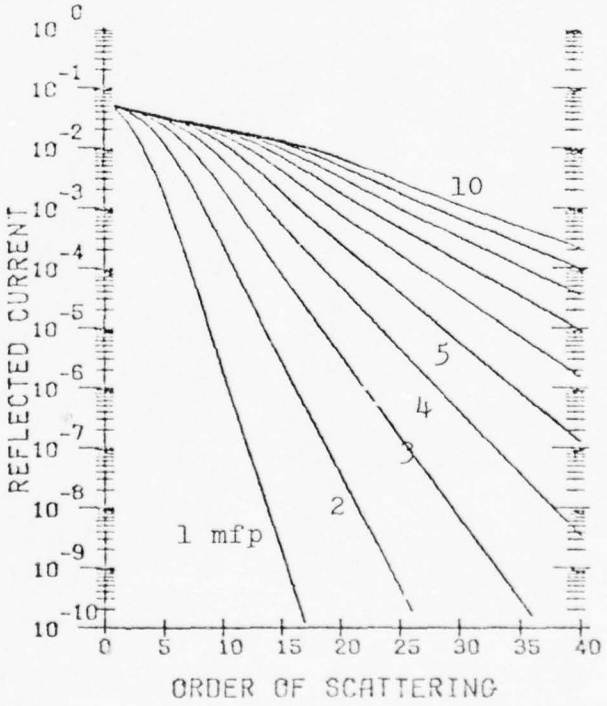

Figure III.B.6b
Reflected current vs. order of scattering for 10 rod lengths: f=0.9

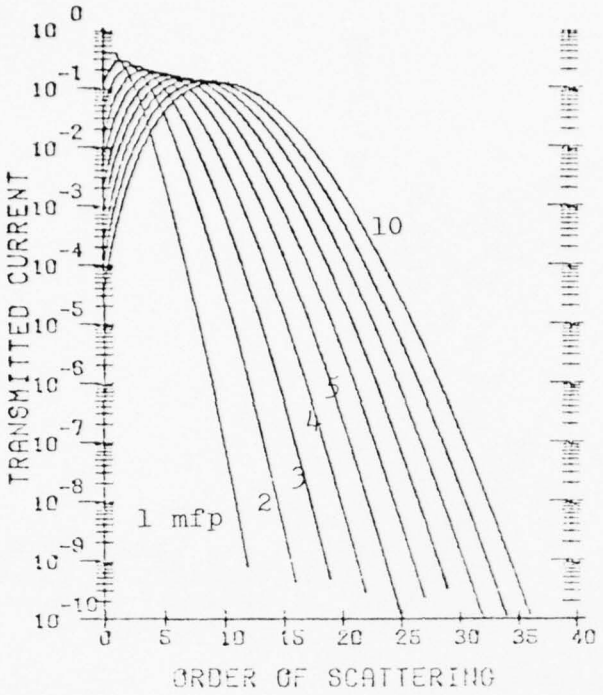

Figure III.B.7a
Transmitted current vs. order of scattering for 10 rod lengths: f=1.0

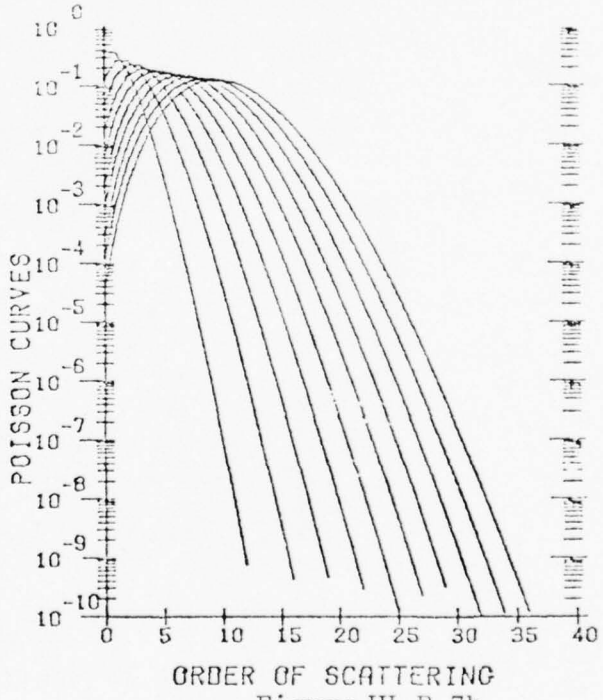

Figure III.B.7b
Poisson curves plotted vs. order of scattering

BEST AVAILABLE COPY

Table III. B. 1

Comparison of Scattered Current Totals to 40 Orders with Infinite Order Exact Values: Transmission; f=0.5, b=0.5

Rod Length (mfp)	$\sum_{n=1}^{40} T_n$	Infinite Order T, Exact Value
.2	.903601837E-01	.903601560E-01
.4	.163013625E+00	.163013287E+00
.6	.220419247E+00	.220410133E+00
.8	.264956889E+00	.264956750E+00
1.0	.298787375E+00	.298787225E+00
1.2	.323805938E+00	.323805788E+00
1.4	.341638473E+00	.341638330E+00
1.6	.353659169E+00	.353659038E+00
1.8	.361017019E+00	.361016901E+00
2.0	.364664820E+00	.364664717E+00
2.2	.365387405E+00	.365387318E+00
2.4	.363827571E+00	.363827501E+00
2.6	.360509072E+00	.360509030E+00
2.8	.355856580E+00	.355856604E+00
3.0	.350212730E+00	.350212932E+00
3.4	.336995398E+00	.336997100E+00
3.8	.322448476E+00	.322456814E+00
4.2	.307554964E+00	.307585068E+00
4.6	.292891789E+00	.292978467E+00
5.0	.278767022E+00	.278976339E+00
5.4	.265313991E+00	.265753689E+00
5.8	.252556973E+00	.253382702E+00
6.2	.240457427E+00	.241873008E+00
6.6	.228946132E+00	.231197771E+00
7.0	.217944629E+00	.221310340E+00
8.0	.193211091E+00	.198664537E+00
9.0	.169413724E+00	.181694772E+00
10.0	.146227483E+00	.166621267E+00

BEST AVAILABLE COPY

Table III. B. 2

Comparison of Scattered Current Totals to 40 Orders with Infinite Order Exact Values: Reflection; f=0.5, b=0.5

Rod Length (mfp)	$\sum_{n=1}^{40} B_n$	Infinite Order B, Exact Value
.2	.909091190E-01	.909090909E-01
.4	.166666744E+00	.166666667E+00
.6	.230769352E+00	.230769231E+00
.8	.285714438E+00	.285714286E+00
1.0	.333333505E+00	.333333333E+00
1.2	.375000182E+00	.375000000E+00
1.4	.411764892E+00	.411764706E+00
1.6	.444444632E+00	.444444444E+00
1.8	.473684396E+00	.473684211E+00
2.0	.500000183E+00	.500000000E+00
2.2	.523809704E+00	.523809524E+00
2.4	.545454720E+00	.545454545E+00
2.6	.565217548E+00	.565217391E+00
2.8	.583333433E+00	.583333333E+00
3.0	.599999932E+00	.600000000E+00
3.4	.629629074E+00	.629629630E+00
3.8	.655164232E+00	.655172414E+00
4.2	.677389412E+00	.677419355E+00
4.6	.696883183E+00	.696969697E+00
5.0	.714076562E+00	.714285714E+00
5.4	.729290196E+00	.729729730E+00
5.8	.742764177E+00	.743589744E+00
6.2	.754682138E+00	.756097561E+00
6.6	.765190373E+00	.767441860E+00
7.0	.774412199E+00	.777777778E+00
8.0	.792546283E+00	.800000000E+00
9.0	.804897162E+00	.818181818E+00
10.0	.812919116E+00	.833333333E+00

BEST AVAILABLE COPY

Table III. B. 3

Comparison of Scattered Current Totals to 40 Orders with Infinite Order Exact Values: Transmission; f=0.8, b=0.2

Rod Length (mfp)	$\sum_{n=1}^{40} T_n$	Infinite Order T, Exact Value
.2	.142807731E+00	.14280770[illegible]8E+00
.4	.255605948E+00	.25560[illegible]5880E+00
.6	.344045625E+00	.34404550[illegible]7E+00
.8	.412740162E+00	.41274000[illegible]1E+00
1.0	.465454086E+00	.46545[illegible]3892E+00
1.2	.505257617E+00	.50525740[illegible]1E+00
1.4	.534653264E+00	.53465[illegible]036E+00
1.6	.555679470E+00	.55567[illegible]240E+00
1.8	.569995455E+00	.56999[illegible]229E+00
2.0	.578950646E+00	.57895[illegible]431E+00
2.2	.583641486E+00	.58364[illegible]286E+00
2.4	.584957904E+00	.58495[illegible]722E+00
2.6	.583621320E+00	.58362[illegible]159E+00
2.8	.580215719E+00	.58021[illegible]578E+00
3.0	.575213051E+00	.57521[illegible]932E+00
3.4	.561864894E+00	.56186[illegible]825E+00
3.8	.545811009E+00	.54581[illegible]046E+00
4.2	.528482270E+00	.52848[illegible]684E+00
4.6	.510779756E+00	.51078[illegible]498E+00
5.0	.493256344E+00	.49326[illegible]053E+00
5.4	.476236853E+00	.47625[illegible]650E+00
5.8	.459897250E+00	.45993[illegible]408E+00
6.2	.444316761E+00	.44439[illegible]141E+00
6.6	.429512231E+00	.42967[illegible]115E+00
7.0	.415460937E+00	.41575[illegible]785E+00
8.0	.383288421E+00	.38427[illegible]922E+00
9.0	.354521771E+00	.35701[illegible]447E+00
10.0	.329172142E+00	.33328[illegible]933E+00

BEST AVAILABLE COPY

Table III.B.4

Comparison of Scattered Current Totals to 40 Orders with Infinite Order Exact Values: Reflection; f=0.8, b=0.2

Rod Length (mfp)	$\sum_{n=1}^{40} B_n$	Infinite Order B, Exact Value
.2	.3846155246E-01	.3846153846E-01
.4	.7407411266E-01	.7407407416E-01
.6	.1071429186E+00	.1071428576E+00
.8	.1379311126E+00	.1379310346E+00
1.0	.1666667556E+00	.1666666676E+00
1.2	.1935484826E+00	.1935483876E+00
1.4	.2187500996E+00	.2187500006E+00
1.6	.2424243436E+00	.2424242426E+00
1.8	.2647059856E+00	.2647058826E+00
2.0	.2857143906E+00	.2857142866E+00
2.2	.3055555616E+00	.3055555566E+00
2.4	.3243243326E+00	.3243243246E+00
2.6	.3421052736E+00	.3421052636E+00
2.8	.3589744706E+00	.3589743596E+00
3.0	.3750000136E+00	.3750000006E+00
3.4	.4047620106E+00	.4047619056E+00
3.8	.4318181886E+00	.4318181826E+00
4.2	.4565214286E+00	.4565217396E+00
4.6	.4791650516E+00	.4791666676E+00
5.0	.4999944326E+00	.5000000006E+00
5.4	.5192151246E+00	.5192307696E+00
5.8	.5369990356E+00	.5370370376E+00
6.2	.5534892086E+00	.5535714296E+00
6.6	.5688037916E+00	.5689655176E+00
7.0	.5830396496E+00	.5833333336E+00
8.0	.6143932586E+00	.6153846156E+00
9.0	.6423595886E+00	.6428571436E+00
10.0	.6615509936E+00	.6666666676E+00

$$\sum_{n=0}^{\infty} T_n(t) = \frac{1}{1+bt} \qquad (9)$$

and

$$\sum_{n=1}^{\infty} B_n(t) = \frac{bt}{1+bt} \quad . \qquad (10)$$

The extent to which these relations hold for currents up to 40 orders is demonstrated in tables III. B. 1-4 where comparisons are given for the cases where $f = 0.5$, $b = 0.5$ (IV. B. 1, 2) and $f = 0.8$, $b = 0.2$ (III. B. 3, 4). Except for large values of t, the agreement seems to be very close.

C. SCATTERING IN A SLAB GEOMETRY

C. 1 Current Equations

Application of the OOSII method to the one-dimensional scattering problem served not only as a demonstration of the principles of the method, but also as a means of verification of the method of numerical solution of the current equations. Further utility beyond this point however, is limited except for the possibility of modelling some three-dimensional problems with one-dimensional solutions through the use of some sort of equivalent mean-free-path, for curve fitting purposes. Greater practical value for the OOSII method can be demonstrated when applied to three-dimensional problems. The problem of particle transport in slabs is a convenient choice from among the class of physically realistic cases since it is the simplest in the geometric sense, and it is representative of a wide variety of physical situations ranging from neutron transport in reactors to laboratory studies of electron transport in thin films to neutron transport in reactors.

Let $\begin{Bmatrix} T_n\left(t, \vec{\Omega}, \vec{\Omega}_o\right) \\ B_n\left(t, \vec{\Omega}, \vec{\Omega}_o\right) \end{Bmatrix} d\Omega$ be the $\begin{Bmatrix} \text{transmitted} \\ \text{reflected} \end{Bmatrix}$

particle current emerging from the $\begin{Bmatrix} \text{right} \\ \text{left} \end{Bmatrix}$ face of the slab of thickness t (figure III. C. 1), after n interactions, in the direction $d\vec{\Omega}$ about $\vec{\Omega}$ because of a unit current incident on the left face in the direction $\vec{\Omega}_o$. Then current equations are[2] for the transmitted current;

$$T_n\left(t, \vec{\Omega}, \vec{\Omega}_o\right) = e^{-t/\mu\lambda_n}\left[\int_{\mu'=0}^{1} \frac{d\Omega'}{\mu'} f\left(\vec{\Omega}' \to \vec{\Omega}\right) \int_o^t \frac{dz}{\lambda_{n-1}} e^{z/\mu\lambda_n} T_{n-1}\left(z, \vec{\Omega}', \vec{\Omega}_o\right)\right.$$

$$\left. + \sum_{m-1}^{n-1} \int_{\mu'=0}^{1} \frac{d\Omega'}{\mu'} \int_{\mu''=-1}^{o} d\Omega'' f\left(\vec{\Omega}' \to \vec{\Omega}''\right) \int_0^t \frac{dz}{\lambda_{n-m-1}} e^{z/\mu\lambda_n} T_{n-m-1}\left(z, \vec{\Omega}', \vec{\Omega}_o\right) B_m\left(z, \vec{\Omega}, \vec{\Omega}''\right)\right] \tag{11}$$

and for the reflected current

$$B_n\left(t, \vec{\Omega}, \vec{\Omega}_o\right) = \sum_{m=0}^{n-1} \int_o^t \frac{dz}{\lambda_{n-m-1}} \int_{\mu''=-1}^{o} d\Omega'' T_m\left(z, \vec{\Omega}, \vec{\Omega}''\right) \int_{\mu'=0}^{1} \frac{d\Omega'}{\mu'} f(\vec{\Omega}' \to \vec{\Omega}'') T_{n-m-1}\left(z, \vec{\Omega}', \vec{\Omega}\right) \tag{12}$$

where λ_n is the scattering mean-free-path at the n-th collision,

μ and μ' are the direction cosines of $\vec{\Omega}$ and $\vec{\Omega}'$, respectively with respect to the normal to the slab surface (i. e. $\vec{\Omega} = \hat{e}_x\sqrt{1-\mu^2}\cos\varphi + \hat{e}_y\sqrt{1-\mu^2}\sin\varphi + \hat{e}_z\mu$, φ being the azimuth about the z-axis).

and $f(\vec{\Omega}' \to \vec{\Omega})\, d\Omega$ is the probability of scattering from the direction $\vec{\Omega}'$ into the solid angle $d\Omega$ about $\vec{\Omega}$.

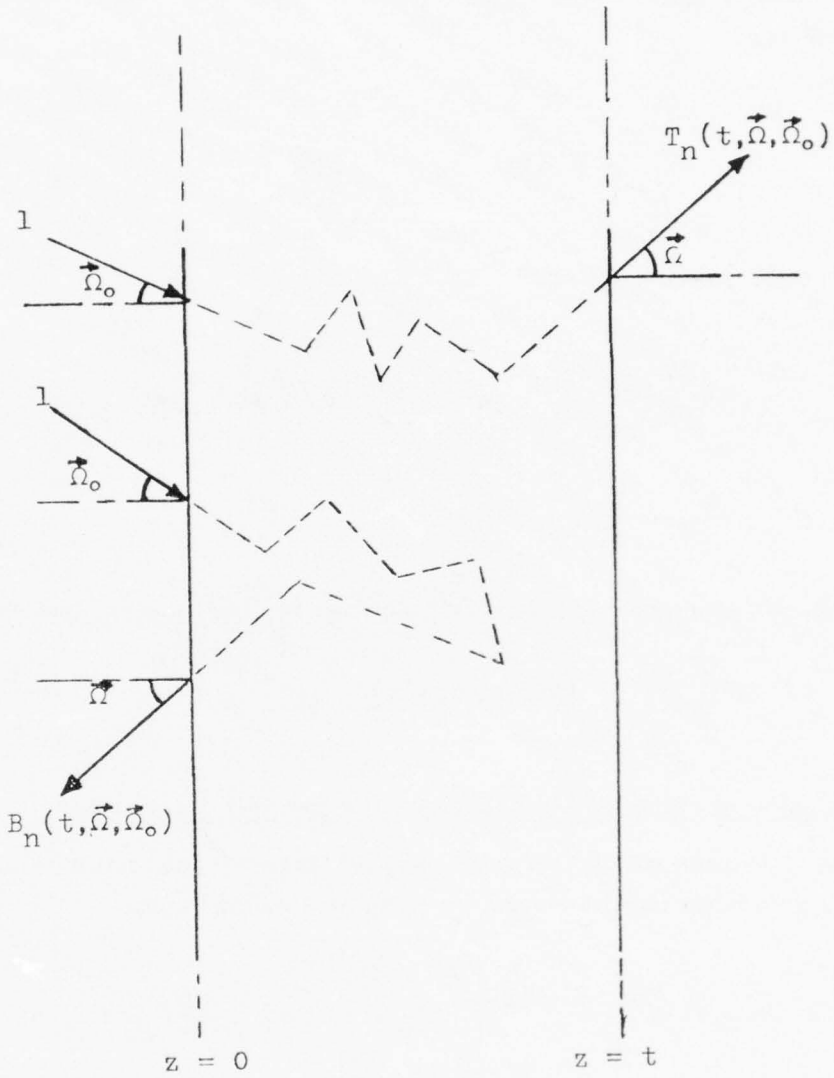

Figure III.C.1

The Slab Geometry

The above equations (11, 12) combined with the appropriate boundary and initial conditions, constitute the set of coupled integral recursion relations for transmitted and reflected currents in the slab geometry. The boundary conditions are

$$T_k\left(0, \vec{\Omega}, \vec{\Omega}_o\right) = 0 \ , \quad k > 0 \tag{13a}$$

$$B_k\left(0, \vec{\Omega}, \vec{\Omega}_o\right) = 0 \ , \quad k > 0 \tag{13b}$$

and the initial conditions are

$$T_o\left(z, \vec{\Omega}, \vec{\Omega}_o\right) = e^{-z/\lambda_o \mu} \ \delta_2\left(\vec{\Omega} \cdot \vec{\Omega}_o\right) \ , \tag{14a}$$

$$B_o\left(z, \vec{\Omega}, \vec{\Omega}_o\right) = 0 \ , \tag{14b}$$

where the three-dimensional delta function $\delta_2\left(\vec{\Omega} \cdot \vec{\Omega}'\right)$ is defined as

$$\delta_2(\vec{\Omega} \cdot \vec{\Omega}') = \delta(\mu - \mu')\ \delta(\varphi - \varphi) \ . \tag{15}$$

C.2 Solution of the Current Equations for the Slab Geometry

The equations which form the coupled integral recursion relations for the slab geometry can be rewritten in the following form:

$$\int_o^{2\pi} d\varphi_o \int_o^{2\pi} d\varphi \ T_n\left(t, \vec{\Omega}, \vec{\Omega}_o\right) = e^{-t/\lambda_n \mu} \Bigg[\int_o^{2\pi} d\varphi_o \int_o^{2\pi} d\varphi \int_o^{2\pi} d\varphi' \int_o^{1} \frac{d\mu'}{\mu'} f\left(\vec{\Omega}' \to \vec{\Omega}\right) \cdot$$

$$\int_o^t \frac{dz}{\lambda_{n-1}} \ e^{z/\lambda_n \mu} T_{n-1}\left(z, \vec{\Omega}', \vec{\Omega}_o\right) + \sum_{m=1}^{n-1} \int_o^{2\pi} d\varphi_o \int_o^{2\pi} d\varphi \int_o^{2\pi} d\varphi' \int_o^{2\pi} d\varphi'' \int_o^{1} \frac{d\mu'}{\mu'} \int_{-1}^{o} d\mu'' \ f\left(\vec{\Omega}' \to \vec{\Omega}''\right) \cdot$$

$$\int_o^t \frac{dz}{\lambda_{n-m-1}} \ e^{z/\lambda_n \mu} T_{n-m-1}\left(z, \vec{\Omega}', \vec{\Omega}_o\right) B_m\left(z, \vec{\Omega}, \vec{\Omega}''\right) \Bigg] , \tag{16}$$

$$\int_0^{2\pi} d\varphi_o \int_0^{2\pi} d\varphi \, B_n\left(t, \vec{\Omega}, \vec{\Omega}_o\right) =$$

(17)

$$\sum_{m=0}^{n-1} \int_0^{2\pi} d\varphi_o \int_0^{2\pi} d\varphi \int_0^t \frac{dz}{\lambda_{n-m-1}} \int_0^{2\pi} d\varphi'' \int_{-1}^{0} d\mu'' \, T_m\left(z, \vec{\Omega}, \vec{\Omega}''\right) \int_0^{2\pi} d\varphi' \int_0^1 \frac{d\mu'}{\mu'} f\left(\vec{\Omega}' \to \vec{\Omega}''\right) T_{n-m-1}\left(z, \vec{\Omega}', \vec{\Omega}_o\right).$$

Since the slab is infinite in extent in the x and y directions, the functions f, T_n and B_n are invariant under rotations about the z-axis. The integrals over azimuth may then be dispensed with given the definition

$$F(\mu, \mu') = \int_0^{2\pi} d\varphi \int_0^{2\pi} d\varphi \, F(\vec{\Omega}, \vec{\Omega}') \tag{18}$$

where F is an arbitrary function of $\vec{\Omega}$ and $\vec{\Omega}'$. Equations (16) and (17) then take the following simplified form:

$$T_n\left(t, \mu, \mu_o\right) = e^{-t/\lambda_n \mu} \left[\int_0^1 \frac{d\mu'}{\mu'} f\left(\mu' \to \mu\right) \int_0^t \frac{dz}{\lambda_{n-1}} e^{z/\lambda_n \mu} T_{n-1}\left(z, \mu', \mu_o\right) \right. \tag{19}$$

$$\left. + \sum_{m=1}^{n-1} \int_0^1 \frac{d\mu'}{\mu'} \int_{-1}^{0} d\mu'' f(\mu' \to \mu'') \int_0^t \frac{dz}{\lambda_{n-m-1}} e^{\frac{z}{\lambda_\mu \mu}} T_{n-m-1}\left(z, \mu', \mu_o\right) B_m\left(z, \mu, \mu''\right) \right],$$

$$B_n\left(t, \mu, \mu_o\right) = \sum_{m=0}^{n-1} \int_0^t \frac{dz}{\lambda_{n-m-1}} \int_{-1}^{0} d\mu'' \, T_m\left(z, \mu, \mu''\right) \int_0^1 \frac{d\mu'}{\mu'} f\left(\mu' \to \mu''\right) T_{n-m-1}\left(z, \mu', \mu_o\right), \tag{20}$$

and the boundary and initial conditions become

$$T_k(0,\mu,\mu_o) = 0 \quad , \qquad k > 0 \quad , \tag{21a}$$

$$B_k(0,\mu,\mu_o) = 0 \quad , \qquad k > 0 \quad , \tag{21b}$$

$$T_o(z,\mu,\mu_o) = e^{-z/\lambda_o\mu}\ \delta(\mu-\mu_o) \tag{22a}$$

$$B_o(z,\mu,\mu_o) = 0 \quad . \tag{22b}$$

Exact solutions are possible for the once scattered currents T_1 and B_1. In fact, knowledge of these solutions is indispensible to the success of the solution scheme to be outlined. Direct substitution of (22a) into (19) yields for n=1,

$$T_1(t,\mu,\mu_o) = \frac{e^{-t/\lambda_1\mu}}{\lambda_o}\int_o^1 \frac{d\mu}{\mu'}\, f(\mu'\to\mu)\int_o^t dz e^{z/\lambda_1\mu}\, T_o(z,\mu',\mu_o)$$

$$= \frac{e^{-t/\lambda_1\mu}}{\lambda_o}\int_o^1 \frac{d\mu'}{\mu'}\, f(\mu'\to\mu)\int_o^t dz e^{z/\lambda_1\mu}\, e^{-z/\lambda_o\mu'}\,\delta(\mu'-\mu_o)$$

$$= \frac{e^{-t/\lambda_1\mu}}{\lambda_o\mu_o}\, f(\mu_o\to\mu)\int_o^t dz\, e^{z\left(\frac{1}{\lambda_1\mu}-\frac{1}{\lambda_o\mu_o}\right)} ,$$

or

$$T_1(t,\mu,\mu_o) = \begin{cases} \dfrac{\lambda_1\mu}{\lambda_o\mu_o-\lambda_1\mu}\, f(\mu_o\to\mu)\left[e^{-t/\lambda_o\mu_o}-e^{-t/\lambda_1\mu}\right], & \mu\neq\mu_o \\ \dfrac{t}{\lambda_o\mu_o}\, e^{-t/\lambda_o\mu_o}\, f(\mu_o\to\mu_o) \quad , & \mu=\mu_o \end{cases} \tag{23}$$

First order reflection is also obtained using (22a), so that

$$B_1(t,\mu,\mu_o) = \frac{\tau}{\lambda_o}\int_o^t dz \int_{-1}^{o} d\mu'' \, T_o(z,\mu,\mu'') \int_o^1 \frac{d\mu'}{\mu'} f(\mu' \to \mu'') \, T_o(z,\mu',\mu_o)$$

$$= \frac{1}{\lambda_o}\int_o^t dz \int_{-1}^{o} d\mu'' \, e^{-z/\lambda_o|\mu''|} \, \delta(\mu-\mu'') \int_o^1 \frac{d\mu'}{\mu'} f(\mu' \to \mu'') \, e^{-z/\lambda_o\mu'} \, \delta(\mu'-\mu_o)$$

$$= \frac{1}{\lambda_o\mu_o}\int_o^t dz \, e^{-z/\lambda_o\mu_o} \int_{-1}^{o} d\mu'' \, e^{-z/\lambda_o|\mu''|} \, \delta(\mu-\mu'') \, f(\mu_o \to \mu'')$$

$$= \frac{1}{\lambda_o\mu_o} f(\mu_o \to \mu) \int_o^t dz \, e^{-z/\lambda_o\left(\frac{1}{|\mu|}+\frac{1}{\mu_o}\right)} \quad ,$$

or

$$B_1(t,\mu,\mu_o) = \frac{|\mu|}{|\mu|+\mu_o} f(\mu_o \to \mu)\left[1 - e^{-t/\lambda_o\left(\frac{1}{\mu_o}+\frac{1}{|\mu|}\right)}\right] \quad . \tag{24}$$

The angular integrals of equations (19) and (20) present a problem which had not occurred previously in the one-dimensional case. It is necessary to cast the equations into a form in which the integrals over angle can be performed both with a sufficient degree of accuracy and within a reasonable amount of computation time. For this reason the method of Gauss quadrature integration was chosen.[4]

Tables of the Gaussian ordinates and their weighting coefficients are readily available from several sources.[5] When equations (19) and (20) are restated in discrete ordinate representation, they appear as

$$T_n\left(t, \mu_\ell, \mu_j\right) \doteq e^{-t/\lambda_n \mu_\ell} \left[\int_o^t \frac{dz}{\lambda_{n-1}} \, e^{z/\lambda_n \mu_\ell} \sum_k A_k f\left(\mu_k, \mu_\ell\right) \frac{T_{n-1}\left(z, \mu_k, \mu_j\right)}{\mu_k} \right.$$

$$\left. + \sum_{m=1}^{n-1} \int_o^t \frac{dz}{\lambda_{n-m-1}} \, e^{z/\lambda_n \mu_\ell} \sum_k A_k \, \frac{T_{n-m-1}\left(z, \mu_k, \mu_j\right)}{\mu_k} \sum_p A_p f\left(\mu_k, \mu_p\right) B_m\left(z, \mu_\ell, \mu_p\right) \right], \tag{25}$$

and

$$B_m\left(t, \mu_\ell, \mu_j\right) \doteq \sum_{m=0}^{n-1} \int_o^t \frac{dz}{\lambda_{n-m-1}} \sum_p A_p T_m\left(z, \mu_\ell, \mu_p\right) \sum_k A_k f\left(\mu_k, \mu_p\right) \frac{T_{n-m-1}\left(z, \mu_k, \mu_j\right)}{\mu_k} . \tag{26}$$

The remaining problem of integration over the slab thickness z is handled in exact analogy to that of the one dimensional case. It is assumed that over a sufficiently small interval, $t_1 \leq z \leq t$, the functions $T_n\left(z, \mu_j, \mu_k\right)$ and $B_n\left(z, \mu_j, \mu_k\right)$ can be considered linear in the variable z so that they may be written as

$$T_n\left(z, \mu_j, \mu_k\right) = m_T^n\left(\mu_j, \mu_k\right) z + b_T^n\left(\mu_j, \mu_k\right) \quad , \tag{27a}$$

$$B_n\left(z, \mu_j, \mu_k\right) = m_B^n\left(\mu_j, \mu_k\right) z + b_B^n\left(\mu_j, \mu_k\right) \quad , \tag{27b}$$

where the $m_T^n\left(\mu_j, \mu_k\right)$ and $m_B^n\left(\mu_j, \mu_k\right)$ are the slopes and the $b_T^n\left(\mu_j, \mu_k\right)$, $b_B^n\left(\mu_j, \mu_k\right)$ are the intercepts of the T_n and B_n, respectively. It is convenient for the expressions for T_n and B_n to be divided into six terms. That is:

$$T_n = T_n^{(1)} + T_n^{(2)} + T_n^{(3)} \quad ,$$

and $$B_n = B_n^{(1)} + B_n^{(2)} + B_n^{(3)} \quad , \tag{28}$$

where if the piecewise linearity assumption (27a, b) is applied and if the integrals of (25) and (26) over z are then performed on the interval $t_1 \leq z \leq t$, the following expressions result for the six terms:

$$T_n^{(1)}\left(t, \mu_\ell, \mu_j\right) = \frac{1}{\lambda_{n-1}} \sum_k A_k \frac{f\left(\mu_k, \mu_\ell\right)}{\mu_k} \cdot$$

$$\left\{ \begin{array}{l} m_T^{n-1}\left(\mu_k, \mu_j\right)\left[\left(\lambda_n \mu_\ell t - \lambda_n^2 \mu_\ell^2\right) e^{t/\lambda_n \mu_\ell} - \left(\lambda_n \mu_\ell t_1 - \lambda_n^2 \mu_\ell^2\right) e^{t/\lambda_n \mu_\ell}\right] \\ + b_T^{n-1}\left(\mu_k, \mu_j\right)\left[\lambda_n \mu_\ell \left(e^{t/\lambda_n \mu_\ell} - e^{t_1/\lambda_n \mu_\ell}\right)\right] \end{array} \right\} \tag{29a}$$

$$T_n^{(2)}\left(t, \mu_\ell, \mu_j\right) = \sum_{m=1}^{n-2} \frac{1}{\lambda_{n-m-1}} \sum_k \frac{A_k}{\mu_k} \sum_p A_p f\left(\mu_k, \mu_p\right) \cdot$$

$$
\left\{
\begin{aligned}
&\left[m_T^{n-m-1}(\mu_k,\mu_j)\, m_B^{m}(\mu_\ell,\mu_p)\right]\cdot\left[\left(\lambda_n\mu_\ell t^2 - 2\lambda_n^2\mu_\ell^2 t + 2\lambda_n^3\mu_\ell^3\right) e^{t/\lambda_n\mu_\ell} - \right.\\
&\qquad\left.\left(\lambda_n\mu_\ell t_1^2 - 2\lambda_n^2\mu_\ell t_1 + 2\lambda_n^3\mu_\ell^3\right) e^{t_1/\lambda_n\mu_\ell}\right]\\
&+\left[b_T^{n-m-1}(\mu_k,\mu_j)\, m_B^{m}(\mu_\ell,\mu_p) + b_B^{m}(\mu_\ell,\mu_p)\, m_T^{n-m-1}(\mu_k,\mu_j)\right]\cdot\\
&\qquad\left[\left(\lambda_n\mu_\ell t - \lambda_n^2\mu_\ell^2\right) e^{t/\lambda_n\mu_\ell} - \left(\lambda_n\mu_\ell t_1 - \lambda_n^2\mu_\ell^2\right) e^{t_1/\lambda_n\mu_\ell}\right]\\
&+\left[b_T^{n-m-1}(\mu_k,\mu_j)\, b_B^{m}(\mu_\ell,\mu_p)\,\lambda_n\mu_\ell\right]\cdot\left[e^{t/\lambda_n\mu_\ell} - e^{t_1/\lambda_n\mu_\ell}\right]
\end{aligned}
\right\} \tag{29b}
$$

$$
T_n^{(3)}(t,\mu_\ell,\mu_j) = \frac{1}{\lambda_o}\sum_p A_p\,\frac{f(\mu_j,\mu_p)}{\mu_j}\cdot
$$

$$
m_B^{n-1}(\mu_\ell,\mu_p)\left\{\left[\left(\frac{\lambda_o\lambda_n\mu_j\mu_\ell}{\lambda_o\mu_j-\lambda_n\mu_\ell}\right) t - \left(\frac{\lambda_o\lambda_n\mu_j\mu_\ell}{\lambda_o\mu_j-\lambda_n\mu_\ell}\right)^2\right] e^{\left(\frac{1}{\lambda_n\mu_\ell}-\frac{1}{\lambda_o\mu_j}\right)t}\right.
$$

$$
\left. - \left[\left(\frac{\lambda_o\lambda_n\mu_j\mu_\ell}{\lambda_o\mu_j-\lambda_n\mu_\ell}\right) t_1 - \left(\frac{\lambda_o\lambda_n\mu_j\mu_\ell}{\lambda_o\mu_j-\lambda_n\mu_\ell}\right)^2\right] e^{\left(\frac{1}{\lambda_n\mu_\ell}-\frac{1}{\lambda_o\mu_o}\right)t_1}\right\} \tag{29c}
$$

$$
+ b_B^{n-1}(\mu_\ell,\mu_p)\left\{\left(\frac{\lambda_o\lambda_n\mu_j\mu_\ell}{\lambda_o\mu_j-\lambda_n\mu_\ell}\right)\left[e^{\left(\frac{1}{\lambda_n\mu_\ell}-\frac{1}{\lambda_o\mu_j}\right)t} - e^{\left(\frac{1}{\lambda_n\mu_\ell}-\frac{1}{\lambda_o\mu_j}\right)t_1}\right]\right\}
$$

$$B_n^{(1)} = \frac{1}{\lambda_{n-1}} \sum_k A_k \frac{f(\mu_k, \mu_\ell)}{\mu_k} \quad .$$

$$\left\{ \begin{array}{l} m_T^{n-1}(\mu_k, \mu_j) \left[\left(\lambda_o \mu_\ell t_1 + \lambda_o^2 \mu_\ell^2 \right) e^{-t_1/\lambda_o \mu_\ell} \right. \\ \qquad \left. - \left(\lambda_o \mu_\ell t + \lambda_o^2 \mu_\ell^2 \right) e^{-t/\lambda_o \mu_\ell} \right] \\ + b_T^{n-1}(\mu_k, \mu_j) \lambda_o \mu_\ell \left[e^{-t_1/\lambda_o \mu_\ell} - e^{-t/\lambda_o \mu_\ell} \right] \end{array} \right\} \qquad (30a)$$

$$B_n^{(2)} = \sum_{m=1}^{n-2} \frac{1}{\lambda_{n-m-1}} \sum_p A_p \sum_k A_k \frac{f(\mu_k, \mu_p)}{\mu_k} \quad . \qquad (30b)$$

$$\left\{ \begin{array}{l} \left[m_T^m(\mu_\ell, \mu_p) \, m_T^{n-m-1}(\mu_k, \mu_j) \right] \left[\frac{t^3}{3} - \frac{t_1^3}{3} \right] \\ + \left[b_T^m(\mu_\ell, \mu_p) \, m_T^{n-m-1}(\mu_k, \mu_j) + b_T^{n-m-1}(\mu_k, \mu_j) \, m_T^m(\mu_\ell, \mu_p) \right] \left[\frac{t^2}{2} - \frac{t_1^2}{2} \right] \\ + \left[b_T^m(\mu_\ell, \mu_p) \, b_T^{n-m-1}(\mu_k, \mu_j) \right] \left[t - t_1 \right] \end{array} \right\}$$

$$B_n^{(3)} = \frac{1}{\lambda_o} \sum_p A_p \frac{f(\mu_j, \mu_p)}{\mu_j} \cdot$$

$$\left\{ \begin{array}{l} m_T^{n-1}(\mu_\ell, \mu_p) \left[\left(\lambda_o \mu_j t_1 + \lambda_o^2 \mu_j^2 \right) e^{-t_1/\lambda_o \mu_j} \right. \\ \qquad \left. - \left(\lambda_o \mu_j t + \lambda_o^2 \mu_j^2 \right) e^{-t/\lambda_o \mu_j} \right] \\ + b_T^{n-1}(\mu_\ell, \mu_p) \lambda_o \mu_j \left[e^{-t_1/\lambda_o \mu_j} - e^{-t/\lambda_o \mu_j} \right] \end{array} \right\} \qquad (30c)$$

The above relations (29, 30) form the basis of a computer program which was written to obtain numerical solutions to the coupled integral recursion relations (19, 20). The remaining requirement is the specification of the scattering matrix $f(\mu, \mu')$, the mathematical description of the physics of the scattering process. In the sections which follow, the results of three OOSII calculations corresponding to three forms for $f(\mu, \mu')$, are reported.

C.3 ISOTROPIC SCATTERING IN THE LABORATORY SYSTEM

The simplest form of the scattering matrix $f(\mu, \mu')$ occurs when all of the elements are constant and equal. This situation corresponds to isotropic scattering in the laboratory system. For any conservative scattering interaction (no absorption)

$$\int_o^{4\pi} d\Omega' \, f\left(\vec{\Omega} \rightarrow \vec{\Omega}'\right) = 1 \quad . \qquad (31)$$

If the scattering is isotropic in the laboratory system (the directions $\vec{\Omega}$ and $\vec{\Omega}'$ are specified with respect to the laboratory frame), then from (31) it is seen that

$$f\left(\vec{\Omega}' \rightarrow \vec{\Omega}\right) = \frac{1}{4\pi}$$

Furthermore, since azimuthal invariance applies, as in equation (18)

$$f\left(\mu, \mu'\right) \equiv f_o = \int_o^{2\pi} d\varphi \, f\left(\vec{\Omega} \rightarrow \vec{\Omega}'\right)$$

$$= \frac{1}{4\pi} \int_o^{2\pi} d\varphi \tag{32}$$

$$= \frac{1}{2} \quad .$$

The above value of f_o was substituted for the $f\left(\mu_i, \mu_j\right)$ in expressions (29) and (30), and computer runs were made to determine the values of $T_n\left(t, \mu_i, \mu_j\right)$ and $B_n\left(t, \mu_i, \mu_j\right)$, where the μ_i and μ_j are Gaussian discrete ordinates corresponding to cosines of the incident and exit polar angles respectively, for 41 values of t ranging from 0.0 to 8.0 mfp in steps of 0.2 mfp. A constant value was assumed for λ_n. This assumption, while not a necessary restriction of the method, serves to simplify the computation. Current values $T_n(t)$ and $B_n(t)$ were then obtained by integrating the functions $T_n\left(t, \mu, \mu'\right)$ and $B_n\left(t, \mu, \mu'\right)$ over the incident and exit cosines μ and μ'. That is

$$T_n(t) = \int_o^1 d\mu \, w(\mu) \int_o^1 d\mu' \, T_n(t, \mu, \mu') \Big/ \int_o^1 d\mu \, w(\mu) \quad , \tag{33}$$

and

$$B_n(t) = \int_o^1 d\mu \, w(\mu) \int_{-1}^{o} d\mu' \, B_n(t, \mu, \mu') \Big/ \int_o^1 d\mu \, w(\mu) \quad , \tag{34}$$

where $w(\mu)$ is the source angular distribution function at the left face of the slab. Results were obtained for two source configurations:

1) cosine current (isotropic particle density) distribution

$$w(\mu) = \mu$$

and 2) isotropic current distribution

$$w(\mu) = 1 \quad .$$

The second of these is not physically realizable since this would correspond to an infinite particle density value along the direction parallel to the slab surface. In other words, if $\Phi(\mu)$ is the angular density or the number of particle per unit volume moving in the direction μ, at the slab surface, then the angular current $J(\mu)$, the number of particles with speed v crossing unit area perpendicular to the direction of μ, is given by $J(\mu) = v\mu\Phi(\mu)$. Therefore, if $J(\mu)$ is to be isotropic, and non-zero, it must have a constant non-zero and finite value at $\mu = 0$.

The numerator integrals of (33) and (34) were evaluated using Gauss quadrature since the functions $T_n(t, \mu, \mu')$ and $B_n(t, \mu, \mu')$ were already evaluated at the Gaussian ordinates, and the denominator integrals were evaluated exactly. For the cosine current source the value of the denominator is 1/2, and for the isotropic current source it has a value of 1. The working expressions for the transmitted and reflected currents then become

$$T_n(t) = 2 \sum_j A_j \mu_j \sum_k A_k T_n(t, \mu_j, \mu_k) \quad , \tag{35}$$

$$B_n(t) = 2 \sum_j A_j \mu_j \sum_k A_k B_n(t, \mu_j, \mu_k) \quad , \tag{36}$$

for the cosine source and

$$T_n(t) = \sum_j A_j \sum_k A_k T_n(t, \mu_j, \mu_k) \quad , \tag{37}$$

$$B_n(t) = \sum_j A_j \sum_k A_k B_n(t, \mu_j, \mu_k) \quad , \tag{38}$$

for the isotropic source.

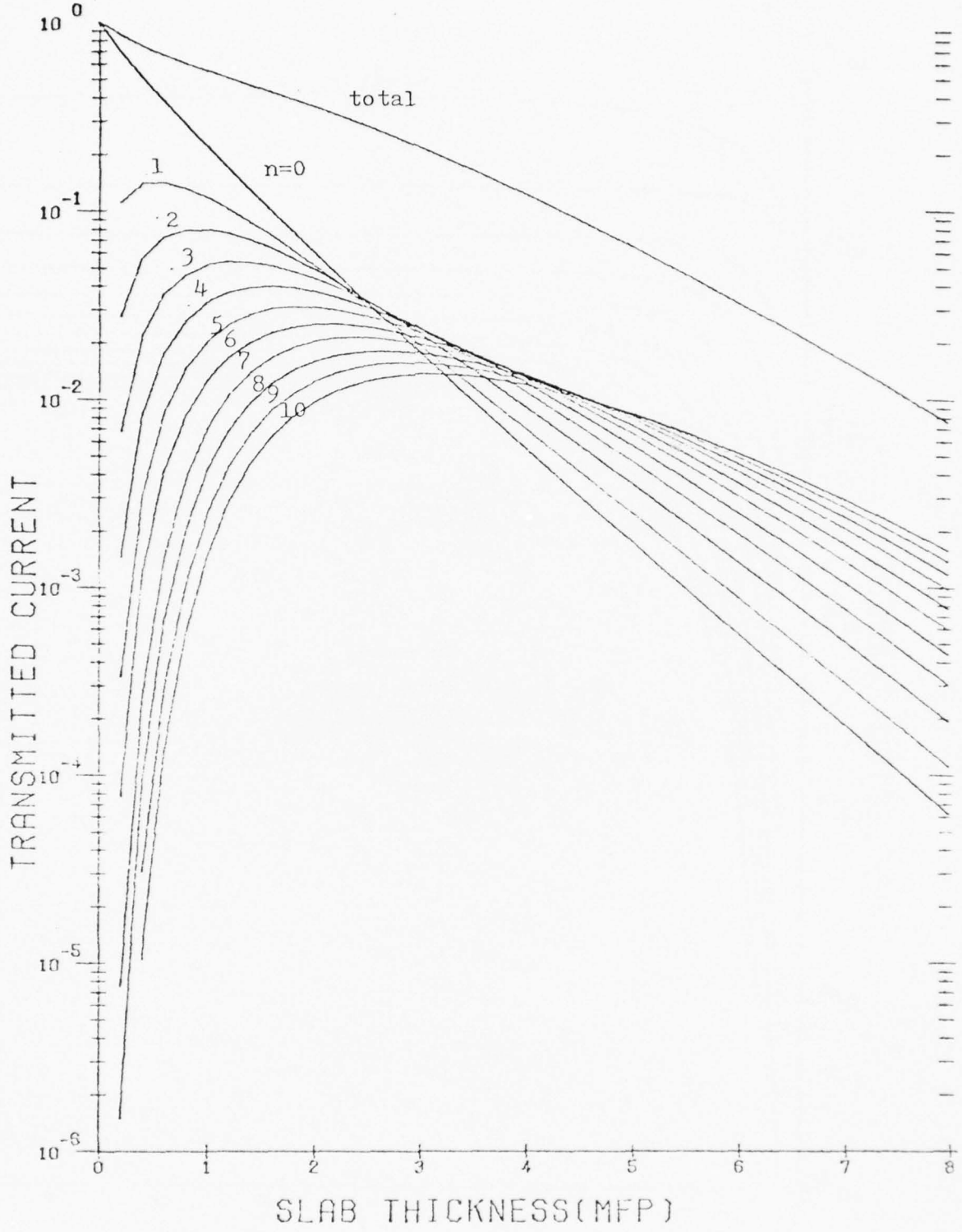

Figure III.C.2

Transmitted current, $T_n(t)$, vs. slab thickness, t, for n-th order isotropic scattering ($0 \leq n \leq 10$); Cosine current source configuration

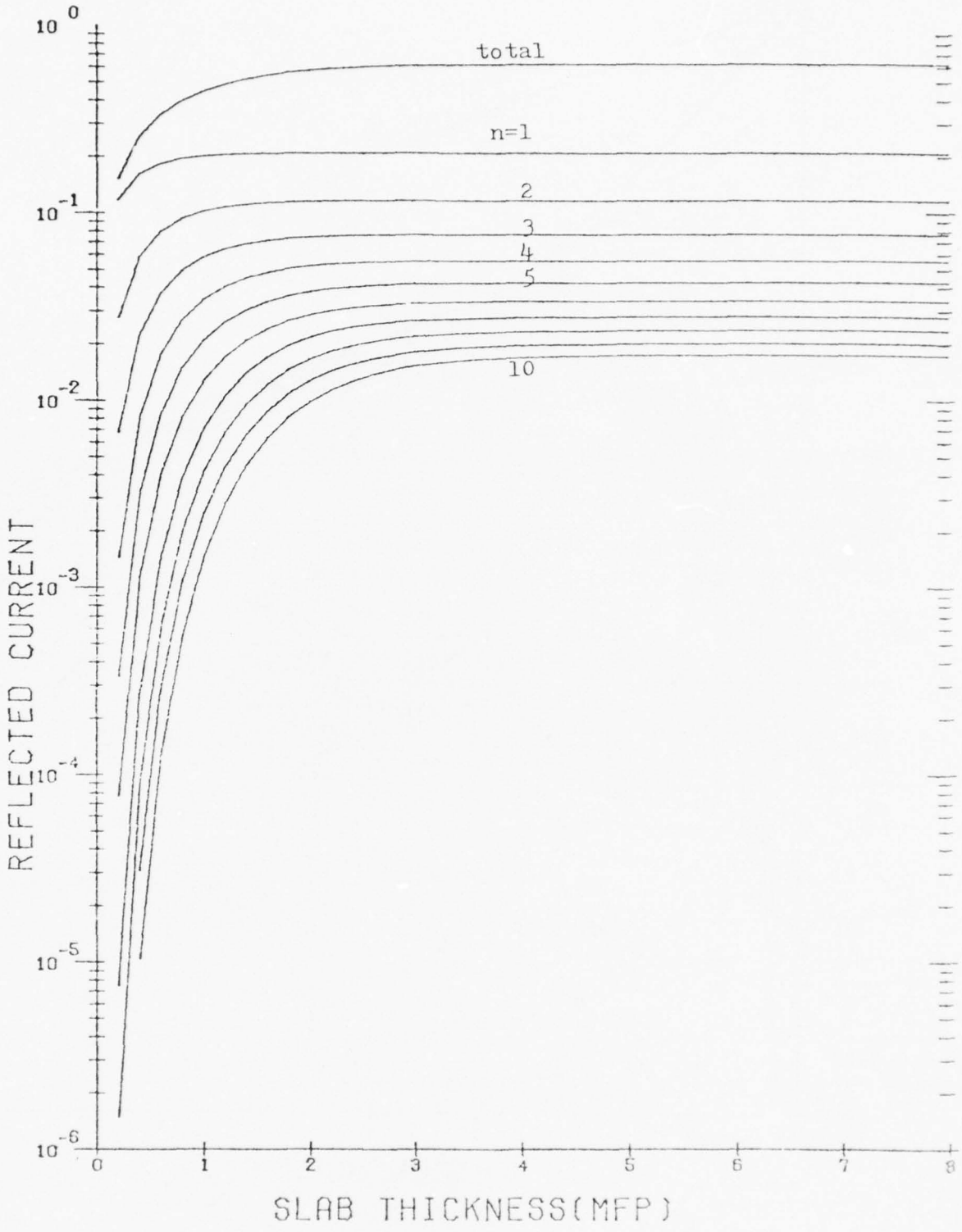

Figure III.C.3

Reflected current, $B_n(t)$, vs. slab thickness, t, for n-th order isotropic scattering ($1 \leq n \leq 10$); Cosine current source configuration

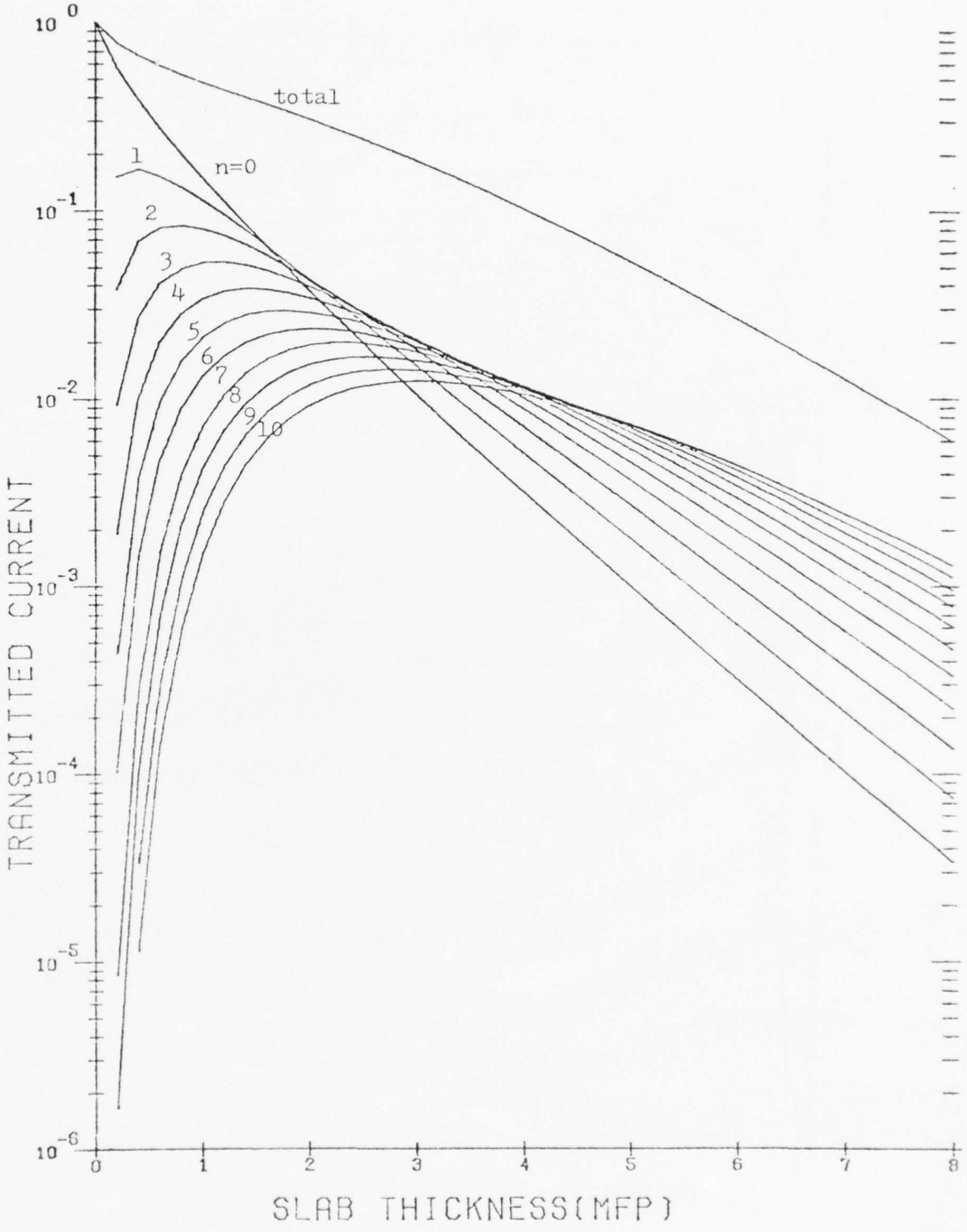

Figure III.C.4

Transmitted current, $T_n(t)$, vs. slab thickness, t, for n-th order isotropic scattering ($0 \leq n \leq 10$); Isotropic current source configuration

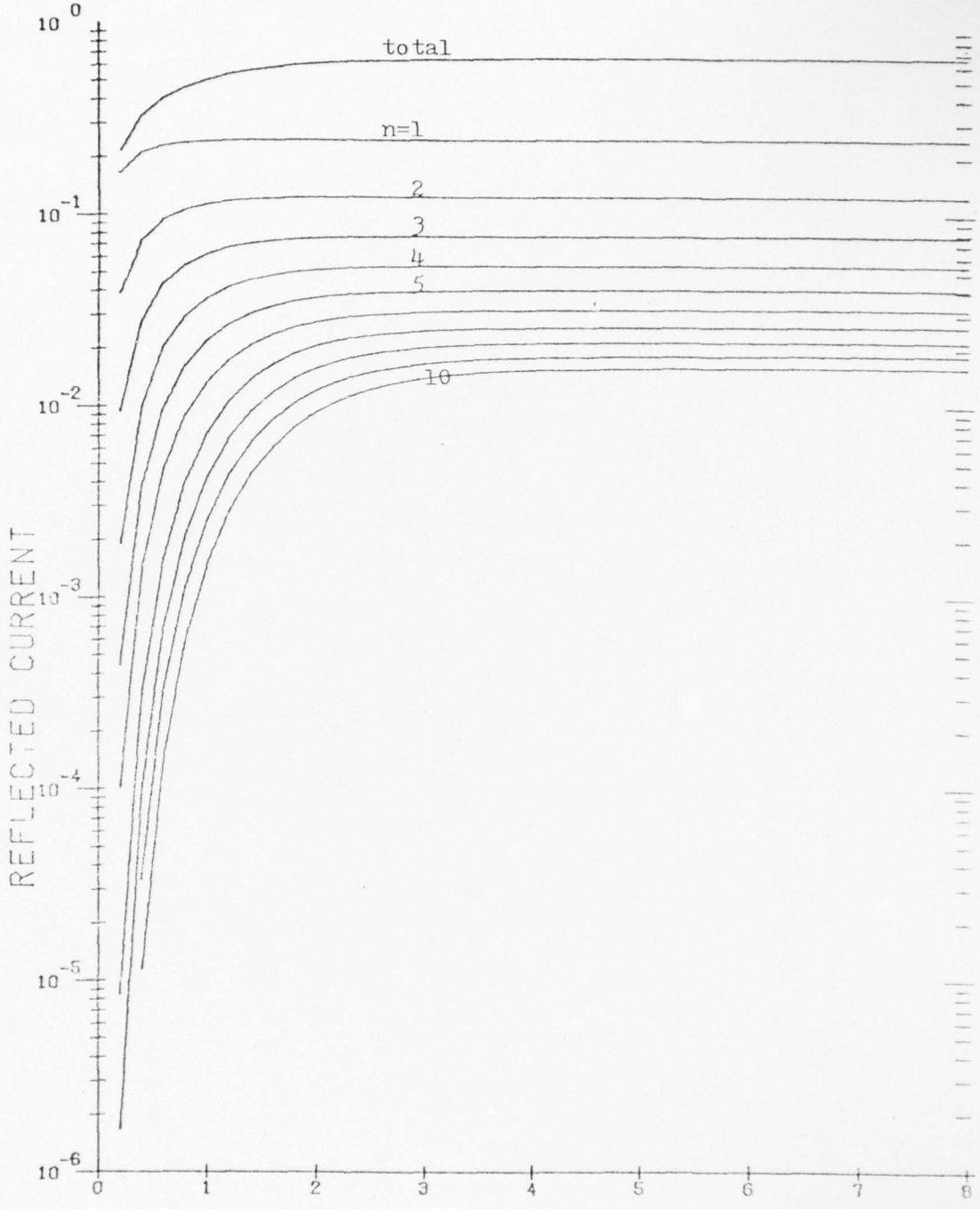

Figure III.C.5

Reflected current, $B_n(t)$, vs. slab thickness, t, for n-th order isotropic scattering ($1 \leq n \leq 10$); Isotropic current source configuration

It was found that good comparisons with other calculations were obtained if six discrete ordinates per quadrant were used for all scatterings up to order ten for slab thicknesses up to one mfp. In this way an artificially low transmitted current at the higher orders could be avoided. The use of only two discrete ordinates per quadrant for the thin slab cases exaggerates the transmission at the lower scattering orders due to the high degree of granularity in angle.

For slab thicknesses greater than 1 mfp six discrete ordinates were used for the first three scattering orders, four were used for orders four through six, and two for orders seven through ten. The reasoning leading to this arrangement is that as the number of scatters becomes sufficiently high, and the slab is sufficiently thick, the granularity inherent in the choice of a low number of discrete ordinates becomes less important. The particle has changed direction several times at this stage so that for isotropic and nearly isotropic scattering, the angular distribution has grown diffuse and an adequate description can be achieved with, say, a Legendre polynomial expansion of two or three terms. This would not be true for anisotropic scattering to be discussed later.

Curves of $T_n(t)$ and $B_n(t)$ plotted vs. t for both source configurations are given in figures III. C. 2-5. Eleven curves, representing values of n ranging from 0 to 10 and a total curve are presented in each graph. A more detailed presentation of the numerical results is given in tables III. E. 1-2 where comparisons with results obtained from Boltzmann equation and Monte Carlo calculations are shown.

D. The One-Dimensional Boltzmann Equation for Isotropic Scattering In Slabs

The process of isotropic, conservative scattering in a slab geometry can be described by the one-dimensional Boltzmann equation.

$$\begin{aligned} \varphi(z) &= \varphi_u(z) + \varphi_s(z) \\ &= \varphi_o E_2\left(\frac{z}{\lambda}\right) + \frac{c}{2\lambda} \int_o^t dz' \, E_1\left(\frac{|z-z'|}{\lambda}\right) \varphi(z') \quad . \end{aligned} \tag{39}$$

where $\varphi(z)$ is the particle density at any point z within the slab, $\varphi_n(z)$ is the unscattered portion, $\varphi_s(z)$ is the scattered contribution, φ_o is the particle source, strength, and E_1, E_2 are exponential integral functions of orders 1 and 2 respectively.

D. 1. Iterative Solution Method and Expressions for Transmitted and Reflected Currents

The integral equation (39) is of the Fredholm type and may be solved by means of an iterative procedure. Let $\varphi_n(z)$ be the n-th approximation to the solution of (39), and let $\varphi_o(z) = E_2(z)$, corresponding to unit source strength. Then $\varphi_n(z)$ is given iteratively by

$$\varphi_n(z) = \varphi_o(z) + 1/2 \int_o^t dz' \, E_1\Big(|z-z'|\Big) \varphi_{n-1}(z') \, . \tag{40}$$

A physical significance can be attributed to these iterations. If the quantity S_n is defined as

$$S_n(z) \equiv \varphi_n(z) - \varphi_{n-1}(z) \quad , \quad n \geq 1 \tag{41a}$$

and

$$S_o(z) \equiv \varphi_o(z) \quad , \tag{41b}$$

then $S_n(z)$ satisfies the equation

$$S_n(z) = 1/2 \int_o^t E_1\Big(|z-z'|\Big) S_{n-1}(z') \, dz' \tag{42}$$

Physically, since $E_1\Big(|z-z'|\Big)$ is the single collision kernel, $S_n(z)$ represents the collision or source density of particles that have collided isotropically n times. In other words, each iteration of equation (40) adds another generation of scattering order to the particle density. The logical extension of this argument is that $\varphi(z) = \varphi_\infty(z)$.

Finally, the transmitted and reflected currents at $z = t$ and $z = 0$, respectively, can be obtained for each order of scattering.

For the transmitted current,

$$T_n^B(t) = \int_o^t dz\ E_2(t-z)\ S_{n-1}(z) \quad , \tag{43}$$

and for the reflected current,

$$B_n^B(t) = \int_o^t dz\ E_2(z)\ S_{n-1}(z) \quad . \tag{44}$$

The currents $T_n^B(t)$ and $B_n^B(t)$ (the superscript denotes results obtained from the Boltzmann equation method) should be directly comparable to those obtained by the orders-of-scattering invariant imbedding method for the cosine (isotropic flux) source. The numerical values obtained by these two methods are in fact very close as is shown in table III. E. 1a, b.

D. 2. Numerical Solution of the One-Dimensional Boltzmann Equation for Isotropic Scatter in Slabs

A computer program was written which solves the integral equation

$$\varphi_n(z) = \varphi_o(z) + 1/2 \int_o^t E_1\left(|z-z'|\right) \varphi_{n-1}(z')\, dz' \quad , \tag{40}$$

If the substitution $y = z - z'$ is made, equation (40) can be rewritten in a form more amenable to computation as follows:

$$\varphi_n(z) = \varphi_o(z) + 1/2 \int_o^{t-z} \varphi_{n-1}(z+y)\ E_1(y)dy + 1/2 \int_o^z \varphi_{n-1}(z-y)\, E_1(y)dy \ . \tag{45}$$

Let the first integral in the above expression be denoted as

$$I = \int_0^{t-z} \varphi_{n-1}(z+y)\, E_1(y)\, dy \quad . \tag{46}$$

The function $E_1(y)$ can be expressed in exact form as

$$E_1(y) = -\gamma - \ell n\, y - \sum_{n=1}^{\infty} \frac{(-1)^n y^n}{n \cdot n!} \quad , \tag{47}$$

where γ is Euler's constant. The integral I can be separated into the following two integrals:

$$I = -\left(I_1 + I_2\right) \quad , \tag{48}$$

where

$$I_1 = \int_0^{t-z} \varphi_{n-1}(z+y) \cdot \ln y\, dy \quad . \tag{49}$$

and

$$I_2 = \int_0^{t-z} \left[\gamma + \sum_{n=1}^{\infty} \frac{(-1)^n y^n}{n \cdot n!}\right] \varphi_{n-1}(z+y)\, dy \quad . \tag{50}$$

The first of these integrals, I_1, can be handled by means of a Gauss quadrature specifically developed for evaluating integrals involving products of logarithms with arbitrary non-singular functions.[5, 6, 7] If the following substitutions are made

$$\Delta \equiv t - z \quad \text{and} \quad u_1 \equiv y/\Delta \quad ,$$

the logarithmic integral becomes

$$I_1 = \Delta \int_0^1 \varphi_{n-1}(z + \Delta u_1)\, \ln(\Delta u_1)\, du_1 \quad . \tag{51a}$$

or

$$I_1 = \Delta \sum_{k=1}^{M_1} A_k \, \varphi_{n-1}\left(z + \Delta u_{1_k}\right) + I_1 a \quad , \tag{51b}$$

with

$$I_1 a = \Delta \ln \Delta \int_0^1 \varphi_{n-1}(z + \Delta w)\, dw \quad . \tag{52}$$

The u_{1_k} are the prescribed quadrature ordinates, and the A_k are their corresponding quadrature coefficients. Since the additional term I_{1a} contains no logarithm in the integrand, it is evaluated by the standard Gauss quadrature procedure as will be outlined for the I_2 integral.

The second integral, I_2, can be evaluated by the standard Gauss quadrature technique. When the transformations $\Delta = t - z$ and $u_2 = \frac{1}{\Delta}(2y - \Delta)$ are made, the result is

$$I_2 = \frac{\Delta}{2} \int_{-1}^{1} \left\{ \gamma + \sum_{\ell=1}^{\infty} \frac{(-1)^{\ell}}{\ell \cdot \ell} \left[\frac{\Delta(1+u_2)}{2} \right]^{\ell} \right\} \varphi_{n-1}\left(z + \frac{\Delta}{2}(1+u_2) \right) du_2 \quad , \tag{53a}$$

$$I_2 = \frac{\Delta}{2} \sum_{k=1}^{M_2} B_k \left\{ \gamma + \sum_{\ell=1}^{60} \frac{(-1)}{\ell \cdot \ell!} \left[\frac{\Delta(1+u_{2_k})}{2} \right]^{\ell} \right\} \varphi_{n-1}\left(z + \frac{\Delta}{2}(1+u_{2_k}) \right) \quad , \tag{53b}$$

where the u_{2_k} and the B_k are the quadrature ordinates and their corresponding coefficients. In the actual calculations, M_1 and M_2 were chosen to be 16 and 32, respectively. The summation over ℓ was not carried out to 60 terms if sufficient convergence could be achieved with a lower ℓ value.

The integrals involving $\varphi_{n-1}(z-y)$ are dealt with in the same manner as those above, so that the resulting computational form for equation (40) becomes

BEST AVAILABLE COPY

$$\varphi_n(z) = \varphi_o(z) - \frac{1}{2} \cdot$$

$$\Delta \sum_{k=1}^{M_1} A_k \varphi_{n-1}\left(z_1 \Delta u_{1_k}\right) + z \sum_{k=1}^{M_1} A_k \varphi_{n-1}\left(z - z u_{1_k}\right)$$

$$+ \frac{\Delta}{2} (\gamma + \ln \Delta) \sum_{k=1}^{M_2} B_k \varphi_{n-1}\left(z + \frac{\Delta}{2} (1 + u_{2_k})\right)$$

$$+ \frac{z}{2} (\gamma + \ln z) \sum_{k=1}^{M_2} B_k \varphi_{n-1}\left(\frac{z}{2} (1 - u_{2_k})\right) \tag{54}$$

$$+ \sum_{k=1}^{M_2} B_k \sum_{\ell=1}^{60} \left(\frac{\Delta}{2}\right)^{\ell+1} \frac{(-1)^{\ell}}{\ell \cdot \ell!} \left(1 + u_{2_k}\right)^{\ell} \varphi_{n-1}\left(z + \frac{\Delta}{2} (1 + u_{2_k})\right)$$

$$+ \sum_{k=1}^{M_2} B_k \sum_{\ell=1}^{60} \left(\frac{z}{2}\right)^{\ell+1} \frac{(-1)^{\ell}}{\ell \cdot \ell!} \left(1 - u_{2_k}\right)^{\ell} \varphi_{n-1}\left(\frac{z}{2} (1 - u_{2_k})\right)$$

The function $\varphi_o(z)$ was taken to be $E_2(z)$.

Typical computational results for the cumulative particle density distribution up to the tenth order of scattering are given in tables III. D. 1-3 for slab thicknesses of 1, 5 and 10 mfp, respectively. A final computation is that of the transmitted and reflected currents as functions of scattering order. The expressions for these, given by equations (43) and (44) are evaluated using a Simpson's rule integration.

Table III. D.1

Cumulative Particle Density Distribution, $\varphi_n(z)$:
Slab Width = 1.0 mfp

z (mfp)	n = 0	1	2	3	4	5
0.00	.100000E+01	.124448E+01	.135864E+01	.142147E+01	.145841E+01	.148074E+01
.05	.872835E+00	.112003E+01	.125760E+01	.133290E+01	.137700E+01	.140360E+01
.10	.722545E+00	.102822E+01	.117937E+01	.126305E+01	.131219E+01	.134185E+01
.15	.641039E+00	.949353E+00	.110948E+01	.119959E+01	.125279E+01	.128496E+01
.20	.574201E+00	.879339E+00	.104517E+01	.114020E+01	.119669E+01	.123095E+01
.25	.517730E+00	.816197E+00	.985214E+00	.108386E+01	.114296E+01	.117892E+01
.30	.469115E+00	.758707E+00	.928888E+00	.103001E+01	.109108E+01	.112838E+01
.35	.426713E+00	.706016E+00	.875712E+00	.978277E+00	.104074E+01	.107903E+01
.40	.389368E+00	.657483E+00	.825329E+00	.928411E+00	.991694E+00	.103065E+01
.45	.356229E+00	.612601E+00	.777447E+00	.880202E+00	.943773E+00	.983059E+00
.50	.326644E+00	.570949E+00	.731823E+00	.833473E+00	.896820E+00	.936115E+00
.55	.300099E+00	.532170E+00	.688233E+00	.788063E+00	.850696E+00	.889688E+00
.60	.276184E+00	.495951E+00	.646474E+00	.743816E+00	.805265E+00	.843656E+00
.65	.254560E+00	.462011E+00	.606336E+00	.700565E+00	.760374E+00	.797842E+00
.70	.234947E+00	.430086E+00	.567609E+00	.658126E+00	.715853E+00	.752112E+00
.75	.217111E+00	.399921E+00	.530060E+00	.616284E+00	.671490E+00	.706243E+00
.80	.200852E+00	.371250E+00	.493413E+00	.574758E+00	.627002E+00	.659949E+00
.85	.185999E+00	.343769E+00	.457304E+00	.533150E+00	.581969E+00	.612794E+00
.90	.172404E+00	.317074E+00	.421171E+00	.490806E+00	.535676E+00	.564031E+00
.95	.159940E+00	.290442E+00	.383894E+00	.446345E+00	.486578E+00	.511999E+00
1.00	.148495E+00	.260733E+00	.340168E+00	.392972E+00	.426895E+00	.448030E+00

BEST AVAILABLE COPY

Table III. D. 1 (cont.)

Cumulative Particle Density Distribution, $\varphi_n(z)$:
Slab Width = 1.0 mfp

BEST AVAILABLE COPY

z (mfp)	n = 6	7	8	9	10
0.00	.149440E+01	.150281E+01	.150801E+01	.151122E+01	.151320E+01
.05	.141987E+01	.142988E+01	.143605E+01	.143987E+01	.144223E+01
.10	.135999E+01	.137114E+01	.137803E+01	.138229E+01	.138492E+01
.15	.130466E+01	.131678E+01	.132426E+01	.132888E+01	.133174E+01
.20	.125194E+01	.126487E+01	.127285E+01	.127778E+01	.128084E+01
.25	.120099E+01	.121459E+01	.122298E+01	.122818E+01	.123139E+01
.30	.115131E+01	.116546E+01	.117420E+01	.117959E+01	.118294E+01
.35	.110262E+01	.111718E+01	.112618E+01	.113175E+01	.113519E+01
.40	.105469E+01	.106954E+01	.107872E+01	.108441E+01	.108792E+01
.45	.100735E+01	.102237E+01	.103166E+01	.103741E+01	.104097E+01
.50	.960454E+00	.975523E+00	.984850E+00	.990622E+00	.994196E+00
.55	.913883E+00	.928877E+00	.938161E+00	.943910E+00	.947468E+00
.60	.867503E+00	.882299E+00	.891466E+00	.897144E+00	.900658E+00
.65	.821170E+00	.835649E+00	.844625E+00	.850184E+00	.853626E+00
.70	.774718E+00	.788761E+00	.797468E+00	.802863E+00	.806203E+00
.75	.727937E+00	.741422E+00	.749786E+00	.754968E+00	.758177E+00
.80	.680536E+00	.693389E+00	.701283E+00	.706205E+00	.709254E+00
.85	.632070E+00	.644063E+00	.651504E+00	.656116E+00	.658973E+00
.90	.581766E+00	.592803E+00	.599653E+00	.603899E+00	.606528E+00
.95	.527902E+00	.537798E+00	.543940E+00	.547747E+00	.550105E+00
1.00	.461683E+00	.470007E+00	.475172E+00	.478373E+00	.480356E+00

Table III. D. 2

Cumulative Particle Density Distribution, $\varphi_n(z)$:
Slab Width = 5.0 mfp

z (mfp)	n = 0	1	2	3	4	5
0.0	.100000E+01	.124980E+01	.137554E+01	.145369E+01	.150833E+01	.154930E+01
.2	.574201E+00	.836917E+00	.106884E+01	.118618E+01	.126873E+01	.133057E+01
.4	.389368E+00	.668122E+00	.857669E+00	.990358E+00	.108766E+01	.116218E+01
.6	.276184E+00	.511377E+00	.691354E+00	.827243E+00	.931655E+00	.101396E+01
.8	.200852E+00	.394994E+00	.558181E+00	.689867E+00	.795771E+00	.881880E+00
1.0	.148495E+00	.307013E+00	.450992E+00	.574172E+00	.677571E+00	.764291E+00
1.2	.111104E+00	.239750E+00	.364540E+00	.476972E+00	.575178E+00	.660063E+00
1.4	.838899E-01	.187919E+00	.294741E+00	.395542E+00	.486889E+00	.568155E+00
1.6	.638032E-01	.147741E+00	.238359E+00	.327511E+00	.411099E+00	.487533E+00
1.8	.488153E-01	.116450E+00	.192801E+00	.270813E+00	.346304E+00	.417155E+00
2.0	.375343E-01	.919877E-01	.155977E+00	.223661E+00	.291110E+00	.355991E+00
2.2	.289827E-01	.728021E-01	.126207E+00	.184520E+00	.244243E+00	.303048E+00
2.4	.224613E-01	.577142E-01	.102131E+00	.150208E+00	.204559E+00	.257384E+00
2.6	.174630E-01	.458209E-01	.826596E-01	.125228E+00	.171040E+00	.218123E+00
2.8	.136152E-01	.364262E-01	.669055E-01	.103029E+00	.142789E+00	.184462E+00
3.0	.106419E-01	.289914E-01	.541582E-01	.846961E-01	.119021E+00	.155670E+00
3.2	.833663E-02	.230977E-01	.438383E-01	.695629E-01	.990508E-01	.131089E+00
3.4	.654396E-02	.184180E-01	.354780E-01	.570759E-01	.822889E-01	.110131E+00
3.6	.514623E-02	.146965E-01	.287043E-01	.467721E-01	.682253E-01	.922753E-01
3.8	.405383E-02	.117320E-01	.232079E-01	.382653E-01	.564217E-01	.770582E-01
4.0	.313823E-02	.936604E-02	.187409E-01	.312295E-01	.464981E-01	.640678E-01
4.2	.252678E-02	.747272E-02	.150986E-01	.253904E-01	.381242E-01	.529343E-01
4.4	.199890E-02	.595132E-02	.121124E-01	.205135E-01	.310074E-01	.433184E-01
4.6	.158321E-02	.471904E-02	.963655E-02	.163854E-01	.248705E-01	.348848E-01
4.8	.125538E-02	.370169E-02	.752824E-02	.127842E-01	.194047E-01	.272355E-01
5.0	.996469E-03	.277679E-02	.540984E-02	.918923E-02	.137938E-01	.192029E-01

Table III. E. 2(cont.) BEST AVAILABLE COPY
BEST AVAILABLE COPY

Table III. D. 2(cont.)

Cumulative Particle Density Distribution, $\varphi_n(z)$:
Slab Width = 5.0 mfp

z (mfp)	n = 6	7	8	9	10
0.0	.153148E+01	.160761E+01	.162936E+01	.164783E+01	.166375E+01
.2	.137904E+01	.141832E+01	.145096E+01	.147863E+01	.150244E+01
.4	.122131E+01	.126962E+01	.130995E+01	.134427E+01	.137389E+01
.6	.108051E+01	.113551E+01	.118185E+01	.122152E+01	.125591E+01
.8	.952992E+00	.101266E+01	.106348E+01	.110732E+01	.114556E+01
1.0	.837535E+00	.900015E+00	.953878E+00	.100078E+01	.104199E+01
1.2	.732404E+00	.797056E+00	.852658E+00	.901570E+00	.944893E+00
1.4	.638969E+00	.703397E+00	.759569E+00	.809522E+00	.854149E+00
1.6	.556577E+00	.618636E+00	.674370E+00	.724492E+00	.769680E+00
1.8	.485530E+00	.542318E+00	.596772E+00	.646306E+00	.691381E+00
2.0	.417098E+00	.473935E+00	.526429E+00	.574733E+00	.619108E+00
2.2	.359531E+00	.412939E+00	.462949E+00	.509496E+00	.552665E+00
2.4	.309085E+00	.358758E+00	.405898E+00	.450272E+00	.491816E+00
2.6	.265039E+00	.310811E+00	.354820E+00	.396705E+00	.436286E+00
2.8	.226702E+00	.268522E+00	.309241E+00	.348412E+00	.385767E+00
3.0	.193424E+00	.231331E+00	.268687E+00	.304997E+00	.339928E+00
3.2	.164600E+00	.198697E+00	.232687E+00	.266053E+00	.298422E+00
3.4	.139674E+00	.170111E+00	.200783E+00	.231172E+00	.260890E+00
3.6	.118135E+00	.145090E+00	.172527E+00	.199949E+00	.226966E+00
3.8	.995197E-01	.123182E+00	.147492E+00	.171983E+00	.196278E+00
4.0	.834009E-01	.103963E+00	.125264E+00	.146876E+00	.168448E+00
4.2	.693853E-01	.870271E-01	.105434E+00	.124227E+00	.143083E+00
4.4	.570984E-01	.719758E-01	.875893E-01	.103611E+00	.119756E+00
4.6	.461545E-01	.593812E-01	.712662E-01	.845358E-01	.979500E-01
4.8	.360674E-01	.456693E-01	.558053E-01	.662670E-01	.768553E-01
5.0	.252709E-01	.318432E-01	.387618E-01	.458816E-01	.530754E-01

BEST AVAILABLE COPY

Table III. D. 3

Cumulative Particle Density Distribution, $\varphi_n(z)$:
Slab Width = 10.0 mfp

z (mfp)	n= 0	1	2	3	4	5
0.0	.100000E+01	.124921E+01	.137644E+01	.145444E+01	.150896E+01	.154986E+01
.5	.324644E+00	.583694E+00	.769793E+00	.990353E+00	.100695E+01	.108593E+01
1.0	.148495E+00	.307014E+00	.450992E+00	.574179E+00	.677598E+00	.764356E+00
1.5	.731008E-01	.166567E+00	.265054E+00	.360008E+00	.447582E+00	.526614E+00
2.0	.375343E-01	.919904E-01	.155991E+00	.223702E+00	.291208E+00	.356191E+00
2.5	.197977E-01	.514211E-01	.919047E-01	.138089E+00	.187259E+00	.237346E+00
3.0	.106419E-01	.290013E-01	.542043E-01	.848290E-01	.119322E+00	.156256E+00
3.5	.580189E-02	.164707E-01	.320023E-01	.519214E-01	.754860E-01	.101863E+00
4.0	.318823E-02	.940672E-02	.189151E-01	.316941E-01	.474811E-01	.658686E-01
4.5	.177869E-02	.539727E-02	.111920E-01	.193072E-01	.297272E-01	.423074E-01
5.0	.996469E-03	.310885E-02	.662673E-02	.117394E-01	.185380E-01	.270175E-01
5.5	.561678E-03	.179664E-02	.392731E-02	.712923E-02	.115228E-01	.171697E-01
6.0	.318258E-03	.104612E-02	.232885E-02	.432345E-02	.714089E-02	.108636E-01
6.5	.181145E-03	.604846E-03	.138220E-02	.262001E-02	.441566E-02	.684927E-02
7.0	.103510E-03	.352007E-03	.820322E-03	.158528E-02	.272290E-02	.430219E-02
7.5	.593527E-04	.205107E-03	.486418E-03	.957325E-03	.167488E-02	.269313E-02
8.0	.341376E-04	.119532E-03	.288088E-03	.577672E-03	.102795E-02	.167982E-02
8.5	.196888E-04	.695397E-04	.170009E-03	.346402E-03	.626535E-03	.104063E-02
9.0	.113836E-04	.402151E-04	.989406E-04	.205334E-03	.378019E-03	.637143E-03
9.5	.659642E-05	.232410E-04	.556177E-04	.118121E-03	.221575E-03	.377954E-03
10.0	.383024E-05	.117937E-04	.275394E-04	.594378E-04	.111066E-03	.189756E-03

BEST AVAILABLE COPY

BEST AVAILABLE COPY

Table III. D. 3(cont.)
Cumulative Particle Density Distribution, $\varphi_n(z)$:
Slab Width = 10.0 mfp

z (mfp)	n = 6	7	8	9	10
0.0	.158200E+01	.160811E+01	.162987E+01	.164838E+01	.166435E+01
.5	.114919E+01	.120117E+01	.124480E+01	.128206E+01	.131434E+01
1.0	.837662E+00	.900240E+00	.954244E+00	.100134E+01	.104281E+01
1.5	.597276E+00	.660303E+00	.716596E+00	.767045E+00	.812452E+00
2.0	.417462E+00	.474548E+00	.527395E+00	.576177E+00	.621175E+00
2.5	.286916E+00	.335047E+00	.381198E+00	.425095E+00	.466635E+00
3.0	.194449E+00	.232986E+00	.271201E+00	.308628E+00	.344965E+00
3.5	.130246E+00	.159923E+00	.190299E+00	.220899E+00	.251361E+00
4.0	.863856E-01	.108555E+00	.131933E+00	.156125E+00	.180798E+00
4.5	.568177E-01	.729822E-01	.905099E-01	.109117E+00	.128541E+00
5.0	.371009E-01	.496561E-01	.615182E-01	.755062E-01	.904365E-01
5.5	.240759E-01	.332015E-01	.414712E-01	.517855E-01	.630309E-01
6.0	.155371E-01	.211726E-01	.277517E-01	.352324E-01	.435551E-01
6.5	.997931E-02	.138415E-01	.184494E-01	.237973E-01	.298627E-01
7.0	.638003E-02	.899967E-02	.121897E-01	.159641E-01	.203237E-01
7.5	.406130E-02	.582115E-02	.800557E-02	.106376E-01	.137306E-01
8.0	.257289E-02	.374361E-02	.522302E-02	.703606E-02	.920092E-02
8.5	.161833E-02	.238856E-02	.337700E-02	.460711E-02	.609725E-02
9.0	.100454E-02	.150118E-02	.214756E-02	.296203E-02	.396065E-02
9.5	.601784E-03	.907392E-03	.130894E-02	.181945E-02	.245056E-02
10.0	.301100E-03	.452189E-03	.649736E-03	.900510E-03	.121004E-02

E. Monte Carlo Calculation of Particle Transport in Slabs

The Monte Carlo method as applied to particle transport consists basically of attempting to describe the behavior of an entire ensemble of particles by tracing the histories of many individual particles as they migrate through the scattering medium and then performing appropriate summations over a sufficiently large number of these histories to arrive at a description of the ensemble as a whole. While this method lacks the elegance and computational efficiency associated with other types of transport calculations, it does provide an extremely high degree of flexibility with regard to the variety of problems that can be handled. Results of Monte Carlo calculations are used here to confirm the results obtained by the O.O.S.I.I. method and the Boltzmann equation solutions. The method is conceptually simple and provides a truly independent means to such a confirmation.

A Monte Carlo program was written to study the transport of particles in scattering slabs. The computation is organized into two main parts. Part I consists of (1) the generation of a plane isotropic (current) source of particles at the boundary of an infinite slab; (2) the tracing of the particle histories through the medium while keeping account and recording the collision site positions, trajectory orientations and orders of scattering. Part II superimposes a source distribution function on the plane isotropic source and calculates the transmitted and reflected currents for each order of scattering and for a number of finite slab thicknesses assumed to be imbedded within the infinite slab.

E.1. Generation of Particle Histories

The discussion which follows pertains only to conservative scattering, isotropic in the laboratory system. Other Monte Carlo programs were written to handle various types of anisotropic scattering. In later sections these will be discussed only to the extent to which they differ from the present calculation.

When a particle history is originated at the source plane, the initial direction, relative to the laboratory coordinate system, of departure from the source point is first determined. The initial polar angle of the trajectory with respect to the z-axis is determined by sampling a uniform

random number distribution. Let r_1 be auniformly distributed random number (actually a computer generated pseudo-random number) where $0.0 < r_1 < 1.0$. Then the cosine of the initial polar angle is

$$\mu_o = \cos\theta_o = r_1 \tag{55}$$

The initial azimuthal direction: φ, is chosen to be zero.

The penetration distance between collisions is determined by inversion of the exponential attenuation formula for particle flux in an attenuating medium. The exponential attenuation factor is selected from a set of uniformly distributed random numbers r_2 where $0.0 < r_2 < 1.0$ so that

$$r_2 = e^{-s_n/\lambda} \tag{56}$$

where λ is the scattering mean-free-path and s_n is the penetration distance after the n-th scatter.

The inverse of this expression yields the following direct determination of s_n:

$$s_n = -\lambda\, \ell_n(r_2) \tag{57}$$

Once the penetration distance is computed, the coordinates of the next point of interaction are determined. Given that the n-th interaction occurs at the point (x_n, y_n, z_n) and the direction of the particle trajectory after the interaction is defined by the angles θ^n, φ^n respectively the polar and azimuthal angles in the laboratory frame, then the coordinates of the point of next interaction are given by

$$x_{n+1} = x_n + s_n \sin\theta^n \cos\varphi^n \quad , \tag{58a}$$

$$y_{n+1} = y_n + s_n \sin\theta^n \sin\varphi^n \quad , \tag{58b}$$

$$z_{n+1} = z_n + s_n \cos\theta^n \quad . \tag{58c}$$

(The superscript n denotes orientation after the n-th collision). The collision positions and trajectory orientations are recorded in a mass storage file for every collision of every particle. This file is subsequently used for the particle current computations.

Selection of the post-collision orientation for isotropic scattering in the laboratory system consists of making a random choice for the cosine of the polar angle θ^n as was done for the initial polar angle. Since the scattering is isotropic in azimuth, the azimuthal orientation is obtained by random selection of the angle on the interval $(0, 2\pi)$. That is, let r_3 be a uniformly distributed random number where $0.0 < r_3 < 1.0$, then

$$\varphi^n = 2\pi r_3 \tag{59}$$

The above described procedure is repeated until the particle has either undergone a pre-specified maximum number of collision in the slab or has been backscattered out of the slab through the source face.

E.2. Determination of Transmitted and Reflected Currents for Slabs of Various Widths

As a result of the operation of Part I, the pertinent statistics of the scattered particles at every collision site are stored and available for analysis. The program which computes the transmitted and reflected currents consists of a straightforward particle counting procedure. A grid of finite slab boundaries is superimposed within the infinite slab (fig. III.E.1) As was previously stated, particle histories are terminated in one of two ways, either by having undergone a maximum allowed number of collisions within the slab or by backscatter out of the slab. The first situation is

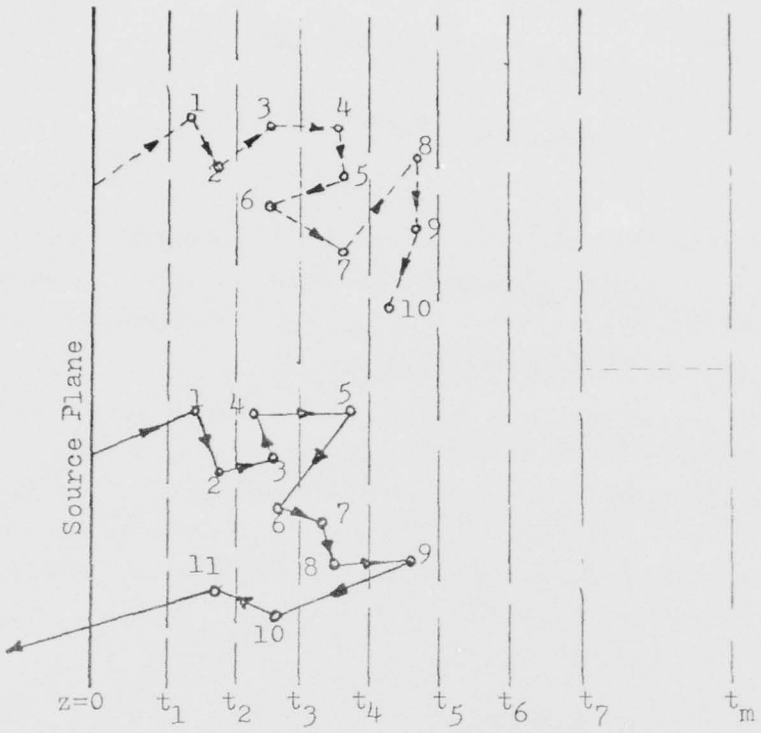

Figure III.E.1

Monte Carlo Slab Configuration

depicted by the dashed line trajectory of fig. III.E.1, and the second by the solid line trajectory. The particle counting procedure executed by the program assigns the following interpretation to the dashed line trajectory;

1) Transmission through a slab of thickness t_1 after 0 collisions
2) " " " " " " t_2 " 2 "
3) " " " " " " t_3 " 3 "
4) " " " " " " t_4 " 7 "

and the following interpretation to the solid line trajectory;

1) transmission through a slab of thickness t_1 after 0 collisions
2) " " " " " " t_2 " 2 "
3) " " " " " " t_3 " 4 "
4) " " " " " " t_4 " 8 "
5) backscatter from a slab of thickness t_5 after 11 collisions
6) " " " " " " t_6 " " "
7) " " " " " " t_7 " " "

.
.
.

" " " " " " t_m " " "

The transmission and reflection current bins are filled by the application of this counting procedure to every particle history. As each history is considered, it is assigned a source weighting factor. For the case of the cosine current (isotropic flux) source, the tallied figure in each bin is simply twice the initial polar angle cosine, μ_o, of each trajectory (the factor of two is required for source normalization), and in the isotropic current source case, the tallied figure in each bin is unity. The final normalized currents are obtained by dividing these sums by the total number of particle histories considered.

The results of these Monte Carlo computations are given in table III. E. 1-2 where a comparison with the results obtained by the two methods previously discussed is readily available. For the isotropic scattering case, 100,000 histories were run.

BEST AVAILABLE COPY

Table III.E.1a

Transmitted Particle Currents, $T_n(t)$, Obtained by Three Methods, through Slabs of Various Widths, t: Unit Current Cosine Distributed Source; Isotropic Scatter

t	n	Transmitted Current, $T_n(t)$		
		OOSII	Boltzmann	Monte Carlo
	0	.219384E+00	.219384E+00	.217266E+00
	1	.116689E+00	.116293E+00	.116196E+00
	2	.793053E-01	.791163E-01	.795006E-01
	3	.516197E-01	.515542E-01	.519376E-01
	4	.327453E-01	.327732E-01	.335511E-01
1.0	5	.205805E-01	.205669E-01	.208948E-01
	6	.127476E-01	.128200E-01	.128867E-01
	7	.789834E-02	.796341E-02	.804417E-02
	8	.488657E-02	.493785E-02	.503798E-02
	9	.302027E-02	.305302E-02	.310136E-02
	10	.186578E-02	.189426E-02	.190455E-02
	0	.602668E-01	.602667E-01	.608177E-01
	1	.507640E-01	.506139E-01	.499433E-01
	2	.487523E-01	.486028E-01	.484898E-01
	3	.435597E-01	.434810E-01	.429898E-01
	4	.372403E-01	.371008E-01	.369740E-01
2.0	5	.308037E-01	.307182E-01	.308832E-01
	6	.249800E-01	.249417E-01	.246029E-01
	7	.203318E-01	.199041E-01	.204526E-01
	8	.159031E-01	.158052E-01	.157407E-01
	9	.124966E-01	.125487E-01	.127935E-01
	10	.973058E-02	.990299E-02	.103213E-01
	0	.178613E-01	.178613E-01	.174868E-01
	1	.191759E-01	.191271E-01	.193656E-01
	2	.222302E-01	.221743E-01	.217870E-01
	3	.236118E-01	.235604E-01	.232296E-01
	4	.236871E-01	.235764E-01	.240183E-01
3.0	5	.227188E-01	.226269E-01	.225202E-01
	6	.211493E-01	.210775E-01	.204169E-01
	7	.196672E-01	.192161E-01	.195733E-01
	8	.176079E-01	.172466E-01	.172665E-01
	9	.155689E-01	.153026E-01	.152780E-01
	10	.136432E-01	.134642E-01	.134051E-01
	0	.552572E-02	.552572E-02	.533401E-02
	1	.696350E-02	.694096E-02	.680952E-02
	2	.916467E-02	.914695E-02	.878921E-02
	3	.109595E-01	.109391E-01	.107912E-01
	4	.122203E-01	.122224E-01	.123640E-01
4.0	5	.130579E-01	.130005E-01	.132089E-01
	6	.133926E-01	.133291E-01	.129778E-01
	7	.135106E-01	.132888E-01	.131539E-01
	8	.131026E-01	.129663E-01	.133520E-01
	9	.126570E-01	.124419E-01	.124103E-01
	10	.119770E-01	.117839E-01	.119171E-01

BEST AVAILABLE COPY

Table III.E.1a(cont.)

Transmitted Particle Currents, $T_n(t)$, Obtained by Three Methods, through Slabs of Various Widths,t: Unit Current Cosine Distributed Source; Isotropic Scatter

t	n	Transmitted Current, $T_n(t)$		
		OOSII	Boltzmann	Monte Carlo
5.0	0	.175560E-02	.175560E-02	.152346E-02
	1	.249686E-02	.248709E-02	.247894E-02
	2	.363551E-02	.359853E-02	.372383E-02
	3	.471388E-02	.470691E-02	.444367E-02
	4	.574410E-02	.572134E-02	.549586E-02
	5	.661721E-02	.658010E-02	.648722E-02
	6	.731065E-02	.728630E-02	.738797E-02
	7	.788730E-02	.778684E-02	.804580E-02
	8	.822048E-02	.811643E-02	.825830E-02
	9	.840564E-02	.828623E-02	.796229E-02
	10	.844041E-02	.831349E-02	.854578E-02
6.0	0	.569208E-03	.569207E-03	.614914E-03
	1	.895422E-03	.893026E-03	.697931E-03
	2	.138164E-02	.137094E-02	.139510E-02
	3	.194011E-02	.193624E-02	.191324E-02
	4	.253101E-02	.252601E-02	.255155E-02
	5	.311022E-02	.309672E-02	.294659E-02
	6	.365447E-02	.363888E-02	.358198E-02
	7	.418247E-02	.412604E-02	.415100E-02
	8	.460644E-02	.454494E-02	.466406E-02
	9	.495542E-02	.488805E-02	.470109E-02
	10	.522713E-02	.515612E-02	.524053E-02
7.0	0	.187213E-03	.187213E-03	.177920E-03
	1	.313078E-03	.313315E-03	.227486E-03
	2	.521129E-03	.520006E-03	.540133E-03
	3	.776366E-03	.774554E-03	.656909E-03
	4	.107192E-02	.106730E-02	.118984E-02
	5	.139112E-02	.138639E-02	.140656E-02
	6	.172032E-02	.171521E-02	.166816E-02
	7	.207047E-02	.206441E-02	.213144E-02
	8	.239020E-02	.238170E-02	.235014E-02
	9	.269736E-02	.268034E-02	.252694E-02
	10	.296004E-02	.293731E-02	.285283E-02
8.0	0	.623614E-04	.623615E-04	.532775E-04
	1	.111072E-03	.111127E-03	.652521E-04
	2	.196559E-03	.198029E-03	.162697E-03
	3	.304786E-03	.303618E-03	.273590E-03
	4	.441752E-03	.439752E-03	.523437E-03
	5	.600273E-03	.598380E-03	.608133E-03
	6	.778417E-03	.775282E-03	.624697E-03
	7	.944010E-03	.945275E-03	.975051E-03
	8	.118410E-02	.116280E-02	.115256E-02
	9	.138543E-02	.136230E-02	.124661E-02
	10	.158278E-02	.155896E-02	.147020E-02

Table III.E.1b

Reflected Particle Currents, $B_n(t)$, Obtained by Three Methods, from Slabs of Various Widths, t: Unit Current Cosine Distributed Source; Isotropic Scatter

t	n	Reflected Current, $B_n(t)$		
		OOSII	Boltzmann	Monte Carlo
1.0	0	0.	0.	0.
	1	.201373E+00	.197120E+00	.197135E+00
	2	.102034E+00	.101542E+00	.102447E+00
	3	.592115E-01	.592546E-01	.583891E-01
	4	.347117E-01	.348082E-01	.345327E-01
	5	.210024E-01	.211008E-01	.206014E-01
	6	.129264E-01	.130120E-01	.126899E-01
	7	.795244E-02	.802594E-02	.810657E-02
	8	.490296E-02	.495619E-02	.464572E-02
	9	.302525E-02	.306467E-02	.298956E-02
	10	.186749E-02	.189590E-02	.194834E-02
2.0	0	0.	0.	0.
	1	.208695E+00	.205742E+00	.204594E+00
	2	.114006E+00	.114141E+00	.114853E+00
	3	.744208E-01	.744603E-01	.739735E-01
	4	.521056E-01	.521647E-01	.516625E-01
	5	.381429E-01	.381710E-01	.378436E-01
	6	.286122E-01	.286579E-01	.283033E-01
	7	.217076E-01	.218547E-01	.218936E-01
	8	.166479E-01	.168286E-01	.167427E-01
	9	.128166E-01	.130372E-01	.135114E-01
	10	.988018E-02	.101386E-01	.990597E-02
3.0	0	0.	0.	0.
	1	.209303E+00	.205126E+00	.204999E+00
	2	.116146E+00	.115565E+00	.116038E+00
	3	.765225E-01	.764240E-01	.761445E-01
	4	.551727E-01	.551677E-01	.546451E-01
	5	.419132E-01	.419022E-01	.416419E-01
	6	.330143E-01	.330205E-01	.326485E-01
	7	.267062E-01	.266704E-01	.271258E-01
	8	.219706E-01	.219179E-01	.218503E-01
	9	.182424E-01	.182365E-01	.186176E-01
	10	.152927E-01	.153092E-01	.152552E-01
4.0	0	0.	0.	0.
	1	.209246E+00	.205456E+00	.205047E+00
	2	.116271E+00	.115507E+00	.116124E+00
	3	.767750E-01	.767737E-01	.763996E-01
	4	.555059E-01	.555358E-01	.551250E-01
	5	.425361E-01	.425235E-01	.421764E-01
	6	.338573E-01	.338583E-01	.335986E-01
	7	.278797E-01	.277318E-01	.281716E-01
	8	.232031E-01	.231087E-01	.231327E-01
	9	.197491E-01	.197219E-01	.200510E-01
	10	.170405E-01	.169768E-01	.168694E-01

BEST AVAILABLE COPY

BEST AVAILABLE COPY

Table III.E.1b(cont.)

Reflected Particle Currents, $B_n(t)$, Obtained by Three Methods, from Slabs of Various Widths, t: Unit Current Cosine Distributed Source; Isotropic Scatter

t	n	Reflected Current, $B_n(t)$		
		OOSII	Boltzmann	Monte Carlo
5.0	0	0.	0.	0.
	1	.209250E+00	.206296E+00	.205047E+00
	2	.116284E+00	.115511E+00	.116140E+00
	3	.768050E-01	.768263E-01	.764577E-01
	4	.556512E-01	.556022E-01	.551794E-01
	5	.426286E-01	.426197E-01	.422247E-01
	6	.339065E-01	.339083E-01	.337570E-01
	7	.280795E-01	.279267E-01	.283678E-01
	8	.235487E-01	.234572E-01	.233697E-01
	9	.201074E-01	.200509E-01	.203978E-01
	10	.174762E-01	.173908E-01	.173130E-01
6.0	0	0.	0.	0.
	1	.209250E+00	.205173E+00	.205047E+00
	2	.116286E+00	.115700E+00	.116140E+00
	3	.768086E-01	.767344E-01	.764577E-01
	4	.556585E-01	.555903E-01	.551794E-01
	5	.426617E-01	.426248E-01	.422391E-01
	6	.340179E-01	.340160E-01	.337772E-01
	7	.281131E-01	.279574E-01	.284103E-01
	8	.235969E-01	.235031E-01	.234125E-01
	9	.201733E-01	.201144E-01	.204572E-01
	10	.175030E-01	.174451E-01	.174338E-01
7.0	0	0.	0.	0.
	1	.209250E+00	.205398E+00	.205047E+00
	2	.116286E+00	.115660E+00	.116140E+00
	3	.768090E-01	.768008E-01	.764577E-01
	4	.556594E-01	.555957E-01	.551794E-01
	5	.426635E-01	.426284E-01	.422573E-01
	6	.340210E-01	.340199E-01	.337772E-01
	7	.281184E-01	.279629E-01	.284199E-01
	8	.236050E-01	.235109E-01	.234218E-01
	9	.201851E-01	.201258E-01	.204602E-01
	10	.175194E-01	.174908E-01	.174492E-01
8.0	0	0.	0.	0.
	1	.209250E+00	.205660E+00	.205047E+00
	2	.116286E+00	.115611E+00	.116140E+00
	3	.768090E-01	.768195E-01	.764577E-01
	4	.556596E-01	.556007E-01	.551794E-01
	5	.426637E-01	.426304E-01	.422573E-01
	6	.340214E-01	.340212E-01	.337772E-01
	7	.281192E-01	.279639E-01	.284199E-01
	8	.236063E-01	.235123E-01	.234218E-01
	9	.201871E-01	.201277E-01	.204602E-01
	10	.175023E-01	.174935E-01	.174492E-01

BEST AVAILABLE COPY

Table III.E.2

Transmitted and Reflected Particle Currents, $T_n(t)$ and $B_n(t)$, Obtained by Two Methods, from Slabs of Various Widths, t: Unit Isotropically Distributed Current Source; Isotropic Scatter

t	n	Transmitted Current, $T_n(t)$		Reflected Current, $B_n(t)$	
		OOSII	Monte Carlo	OOSII	Monte Carlo
1.0	0	.148405E+00	.147040E+00	0.	0.
	1	.112627E+00	.112430E+00	.244480E+00	.245940E+00
	2	.797412E-01	.786850E-01	.113837E+00	.114170E+00
	3	.529593E-01	.530700E-01	.627664E-01	.631200E-01
	4	.339605E-01	.343950E-01	.368739E-01	.366900E-01
	5	.213789E-01	.216600E-01	.223543E-01	.218250E-01
	6	.133368E-01	.133550E-01	.135950E-01	.134500E-01
	7	.827293E-02	.846500E-02	.835216E-02	.850000E-02
	8	.512077E-02	.551000E-02	.514498E-02	.494000E-02
	9	.316611E-02	.333500E-02	.317345E-02	.319000E-02
	10	.195649E-02	.201500E-02	.195863E-02	.205500E-02
2.0	0	.375343E-01	.378100E-01	0.	0.
	1	.424972E-01	.418650E-01	.249648E+00	.251190E+00
	2	.429093E-01	.428650E-01	.123991E+00	.124030E+00
	3	.394960E-01	.389550E-01	.763211E-01	.762700E-01
	4	.344096E-01	.338950E-01	.519736E-01	.518250E-01
	5	.288192E-01	.289850E-01	.374030E-01	.370600E-01
	6	.235590E-01	.230400E-01	.277937E-01	.276950E-01
	7	.193065E-01	.191600E-01	.209224E-01	.210150E-01
	8	.152609E-01	.149500E-01	.150648E-01	.159400E-01
	9	.119075E-01	.122300E-01	.122602E-01	.129050E-01
	10	.928672E-02	.967000E-02	.945162E-02	.955550E-02
3.0	0	.136419E-01	.104800E-01	0.	0.
	1	.149042E-01	.149650E-01	.249972E+00	.251440E+00
	2	.132247E-01	.179300E-01	.124872E+00	.124880E+00
	3	.200259E-01	.198000E-01	.779058E-01	.779250E-01
	4	.205563E-01	.208050E-01	.543191E-01	.541000E-01
	5	.200394E-01	.197100E-01	.404527E-01	.401500E-01
	6	.189723E-01	.180950E-01	.314361E-01	.312650E-01
	7	.177609E-01	.174050E-01	.251382E-01	.252750E-01
	8	.159929E-01	.155350E-01	.205061E-01	.203150E-01
	9	.141983E-01	.139650E-01	.169636E-01	.174100E-01
	10	.124779E-01	.121150E-01	.141736E-01	.142850E-01
4.0	0	.319823E-02	.310500E-02	0.	0.
	1	.515903E-02	.505000E-02	.249997E+00	.251470E+00
	2	.717123E-02	.703000E-02	.124956E+00	.124930E+00
	3	.888635E-02	.871500E-02	.780854E-01	.781100E-01
	4	.102127E-01	.102150E-01	.546323E-01	.544500E-01
	5	.110622E-01	.111050E-01	.409290E-01	.405650E-01
	6	.114993E-01	.111750E-01	.320966E-01	.320100E-01
	7	.117406E-01	.113050E-01	.259479E-01	.261250E-01
	8	.115730E-01	.116350E-01	.215662E-01	.213800E-01
	9	.111785E-01	.108400E-01	.182151E-01	.185750E-01
	10	.106208E-01	.105300E-01	.155991E-01	.156400E-01

BEST AVAILABLE COPY

Table III.E.2(cont.)

Transmitted and Reflected Particle Currents, $T_n(t)$ and $B_n(t)$, Obtained by Two Methods, from Slabs of Various Widths, t; Unit Isotropically Distributed Current Source; Isotropic Scatter

t	n	Transmitted Current, $T_n(t)$		Reflected Current, $B_n(t)$	
		OOSII	Monte Carlo	OOSII	Monte Carlo
	0	.996459E-03	.870000E-03	0.	0.
	1	.178365E-02	.172000E-02	.250000E+00	.251470E+00
	2	.272619E-02	.287000E-02	.124964E+00	.124940E+00
	3	.369712E-02	.353500E-02	.781059E-01	.781450E-01
	4	.462747E-02	.440000E-02	.546723E-01	.544950E-01
5.0	5	.543700E-02	.543500E-02	.409971E-01	.406000E-01
	6	.610041E-02	.621000E-02	.322015E-01	.321400E-01
	7	.666174E-02	.660500E-02	.261508E-01	.262750E-01
	8	.702184E-02	.716000E-02	.217730E-01	.215700E-01
	9	.723269E-02	.692000E-02	.184825E-01	.188550E-01
	10	.731138E-02	.739000E-02	.159320E-01	.160000E-01
	0	.318258E-03	.345000E-03	0.	0.
	1	.617761E-03	.505000E-03	.250000E+00	.251470E+00
	2	.101758E-02	.102500E-02	.124965E+00	.124940E+00
	3	.149256E-02	.149000E-02	.781083E-01	.781450E-01
	4	.199713E-02	.195500E-02	.546774E-01	.544950E-01
6.0	5	.249324E-02	.234500E-02	.410064E-01	.406100E-01
	6	.297844E-02	.301000E-02	.322171E-01	.321600E-01
	7	.345125E-02	.338500E-02	.261758E-01	.263000E-01
	8	.384426E-02	.390500E-02	.218096E-01	.216000E-01
	9	.417457E-02	.399500E-02	.185333E-01	.189000E-01
	10	.443752E-02	.438500E-02	.159998E-01	.160900E-01
	0	.103510E-03	.100000E-03	0.	0.
	1	.214500E-03	.150000E-03	.250000E+00	.251470E+00
	2	.375834E-03	.365000E-03	.124965E+00	.124940E+00
	3	.590874E-03	.515000E-03	.781086E-01	.781450E-01
	4	.824198E-03	.875000E-03	.546780E-01	.544950E-01
7.0	5	.109269E-02	.110000E-02	.410076E-01	.406200E-01
	6	.137650E-02	.132000E-02	.322104E-01	.321600E-01
	7	.168265E-02	.168000E-02	.261797E-01	.263050E-01
	8	.196440E-02	.197500E-02	.218156E-01	.216050E-01
	9	.223185E-02	.214000E-02	.185422E-01	.189100E-01
	10	.247757E-02	.243000E-02	.160123E-01	.161000E-01
	0	.341376E-04	.300000E-04	0.	0.
	1	.747801E-04	.500000E-04	.250000E+00	.251470E+00
	2	.137881E-03	.115000E-03	.124965E+00	.124940E+00
	3	.224043E-03	.195000E-03	.781086E-01	.781450E-01
	4	.333760E-03	.385000E-03	.546781E-01	.544950E-01
8.0	5	.463882E-03	.475000E-03	.410078E-01	.406200E-01
	6	.611551E-03	.495000E-03	.322107E-01	.321600E-01
	7	.784477E-03	.765000E-03	.261803E-01	.263050E-01
	8	.954702E-03	.930000E-03	.218165E-01	.216050E-01
	9	.112882E-02	.980000E-03	.185436E-01	.189100E-01
	10	.130204E-02	.123500E-02	.160145E-01	.161000E-01

F. Neutron Slowing-Down in Hydrogen - An Example of Highly Anisotropic Scattering

Thus far, the discussion of particle transport has been confined to interactions where the scattering is isotropic in the laboratory coordinate system. As has been stated previously, this case was adopted because of its inherent simplicity and the accessibility of at least two other independent calculational methods for verification of the results. However, many important processes can be decribed adequately only by anisotropic scattering. Such is the case for neutron slowing-down in Hydrogen where the scattering is isotropic[8] in the center of mass coordinate system. In the laboratory system this translates into a scattering probability density which is proportional to the cosine of the deflection angle. If $\vec{\Omega}_1$ and $\vec{\Omega}_2$ are defined as the pre and post-collision directions of motion, respectively, of the scattered particle in the laboratory system where (figure III.F.1)

$$\vec{\Omega}_1 = \hat{e}_x \sin\theta_1 \cos\varphi_1 + \hat{e}_y \sin\theta_1 \sin\varphi_1 + \hat{e}_z \cos\theta_1 \tag{60a}$$

$$\vec{\Omega}_2 = \hat{e}_z \sin\theta_2 \cos\varphi_2 + \hat{e}_y \sin\theta_2 \sin\varphi_2 + \hat{e}_z \cos\theta_2 \tag{60b}$$

and if ω_ℓ is defined as the scattering deflection angle in the laboratory system, then

$$\cos\omega_\ell = \vec{\Omega}_1 \cdot \vec{\Omega}_2 \quad . \tag{61}$$

Since the scattering occurs between two particles of equal (or very nearly so) mass, there can be no single collision backscatter in the laboratory reference frame. Therefore,

$$\vec{\Omega}_1 \cdot \vec{\Omega}_2 \geq 0 \tag{62}$$

or

$$\sin\theta_1 \sin\theta_2 \cos(\varphi_1 - \varphi_2) + \cos\theta_1 \cos\theta_2 \geq 0 \quad . \tag{63}$$

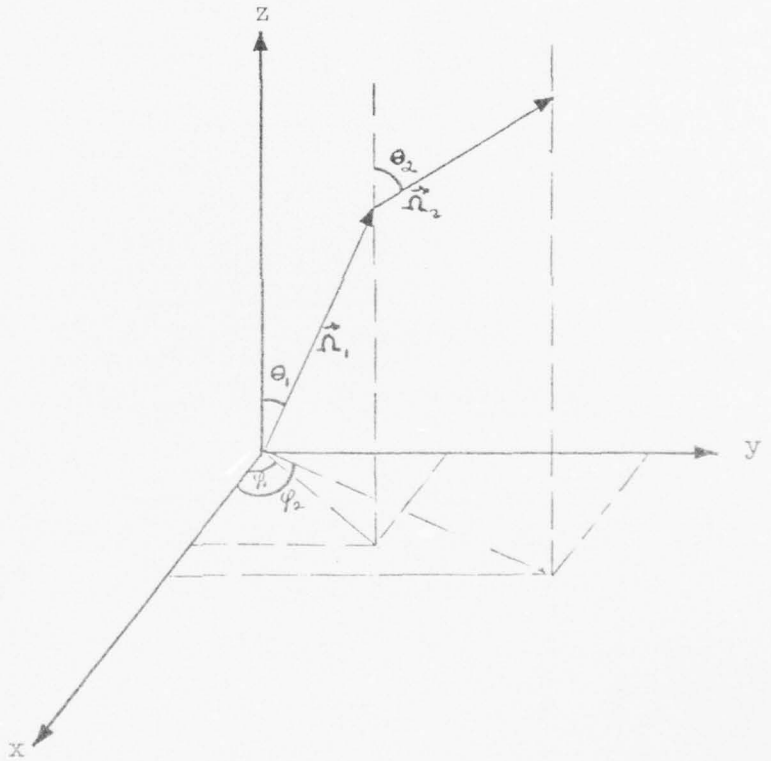

Figure III.F.1

Pre-and Post-Collision
Particle Orientations

Table III.F.1a

Upper-left Submatrix, $f(\mu_i,\mu_j)$, for Both Angles in Same Quadrant; Neutron Scattering in Hydrogen

j \ i	1	2	3	4	5	6
1	1.9629	1.7749	1.5114	1.1530	.72210	.27005
2	1.7749	1.6349	1.3922	1.0620	.68095	.39279
3	1.5114	1.3922	1.1855	.91807	.70488	.50417
4	1.1530	1.0620	.91807	.82125	.71504	.58689
5	.72230	.68095	.70488	.71504	.69254	.63412
6	.27005	.39279	.50417	.58689	.63412	.64240

Table III.F.1b

Lower-left Submatrix, $f(\mu_i,\mu_j)$, for Angles in Different Quadrants; Neutron Scattering in Hydrogen

j \ i	1	2	3	4	5	6
6	.024198	.16634	.31133	.43979	.54199	.61103
5	0	.015826	.13849	.28297	.42194	.54199
4	0	0	.013711	.13136	.28297	.43979
3	0	0	0	.013711	.13849	.31133
2	0	0	0	0	.015826	.16634
1	0	0	0	0	0	.024198

matrix was then substituted into the expressions (29, 30) and the OOSII computer program was run to provide computations of transmitted and reflected currents.

The choice of six discrete ordinates per quadrant was made for all orders of scattering up to 10 because it was found that a lesser number was not adequate to provide an accurate description of the forward peaked nature of the scattering angular distribution. The adoption of this number of ordinates was accomplished with virtually no further sacrifice of computational efficiency over that attained for the isotropic scatter case. This was done by coarsening the spatial integration step by a factor of four, a modification which produced only third or fourth decimal place changes in the answers. Also a constant mean-free-path was assumed as is actually the case for neutron scattering in Hydrogen at energies ranging from 1 KeV down to thermal.

Curves of Tn(t) and $B_n(t)$ are plotted vs. t for both the cosine and isotropic source configurations in figures III. F. 2-5. As before, eleven curves representing values of n ranging from 0 to 10 mfp and a twelfth curve for the total are presented in each graph. A more detailed presentation of the numerical results is given in tables III. F. 2-3 where a comparison with Monte Carlo results is made.

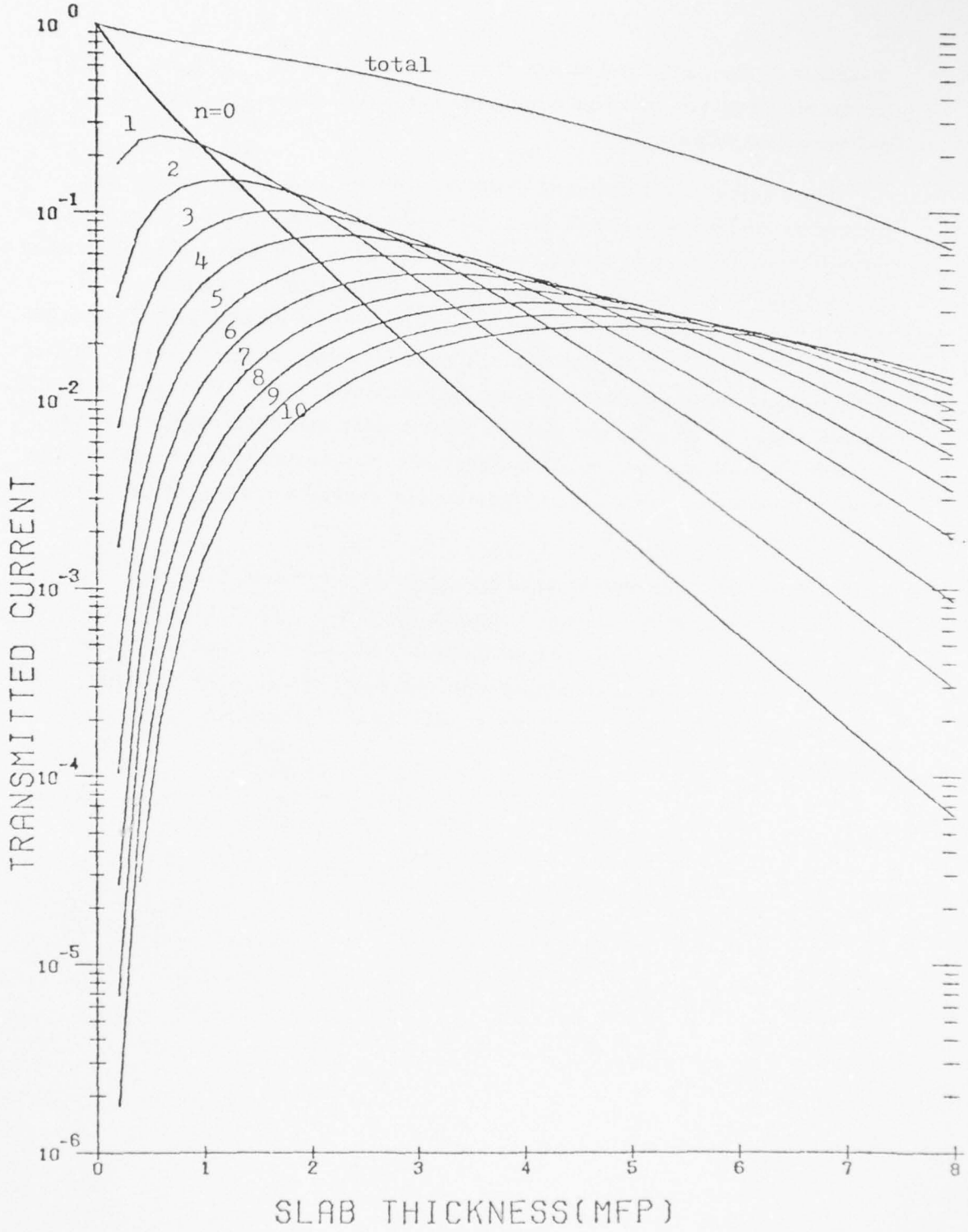

Figure III.F.2
Transmitted current, $T_n(t)$, vs. slab thickness, t, for n-th order neutron scattering in Hydrogen ($0 \leq n \leq 10$); Cosine current source configuration

AD-A040 378 ARCON CORP WAKEFIELD MASS F/G 12/1
INTERACTIVE MATH MODELING.(U)
FEB 77 S WOOLF, J V O'BRIEN, E COHEN, D BAKER F19628-74-C-0049
UNCLASSIFIED RADC-TR-77-86 NL

2 OF 3
AD
A040 378

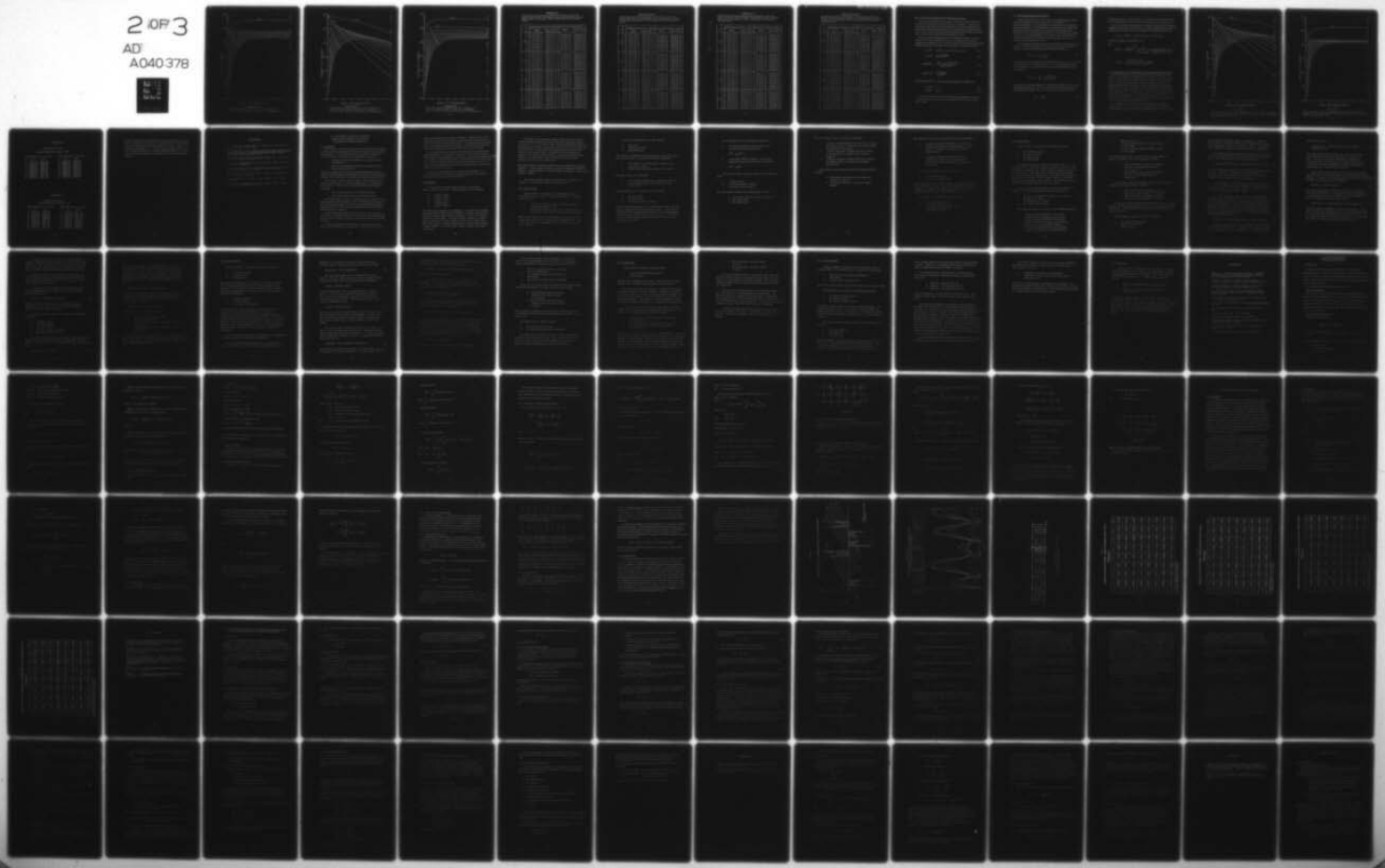

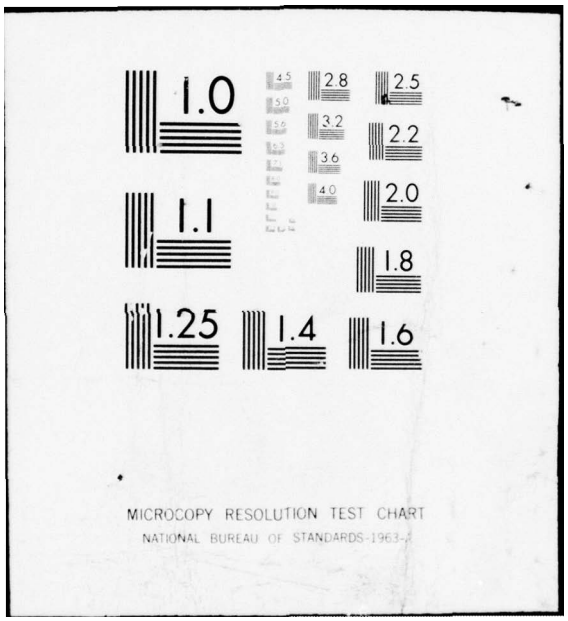
1.0
1.1
1.25
1.4
1.6
1.8
2.0
2.2
2.5
2.8
3.2
3.6
4.0
4.5
5.0
5.6
6.3
MICROCOPY RESOLUTION TEST CHART
NATIONAL BUREAU OF STANDARDS-1963-A

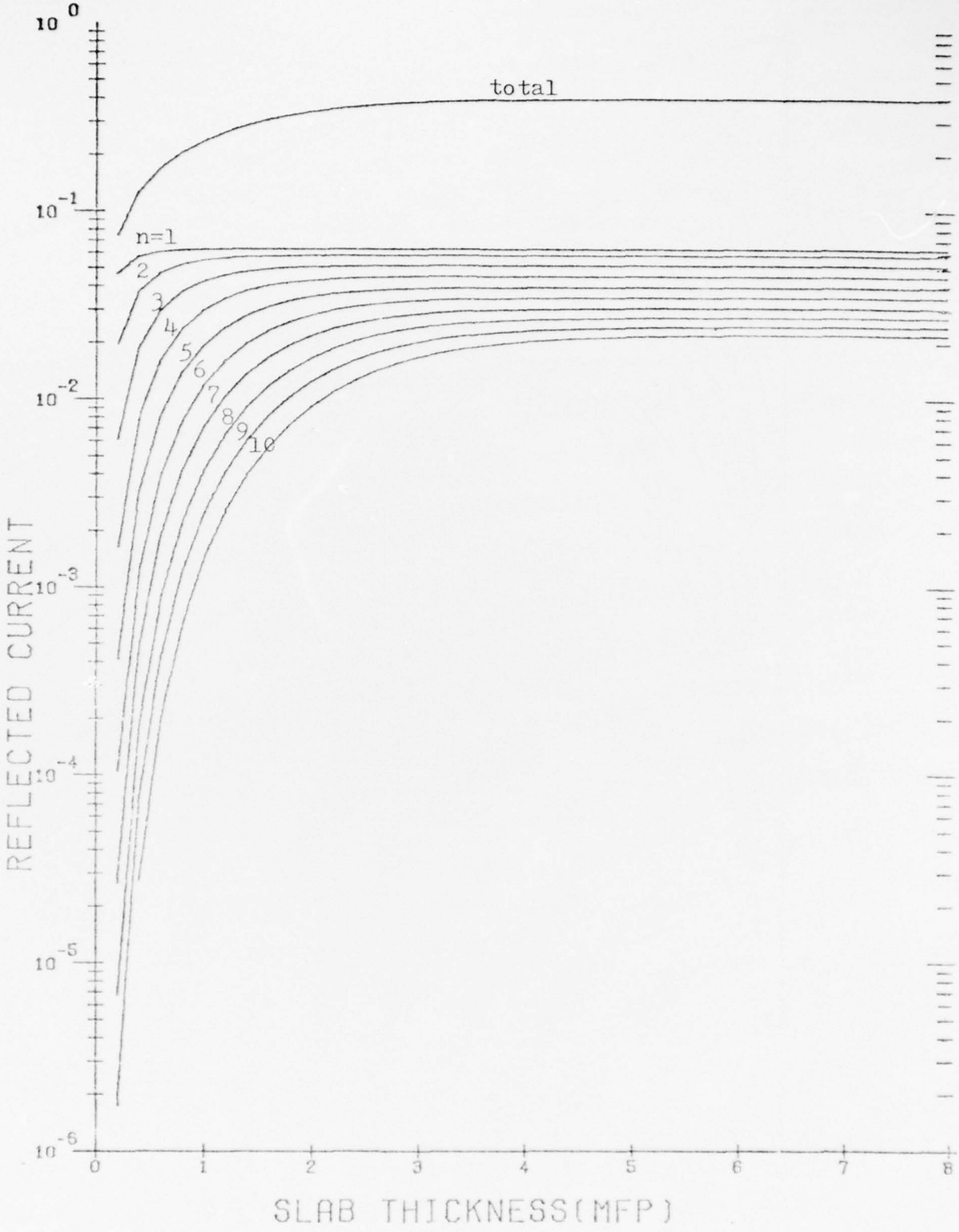

Figure III.F.3
Reflected current, $B_n(t)$, vs. slab thickness, t, for n-th order neutron scattering in Hydrogen ($1 \leq n \leq 10$); Cosine current source configuration

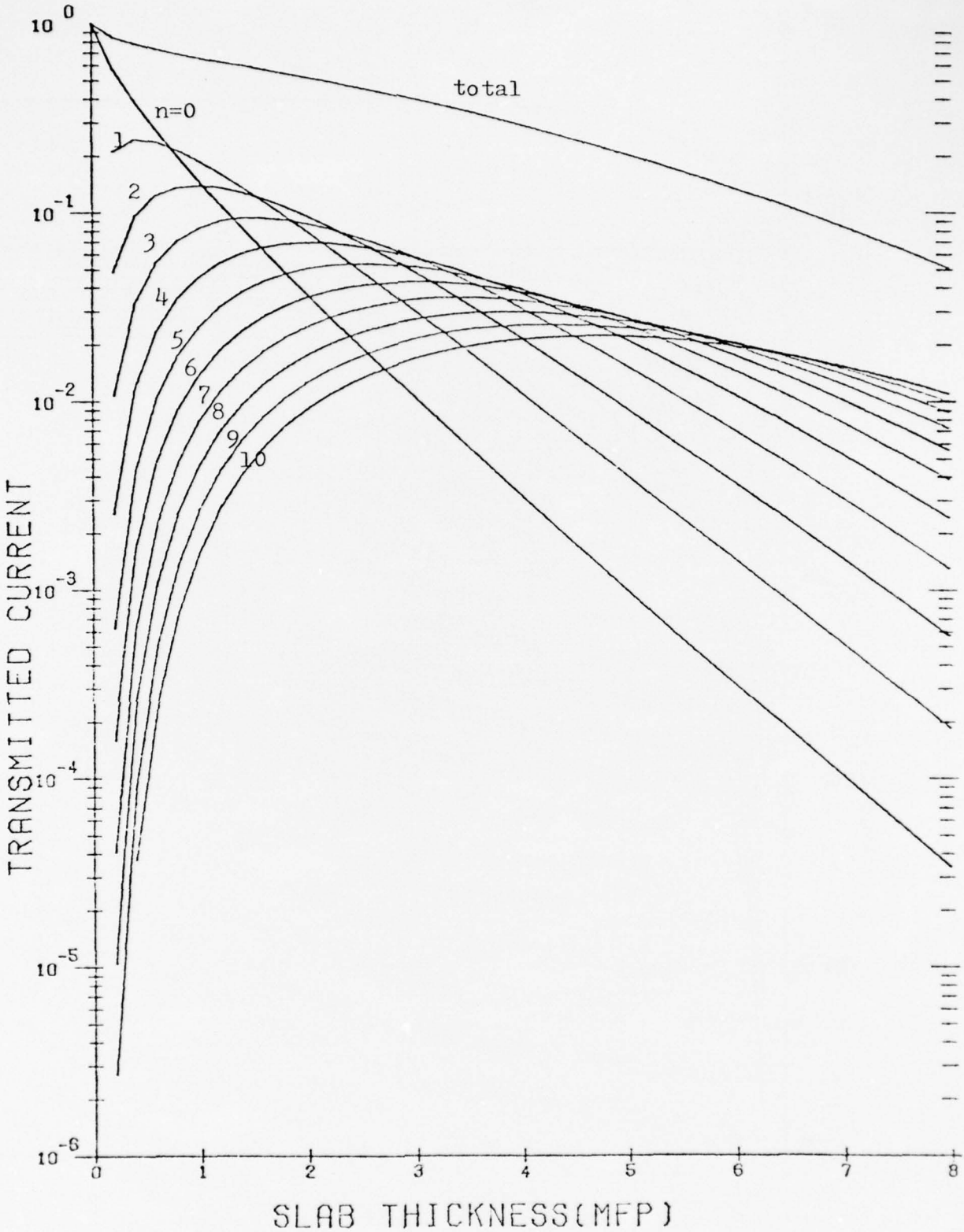

Figure III.F.4

Transmitted current, $T_n(t)$, vs. slab thickness, t, for n-th order neutron scattering in Hydrogen ($0 \leq n \leq 10$); Isotropic current source configuration

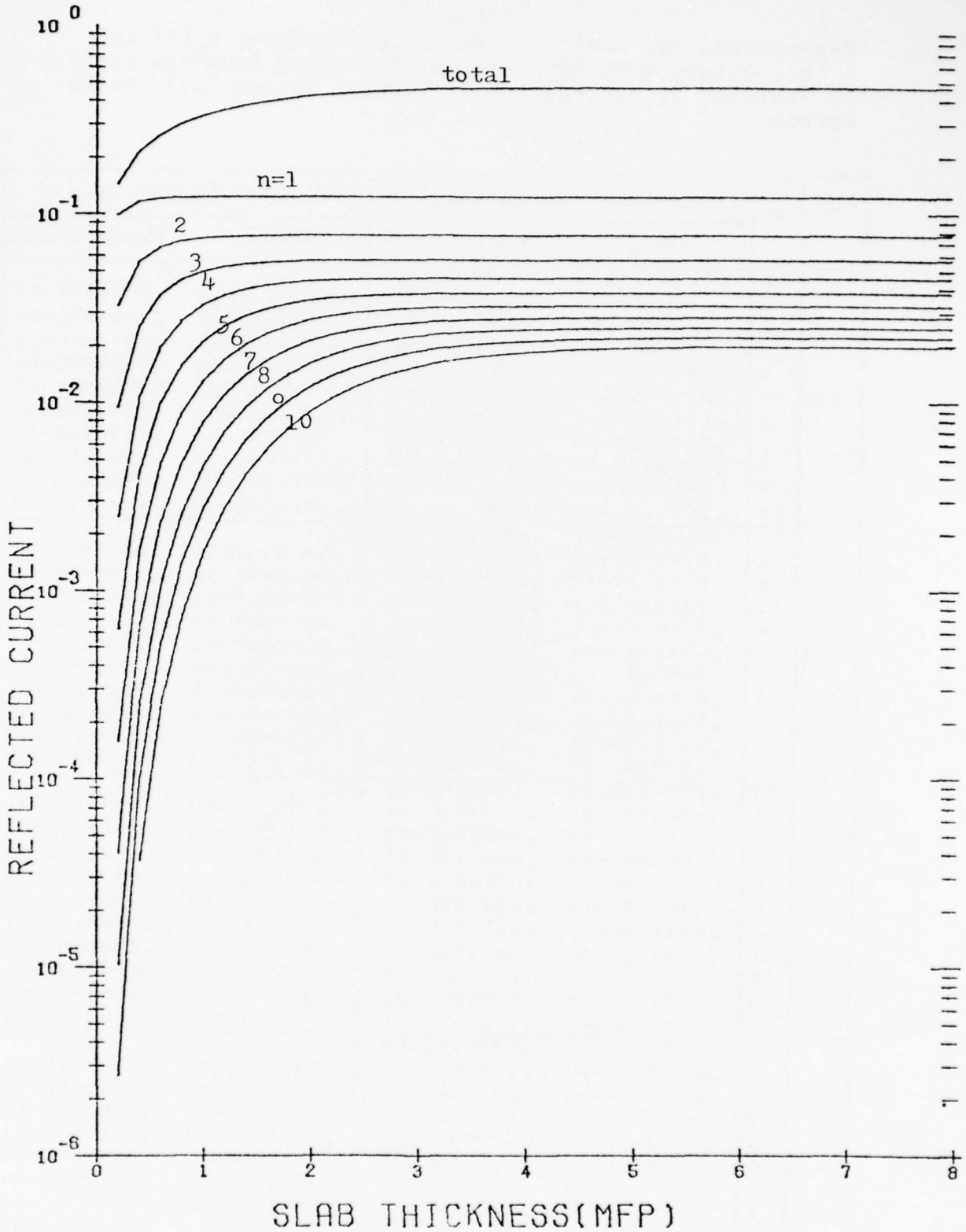

Figure III.F.5

Reflected current, $B_n(t)$, vs. slab thickness, t, for n-th order neutron scattering in Hydrogen ($1 \leq n \leq 10$); Isotropic current source configuration

BEST AVAILABLE COPY

Table III.F.2

Transmitted and Reflected Particle Currents, $T_n(t)$ and $B_n(t)$, Obtained by Two Methods, Resulting from the Scatter of Neutrons by Hydrogen: Unit Current Cosine Distributed Source

t	n	Transmitted Current, $T_n(t)$		Reflected Current, $B_n(t)$	
		OOSII	Monte Carlo	OOSII	Monte Carlo
	0	.213394E+00	.217556E+00	0.	0.
	1	.225017E+00	.226632E+00	.626810E-01	.585498E-01
	2	.145704E+00	.143102E+00	.548762E-01	.548400E-01
	3	.797680E-01	.797376E-01	.425851E-01	.437332E-01
	4	.418482E-01	.426760E-01	.298380E-01	.301978E-01
1.0	5	.223960E-01	.226424E-01	.193945E-01	.196888E-01
	6	.124442E-01	.115718E-01	.119783E-01	.127054E-01
	7	.713851E-02	.701230E-02	.717298E-02	.717474E-02
	8	.415302E-02	.470014E-02	.422721E-02	.454738E-02
	9	.243915E-02	.246574E-02	.247483E-02	.246562E-02
	10	.143345E-02	.129793E-02	.144671E-02	.132911E-02
	0	.602568E-01	.603430E-01	0.	0.
	1	.109209E+00	.107865E+00	.630936E-01	.590488E-01
	2	.116803E+00	.115960E+00	.580285E-01	.579918E-01
	3	.991389E-01	.100530E+00	.507866E-01	.518410E-01
	4	.741942E-01	.746754E-01	.429448E-01	.434990E-01
2.0	5	.522778E-01	.516652E-01	.352708E-01	.355512E-01
	6	.361547E-01	.345814E-01	.281497E-01	.294068E-01
	7	.251255E-01	.244663E-01	.219870E-01	.213594E-01
	8	.177116E-01	.185988E-01	.164535E-01	.169444E-01
	9	.126735E-01	.131761E-01	.124662E-01	.120943E-01
	10	.917304E-02	.937832E-02	.922768E-02	.894896E-02
	0	.178613E-01	.184905E-01	0.	0.
	1	.438918E-01	.440192E-01	.631021E-01	.590576E-01
	2	.636021E-01	.632364E-01	.581955E-01	.581540E-01
	3	.708496E-01	.698019E-01	.515609E-01	.526088E-01
	4	.673154E-01	.671464E-01	.449280E-01	.453542E-01
3.0	5	.579709E-01	.571100E-01	.388881E-01	.393660E-01
	6	.471405E-01	.467314E-01	.334374E-01	.348814E-01
	7	.372140E-01	.362756E-01	.285101E-01	.281626E-01
	8	.290657E-01	.288534E-01	.246722E-01	.243764E-01
	9	.227147E-01	.229126E-01	.201198E-01	.198894E-01
	10	.178502E-01	.177856E-01	.166571E-01	.164842E-01
	0	.553272E-02	.533810E-02	0.	0.
	1	.167247E-01	.167973E-01	.631023E-01	.590576E-01
	2	.298673E-01	.300914E-01	.582060E-01	.581540E-01
	3	.404704E-01	.406784E-01	.516329E-01	.526870E-01
	4	.460718E-01	.473634E-01	.451798E-01	.455788E-01
4.0	5	.466209E-01	.465940E-01	.394939E-01	.399264E-01
	6	.435629E-01	.429772E-01	.345781E-01	.358244E-01
	7	.386264E-01	.379286E-01	.303145E-01	.297556E-01
	8	.331625E-01	.331824E-01	.265779E-01	.269204E-01
	9	.279751E-01	.275763E-01	.232682E-01	.228112E-01
	10	.234227E-01	.233496E-01	.203156E-01	.201930E-01

BEST AVAILABLE COPY

Table III.F.2(cont.)

Transmitted and Reflected Particle Currents, $T_n(t)$ and $B_n(t)$, Obtained by Two Methods, Resulting from the Scatter of Neutrons by Hydrogen: Unit Current Cosine Distributed Source

t	n	Transmitted Current, $T_n(t)$		Reflected Current, $B_n(t)$	
		OOSII	Monte Carlo	OOSII	Monte Carlo
	0	.175560E-02	.162074E-02	0.	0.
	1	.622027E-02	.607382E-02	.631024E-01	.590576E-01
	2	.130014E-01	.132612E-01	.582068E-01	.581540E-01
	3	.205105E-01	.201883E-01	.516398E-01	.526870E-01
	4	.269787E-01	.277783E-01	.452102E-01	.456120E-01
5.0	5	.311773E-01	.313124E-01	.395838E-01	.400422E-01
	6	.328510E-01	.327042E-01	.347832E-01	.360120E-01
	7	.323764E-01	.329834E-01	.307027E-01	.301876E-01
	8	.304356E-01	.305473E-01	.272167E-01	.275920E-01
	9	.277042E-01	.276998E-01	.242099E-01	.239690E-01
	10	.247027E-01	.237493E-01	.215865E-01	.214976E-01
	0	.569208E-03	.577124E-03	0.	0.
	1	.228164E-02	.225614E-02	.631024E-01	.590576E-01
	2	.549808E-02	.521483E-02	.582068E-01	.581540E-01
	3	.966009E-02	.103059E-01	.516405E-01	.526870E-01
	4	.143053E-01	.141999E-01	.452138E-01	.456120E-01
6.0	5	.185037E-01	.183902E-01	.395964E-01	.400484E-01
	6	.216416E-01	.223212E-01	.348165E-01	.360744E-01
	7	.234549E-01	.242833E-01	.307758E-01	.302768E-01
	8	.240049E-01	.236130E-01	.273548E-01	.278372E-01
	9	.235302E-01	.236188E-01	.244422E-01	.242754E-01
	10	.223742E-01	.223010E-01	.210423E-01	.218644E-01
	0	.187313E-03	.156233E-03	0.	0.
	1	.833352E-03	.775310E-03	.631024E-01	.590576E-01
	2	.218460E-02	.218868E-02	.582068E-01	.581540E-01
	3	.432864E-02	.406104E-02	.516406E-01	.526870E-01
	4	.708473E-02	.765428E-02	.452143E-01	.456120E-01
7.0	5	.101029E-01	.105515E-01	.395981E-01	.400484E-01
	6	.129508E-01	.133981E-01	.348217E-01	.360744E-01
	7	.152883E-01	.154384E-01	.307884E-01	.302768E-01
	8	.169217E-01	.172782E-01	.273816E-01	.279152E-01
	9	.178083E-01	.178813E-01	.244927E-01	.243218E-01
	10	.182202E-01	.179335E-01	.220285E-01	.219468E-01
	0	.623514E-04	.390856E-04	0.	0.
	1	.300771E-03	.306426E-03	.631024E-01	.590576E-01
	2	.864497E-03	.971474E-03	.582068E-01	.581540E-01
	3	.187149E-02	.153905E-02	.516406E-01	.526870E-01
	4	.334506E-02	.335922E-02	.452143E-01	.456120E-01
8.0	5	.518910E-02	.561360E-02	.395984E-01	.400484E-01
	6	.721467E-02	.735089E-02	.348224E-01	.360744E-01
	7	.919776E-02	.955008E-02	.307905E-01	.302768E-01
	8	.109301E-01	.114750E-01	.273865E-01	.279152E-01
	9	.123026E-01	.120364E-01	.245027E-01	.243218E-01
	10	.132321E-01	.134813E-01	.220473E-01	.219468E-01

BEST AVAILABLE COPY

Table III.F.3

Transmitted and Reflected Particle Currents, $T_n(t)$ and $B_n(t)$, Obtained by Two Methods, Resulting from the Scatter of Neutrons by Hydrogen: Unit Isotropically Distributed Current Source

t	n	Transmitted Current, $T_n(t)$		Reflected Current, $B_n(t)$	
		OOSII	Monte Carlo	OOSII	Monte Carlo
	0	.149405E+00	.147480E+00	0.	0.
	1	.189260E+00	.188330E+00	.123114E+00	.125152E+00
	2	.139568E+00	.137130E+00	.742554E-01	.739808E-01
	3	.832297E-01	.830200E-01	.496732E-01	.509800E-01
	4	.458164E-01	.468900E-01	.329962E-01	.334602E-01
1.0	5	.250077E-01	.258800E-01	.211342E-01	.213600E-01
	6	.139351E-01	.133905E-01	.135523E-01	.135705E-01
	7	.795253E-02	.806000E-02	.784963E-02	.813000E-02
	8	.461332E-02	.518002E-02	.464592E-02	.489002E-02
	9	.259962E-02	.270003E-02	.272812E-02	.273008E-02
	10	.158469E-02	.146100E-02	.159731E-02	.140000E-02
	0	.375343E-01	.374302E-01	0.	0.
	1	.891216E-01	.794800E-01	.123535E+00	.125710E+00
	2	.964602E-01	.952505E-01	.769543E-01	.766805E-01
	3	.833089E-01	.892500E-01	.565247E-01	.578800E-01
	4	.696236E-01	.693502E-01	.441137E-01	.446602E-01
2.0	5	.507545E-01	.506202E-01	.349478E-01	.352208E-01
	6	.357789E-01	.347900E-01	.274974E-01	.282900E-01
	7	.259620E-01	.250102E-01	.212995E-01	.214202E-01
	8	.176847E-01	.186900E-01	.162267E-01	.164000E-01
	9	.126256E-01	.131605E-01	.121836E-01	.121805E-01
	10	.911691E-02	.947000E-02	.904742E-02	.875000E-02
	0	.106419E-01	.109902E-01	0.	0.
	1	.334394E-01	.305302E-01	.123543E+00	.125728E+00
	2	.486808E-01	.480400E-01	.770792E-01	.768000E-01
	3	.588842E-01	.572502E-01	.570913E-01	.584302E-01
	4	.583506E-01	.578200E-01	.455944E-01	.460300E-01
3.0	5	.519008E-01	.512105E-01	.377313E-01	.380905E-01
	6	.433350E-01	.433700E-01	.316910E-01	.325300E-01
	7	.347902E-01	.343702E-01	.267084E-01	.268802E-01
	8	.274352E-01	.273302E-01	.224403E-01	.224108E-01
	9	.215204E-01	.214500E-01	.187345E-01	.188000E-01
	10	.169390E-01	.169202E-01	.155233E-01	.152502E-01
	0	.319853E-02	.308000E-02	0.	0.
	1	.111717E-01	.112100E-01	.123543E+00	.125725E+00
	2	.217981E-01	.218400E-01	.770864E-01	.768000E-01
	3	.314738E-01	.315202E-01	.571400E-01	.584902E-01
	4	.375896E-01	.382502E-01	.457691E-01	.461808E-01
4.0	5	.394856E-01	.391500E-01	.381654E-01	.384900E-01
	6	.379715E-01	.377602E-01	.325353E-01	.332302E-01
	7	.343969E-01	.337800E-01	.280843E-01	.281500E-01
	8	.299804E-01	.300605E-01	.244027E-01	.243405E-01
	9	.255409E-01	.255100E-01	.212591E-01	.211600E-01
	10	.215070E-01	.217002E-01	.185179E-01	.182502E-01

BEST AVAILABLE COPY

Table III.F.3(cont.)

Transmitted and Reflected Particle Currents, $T_n(t)$ and $B_n(t)$, Obtained by Two Methods, Resulting from the Scatter of Neutrons by Hydrogen: Unit Isotropically Distributed Current Source

t	n	Transmitted Current, $T_n(t)$		Reflected Current, $B_n(t)$	
		OOSII	Monte Carlo	OOSII	Monte Carlo
	0	.996449E-03	.920000E-03	0.	0.
	1	.404000E-02	.395000E-02	.123543E+00	.127720E+00
	2	.917332E-02	.932000E-02	.770869E-01	.768002E-01
	3	.153513E-01	.150500E-01	.571445E-01	.584900E-01
	4	.211364E-01	.217200E-01	.457892E-01	.462005E-01
5.0	5	.253412E-01	.253100E-01	.382270E-01	.385600E-01
	6	.274965E-01	.272400E-01	.326802E-01	.334002E-01
	7	.277365E-01	.284300E-01	.283670E-01	.284908E-01
	8	.265400E-01	.263600E-01	.248804E-01	.248300E-01
	9	.244956E-01	.245500E-01	.219803E-01	.220302E-01
	10	.220564E-01	.214900E-01	.195121E-01	.193100E-01
	0	.312258E-03	.330005E-03	0.	0.
	1	.145147E-02	.146000E-02	.123543E+00	.125720E+00
	2	.371929E-02	.361002E-02	.770869E-01	.768002E-01
	3	.702692E-02	.745002E-02	.571449E-01	.584908E-01
	4	.109677E-01	.107400E-01	.457915E-01	.462000E-01
6.0	5	.145644E-01	.142402E-01	.382353E-01	.385702E-01
	6	.175300E-01	.177500E-01	.327030E-01	.334400E-01
	7	.194608E-01	.202205E-01	.284184E-01	.285505E-01
	8	.203175E-01	.199000E-01	.249802E-01	.250000E-01
	9	.202364E-01	.202500E-01	.221922E-01	.222202E-01
	10	.194721E-01	.193408E-01	.197810E-01	.195808E-01
	0	.103510E-03	.900000E-04	0.	0.
	1	.519579E-03	.490002E-03	.123543E+00	.125722E+00
	2	.147221E-02	.149000E-02	.770869E-01	.768000E-01
	3	.307664E-02	.298005E-02	.571450E-01	.584905E-01
	4	.525403E-02	.555000E-02	.457918E-01	.462000E-01
7.0	5	.774805E-02	.796002E-02	.382364E-01	.385702E-01
	6	.102211E-01	.105502E-01	.327064E-01	.334408E-01
	7	.123505E-01	.122704E-01	.284271E-01	.285500E-01
	8	.139508E-01	.144602E-01	.249991E-01	.250502E-01
	9	.149300E-01	.151204E-01	.221885E-01	.222500E-01
	10	.153333E-01	.150705E-01	.198443E-01	.196505E-01
	0	.341376E-04	.200000E-04	0.	0.
	1	.185603E-03	.200002E-03	.123543E+00	.125722E+00
	2	.573003E-03	.640002E-03	.770869E-01	.768008E-01
	3	.130567E-02	.116000E-02	.571450E-01	.584900E-01
	4	.242923E-02	.247002E-02	.457918E-01	.462002E-01
8.0	5	.389504E-02	.408002E-02	.382365E-01	.385700E-01
	6	.556914E-02	.563005E-02	.327069E-01	.334405E-01
	7	.727114E-02	.735000E-02	.284284E-01	.285500E-01
	8	.883505E-02	.924002E-02	.250024E-01	.250502E-01
	9	.101010E-01	.987002E-02	.221956E-01	.222508E-01
	10	.110253E-01	.112300E-01	.198579E-01	.196500E-01

F.2. Monte Carlo Calculations for Anisotropic Scattering

Monte Carlo computations were made to verify the results obtained for the anisotropic scattering cases that have been considered. The computer code used was the same as that for the isotropic scattering simulation with the exception of the calculation of the post-collision particle trajectory orientation. This is due to the fact that the scattering must be treated as isotropic in the center-of-mass rather than the laboratory system.

The cosine of the deflection angle in the laboratory system is given by equation (61). The azimuthal deflection, ρ, is determined by a uniform sampling on the interval $(0, 2\pi)$. Then if θ^n and φ^n are the polar and azimuthal angles respectively in the laboratory system prior to the n-th interaction

$$\cos \theta^{n+1} = \cos \theta^n \cos \omega_\ell + \sin \theta^n \sin \omega_\ell \cos \rho \tag{67a}$$

$$\sin \theta^{n+1} = \sqrt{1 - \cos^2 \theta^{n+1}} \quad , \tag{67b}$$

$$\cos(\varphi^{n+1} - \varphi^n) = \frac{\cos \omega_\ell - \cos \theta^n \cos \theta^{n+1}}{\sin \theta^n \sin \theta^{n+1}} \quad , \tag{68a}$$

$$\sin(\varphi^{n+1} - \varphi^n) = \frac{\sin \rho \sin \omega_\ell}{\sin \theta^{n+1}} \quad , \tag{68b}$$

If $(\sin \theta^n) \cdot (\sin \theta^{n+1}) = 0$, then the last two relations are replaced by

$$\cos \varphi^{n+1} = \cos \rho \quad , \tag{69a}$$

$$\sin \varphi^{n+1} = \sin \rho \quad . \tag{69b}$$

The Monte Carlo results for neutron scattering in Hydrogen are given in tables III. F. 2-3 where they may be compared with their corresponding OOSII results.

G. The Screened Rutherford Interaction

Another application of the OOSII method can be found in the investigation of the scattering of low evergy electrons in thin films.[1] of empirical studies, it is believed that the contribution, due to electron-phonon interactions, to the transmitted and reflected electron yields from thin films which have undergone electron beam bombardment may be estimated if the scattering angular distribution of this interaction is characterized by a screened Rutherford cross-section. The OOSII formulation is a natural choice for such an analysis since the average energy loss per electron-phonon interaction is known.

The Rutherford scattering formula for unscreened coulomb interactions states, as is well known, that in the laboratory system, the probability density of a particle undergoing deflection through an angle ω_ℓ is

$$f(\cos \omega_\ell) \propto \frac{1}{(1 - \cos \omega_\ell)^2} \tag{70}$$

This formula has a singularity in the forward direction ($\cos \omega_\ell = 1$). To overcome this difficulty, a screening factor, $\eta > 0$, can be introduced so that, when normalized, the following modified form of the Rutherford formula would result:

$$f(\cos \omega_\ell) = \frac{1}{2\pi} \frac{\eta(1+\eta/2)}{(1+\eta - \cos \omega_\ell)^2} \quad . \tag{71}$$

The degree to which the parameter η influences the anisotropy of f is seen in the expression for $\mu_{1/2}$, the cosine of the deflection angle for which the probability of occurrence is 0.5. It is easily shown that in terms of η,

$$\mu_{1/2} = \frac{1}{1+\eta} \quad . \tag{72}$$

It is apparent that as η tends toward ∞, the scattering tends toward isotropic, and as η tends toward zero, the scattering becomes more forward peaked.

As in the previous scattering cases considered, the form of the scattering probability density function required for use with the OOSII algorithm must be independent of azimuth. This is accomplished in the following way: since

$$\cos \omega_\ell = \vec{\Omega}_1 \cdot \vec{\Omega}_2 = \sin \theta_1 \sin \theta_2 \cos \varphi + \cos \theta_1 \cos \theta_2$$

where $\vec{\Omega}_1$ and $\vec{\Omega}_2$ are as defined in (60),

then

$$f(\mu_1, \mu_2) = \frac{\eta(1+\eta/2)}{2\pi} \int_0^{2\pi} \frac{d\varphi}{\left[\left(1+\eta - \mu_1\mu_2\right) - \left(\sqrt{1-\mu_1^2}\left(1-\mu_2^2\right)\right) \cos \varphi\right]^2} , \tag{73}$$

or

$$f(\mu_1, \mu_2) = \frac{\eta(1+\eta/2)\ (1+\eta - \mu_1\mu_2)}{\left[\eta^2 + 2\eta(1 - \mu_1\mu_2) + (\mu_1 - \mu_2)^2\right]^{3/2}} . \tag{74}$$

G. 1. Application of the OOSII Program to Screened Rutherford Scattering

The scattering matrix $f(\mu_1, \mu_2)$ of equation (74) was evaluated for five values of η corresponding to average deflection angles of 15°, 30°, 45°, 60°, and 75°. Thus, a full range of anisotropy was covered. For each of these cases, this matrix was substituted into the expressions (29, 30) and the OOSII computer program was run to provide computations of transmitted and reflected currents. To serve as an illustration of the results obtained for the case of extreme anisotropy, the 15° average deflection angle, plots of $T_n(t)$ and $B_n(t)$ vs. t are given in figures III.G.1-2, respectively, for the cosine source configuration. The contrast between these curves and those of the isotropic scattering case is quite noticeable if reference is again made to the corresponding plots of figures III.C.2-3.

An independent verification of the screened Rutherford results was possible since in 1974, J. C. Garth[1] made Monte Carlo calculations of the transmitted low energy electron current through LiF thin films assuming

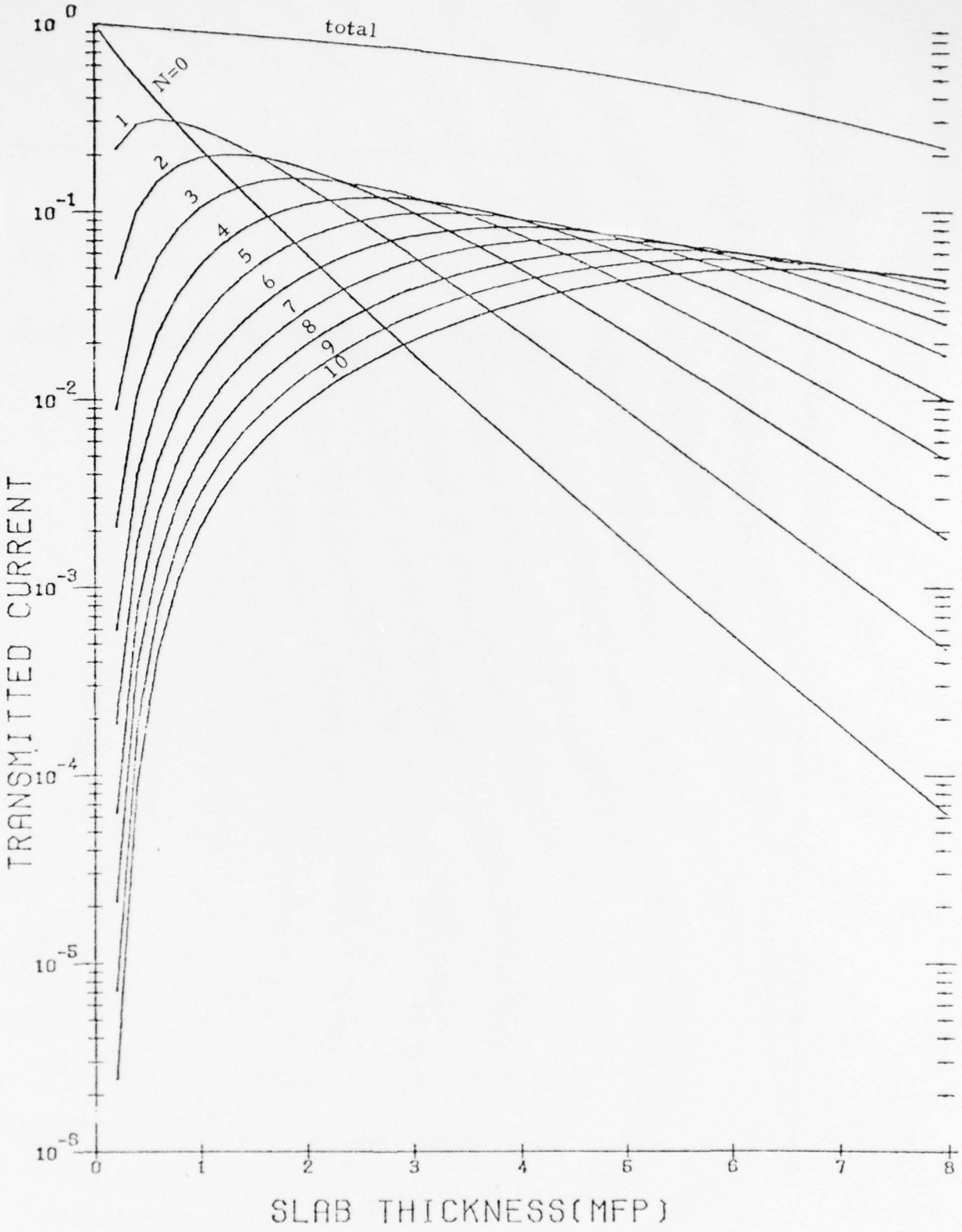

Figure III.G.1

Transmitted current, $T_n(t)$, vs. slab thickness, t, for n-th order screened Rutherford electron scattering ($0 \leq n \leq 10$); cosine current source configuration. Average scattering angle = 15°.

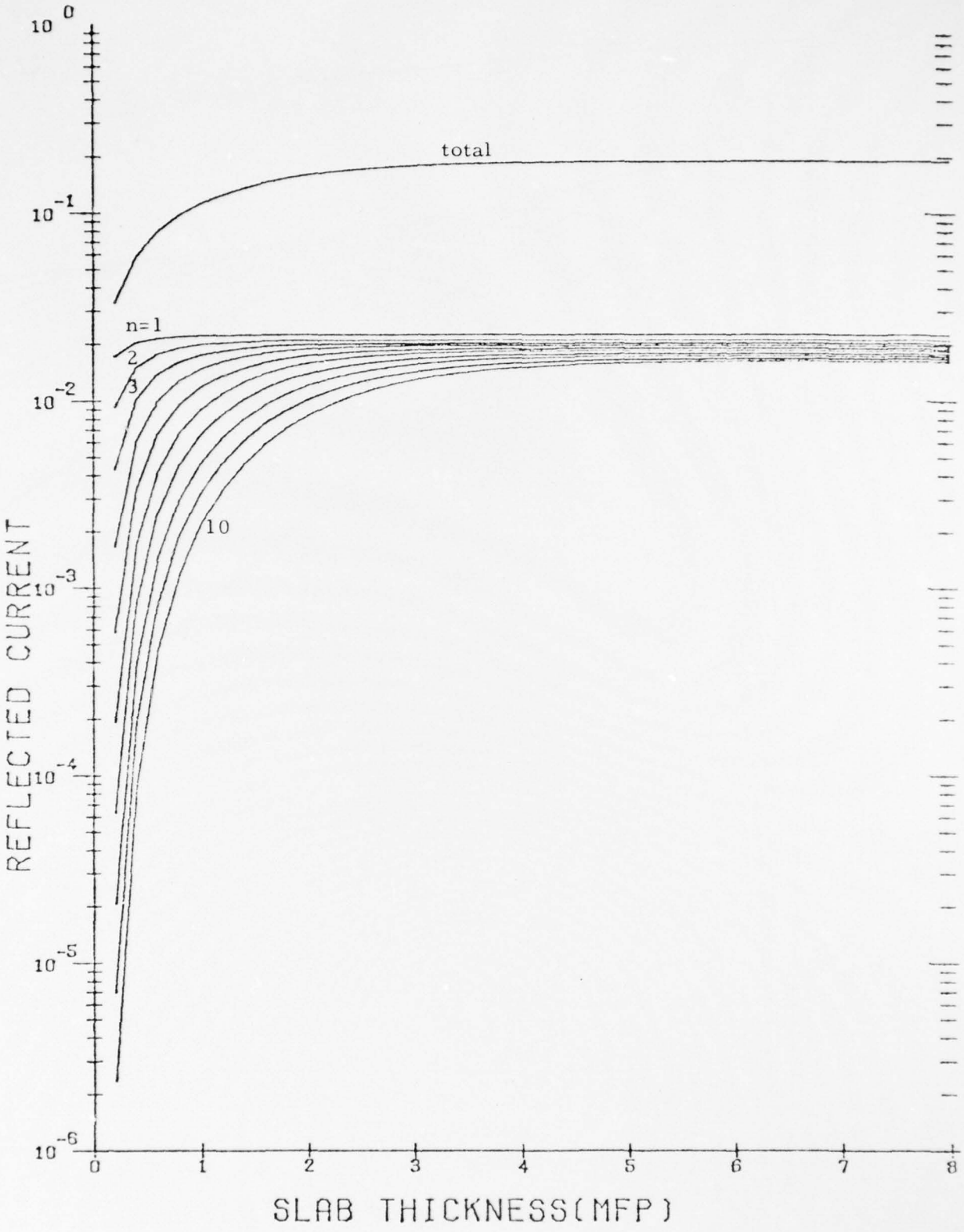

Figure III.G.2

Reflected current, $B_n(t)$, vs. slab thickness, t, for n-th order screened Rutherford electron scattering ($1 \leq n \leq 10$); cosine current source configuration. Average scattering angle = 15°.

Table III.G.1

Transmitted Current

Average Scattering Angle = 15°

Slab Thickness = 1.0 mfp			Slab Thickness = 3.6 mfp		
n	I.I.	M.C.	n	I.I.	M.C.
1	.2762 00	.2721 00	1	.3347-01	.3320-01
2	.1930 00	.1898 00	2	.6661-01	.6501-01
3	.1039 00	.1007 00	3	.9285-01	.8874-01
4	.5108-01	.4965-01	4	.1027 00	.9756-01
5	.2554-01	.2357-01	5	.9682-01	.9247-01
6	.1370-01	.1282-01	6	.8193-01	.7693-01
7	.7935-02	.739 -02	7	.6469-01	.6058-01
8	.4886-02	.459 -02	8	.4919-01	.4558-01
9	.3140-02	.287 -02	9	.3691-01	.3379-01
10	.2071-02	.208 -02	10	.2782-01	.2519-01

Table III.G.2

Transmitted Current

Average Scattering Angle = 30°

Slab Thickness = 1.0 mfp			Slab Thickness = 7.0 mfp		
n	I.I.	M.C.	n	I.I.	M.C.
1	.2388 00	.2382 00	1	.9883-03	.92 -03
2	.1542 00	.1551 00	2	.2824-02	.285 -02
3	.8205-01	.8109-01	3	.5738-02	.584 -02
4	.4196-01	.4276-01	4	.9540-02	.957 -02
5	.2224-01	.2208-01	5	.1346-01	.1333-01
6	.1246-01	.1272-01	6	.1691-01	.1721-01
7	.7299-02	.751 -02	7	.1946-01	.1956-01
8	.4385-02	.482 -02	8	.2095-01	.2051-01
9	.2665-02	.271 -02	9	.2144-01	.2069-01
10	.1626-02	.155 -02	10	.2115-01	.2086-01

screened Rutherford scattering to hold. The next two tables, III. G. 1 and III. G. 2, compare these results for 10 scattering orders. The first table shows the comparison for two slab thicknesses, 1.0 and 3.6 mfp, for an average scattering angle of 15°, while the second compares results for 1.0 and 7.0 mfp thicknesses given an average scattering angle of 30°. In all cases, six discrete ordinates per quadrant were used in the angular integrations.

REFERENCES

1. J. C. Garth, N. G. Parke, and T. H. DeStefano, Bul. Am. Phys. Soc., Ser. II, 19, No. 3, P. 232 (1974).

2. J. C. Garth and S. Woolf, An Orders-of-Scattering Approach to Electron and Neutron Transport: An Invariant Imbedding Analysis, AFCRL IN-House Report to be published in 1975.

3. G. M. Wing, An Introduction to Transport Theory, John Wiley and Sons, Inc., New York, Pp. 6-23(1962).

4. C. Lanczos, Applied Analysis, Prentice Hall, Inc. Englewood Cliffs, N. J. 1956, Pp. 396-404.

5. A. H. Stroud and D. Secrest, Gaussian Quadrature Formulas, Prentice Hall, Englewood Cliffs, N. J. (1966).

6. A. L. Crosbie, R. L. Merriam, and R. Viskanta, J. Quant, Spectr. Rad. Transfer, 8, 1609 (1968).

7. R. Viskanta and A. L. Crosbie, J. Quant. Spectr. Rad. Transfer, 7, 871 (1967).

8. J. R. Lamarsh, Nuclear Reactor Theory, Addison Wesley, Reading, Mass., Pp. 53-54 (1966).

IV. LOW ENERGY ELECTRON TRANSPORT PERTURBATION METHOD FOR SOLVING THE LINEAR BOLTZMANN EQUATION

A. Introduction

In the previous report, the problem of electron transport of secondary electrons excited by a primary beam of electrons (electron beam problem) was considered. A code (Program LEET) was written to compute the electron transport. In the above, two assumptions were made:

1. Homogeneous boundary conditions are assumed (collision dominated case).
2. The source distribution generated by the primary electron beam is spatially uniform.

The above assumptions were used to simplify the Boltzmann equation. A numerical solution (Gaussian elimination) was found to solve the Boltzmann equation.[1] This solution was incorporated in a program (program LEET).

In this report a program written to obtain a more general solution to the BE will be described. This more general solution is a perturbation series solution. There are two kinds of perturbation methods that are considered:

1. The collision dominated (CD) perturbation method
2. The boundary dominated (BD) perturbation method.

The CD perturbation method is a generalization of the Gaussian elimination algorithm found in program LEET. The starting approximation in the CD perturbation method is the Gaussian elimination solution found in program LEET. However, successive improvements are made that include the boundary conditions.

The BD perturbation method, on the other hand, is in a sense the reverse of the CD perturbation method. It takes as its initial approximation the source flux. However, successive improvements are made to include collisions.

For any given problem, both perturbation methods should give the same answer (providing they both converge). Using this fact, the pertur-

bation methods may be tested against each other. Additional tests of the perturbation methods may be made by comparing with special solutions, in particular the solution of the Milne equation. Also the perturbation method may be checked by the Monte-carlo method. The CD and BD perturbation methods are applied to several cases (electron beam, photo beam).

A program (TRAN) was written that includes both the CD and BD perturbation methods. Several derived quantities, are included in program TRAN (yields, escape probabilities, currents). Other programs (MIL, MONTE) were written to check program TRAN. Program MIL solves the Milne equation. Program MONTE implements a Monte-Carlo method of solution. A special program (PHOTO) was written that computes the first order energy yield for the photon beam case.

The purpose of this report is to describe these programs. The physical assumptions and theoretical analysis upon which the programs are based are given in a separate document.[2]

B. Programs

In this section, several programs based on the previous analysis shall be considered. These programs are the following:

1. program TRAN
2. program LEET
3. program PHOTO
4. program MIL
5. program MONTE

All of the above programs are maintained in an update library (LEET). Programs TRAN, LEET, MIL and MONTE generate the electron flux by various methods under varying assumptions. These four programs all have a yield segment. The yield segment computes the various types of yields (net, energy, angular) in terms of the electron flux. This yield segment is virtually identical for all of the above programs. Program PHOTO, on the other hand, computes only the first order energy yield.

Of the above five programs, program TRAN is the most general. Program TRAN implements both the CD and BD perturbation methods (see sections C.2, C.3 of Reference (2)). Program TRAN also incorporates both idealistic and realistic source fluxes and S-matrices (see sections F, G of Reference (2)). Program LEET and program PHOTO are much more restrictive than program TRAN. Program LEET carries out the first iteration of the CD perturbation for the case of an electron beam; program PHOTO, on the other hand, carries out the first iteration of the BD perturbation for the case of a photon beam.

Both program MIL and program MONTE are used primarily as checking programs. Program MIL implements an iterative solution to the Milne equation. Program MONTE, on the other hand, implements a Monte-Carlo method of solution.

These five programs shall be discussed in more detail in the following. Program TRAN shall be considered first.

B.1 Program TRAN

Program TRAN is maintained in an update library that is a sub-library of library LEET. The TRAN sub-library is composed of several decks:

1. A deck that implements the CD and BD perturbation methods (perturbation deck)
2. Several decks that each implement a certain class of source fluxes and S-matrices (source-scattering decks)

When program TRAN is run, the perturbation deck is put on the compile file together with a particular source-scattering deck. For a run, only one source-scattering deck is put on the compile file to save memory.

The source-scattering decks are the following:

1. ideal deck
2. electron-beam deck
3. photo-beam deck

The ideal deck implements the ideal S-matrices and source fluxes (see section F, Ref. 2). The electron beam deck implements:

1. all S-matrices except the Spicer S-matrices (see section G.1.1, Ref. 2)
2. electron beam source (see section G.2.1, Ref. 2)

The photon beam deck implements:

1. the e-e Spicer S-matrix (see section G.1.2, Ref. 2)
2. the Spicer photo-beam source flux (see section G.2.2, Ref. 2)

The perturbation deck is made up of three segments:

1. the CD segment
2. the BD segment
3. the derived quantities segment

The CD segment implements the CD perturbation method. The BD segment implements the BD perturbation method. In particular it implements the BD hybrid iteration algorithm for the determination of the electron flux (see section C.4 Eq. 92 of Ref. (2)). The derived quantities segment computes the derived quantities (yields, escape probabilities, currents).

The BD segment contains the following subroutines:

1. a subroutine (JSOR) to produce a new source flux from the present electron flux:

$$B^{(n)} = L_c F^{(n)} + S$$

2. a subroutine (DIST) to produce a new electron distribution from the present source distribution:

$$F^{(n)} = G_f B^{(n)}$$

The derived quantities segment is made up of the following parts:

1. a yield segment
2. an escape probability segment
3. an electron current segment

The yield segment computes the following kinds of yield:

a. the electron yield (see section E. 1, Ref. (2))
b. the energy yield
c. the angular yield

The yield segment contains the following subroutines:

1. a function subroutine ((YIELD (E1, CS1)) that computes the electron yield as a function of the external energy E1 and external direction CS1
2. a function subroutine ((EYIELD E1)) that computes the energy yield as a function of the external energy E1
3. a function subroutine ((AYIELD (CS1)) that computes the angular yield as a function of the external direction CS1

The electron current segment computes the following kinds of currents:

a. the forward, backward and net currents (see section E.3, Ref. (2))
b. the forward, backward, and net flow charge profiles

The electron current segment contains the following subroutines:

1. a function subroutine (CURRENT (E, CS, K)) that computes the forward (K = 1) backward (K = -1) and net (K = 0) currents as a function of energy E and direction CS.

2. a function subroutine (PROFILE (X, K)) that computes the forward (K=1), backward (K=-1) and net (K=0) charge flow profiles as a function of position X.

The input to program TRAN is in two parts:

1. the perturbation input
2. the source-scattering input

The perturbation input (namelist (PARM) is embedded in the perturbation methods of solution. The source-scattering input (namelist PARMS) is embedded in the source-scattering deck. It contains the parameters that specify the source flux and the S-matrix.

The output to program TRAN is the following:

1. the electron flux $F(x, E, \mu)$
2. the source distribution $B(x, E, \mu)$
3. the derived quantities (yields, escape probabilities, currents)

B.2 Program LEET

Program LEET is composed of the following segments:

1. the scattering segment
2. the source segment
3. the flux segment
4. the yield segment

The scattering segment computes the S-matrix, and the e-e and e-p path lengths. The source segment computes the source flux and its Legendre coefficients LCs. The flux segment computes the electron flux and its LCs. The yield segment computes the electron yield, the energy yield and the angular yield. The yield segment depends on the angular flux segment. The flux segment depends on both the scattering segment and the source segment. The scattering segment and the source segment depend on input parameters.

The scattering segment implements the various S-matrices. In particular, the scattering segment implements the following:

1. the RPA e-e S-matrix (see section G.1.1, Ref. (2))
2. the RPA e-p S-matrix
3. the Rutherford e-e S-matrix
4. the isotropic (CM) S-matrix

The scattering segment is comprised of the following subroutines:

1. a function subroutine (SKERN (E, El, L)) that computes the LP scattering kernal K_ℓ (E, E')
2. a function subroutine (GREEN (E, El, L)) that computes the LP e-e scattering Green's function G_e (ℓ, E, E') for isotropic (CM) scattering
3. a function subroutine (GREENP (E, El, L)) that computes the LPR RPA e-p scattering Green's

function $G_p(\ell, E, E')$

4. a function subroutine (FPLEL(E)) that computes e-e path lengths
5. a function subroutine (FPLPL(E)) that computes e-p path lengths

The subroutine FPLEL(E) computes various e-e path lengths at energy E depending on the control parameter LPLEL:

a. When (LPLEL=1), the subroutine computes the RPA e-e path length (see section G.1.1, Ref. 2)
b. When LPLEL=2), the subroutine computes the RPA e-e path length in the low energy limit

The subroutine FPLPL(E) computes various e-p path lengths depending on the control parameter LPLPL:

a. When (LPLPL=1), the subroutine computes the Pines e-p path length (Eqn. 190), Ref. 2)
b. When (LPLPL=1), the subroutine computes the Quinn e-p path length (Eqn. 198), Ref. 2)

The source segment implements the Streitwolf source flux (Eqn. (241), Ref. 2). The Streitwolf source flux S (E, μ) is represented by the function FSOR(E, CS). The LP Streitwolf source flux $S_\ell(E)$ is represented by the function FSOR (E, L).

The flux segment computes flux by three methods:

1. Gaussian elimination method
2. Green's function method
3. Amelio method

In the Gaussian elimination method, an energy net is specified. This energy net converts the LPR (Legendre polynominal representation) homogeneous BE into a set of linear equations. This set of linear equations is solved by the method of Gaussian elimination.

The Gaussian elimination method is incorporated into subroutine GAUSS. In this subroutine, we proceed as follows; the LPR homogeneous BE, written terms of LEET program structures is:

$$\sum \text{SKERN (N*DE, N1*DE, L) * COFF (N1, L) = COSOR (N*DE, L)} \qquad (1)$$

We observe that the scattering kernal SKERN(N*DE, N1*DE, L) vanishes for N>N1. Therefore, the above set of equations (288) has a triangular form. The equations may be solved for the LP flux COFF(N1, L) by the method of Gaussian elimination.[1]

We observe that both the LP scattering kernal SKERN and the LP source flux COSOR are function subroutines. They, therefore, do not require storage. The LP flux COFF(N1, L), on the other hand, is an array, and therefore requires storage.

In the Green's function method, the LP e-e isotropic (CM) scattering Green's function acts on the LP source flux to produce the LP electron flux. The Green's function method is incorporated into the subroutine GRMETH. The subroutine GRMETH computes the LP flux array COFF(N, L) by having the LP scattering Green's function GREEN(E, E1, L) act on the LP source flux COSOR(E, L) to produce the LP source flux array COFF(N1, L). In terms of LEET program structures the above becomes:

$$\text{COFF(N, L)} = \sum \text{GREEN (N*DE, N1*DE, L) * COSOR (N1*DE, L)} \qquad (2)$$

The Amelio approximation to the LP scattering Green's function is a weighted sum of the LP e-e scattering Green's function and the LP e-p scattering Green's function ((233, Ref. 2). In terms of LEET

structures this becomes:

$$\text{GREEN}(E, E1, L) = \text{ETAE}*\text{GREENE}(E, E1, L) + \text{ETAP}*\text{GREENP}(E, E1, L) \quad (3)$$

The weight ETAE (ETAP) is equal to the e-e (e-p) total cross section divided by the net total cross section (e-e plus e-p) (222). The function subroutine GREENE(E, L) computes the scattering Green's function due to e-e isotropic (CM) scattering. The function subroutine GREENP(E, L) computes the Amelio e-p scattering Green's function ((229, 230), Ref. 2).

In the Amelio method, Amelio's expressions for the LP flux are programmed. The Amelio method is incorporated into subroutine AMELIO. The Amelio subroutine computes the LP flux array COFF(N, L) by calling the Amelio function COFFAM(E, L):

$$\text{COFF}(N, L) = \text{COFFAM}(N*DE, L) \quad (4)$$

The LP flux $F_\ell(E)$ in the Amelio approximation is represented by the function COFFAM(E, L). The Amelio flux function COFFAM(E, L) is the weighted sum of the e-e Amelio flux function COFFEA(E, L) and the e-p Amelio flux function COFFPA(E, L)

$$\text{COFFAM}(E, L) = \text{ETAE}*\text{COFFEA}(E, L)+\text{ETAP}*\text{COFFPA}(E, L) \quad (5)$$

The above weighting constitutes the Amelio approximation. The e-e Amelio flux function COFFEA(E, L) represents the LP flux $F_\ell(E)$ due to e-e isotropic (CM) scattering and a Streitwolf source flux. The e-p Amelio flux function COFFPA(E, L) represents the LP flux $f_\ell(E)$ due to RPA e-p scattering and a Streitwolf source flux.

In order to save memory, all three subroutines (GAUSS, GRMETH, AMELIO) store the LP flux in the same LP flux array COFF(N, L). This means that the LP flux array and all quantities that depend on the LP flux array must be printed out after each of the subroutines (GAUSS, GRMETH and AMELIO) is executed.

In addition to the array representation of the LP flux, the LP flux $F_{\ell}(E)$ may be represented by the function FCOFF(E, L). The LP function FCOFF(E, L) is defined in terms of the LP flux array COFF(E, L) by interpolation.

The flux $F(E, \mu)$ is represented by the function FF(E, CS). The flux function FF(E, CS) is defined in terms of the LP flux function FCOFF(E, L) :

$$FF(E, CS) = \sum FCOFF(E, L) * POLY(L) \qquad (6)$$

The array POLY(L) represents the L'th Legendre polynomial evaluated at CS. The above (247) is the Legendre polynomial expansion of the flux function FF(E, CS).

In summary, the flux segment is comprised of the following subroutines:

1. subroutine GAUSS
2. subroutine GRMETH
3. subroutine AMELIO
4. function subroutine FCOFF(E, L)
5. function subroutine FF(E, CS)

The yield segment computes various yields. The backward yield $Y_B(E, \mu')$ is represented by the function YIELD(E1, CS1). The yield function is defined in terms of the electron flux function (Eqns. 108, 109), Ref. 2):

$$YIELD(E1, CS1) = FF(E, CS) \qquad (7)$$

The internal and external energies (E, E1) differ by the work potential WORK. The internal and external directions (CS1, CS) are related by the refraction relations. The backward energy yield $Y_B(E1)$ is represented by the function EYIELD(E1). The energy yield function EYIELD(E1) is the integral of the yield function EYIELD(E1, CS1) over the external direction CS1 (Eqns. (110, 111), Ref. 2)

$$\text{EYIELD(E1)} = \int \text{DSCI} * \text{YIELD(E1, CS1)} \tag{7}$$

The backward angular yield $Y_B(\mu')$ is represented by the function AYIELD(CS1). The angular yield function AYIELD(CS1) is the integral of the yield function YIELD(E1, CS1) over the external energy E1 (Eqn. (112), Ref. 2)

$$\text{AYIELD(CS1)} = \int \text{DE1} * \text{YIELD(E, CS1)} \tag{8}$$

Included in the input to program LEET are:

1. the electron beam energy EPRIM
2. the work potential WORK
3. parameter that governs the selection of e-e path length LPLEL
4. parameter that governs the selection of e-p path length LPLPL

The output of program LEET are the yields (electron yield, energy yield, angular yield). These yields are both printed and plotted. The main program (LEET) puts the yields on disk and a separate plotting program (GRAF) plots the yields.

B.3 Program PHOTO

Program PHOTO is composed of the following segments:

1. a scattering segment
2. a source segment
3. a yield segment

The yield segment depends on the scattering and source segments. The scattering segment and the source segment depend on input parameters. The scattering segment implements the e-e scattering in several approximations. In particular, the scattering segment implements the following:

1. e-e Spicer scattering
2. e-e RPA scattering
3. e-e isotropic (CM) scattering

The Spicer energy scattering transition probability p(E, E') is represented by the function TRANC(E, El). For Spicer e-e scattering, the energy scattering transition probability p(E, E') is defined in terms of the density of states (DOS) (218). The DOS ρ(E) is represented by a pair of arrays (ENET(N), DNET(N)). The value DNET(N) is the DOS at energy ENET(N). The DOS ρ(E) is also represented by the function DENST(E). The DOS function DENST(E) is defined in terms of the DOS array pair (ENET(N), DNET(N) by interpolation.

The energy scattering transition probability function TRANC(E, El) is defined in terms of the DOS function DENST(E).

The energy scattering probability W(El) is represented by the function WPROB(El). The energy scattering probability function

WPROB(E1) is the integral of the energy scattering transition probability function TRANC(E, E1) over the final energy E (163):

$$\text{WPROB(E1)} = \int \text{DE} * \text{TRANC(E, E1)} \tag{9}$$

The Spicer path length $\lambda(E)$ is represented by an array APL(N). The Spicer path length array APL(N) is defined in terms of the Spicer energy scattering probability function WPROB(E):

$$\text{APL(N)} = \text{V/WPROB (N*DE)} \tag{10}$$

The Spicer path length $\lambda(E)$ is also represented by a function FPL(E). The Spicer path length function FPL(E) is defined in terms of the Spicer path length array APL(N) by interpolation. The path length array APL(N) is defined in terms of the energy scattering probability function:

$$\text{APL(N)} = \text{V/WPROB(N*DE)} \tag{11}$$

The Spicer path length function FPL(E) is defined in terms of the Spicer path length array APL(N) by interpolation. The path length array APL(N) is generated once in the beginning of the program. This storage of path lengths is done to minimize redundant computation.

The source segment implements the Spicer source flux. The Spicer source flux depends on the DOS $\rho(E)$. The DOS correlation C(E) is represented by the function CORCV(E). The DOS correlation function CORCV(E) is defined in terms of the DOS function DENST(E) (Eqn. (257), Ref. 2)

$$\text{CORCV(E)} = \int \text{dE1} * \text{DENST(E)} * \text{DENST(E-E1)} \tag{12}$$

The energy source transition probability $P_s(E, E-h\nu)$ (Eqn., Ref. 2) represented by the function TRANP(E). The energy source transition

probability function is defined in terms of the DOS function, and the DOS correlation function (Eqn. (251), Ref. 2):

$$\text{TRANP(E)} = \text{DENST(E)} * \text{DENST(E-HNU)}/\text{CORCV(E)} \tag{13}$$

The source flux energy is HNU.

The energy source flux S(E) is represented by the function FSORO(E). The absorption $\alpha(E)$ is represented by the function ABSORB(E). Both functions are proportional to the energy source transition probability TRANP(E):

$$\begin{aligned} \text{FSORO(E)} &= \text{POYNT} * \text{FACA} * \text{TRANP(E)} \\ \text{ABSORB (E)} &= \text{FACA} * \text{TRANP(E)} \end{aligned} \tag{14}$$

The source flux S(x, E) is represented by the function FSOR(E, x). The source flux function FSOR(E, X) is defined in terms of the energy source flux function FSORO(E) (258):

$$\text{FSOR(E, X)} = \text{POYNT} * \text{EXP (-ALPHA*X)} * \text{FSORO(E)}$$

The yield segment implements the computation of the first order backward energy yield $Y_B^{(1)}(E)$ as a function of external energy E1. The 0-point backward energy yield $Y_{B0}(E')$ is represented by the function EYIELD0(E1). The 1-point backward energy yield $Y_{B1}(E')$ is represented by the function EYIELD1(E1). The 0-point backward energy yield function EYIELD0(E1) is defined in terms of the energy source flux function FSORO(E) (Eqn. (269), Ref. 2):

$$\text{EYIELD0(E)} = \text{T} * \text{FSORO(E)}$$

The number T is the corrected threshold (Eqn. (270), Ref. 2):

The 1-point backward energy yield $Y_B(E')$ is represented by the function EYIELD1(E1). The 1-point backward energy yield function EYIELD1(E1) is defined in terms of (Eqn. (274), Ref. 2)

1. the energy scattering transition probability function TRANC(E, E1)
2. the energy scattering probability function WPROB(E1)
3. the energy source flux function FSORO(E)

There are two options for the computation of the 1-point function EYIELD1(E1) depending on the value of the parameter LYLD:

a. When (LYLD=1,) the 1-point yield is computed on the basis of Spicer e-e scattering.
b. When (LYLD=2), the 1-point yield is computed on the basis of non-Spicer scattering.

When non-Spicer scattering prevails (LYLD=2), then the selection of e-e scattering is determined by the control parameter LPLEL. (see section B.2).

The input to program PHOTO includes:

1. the photo beam energy HNU
2. the DOS array pair (ENET(N), DNET(N))

The output of program PHOTO is the 0-point and 1-point backward energy yields at various beam energies. These energy yields are both printed and plotted. The main program (PHOTO) puts the yields on disk and a separate plotting program (GRAF) plots the yields.

B.4 Program MIL

Program MIL is comprised of two segments:

1. a source distribution (SD) segment
2. a flux segment

The SD segment computes the SD B(x). The flux segment computes the flux F(x). The flux segment depends on the SD segment.

The basic task of the SD segment is to implement the iterative perturbation solution to the Milne equation. This task is performed in subroutine MILNE. In order to start the iteration procedure, the source flux S(x) is needed. The source flux S(x) is represented by the function GSOR(x). This function is called by subroutine MILNE. The source flux function GSOR(x) is to be defined by the programmer.

In order to compute the new SD from the old SD, subroutine MILNE is faced with the task of evaluating the Milne integral. The evaluation of the Milne integral is done in two parts:

1. the evaluation of the Milne integral in the vicinity of the singularity
2. the evaluation of the Milne integral in the rest of the interval (total interval minus the vicinity of the singularity).

The first part is done by making a call to subroutine SING. The second part is done by making a call to either subroutine TRAP or subroutine TRAPR. Subroutine TRAP computes the nonsingular part of the Milne integral by the trapazoidal method. Subroutine TRAPR computes the non-singular part of the Milne integral by the Romberg method. Which subroutine is called depends on the value of the parameter LQUAD:

a. When (LQUAD=1), subroutine TRAP is called.

b. When (LQUAD=2), subroutine TRAPR is called.

The source distribution (SD) is represented by an array BS(I). Subroutine MILNE stores the new SD in the array BS(I). The SD B(X) is also represented by the function BSOR(X). The SD function BSOR(X) is defined in terms of the source distribution array BS(I) by interpolation.

The basic task of the flux section is to compute the electron flux. The flux $F(x, \mu)$ is represented by an array AF(I, L). The flux array AF(I, L) is computed in subroutine DIST, by having the flow propagator G_f act on the SD function BSOR(X). The flux $F(x, \mu)$ is also represented by a function FF(X, CS). The flux function FF(X, CS) is defined in terms of the flux array AF(I, L) by interpolation.

The input to program MIL includes the width D of the slab in units of path length. The output to program MIL is both the SD and the flux. Both of these quantities may be printed out after each iteration.

B.5 Program MONTE

Program MONTE is maintained in the same update library as program TRAN. The MONTE library is composed of several decks.

1. the Monte-Carlo deck that implements the MC method
2. several source-scattering decks

The source-scattering decks are the same decks used in program TRAN.

The MONTE deck is composed of the following segments:

1. the history ensemble segment
2. the tabulation segment
3. the derived quantities segment

The history ensemble segment constructs a history ensemble. This ensemble is stored on disk. The tabulation segment tabulates the history ensemble to produce the electron flux. The derived quantities segment computes the derived quantities (yields, escape probabilities, currents).

The history ensemble segment is made up of the following subroutines:

1. subroutine HISTORY
2. subroutine HIST
3. subroutine GEN

Subroutine HISTORY generates a starting statistic by playing on the source PD. Subroutine HISTORY then calls subroutine HIST. Subroutine HIST generates the electron history from the starting statistics. The generated electron history is then stored on disk.

A new starting statistic and corresponding history is then generated as above. Histories are repeatedly generated and stored on disk until a predetermined maximum (NHIST) is reached.

An electron history is represented by an array AH(3, NC). The columns of the history array are the statistics that comprise the history:

a. AH(1, NC) - position of node NC
b. AH(2, NC) - post energy of node NC
c. AH(3, NC) - post direction of node NC

The starting statistics is represented by an array ASTO(3). The starting statistics array is the first column of the electron history array.

Subroutine HIST repeatedly calls subroutine GEN to generate new nodes in the history until a predetermined maximum (NCOLL) is reached or a boundary is met. If a predetermined maximum NCOLL is reached, the control is returned to the calling program HISTORY. If a boundary is met then a decision is made as to whether the previous node is inside or outside the escape cone. If the previous node is inside, the generation process is concluded, and control is returned back to the calling program HISTORY. If the previous node is outside the escape cone, then the free path out of the previous collision site is bent in accordance to the reflection principle. The correct post-collision site is located and the generation process continues. The statistics of each node is stored in the electron history array AH(3, NC).

Subroutine GEN(BST1, BST) generates the post statistics BST of a node from the pre-statistics BST1 of the node by playing on the pre-S-matrix.

The tabulate segment is made up of one subroutine (PROCESS) that tabulates the history ensemble to produce the electron flux. This tabulation is done by:

1. buffering in each history record from disk
2. counting the number of nodes that occur in each phase space cube

In this way, the electron flux array AF(I, N, L) is generated. The electron flux function FF(X, E, CS) is defined in terms of the generated flux array AF(I, N, L) by interpolation. The derived quantities segment is virtually identical to that of program TRAN.

B.6 Conclusions

Programs LEET, PHOTO and MIL are completed. Programs TRAN and MONTE are not complete. The BD perturbation segment of program TRAN, however, is complete. This segment has been checked against program MIL. A comparison has been made between:

1. the BD perturbation method in program TRAN and
2. the iterative solution to the Milne equation in program MILNE.

The above comparison checks at each iteration in both programs. The CD algorithm segments have not been complete. The realistic scattering segments and realistic source function segments have been incorporated into program TRAN. However, the interface problems have not been fully resolved. These realistic segments have been taken from Program LEET and Program PHOTO and incorporated into Program TRAN.

REFERENCES

1. O'Brien, J., Low Energy Electron Transport - Boltzmann Equation Treatment, Arcon Corporation Scientific Report No. 1, AFCRL Contract F19628-74-C-0049.

2. O'Brien, J., Electron Transport, Arcon Corporation Scientific Report No. 3, AFCRL Contracl F19628-71-C-0034.

3. G. Hackenberg and W. Brauer, Advances in Electronics and Electron Physics II, Academic Press, 1959, 413.

4. R.H. Ritchie, M.V. Nakai, R.D. Birkhauff, Low Energy Mean Free Paths in Slids, Advances in Radiation Biology, 3, pp 1-28, 1969.

5. D. Pines and P. Nozieres, The Theory of Quantum Liquids, W.A. Benjamin, Incorporated, 1966.

6. G.F. Amelia, The Journal of Vacuum Science and Technology 7 (6), 594.

7. C.N. Berglund and W.E. Spicer, Phys. Rev. 136 (4A, A1030.

8. E. Everhart, Phys. Rev., 99, 1287 (1955).

9. H. Puff, Physical Status Solidi, 4, 1964, 125-138.

10. Richtmyer and Morton, Difference Methods for Initial Value Problems, Interscience Publishers.

11. J.R. Schrieffer, Superconductivity, W.A. Benjamin, Inc. Reading, Mass. (1964).

12. R.D. Evans, The Atomic Nucleus, McGraw-Hill (1955).

V. ELECTRON TRANSPORT — SPENCER-LEWIS EQUATION

A. Introduction

Program HYPES solves numerically the Spencer-Lewis integro-differential equation for kilovolt electron transport. Quantities calculated include current flow, charge and energy deposition profiles, and forward and backward emissions from a plane slab under electron-beam and x-ray photo-electron radiation sources.

Program HYPES performs the following four tasks:

Task 1: Initialization

Slab, source, scattering, range, and printer and plotter control parameters are read via namelist PARAMS. Based on this information, the slab width L is subdivided into intervals of size $\Delta\chi$ and the range cutoff s_{cut} is subdivided with intervals of size Δs. Also, the scattering matrix $P(\mu', \mu)$, the source function $S(\chi, \mu, s)$, and the initial electron distribution functions $f(\chi, \mu, s)$, are constructed.

Task 2: Numerical Integration

The Spencer-Lewis equation

$$\frac{\partial f(\chi, \mu, s)}{\partial s} + \mu \frac{\partial f(\chi, \mu, s)}{\partial \chi}$$

$$= \frac{1}{\lambda(s)} \int_{-1}^{1} P(\mu' \rightarrow \mu; s) \left[f(\chi, \mu', s) - f(\chi, \mu, s) \right] d\mu' + S(\chi, \mu, s)$$

is integrated numerically for $J = s_{cut}/\Delta s$ iterations. In the above equation

χ = electron position,

μ = electron direction-cosine,

s = electron range,

$\lambda(s)$ = electron mean free path,

$P(\mu' \rightarrow \mu; s)$ = scattering probability from μ' into μ

$S(\chi, \mu, s)$ = electron source function,

and $f(\chi, \mu, s)$ = electron distribution function.

The solid-vacuum boundary conditions are

$$f(\chi = 0, \mu, s) = 0 \text{ if } \mu > 0$$

and $$f(\chi = L, \mu, s) = 0 \text{ if } \mu < 0 .$$

These are the following six source types from which to choose:

Type 1. Monodirectional, monoenergetic point source at the front face of the slab.

$$S(\chi, \mu, s) = \delta(\chi)\ \delta(\mu - \mu_o)\ \delta(s),$$

where δ is the Dirac δ-function;

Type 2. Monodirectional, monoenergetic point source located within the slab at $\chi = a$

$$S(\chi, \mu, s) = \delta(\chi - a)\ \delta(\mu - \mu_o)\ \delta(s);$$

Type 3. Isotropic, monoenergetic point source located within the slab at $\chi = a$

$$S(\chi, \mu, s) = \frac{1}{2}\ \delta(\chi - a)\ \delta(s) ;$$

Type 4. Monodirectional, monoenergetic line source uniformly distributed over the slab

$$S(\chi, \mu, s) = \frac{1}{L} [H(\chi) - H(\chi - L)] \delta(\mu - \mu_o) \delta(s) ,$$

where H is the Heaviside unit function;

Type 5. Monodirectional, monoenergetic line source uniformly distributed between $\chi = a$ and $\chi = b$ within the slab

$$S(\chi, \mu, s) = \frac{1}{(b-a)} [H(\chi - a) - H(\chi - b)] \delta(\mu - \mu_o) \delta(s) ,$$

where $b > a$;

Type 6. Monodirectional, energy-dependent, once-scattered electron beam which moves along the electron path length

$$S(\chi, \mu, s) = \frac{P(\mu_o \rightarrow \mu)}{\lambda} e^{-s/\lambda} \delta(s - \chi/\mu) ,$$

where $P(\mu_o \rightarrow \mu)$ = probability of scattering from μ_o into μ

and λ = electron transport mean free path.

The first five source types are handled as initial conditions; the sixth is inserted before each iteration step of the numerical integration.

Task 3. Calculation of Quantities

After each iteration step in Task 2 contributions to the following are calculated:

current flow

$$I(\chi, s) = \int_o^{s_{cut}} ds \int_{-1}^{1} \mu f(\chi, \mu, s)\, d\mu;$$

forward emission

$$F(s) = \int_o^{1} \mu f(\chi = L, \mu, s)\, d\mu;$$

backward emission

$$B(s) = \int_{-1}^{o} |\mu|\, f(\chi = 0, \mu, s)\, d\mu;$$

and energy deposition profile

$$W(\chi, s) = \int_o^{s_{cut}} \left|\frac{dE}{dS}\right| dS \int_{-1}^{1} f(\chi, \mu, s)\, d\mu + E(s_{cut}) * Q(x, s_{cut}),$$

where dE/dS is the stopping power and

$$E(s_{cut}) = E(0) - \int_o^{s_{cut}} \left|\frac{dE}{dS}\right| dS$$

is the electron energy in the continuous slowing-down approximation.

The charge deposition profile $Q(\chi, s) = \int_{-1}^{1} f(\chi, \mu, s)\, d\mu$ is calculated at the end of the numerical integration.

Task 4: Plotting

The numerical integration is interrupted periodically in order to plot the electron distribution functions. The current flow, charge and energy deposition profiles and the forward and backward emissions are plotted at the end of the numerical integration. Samples of these quantities are printed.

B. Numerical Integration Methods

The Spencer-Lewis equation is treated in discrete ordinates form

$$\frac{\partial f_m(\chi, s)}{\partial s} + \mu_m \frac{\partial f_m(\chi, s)}{\partial \chi}$$

$$= \frac{1}{\lambda(s)} \sum_{n=1}^{M} P_{mn} A_n \left[f_n(\chi, s) - f_m(\chi, s) \right] + S_m(\chi, s) ,$$

where $f_m(\chi, s) = f(\chi, \mu_m, s)$,

μ_m = Gaussian quadratures node

A_m = Gaussian quadratures weight,

P_{mn} = Probability of scattering from μ_n into μ_m

$S_m = S(\chi, \mu_m, s)$,

and M = Number of Gaussian quadratures nodes.

The partial differentials are replaced with finite-difference approximations which are taken at points

$$(\chi_k, s_j) = (k\Delta\chi, j\Delta s) \equiv (k, j) .$$

In terms of this abreviated notation,

$$f_m(k, j) \equiv f_m(\chi_k, s_j)$$

and quantities are calculated as follows:

$$I(k, j) = \sum_{j=0}^{J} \Delta s \sum_{m=1}^{M} a_m \mu_m f_m(k, j) ;$$

forward current

$$F(j) = \sum_{m}^{*} A_m \mu_m f_m (k = L/\Delta\chi, j) ,$$

where $\sum_{m}^{*}$ includes m's for which $\mu_m > 0$;

backward current

$$B(j) = \sum_{m}^{*} A_m |\mu_m| f_m (k = 0, j) ,$$

where $\sum_{m}^{*}$ includes m's for which $\mu_m < 0$;

energy deposition profile

$$W(k, j) = \sum_{j=0}^{J} (\Delta E)_j \sum_{m=1}^{M} A_m f_m (k, j) + E(J) * Q(k, J) ,$$

where $(\Delta E)_j = \left| dE/dS \right|_j \Delta S$

and $E(J) = E(0) - \sum_{j=0}^{J} (\Delta E)_j$;

and charge deposition profile

$$Q(k, j) = \sum_{m=1}^{M} A_m f_m (k, j) .$$

Two alternative numerical integration algorithms are included in program HYPES in the form of function routines HNUM2 and HNUM3. Other algorithms may be substituted by the user. In the ensuing expositions the source term will be ignored.

B. 1. Algorithm 1: Method of Characteristics

This algorithm is designed for the M = 2 case. Let

$$\frac{df_m(t)}{dt} = \frac{\partial f_m(t)}{\partial s}\,\frac{ds}{dt} + \frac{\partial f_m(t)}{\partial \chi}\,\frac{d\chi}{dt}$$

$$= \frac{\partial f_m(\chi, s)}{\partial s} + \mu_m \frac{\partial f_m(\chi, s)}{\partial \chi} \quad ,$$

where $t = t(\chi, s)$

Then $ds = d\chi/\mu_m = dt$ determines a one-parameter family of characteristic curves along which

$$\frac{df_m(t)}{dt} = \sum_{n=1}^{M} P_{mn} A_n \left[f_n(t) - f_m(t) \right]$$

or $$\int_{t_1}^{t_2} df_m(t) = \int_{t_1}^{t_2} \sum_{n=1}^{M} P_{mn} A_n \left[f_n(t) - f_m(t) \right] dt$$

Let $\Delta t = t_2 - t_1$ become small. Then

$$f_m(t_2) - f_m(t_1) - \left(\frac{\Delta t}{2}\right) \sum_{m=1}^{M} P_{mn} A_n \left[f_n(t_2) + f_n(t_1) - f_m(t_2) - f_m(t_1) \right]$$

via the trapezoidal rule.

Consider the lattice shown in figure 1. For M = 2 one family of characteristics is generated from

$$ds_+ = d\chi/\mu_1$$

and the other from

$$ds_- = d\chi/\mu_2 = -d\chi/\mu_1 \quad .$$

Choose points along these characteristics such that

$$t_1 = (k, j)$$

and

$$t_{2\pm} = (k \pm 1/2,\ j + 1/2) \quad ,$$

where $\Delta t = \left(\frac{\Delta\chi}{2}\right)/\mu_1 = \frac{\Delta s}{2}$.

Then

$$f_m(k, j + 1/2) - f_m(k, j)$$

$$= \frac{1}{\lambda}\left(\frac{1}{2}\right)\left(\frac{\Delta\chi}{2}\right)\left(\frac{1}{\mu_1}\right) \sum_{n=1}^{M} P_{mn} A_n \left[f_n\left(k \pm 1/2,\ j + 1/2\right) \right.$$

$$\left. + f_n(k, j) - f_m\left(k \pm 1/2,\ j + 1/2\right) - f_m(k, j) \right]$$

where $k+1/2$ is used for $m=1$

and $k-1/2$ is used for $m=2$.

The foregoing equations may be solved for $f_m(k+1/2,\ j+1/2)$, where $m=1, 2$, as follows.

Since

$$1 = \int_{-1}^{1} P(\mu' \rightarrow \mu)\, d\mu = \sum_{n=1}^{M} P_{mn} A_n = \sum_{n=1}^{M} P_{mn},$$

if $M=2$, then

$$P_{11} + P_{12} = 1$$

and

$$P_{22} + P_{21} = 1.$$

By microreversibility $P_{12} = P_{21} = P$.

Consequently, $P_{11} = P_{22} = 1-P$.

Now let $A = \Delta\chi/4\lambda\mu$, then

$$f_1(k+1/2,\ j+1/2) = \left[(1+AP)\, C_1(k,j) + APC_2(k+1,j)\right]/(1+2AP)$$

and $$f_2(k+1/2,\ j+1/2) = \left[APC_1(k,j) + (1+AP)\, C_2(k+1,j)\right]/(1+2AP)$$

where $C_1(k,j) = (1-AP)\, f_1(k,j) + AP\, f_2(k,j)$

and $C_2(k,j) = APf_1(k+1,j) + (1-AP)\, f_2(k+1,j)$

One iteration step is completed after these $f_m(k+1/2,\ j+1/2)$ are in turn inserted into the foregoing equations in order to obtain $f_m(k+1,\ j+1)$.

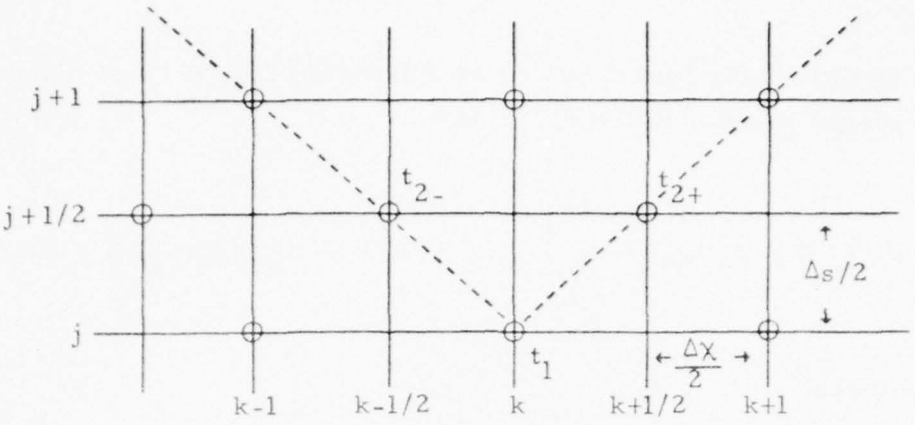

Figure V. B. 1

Figure 1: Lattice for Method of Characteristics

Point t_1 lies at (k, j). Point t_{2+} lies at (k+1/2, j) along the characteristic generated from $ds_t = d\chi/\mu_1$. Point t_{2-} lies at (k-1/2, j) along the characteristic generated from $ds_- = -d\chi/\mu_1$.

B. 2. Algorithm 2: Implicit Method with Fractional Indices

This algorithm handles M quadrature nodes. Consider the lattice shown in figure 2. Approximate the discrete ordinates equation via implicit finite-differences such that

$$\left[f_m(k, j+1) - f_m(k, j)\right]/\Delta s + \mu_m\left[f_m(k \pm 1, j+1) - f_m(k, j+1)\right]/\Delta\chi$$

$$= \frac{1}{\lambda}\sum_{n=1}^{M} P_{mn} A_n \left[f_n(k, j+1) - f_m(k, j+1)\right],$$

where $k+1$ is used if $\mu_m > 0$

and $k-1$ is used if $\mu_m < 0$.

Let the iteration step from j to j+1 be subdivided into M equal substeps which are indexed $j+n/M$, $n \in \{1, 2, \ldots, M\}$.

Then

$$f_m(k, j+1) - f_m(k, j) = \sum_{n=1}^{M} \left[f_m(k, j+n/M) - f_m\left(k, j+\frac{n-1}{M}\right) \right], \text{ exactly,}$$

while in the mean

$$\frac{1}{\lambda} \sum_{n=1}^{M} P_{mn} A_n \left[f_n(k, j+1) - f_m(k, j+1) \right]$$

$$\simeq \frac{1}{\lambda} \sum_{n=1}^{M} P_{mn} A_n \left[f_n\left(k, j+\frac{n}{M}\right) - f_m\left(k, j+\frac{n}{M}\right) \right]$$

and

$$f_m(k \pm 1, j+1) - f_m(k, j+1) \simeq \frac{1}{M} \sum_{n=1}^{M} \left[f_m\left(k \pm 1, j+\frac{n}{M}\right) - f_m\left(k, j+\frac{n}{M}\right) \right]$$

Substitute these expressions into the finite-differences equation such that

$$\left(\frac{1}{\Delta s}\right) \sum_{n=1}^{M} \left[f_m\left(k, j+\frac{n}{M}\right) - f_m\left(k, j+\frac{n-1}{M}\right) \right]$$

$$+ \frac{\mu_m}{M \Delta \chi} \sum_{n=1}^{M} \left[f_m\left(k \pm 1, j+\frac{n}{M}\right) - f_m\left(k, j+\frac{n}{M}\right) \right]$$

$$\simeq \frac{1}{\lambda} \sum_{n=1}^{M} P_{mn} A_n \left[f_n\left(k, j+\frac{n}{M}\right) - f_m\left(k, j+\frac{n}{M}\right) \right]$$

If term-by-term equality is assumed,

$$f_m\left(k, j+\frac{n}{M}\right) = f_m\left(k, j+\frac{n-1}{M}\right)$$

$$- \frac{\mu_m \Delta s}{M \Delta \chi}\left[f_m\left(k \pm 1, j+\frac{n}{M}\right) - f_m\left(k, j+\frac{n}{M}\right)\right.$$

$$+ \left(\frac{\Delta s}{\lambda}\right) P_{mn} A_n \left[f_n\left(k, j+\frac{n}{M}\right) - f_m\left(k, j+\frac{n}{M}\right)\right]$$

where $n \in \{1, 2, \ldots, M\}$.

The foregoing equations may be solved for $f_m(k \pm 1, j + n/M)$ as follows. Let $A_m = |\mu_m \Delta s / M \Delta \chi|$ and $B_{mn} = \Delta s\, P_{mn} A_{n/\lambda}$, then

$$f_m(k \pm 1, j + n/M) = f_m(k, j + (n-1)/M)$$

$$+ B_{mn} f_n(k, j + n/M)$$

$$+ (A_m - B_{mn} - 1) f_m(k, j + n/M)$$

For $m = n$ this espression may be simplified; that is,

$$f_m(k \pm 1, j + m/M) = f_m(k, j + (m-1)/M)$$

$$+ (A_m - 1) f_m(k, j + m/M)$$

Since $f_m(k, j = 0)$ is known from initial conditions, and the boundary conditions yield $f_m\left(k = 0, j + \frac{m}{M}\right)$ for $\mu_m > 0$, and $f_m\left(k = L/\Delta\chi, j + \frac{m}{M}\right)$ for $\mu_m < 0$, it is possible to obtain the $f_m\left(k, j + \frac{n}{M}\right)$ by successive substitutions. Each $f_m(k, j)$ requires M of these substitutions in order to reach $f_m(k, j+1)$. Consequently, M^2 substitutions are required per iteration step in order to update all of the f_m.

The foregoing procedure is stable as long as

$$A_m - B_{mn} \geq 1$$

or $$\Delta s \geq \max \{1/(A_m - B_{mn})\} .$$

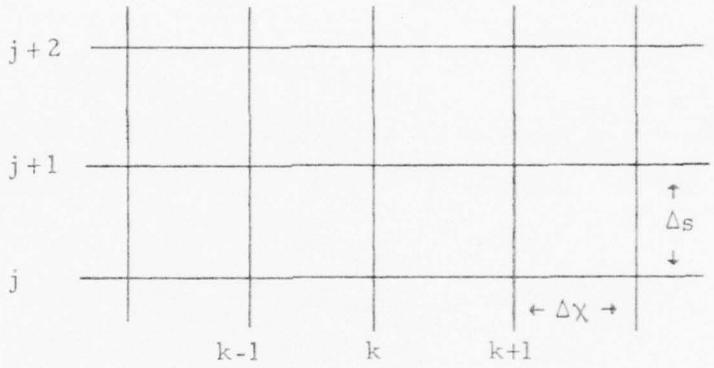

Figure V.B.2

Figure 2: Lattice for Implicit Method with Fractional Indices

The lattice parameters are $\Delta\chi$ and Δs, where $\Delta s = \max\{1/(A_m - B_{mn})\}$ as defined in the text.

VI. SURFACE ACOUSTIC WAVE FILTER DESIGN

A. Introduction

The problem of determining the charge densities, or equivalently the normal component of $\underline{D}$, at the surfaces of a planar array of perfectly conducting strips held at various potentials plays a major role in the design of many SAW devices. In particular, to synthesize withdrawal weighted SAW filters by Hartmann's method[1], a table derived from the Fourier Transform of D_z at the electrode-substrate interface is required. Hartmann developed a table for single electrode devices operating at the synchronous frequency: he took into account the electrostatic interaction between a central electrode and its three nearest neighbors situated within another array of electrodes having spatially alternating polarities. D_z was determined by solving the corresponding boundary-value problem using a method described in an earlier paper.[2]

Presented below are design tables (I-IV) for single electrode transducers operating at the synchronous frequency and fifth harmonic. A table for double electrode configurations has also been computed and is included with other related results of interest. The method used for computing D_z was based upon a formulation by Smith and Pedler[3] which required the solution of coupled integral equations for the charge density expansion coefficients. Instead of reducing the integral equations to a system of algebraic equations by a collocation method as they did, the results stated in this report were obtained by applying a Galerkin technique[4] to effect the reduction. When compared with J. J. Thomson's exact solution for the two electrode problems,[5] the Galerkin regime was found to yield 7 or more significant digit accuracy for a charge density expansion composed of 10 terms.

B.1. Analysis

The coupled integral equations[3] governing the potential difference on the k^{th} strip due to charge on all strips, and the condition that the total charge must vanish, can be cast into dimensionless variables and expressed as follows:

$$V(W_k) - V_o = \left(\frac{s}{2}\,\alpha_o\right) \sum_{j=1}^{J} \int_{-1}^{1} \sigma(U_j)\, \ell n \left| W_k - U_j + 2(k-j)/\eta \right| dU_j$$

$$O = \sum_{j=1}^{J} \int_{-1}^{1} \sigma(U_j)\, dU_j$$

for $\quad k = 1, 2, \ldots, j, \ldots, J$

where

U_j, W_k = normalized distance on the j^{th} and k^{th} strips, respectively, as measured from the center of each strip.
Note: $-1 \le U, W \le 1$

V = potential applied to a strip.

σ = surface charge density.

η = (strip width)/(center-center strip separation)

$$= \frac{1}{2\pi}\left[\left(\epsilon_{xx}\epsilon_{zz} - \epsilon_{xz}^2\right)^{1/2} + \epsilon_o\right]^{-1}, \quad \text{where the}$$

$\epsilon_{\ell m}$ = dielectric permittivities of the piezolectric substrate

s = strip width

V_o = a reference potential

J = total number of electrode strips in the array

Following the lead of Smith and Pedler, [3] a solution of the form

$$\sigma(U_j) \equiv \left(\frac{2}{s\alpha_o}\right)(1 - U_j^2)^{-1/2} \sum_{n=0}^{N-1} C_n^{(j)} \; T_n(U_j)$$

is assumed and substituted into the integral equations. Evaluating the ensuing Cauchy Principal-Valued integrals yields

$$V(W_k) - V_o = \sum_{n=0}^{N-1} C_n^{(k)} \mu_n \, T_n(W_k)$$

$$+ \sum_{j \neq k} \sum_{n=0}^{N-1} C_n^{(j)} \int_o^{\pi} \cos n\theta \; \ell n \left| W_k - \cos\theta + 2(k-j)/\eta \right| d\theta$$

$$O = \sum_{j=1}^{J} C_o^{(j)}$$

$(k = 1, 2, \ldots, j, \ldots, J)$

where

$T_n(U)$ = n^{th}-order Chebyshev polynomial of the first kind

$$\mu = -\pi \ell n\, 2$$

$$\mu_n = -\pi/n \qquad n=1, 2, \ldots, N-1$$

The integral in the double sum can also be evaluated in closed form.

The Galerkin approach requires that the previous equations be reduced to a system of algebraic equations by multiplying both sides with weighting functions, and integrating over (-1, 1). In view of the orthogonal functions on the right-hand side of the equations, a fortuitous choice of weighting functions is

$$T_m(W_k) \qquad (1 - W_k^2)^{-1/2} \qquad m=0, 1, \ldots, N-1$$

A linear system of algebraic equations thereby results for the unknown $C_n^{(j)}$ and V_o. Using a 128-point Trapezoidal Rule quadrature in conjunction with a Fast Fourier transform package, integrals that could not be evaluated analytically were numerically determined to 9 significant digits. In this fashion, $C_n^{(j)}$ has been determined for arrays composed of 22 electrodes or less. Figure VI.A.1 illustrates D_z for a seven electrode array in which two electrodes have been removed.

B.2. Design Tables

The design tables presented herein are to be interpretted in the same manner as Hartmann's.[1] The top entries of each row refer to the strength

or weight associated with the normalized magnitude of the acoustic response of the central electrode(s) comprising a specific array. The bottom entries correspond to the phase-slope of the acoustic response.

For the N^{th} configuration of electrodes, the weight for a transducer operating at the ν^{th} multiple of the synchronous frequency, f_o, is defined by

$$H_o(N) \equiv \frac{|A_N(\nu)|}{|A_o(\nu)|} = \frac{|{}_nD_z(\nu)|}{|{}_oD_z(\nu)|}$$

where

$$A(\nu) = \text{acoustic response function}$$

$$\sim \sqrt{\nu}\ D_z(\nu)$$

Both A and D_z pertain to the central electrode or electrode pair in the array. The k=0 arrangement of electrodes refers to an array with spatially alternating polarities in which no electrodes have been removed.

For the j^{th} single electrode in an array

$$D_z^{(j)}(\nu) \sim \sum_{n=0}^{N-1} C_n^{(j)} (-i)^n J_n(\tfrac{\pi}{2}\eta\nu) \quad ,$$

while for double electrodes the total D_z for the pair can be shown to be expressed as follows:

$$D_z(\nu) \sim e^{i\frac{\pi}{4}\nu} \sum_{n=0}^{N-1} C_n^{(r)} (-i)^n J_n(\tfrac{\pi}{4}\eta\nu)$$

$$+ e^{-i\frac{\pi}{4}\nu} \sum_{n=0}^{N-1} C_n^{(\ell)} (-i)^n J_n(\tfrac{\pi}{4}\eta\nu)$$

(r) and (ℓ) refer to the right and left electrodes, respectively, of the central electrode pair. $J_n(\cdot)$ is the n^{th} order Bessel function of real argument.

The second number in each table entry is $d_o(N)$, where $d_o(n) \sim d\varphi(n,\nu)/d\nu$ is the phase slope of $A(\nu)$. $d_o(n)$ is a measure of the displacement of the effective source driving strength from the center of the electrode. Figure VI.B.1. depicts the magnitude of the acoustic response for electrode pairs in double electrode configurations.

C.1 A SAW Filter Design Program

A computer program was to be developed that would automate the design of withdrawal weighted surface acoustic wave (WWSAW) filters. Such filters are composed of arrays of electrodes and gaps (missing electrodes) as illustrated in figure VI.C.1. The problem was to determine the sequence of electrodes and gaps that generates a transfer function which matches as closely as possible the transfer function resulting from a specified sampled impulse response function, $h_D(t_i)$.

C.2 Filter Design Criterion

To synthesize a WWSAW filter, it was postulated that by minimizing the difference between the cumulative sample response function of the WWSAW filter and $h_D(t_i)$, at all values of i where an electrode or gap was situated, the transfer functions would match up closely over some frequency interval. The design criterion that was initially adopted, therefore, took the form that

$$|A_D(t_i) - A_{ww}(t_i)|$$

should be a minimum for all t_i. The cumulative sample response functions are defined by

$$A_D(M\Delta t) \equiv \int_0^{M\Delta t} h_D(t)\, dt \quad \text{for a theoretical filter} \quad ,$$

$$A_{ww}(M\Delta t) \equiv \int_0^{M\Delta t} h_{ww}(t) \quad \text{for the WWSAW filter} \quad ,$$

with $M = 1, 2, \ldots,$ NMAX and Δt set to unity for convenience.

The value of h_{ww} at t_i depends on the presence or absence of the electrodes at t_{i-3}, t_{i-2}, t_{i-1}, t_i, t_{i+1}, t_{i+2}, and t_{i+3}. Reference 1 presents tabulated values of $h_{ww}(t_i)$ for all possible configurations about t_i. For example, if a 1 signifies the presence of an electrode and a 0 signifies a gap, then the configuration

1	1	0	1	1	0	0
i-3	i-2	i-1	i	i+1	i+2	i+3

corresponds to $h_{ww}(i) = 0.710$. To evaluate $h_{ww}(i+1)$ it is necessary to determine whether an electrode or gap is present at i+4. The configurations to be considered are a and b:

(a)	1	0	1	1	0	0	0
	i-2	i-1	i	i+1	i+2	i+3	i+4
(b)	1	0	1	1	0	0	1

According to the table, $h_{ww}^{(a)}(i+1) = 0.778$ while $h_{ww}^{(b)}(i+1) = 0.869$. To decide which of the two configurations is best, and consequently which value of h_{ww} is appropriate, the minimum cumulative error criterion

$$e(i+1) \equiv |A_D(i+1) - A_{ww}(i+1)| \quad \text{has to be invoked.}$$

Since $h_D(t)$ is given initially, $A_D(i+1)$ can be found using a suitable quadrature. $A_{ww}(i+1)$ can be found by noting that $A_{ww}(i+1) \approx A_{ww}(i) + \frac{1}{2}[h_{ww}(i) + h_{ww}(i+1)]$, with $h_{ww}(1) \equiv 1$ and $A_{ww}(1) \equiv 0.5$. Two values of $A_{ww}(i+1)$ were separately inserted into the error criterion; one quadrature based on $h_{ww}^{(a)}(i+1)$ and the other on $h_{ww}^{(b)}(i+1)$. Whichever gave the smaller error was judged to be the best, and defined the complete configuration about t_{i+1}.

C.3 The Gap Problem

Assume, for example, it was determined that an electrode should be present at i+4. With $h_{ww}(i+1)$ now defined, it is desired to find $h_{ww}(i+2)$, $h_{ww}(i+3)$, ..., $h_{ww}(NMAX)$. Using the configuration shown in section C.2, the next situation to analyze is the following.

0	1	1	0	0	1	?
i-1	i	i+1	i+2	i+3	i+4	i+5

But h_{ww} is defined as zero whenever the pivotal point of the computation, in this case i+2, is located at a gap, regardless of the presence of a gap or electrode at i+5. This means there is no way to tell whether to place a gap or electrode at i+5 by the decision making rule based on the minimization of $|A_D(i+2) - A_{ww}(i+2)|$. Without this knowledge the design process terminates.

To surmount the obstacle it became necessary to consider more complex optimization schemes. The procedures followed became a function of the number of consecutive gaps encountered at a pivotal point. It was found that the longer the string of gaps, the more crucial it was that the error be distributed over the neighborhood of the gaps. It became necessary to change the decision criterion to

$$|A_D(i) - A_{ww}(i) - \text{tolerance (\# of consecutive gaps)}|$$

Different logic was required for treating one, two, three, and more than three consecutive gaps.

C.4 Iterative Design

It became evident after observing the errors, $\{e(i) = |A_D(i) - A_{ww}(i)| : i = 1, 2, \ldots, NMAX\}$, that there were clumps of large errors at various i-locations which were leading to transfer function curves less satisfactory than expected. In an effort to remedy the situation, it was decided to cycle back to the lowest value of i, i^*, where the error exceeded some tolerance level, and to modify one electrode or gap in that region in such a manner as to reduce the error at i^*. Once this was accomplished, the program would be allowed to march forward in the usual manner. The change would alter the configuration in the vicinity and beyond i^* leading to new errors some of which would again exceed the tolerance level. Usually, the tolerance would be exceeded closer to i=NMAX, and cycling back to a new i^* would occur to make new alterations. The cycling back operation was to continue until all points yielded errors less than the tolerance threshold.

This iterative design process appears to be effective in the sense that it reduces the sum of the squares of the errors by a factor of 6 over the one-pass procedure. If the tolerance level is lowered too much, however, each cycle can lead to design configurations having larger errors: the process becomes unstable. The best results achieved thus far have occurred when the tolerance level was allowed to decrease linearly with increasing i, but more work may be required with different functional forms to find the best one to use.

The program is currently being used for IDT design. The matching of transfer functions improves markedly as the number of electrodes, NMAX, is increased. But even for relatively few electrodes, the matching is quite satisfactory out to three sidelobes from the main lobe.

FIGURE VI. A. 1.

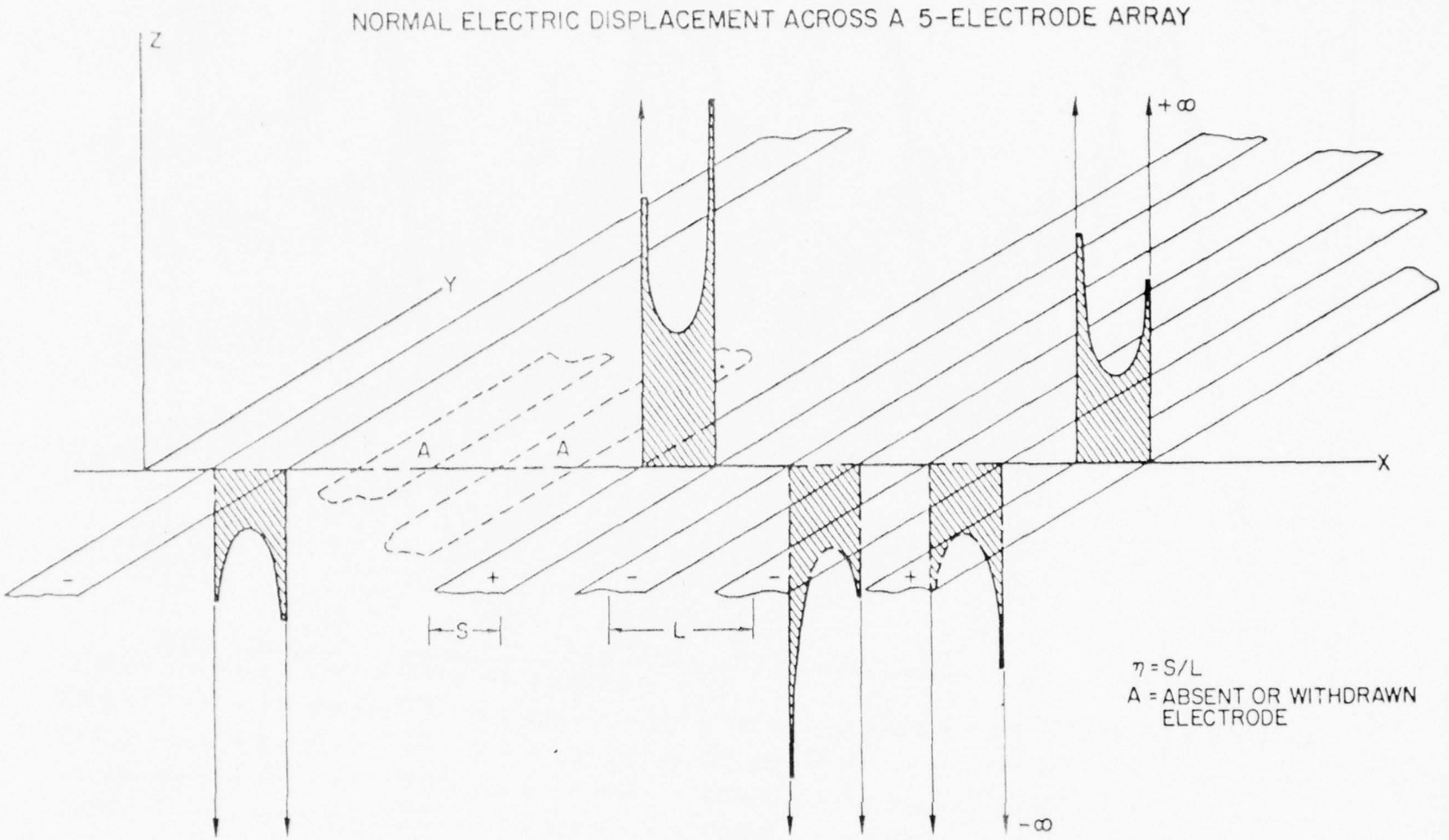
NORMAL ELECTRIC DISPLACEMENT ACROSS A 5-ELECTRODE ARRAY
Z
Y
X
+∞
-∞
A
A
S
L
η = S/L
A = ABSENT OR WITHDRAWN ELECTRODE

FIGURE VI. B. 1.

ACOUSTIC RESPONSE OF CENTRAL ELECTRODE PAIRS
IN TYPICAL ARRAY CONFIGURATIONS

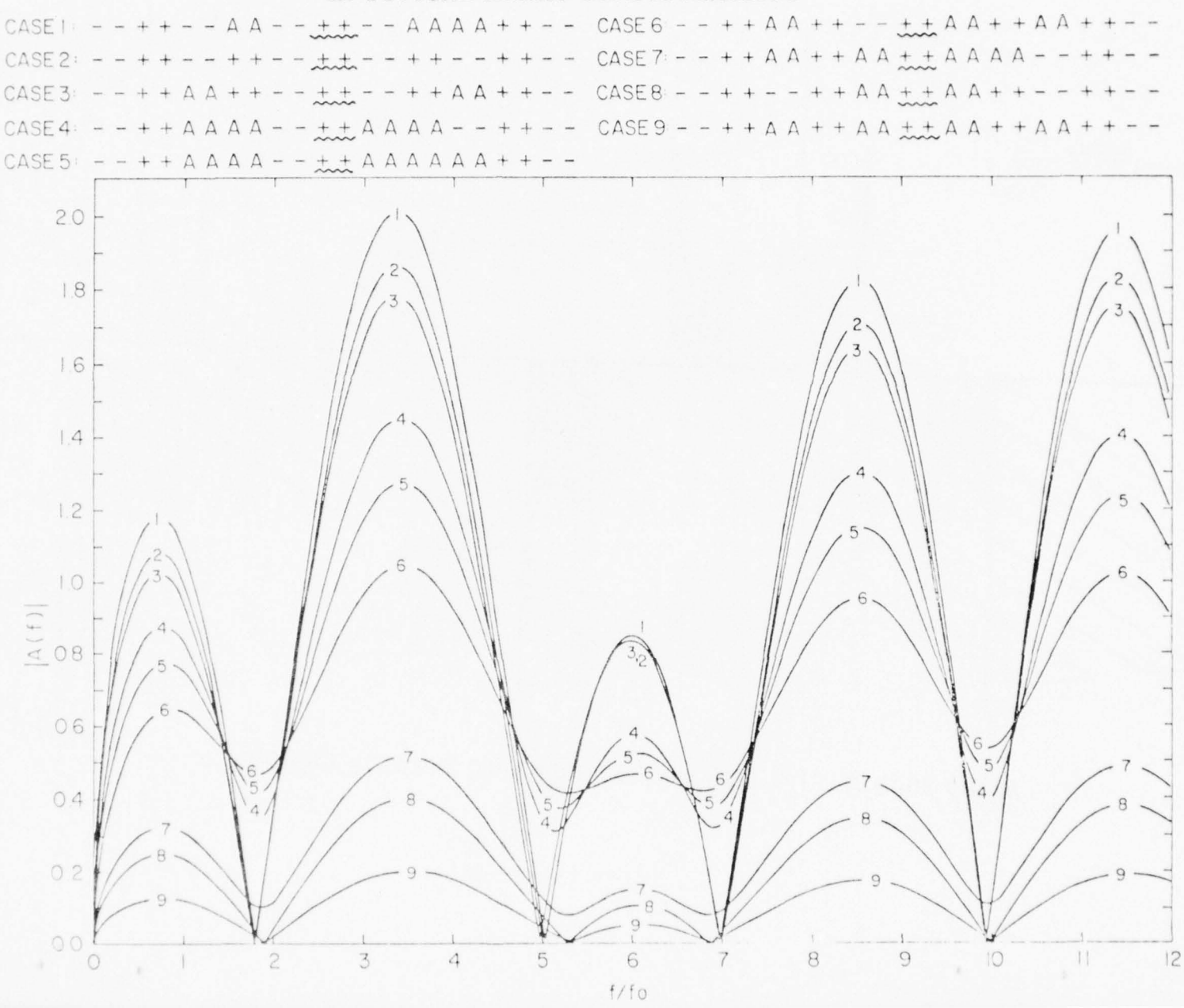

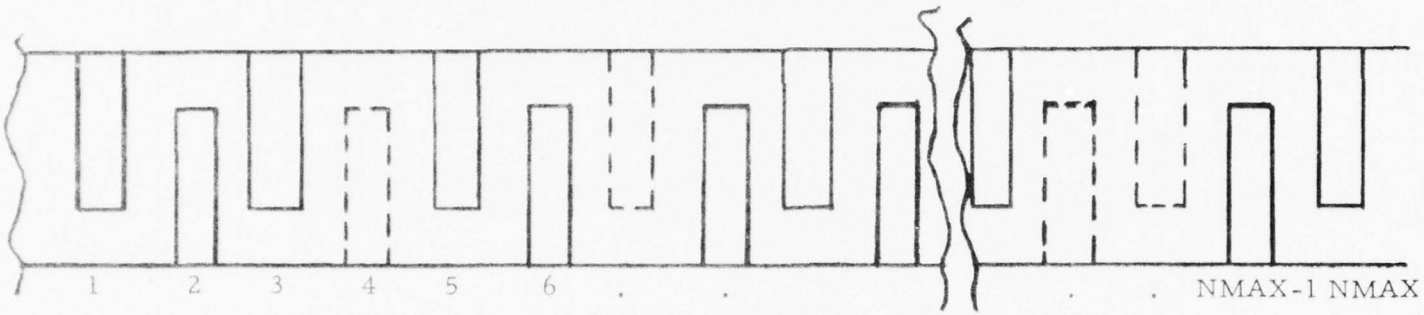

Figure VI. C. 1

CONFIGURATION OF ELECTRODES AND GAPS
IN A WWSAW FILTER

TABLE I

SINGLE ELECTRODE WITHDRAWL WEIGHTING DESIGN TABLE (f/fo=1)

$\hat{H}o(N)/do(N)$

	III	IIA	IAI	IAA	AII	AIA	AAI	AAA
III	1.000000 -0.000000	0.968079 -0.000553	1.069472 0.001710	1.028224 0.000962	0.664949 0.028914	0.608880 -0.034560	0.784819 -0.017883	0.672299 -0.027344
AII	0.968079 0.000553	0.935557 -0.000000	1.037086 0.002253	0.994639 0.001491	0.626377 -0.030408	0.569518 -0.036637	0.742766 -0.018888	0.627187 -0.029445
IAI	1.069472 -0.001710	1.037086 -0.002253	1.141412 -0.000000	1.100374 -0.000720	0.742484 -0.027464	0.685663 -0.032344	0.869783 -0.017226	0.758482 -0.025283
AAI	1.028224 -0.000962	0.994639 -0.001491	1.100374 0.000720	1.057410 -0.000000	0.691923 -0.028846	0.633393 -0.034328	0.816182 -0.018080	0.699999 -0.027213
IIA	0.664949 0.028914	0.626377 0.030408	0.742484 0.027464	0.691923 0.028846	0.260875 -0.000000	0.191575 -0.007799	0.387285 0.010746	0.246136 0.001045
AIA	0.608880 0.034560	0.569518 0.036637	0.685663 0.032344	0.633393 0.034328	0.191575 0.007799	0.120240 -0.000000	0.313857 0.017328	0.166698 0.008764
IAA	0.784819 0.017883	0.742766 0.018888	0.869783 0.017226	0.816182 0.018080	0.387285 -0.010746	0.313857 -0.017328	0.526970 -0.000000	0.381768 -0.009152
AAA	0.672299 0.027344	0.627187 0.029445	0.758482 0.025283	0.699999 0.027213	0.246136 -0.001045	0.166698 -0.008764	0.381768 0.009152	0.221665 -0.000000

I—→ DENOTES PRESENCE OF AN ELECTRODE

TABLE II

SINGLE ELECTRODE WITHDRAWL WEIGHTING DESIGN TABLE (f/fo=5)

$\hat{H}o(N)/do(N)$

	III	IIA	IAI	IAA	AII	AIA	AAI	AAA
III	1.000000 -0.000000	0.972857 -0.000782	1.060748 0.002459	1.025316 0.001376	0.648834 -0.043493	0.594991 -0.052109	0.767482 -0.026714	0.658492 0.040918
AII	0.972857 0.000782	0.945209 -0.000000	1.033166 0.003221	0.996717 0.002119	0.614652 -0.045527	0.559901 -0.055000	0.730054 -0.028089	0.617870 -0.043865
IAI	1.060748 -0.902459	1.033166 -0.003221	1.123730 -0.000000	1.088433 -0.001037	0.718142 -0.041619	0.663830 -0.049123	0.843770 -0.025905	0.736328 -0.038107
AAI	1.025316 -0.001376	0.996717 -0.002119	1.088433 0.001037	1.051492 -0.000000	0.673219 -0.043499	0.617193 -0.051885	0.795921 -0.027067	0.683668 -0.040822
IIA	0.648834 0.043493	0.614652 0.045527	0.718142 0.041619	0.673219 0.043499	0.242094 -0.000000	0.177161 -0.012241	0.363326 0.016646	0.229749 0.001645
AIA	0.594991 0.052109	0.559901 0.055000	0.663830 0.049123	0.617193 0.051885	0.177161 0.012241	0.110622 -0.000000	0.293876 0.026946	0.155092 0.013694
IAA	0.767482 0.026714	0.730054 0.028089	0.843770 0.025905	0.795921 0.027067	0.363326 -0.016646	0.293876 -0.026946	0.498544 -0.000000	0.359990 -0.014080
AAA	0.658492 0.040918	0.617870 0.043865	0.736328 0.038107	0.683668 0.040822	0.229749 -0.001645	0.155092 -0.013694	0.359990 0.014080	0.208077 -0.000000

I ⟶ DENOTES PRESENCE OF AN ELECTRODE

A⟶DENOTES ABSENCE OF AN ELECTRODE

TABLE III

DOUBLE ELECTRODE-PAIR REMOVAL WITHDRAWL WEIGHTING DESIGN TABLE (f/fo = 3)

$A_o(N)/d_o(N)$

	III	IIA	IAI	IAA	AII	AIA	AAI	AAA
III	1.000000 0.000000	0.979703 -0.000789	1.047271 0.002813	1.022995 0.001800	0.629275 -0.076038	0.588089 -0.087123	0.739393 -0.049585	0.650436 -0.069315
AII	0.979703 -0.000789	0.958980 -0.000000	1.026697 0.003587	1.001510 0.002549	0.602392 -0.080076	0.560459 -0.092228	0.709262 -0.052656	0.616987 -0.074746
IAI	1.047271 0.002813	1.026697 0.003587	1.096087 -0.000000	1.072165 -0.000966	0.685666 -0.071018	0.644215 -0.080675	0.802204 -0.046304	0.715627 -0.062996
AAI	1.022995 0.001800	1.001510 0.002549	1.072165 -0.000966	1.046829 -0.000000	0.653149 -0.074725	0.610205 -0.085469	0.767163 -0.048960	0.673899 -0.887855
IIA	0.629275 -0.076038	0.602392 -0.080076	0.685666 -0.071018	0.653149 -0.074725	0.205679 -0.000000	0.154504 -0.014177	0.320819 0.025739	0.208805 0.007352
AIA	0.588089 -0.087123	0.560459 -0.092223	0.644215 -0.080675	0.610205 -0.085469	0.154504 -0.014177	0.101954 -0.000000	0.265484 0.037958	0.148219 0.021209
IAA	0.739393 -0.049585	0.709262 -0.052658	0.802204 -0.046304	0.767163 -0.048960	0.320814 0.025739	0.265484 0.037958	0.449648 0.000000	0.334162 -0.017883
AAA	0.650436 -0.069315	0.616987 -0.074746	0.715627 -0.062996	0.675899 -0.067855	0.208885 0.007352	0.148219 0.021209	0.334152 -0.017683	0.204533 -0.000000

TABLE IV

DOUBLE ELECTRODE–PAIR REMOVAL WITHDRAWL WEIGHTING DESIGN TABLE (f/fo = 1)

$\hat{H}o(N)/do(N)$

	III	IIA	IAI	IAA	AII	AIA	AAI	AAA
III	1.000000 -0.000000	0.972709 0.002994	1.061345 0.010397	1.029078 0.006689	0.702293 -0.185827	0.666947 -0.195536	0.794015 -0.144964	0.714443 -0.178809
AII	0.932769 -0.002994	0.944948 -0.000000	1.033831 0.013353	1.000328 -0.009559	0.671711 -0.190714	0.636549 0.199611	0.758991 -0.151950	0.678152 -0.188260
IAI	1.061345 0.010397	1.033831 0.013353	1.124442 -0.000000	1.092749 -0.003563	0.769707 -0.178522	0.732763 -0.188763	0.869549 -0.136809	0.789813 -0.168319
AAI	1.029078 0.006689	1.000328 0.009559	1.092749 -0.003563	1.059156 -0.000000	0.731762 -0.183711	0.694045 -0.193625	0.828158 -0.143184	0.745235 -0.176205
IIA	0.702293 -0.185827	0.671711 -0.190714	0.769707 -0.178522	0.731762 -0.183711	0.235713 -0.000000	0.178186 -0.044948	0.364111 0.080218	0.236870 0.023594
AIA	0.666947 -0.195536	0.636549 -0.199611	0.732763 -0.188763	0.894045 -0.193625	0.178186 -0.044948	0.118008 -0.000000	0.304525 0.112485	0.169497 0.066494
IAA	0.794015 -0.144964	0.758991 -0.151950	0.869549 -0.136809	0.828158 -0.143184	0.364111 0.080218	0.304525 0.112485	0.499906 0.000000	0.374318 -0.056915
AAA	0.714443 0.178809	0.678152 0.186260	0.789813 0.168319	0.745235 0.176205	0.236870 0.023594	0.169497 0.066494	0.374318 -0.056915	0.229564 0.000000

I ⟶ DENOTES PRESENCE OF DOUBLE ELECTRODE PAIR

A ⟶ DENOTES ABSENCE OF DOUBLE ELECTRODE PAIR

VI. REFERENCES

1. Hartmann, C.A., "Weighting Interdigital Surface Wave Transducer by Selective Withdrawal of Electrodes," 1973 IEEE Ultrasonics Symposium, pp. 423-426, November 1973.

2. Hartmann, C.A., and Seacrest, B.G., "End Effects In Interdigital Surface Wave Transducer," 1972 IEEE Ultrasonics Symposium, pp. 413-416, October 1972.

3. Smith, W.R., and Pedler, W.F., "Fundamental- and Harmonic-Frequency Circuit-Model Analysis of Interdigital Transducer with Arbitrary Metallization Ratios and Polarity Sequences," IEEE Trans. on Microwave Theory and Techniques, Vol. MTT-23, No. 11, November 1975.

4. Hildebrand, F.B., Methods of Applied Mathematics, Prentice-Hall, New Jersey, pp. 451-458, 1952.

5. Thomson, J.J., Recent Researches In Electricity and Magnetism, Clarendon Press, Oxford, pp. 236-239, 1893.

VII. PROCESSING AND ANALYSIS OF THE CALIBRATION CURVES OF PHOTO-DEVICE OUTPUT VS. ATMOSPHERIC PRESSURE

A. Introduction

A direct measurement of pressure is difficult to make in the upper atmosphere. An alternative method is to transmit a light beam through the atmosphere and measure the intensity of the radiated light (fluorescent light) from the atmosphere. In this report, we consider the problem of atmospheric density determination of means of fluorescent radiation.

The report is divided into two segments. In the first segment, we discuss some background information. In the second segment, we discuss a program (program DENS) that processes calibration curves of photo-device output vs. pressure.

B. Background

In this section, we consider some background information necessary to understanding program DENS. The atmospheric density determination by means of fluorescent radiation shall be considered first, then photo-devices used to measure fluorescent radiation, and then the calibration curves obtained from these photo-devices. Finally, the linear regression statistics obtained from the calibration curves shall be discussed.

B.1 Density Determination by means of Fluorescent Radiation

When a beam of light is transmitted through the atmosphere at the proper frequency, the light beam excites the atmospheric molecules. The molecules eventually de-excite, radiating light. The intensity of this radiated light (fluorescent light) is proportional to

1. the atmospheric density
2. the light beam intensity.

If the coefficient of proportionality were known, it would be possible to determine the atmospheric density by measuring the radiated light intensity. This coefficient of proportionality must be determined by calibrating the light intensity vs. the atmospheric density under laboratory conditions.

The radiated light intensity is measured by means of certain photo-devices.

B.2 Photo-devices

The radiated light intensity is measured by two kinds of photo-devices:

1. photocounters
2. photometers

B.2.1 Photocounters

The input photocount rate of this device is proportional to the radiated light intensity. However, it is the output photocount rate that is measured, rather then the input count rate.

The count rate R coming out of a counter is not the same as the count rate R' entering the counter. Because the counter is incapable of resolving two counts that occur within a time interval τ (dead time, resolution time).

Assuming the counts have a Poisson distribution in time, it can be shown that the output counting rate R is related to the input counting rate R' as follows:

$$R' = R/(1.0 - R_1 \tau) \tag{1}$$

The threshold counting rate R_1 is the lowest observed output counting rate that is not considered to be noise.

As was noted above, the radiated light-intensity is proportional to the light beam intensity. The light beam intensity is in turn proportional to the beam current. We therefore normalize the input count rate R' by dividing by the beam current I. The normalized input count rate R^* (reduced count rate) is thus obtained:

$$R^* = R'/I \tag{2}$$

Corresponding to the threshold output count rate R_1, there is a threshold pressure p_1. The threshold pressure p_1 is the pressure that produces the threshold output count rate R_1. The reduced pressure P^* is the difference between the actual pressure p and the threshold pressure p_1:

$$P^* = p - p_1 \quad . \tag{3}$$

The reduced count rate R^* is linearly related to the reduced pressure p^*

$$R^* \sim p^* \quad . \tag{4}$$

B.2.2 Photometers

Photometer output is proportional to the radiated light intensity.

The threshold beam current I_1 is the smallest beam current that is not considered to be noise. The threshold photometer output R_1 is the photome output produced by the light beam at threshold current I_1. The threshold pressure P_1 is the observed pressure, when the beam current is at thresho

The photometer output R is proportional to the pressure p:

$$R \sim p \quad . \tag{5}$$

Since the threshold photometer output R_1 corresponds to the threshold pres p_1, the subtracted photometer output $(R - R_1)$ is proportional to the reduced pressure $p - p_1$:

$$R - R_1 \sim p - p_1 \quad . \tag{6}$$

As was noted above, the radiated light intensity is proportional to the light beam intensity. The light beam intensity is, in turn, proportional to beam current. We, therefore, normalize the subtracted photometer outpu $R - R_1$ by dividing by the beam current, thus obtaining the reduced photome output R^*:

$$R^* = (R - R_1)/I \quad . \tag{7}$$

The reduced photometer output is proportional to the reduced pressure:

$$R^* \sim p^* \quad . \tag{8}$$

B.3 Calibration Curves

B.3.1 Calibration Curve Recording

The generation of the calibration curve for a photo-device consists in varying the atmospheric pressure and observing the corresponding output of the photo-device. The change in pressure may also be accompanied by a change in beam current. For this reason, the beam current is divided out.

In making the calibration curves for both photocounter and photometer output vs. pressure, two light beams were employed. When one is on, the other is off. A calibration curve is made for:

1. each photocounter and each beam
2. each photometer and each beam

The information relating to each calibration curve is stored on tape in a packed format.

The raw calibration curves contain a certain amount of jitter due to noise. The jitter may be reduced by a filtering (smoothing) process. This smoothing process shall be discussed in the next section.

B.3.2 Calibration Curves Smoothing

The smoothing of the calibration curves is a kind of averaging process. In particular, the smoothing of a calibration curve consists of the following steps:

Having considered the reduction of smoothed physical data, the

1. partitioning the pressure points into groups of contiguous points,
2. averaging the pressures in each group of the partition, thus forming a smoothed pressure sequence,
3. averaging the photo-device output in each of the corresponding groups, thus forming a corresponding smoothed photo-device output sequence.

The smoothed calibration curve consist of the smoothed photo-device output sequence vs. the smoothed pressure sequence.

B.3.3 Calibration Curve Reduction

Corresponding to each smoothed calibration curve there is a reduced smoothed calibration curve. This reduced curve consists of reduced photo-device output vs. reduced pressure.

The reduced smoothed pressure $\overline{p}_j^*$ is the difference between smoothed pressure $\overline{p}_j$ and the smoothed threshold pressure $\overline{p}_1$:

$$\overline{p}_j^* = \overline{p}_j - \overline{p}_1 \quad . \tag{9}$$

In the case of the photocounters, we obtain the reduced smoothed photo-counts as follows: The smoothed input counting rate $\overline{R}_j$ is related to the smoothed output counting rate $\overline{R}_j$:

$$\overline{R}_j' = \overline{R}_j/(1 - \overline{R}, \tau) \quad . \tag{10}$$

The smoothed threshold counting rate $\overline{R}_1$ is the lowest observed smoothed output counting rate. The reduced smoothed counting rate $\overline{R}_j^*$ is obtained by dividing the smoothed input counting rate $\overline{R}_j'$ by the smoothed current $\overline{I}_j$:

$$\overline{R}_j^* = \overline{R}_j'/\overline{I}_j \quad . \tag{11}$$

The reduced smoothed photocounts are linearly related to the reduced smoothed pressure:

$$\overline{R}^* \sim \overline{P}^* \quad . \tag{12}$$

In the case of photometers we proceed as follows:

The reduced smoothed photometer output $\overline{R}_j^*$ is given by:

$$\overline{R}_j^* = (\overline{R}_j - \overline{R}_1)/\overline{I} \quad , \tag{13}$$

where $\overline{R}_j^*$ is the smoothed threshold photometer output. The reduced smoothed photometer output is linearly related to the reduced smoothed pressure:

$$\overline{R}_j^* \sim \overline{P}_j^* \quad . \tag{14}$$

Having considered the reduced smoothed calibration curves, we shall next consider the linear regression statistics obtained from these reduced calibration curves.

B.4 Linear Regression Statistics[1]

As has been mentioned previously, the calibration curves are expected to be linear. Due to uncertainties of one sort or another, the calibration points do not fall exactly on a line. Rather, they exhibit a fluctuation about some line. We wish to determine the best line (regression line) that fits the calibration points. We also wish to know just how good a fit to the data this line is. In some cases, the calibration points indicate an independence between a photo-device output and the pressure. We wish to try to get a measure of that independence. The above questions are answered by the linear regression statistics.

This section is divided into three parts. In the first part, the regression estimators are determined. In the second part, the distribution of the regression estimators is considered. In the last part, the problem of independence between photo-device output and pressure is considered.

B.4.1 Linear Regression Estimators

We assume that the calibration points are normally distributed about some line (linear regression line). More precisely, the probability f(y) of the photo-device output being y at pressure x is

$$f(y) = \frac{1}{\sqrt{2\pi}\ \sigma'} \exp\left[\frac{1}{2(\sigma')^2}\left(y - (b'_o + b'x)\right)\right]^2 \qquad (15)$$

Using the method of maximum likelyhood the parameters $\left((\sigma')^2,\ b'_o, b'\right)$ in the above (15) normal distribution can be estimated. The estimator b (linear regression coefficient) to the parameter b' is given by:

$$b = r\,\sigma_y/\sigma_x \quad , \qquad (16)$$

where σ_y and σ_x are the standard deviations in y and x, respectively, as defined below.

The coefficient of correlation r between the photo-device output y and pressure x is given by:

$$r = \sum_{i=1}^{N} \left(x_i - \bar{x}\right)\left(y_i - \bar{y}\right)/\sigma_x\,\sigma_y \quad . \qquad (17)$$

The pair (x_i, y_i) is a calibration point.

The total number of observation points is N.

The average pressure $\bar{x}$ is defined as:

$$\bar{x} = \frac{1}{N}\sum_{i=1}^{N} x_i \quad . \qquad (18)$$

The averaged photo-device output $\bar{y}$ is defined as:

$$\bar{y} = \frac{1}{N}\sum_{i=1}^{N} y_i \quad . \qquad (19)$$

The standard deviation σ_x (fluctuation) in pressure is defined as:

$$\sigma_x^2 = \frac{1}{N} \sum_{i=1}^{N} (x_i - \bar{x})^2 \quad . \tag{20}$$

The standard deviation σ_y (fluctuation) in photo-device output is similarly defined.

The coefficient of correlation r must lie between -1 and +1 :

$$-1 \leq r \leq +1 \quad . \tag{21}$$

The estimator b_o (linear regression intercept) to the parameter b_o' in (15) is given by:

$$b_o = \bar{y} - b\bar{x} \quad . \tag{22}$$

The estimator σ^2 (sum of squares of deviation from regression SSDR) to the parameter $(\sigma')^2$ is given by:

$$\sigma^2 = \frac{1}{N} \sum_{i=1}^{N} \left(y_i - (b x_i + b_o) \right)^2 \quad . \tag{23}$$

The sum of the squares of deviation from regression (SSDR) is a measure of how good the linear regression line is. The smaller σ^2 is the better the regression line fits the data. The regression estimators b and b_o are values that minimize SSDR (σ^2).

A normalized measure of how well the regression line fits the data is the standard error of estimate SE:

$$(SE)^2 = \sigma^2/(N-2) \quad .$$

Having introduced certain linear regression estimators, we shall next consider the distribution of these estimators.

B.4.2 Distribution of Regression Estimators

The photo-device output y_i evaluated at the pressure x_i is normally distributed. Because SSDR is a quadratic in the variables y_i and each y_i is normally distributed, the SSDR must have a chi-square distribution. If the variables y_i were independently distributed, then SSDR would be a quadratic in N independent variables y_i, i = 1, N. Therefore, SSDR would have a chi-square distribution with N degrees of freedom. However, the y_i, i = 1, N are not independently distributed. The y_i are subjected to the constraints of two equations (16, 22). Therefore, SSDR has a chi-square distribution with N-2 degrees of freedom.

A linear combination of variables that are normally distributed is also normally distributed. Since the regression estimators b and b_o are both linear functions of the variables y_i, the regression estimators are also each normally distributed.

We shall next discuss how a distribution for the estimator b may be constructed.

The evaluation of the formula (16) may be considered a sample from the normal population for the estimator b. To evaluate this formula (16), we must do an experiment to obtain a set of calibration points. If the experiment were repeated, a slightly different set of calibration points would be obtained. Hence, a slightly different value for the estimator would be obtained. If the experiment is repeated a large number of times, a distribution for the estimator b may be constructed.

The estimator to the regression coefficient (slope b) has a normal distribution characterized by a mean μ_b and a standard deviation σ_b. It can be shown that the standard deviation is equal to the ratio between the standard error of estimate SE and the standard deviation in pressure x:

$$\sigma_b = SE/\sigma_x \quad . \tag{25}$$

From the above (25), it is seen that the better the calibration points approximate a line (the smaller SE is), the less fluctuation there is in the slope b (the smaller σ_b is).

B.4.3 *Measure of Dependence*

The question of whether photo-device output is independent of pressure may be phrased in terms of hypothesis testing. We may think that the coefficient of correlation r gives a good measure of dependence between x and y. However, the correlation r can be near one but the regression coefficient b may be close to zero. If the slope b is small, then a change in x has very little effect on the dependent variable y. If the slope b is small, we would say that the dependence of y on x is weak, in spite of the fact that the correlation r is near one. Although the slope b gives some measure of the dependence of y on x, the question remains just how small must the slope b be in order to consider y to be independent of x. The question of whether y is independent of x may be phrased in terms of hypothesis testing.

The hypothesis that y is independent of x is equivalent to the hypothesis that the mean μ_b of the distribution for the slope b is zero. The question arises as to how far from zero must the sample of the slope b be before the hypothesis is rejected. A sample of the slope b is gotten by evaluating (16) for a particular experiment (set of calibration points).

The range of the slope b will be divided into two regions:

1. the acceptance region
2. the rejection region (critical region)

If the value of the slope b given in expression (16) is in the acceptance region, the hypothesis will be accepted whereas, if b is in the rejection region, the hypothesis will be rejected.

The critical region is the region under the two tails of the distribution f(b) for b such that the total area of the tails is a prescribed number ε :

$$\int_{-\infty}^{+\infty} dbf(b) + \int_{\varepsilon}^{\infty} dbf(b) = \varepsilon \quad . \tag{26}$$

The region $[-\infty, -c] \cup [c, +\infty]$ is the critical region at the ε level. If the value of the regression coefficient is in the critical region, then the hypothesis that $\mu_b = 0$ is rejected. The probability of rejecting the hypothesis when it is in fact true is the significance level ε .

The distribution f(b) involves two parameters, the mean μ_b and the standard deviation σ_b. Therefore, the critical region for the mean μ_b will involve the standard deviation σ_b. Since σ_b is not a-priori known, it is better to formulate the critical region for μ_b in terms of a distribution that involves only the one parameter μ_b. Such a distribution is found in the student t distribution.

If the variable u has a normal distribution with a mean of zero, and the quantity v has a chi-square distribution with k degrees of freedom, then the quantity t:

$$t = u/\sqrt{v/k} \tag{27}$$

has the student t distribution with k degrees of freedom.

The estimator σ_b^2 has a chi-square distribution with N-2 degrees of freedom. The estimator b has a normal distribution. Hence, b-b' has a normal distribution with mean of zero. Therefore:

$$t = (b - b')/\sqrt{\sigma_b^2/(N-2)} \tag{28}$$

has a student t distribution with N-2 degrees of freedom.

In terms of the foregoing (26), we may define a critical region in terms of the variable t. The cumulative t-distribution of various degrees of freedom is tabulated. From such a table, it is a simple matter to determine the critical region at a specified level of significance ϵ. In order to see whether to accept or reject the hypothesis that $\mu_b = 0$, one simply evaluates t in the above (28) with $\mu_b = 0$. If t is in the acceptance region, the hypothesis is accepted. If t is in the rejection (critical) region, the hypothesis is rejected.

In the foregoing, we have discussed the hypothesis testing of the parameter μ_b (the mean of the estimator b). Sometimes, it is desirable to test the hypothesis of the vanishing of both the parameter μ_b and the parameter μ_{bo} (the mean of the estimator b_o). A critical region for such a hypothesis is conveniently defined in terms of the F-distribution.

If the variable u has a chi-square distribution with m degrees of free
dom and the variable v has a chi-square distribution with n degrees of fr
dom, then the ratio F :

$$F = \frac{u/m}{v/n}$$

has an F-distribution p(F) with (m, n) degrees of freedom.

The quadratic form Q :

$$Q = \sum_{i,j=1}^{2} Q_{ij} u_i u_j , \quad u_1 = b_o, \quad u_2 = b_1$$

has a chi-square distribution with two degrees of freedom. The matrix Q
of the quadratic form Q is the inverse of the covariance matrix C_{ij} genera
by b_o and b_1 :

$$c_{11} = < \left(b_o - \mu_{bo}\right)^2 > ,$$

$$c_{12} = c_{21} = < \left(b_o - \mu_{bo}\right)\left(b - \mu_b\right) > ,$$

$$c_{22} = < \left(b - \mu_b\right)^2 > \quad .$$

The SSDR σ^2 has a chi-square distribution with N-2 degrees of freed
Therefore, the F-ratio:

$$F = Q/\sigma^2$$

has an F-distribution with (2, n-2) degrees of freedom.

We may define a critical region in terms of the variable F. The cum
tive F-distribution of various degrees of freedom is tabulated. From suc
table it is a simple matter to determine the critical region at a specified
level of significance ϵ. In order to determine whether to accept or rejec
hypothesis that $\mu_b = 0$ and $\mu_{bo} = 0$, one simply evaluates F in the above (32)
with $\mu_b = 0$ and $\mu_{bo} = 0$. If F is in the acceptance region, the hypothesis is
accepted. If F is in the rejection (critical) region, the hypothesis is reje

In the foregoing, we have considered the analysis of calibration curves of photo-device output vs. pressure. In the next section, a program (program DENS) that incorporates the above analysis shall be considered.

C. Program System DENS

The purpose of program system DENS is to process a tape containing data relating to calibration curves of photocounters and photometer output vs. pressure.

The program system is divided into the following segments:

1. reading the tape
2. unpacking of data
3. construction of physical quantities from unpacked data
4. smoothing of the physical data
5. suppression of bad physical data
6. reordering of physical data in accordance with increasing pressure
7. reduction of physical data
8. computation of linear regression statistics
9. ploting of calibration points and linear regression line of a photo-device on same graph

The above segments of program system DENS will be discussed in succession.

C.1 Reading of Tape

The data has been recorded on tape in the form of several files, each file contains a number of records. Each file ends with an end of file mark. There is a double end of file mark at the end of the last file.

The data on the tape is in CDC binary form. Five packed words have been packed into each CDC word. The tape has been generated by a Honeywell H-316 Data Acquisition System[3]. The generated tape is not a standard SCOPE tape. It, therefore, must be treated as a stranger tape on the CDC computer.

A record is buffered in. A test for end of file is then made. When an end of file is reached, the next file is accessed. The total number of files is given.

Having considered the reading of the tape, the unpacking of data shall be considered next.

C.2 Unpacking of Data

The data has been recorded on tape in packed format. When a record from a tape is buffered in, we are faced with the task of unpacking the record[2]. Five packed words are packed into each CDC word. Each packed word consists of 12 bits, including a sign bit. The sign bit is the left most bit of the packed word. The unpacking of a record is accomplished through shifting and masking operations. This unpacking is accomplished in subroutine UNPACK[2].

As has been stated previously, a file consists of a number of frames. A frame consists of the packed words corresponding to one pressure point. These packed words in a frame specify:

1. the pressure
2. both beam currents
3. the photo-device outputs for each beam at the given pressure and beam current.

The unpacked data for the first frame of the first file is printed out. This is done in subroutine PRINTR.

Having discussed the unpacking of data, we shall next consider the construction of physical quantities from the unpacked data.

C.3 Construction of Physical Quantities from Unpacked Data

The unpacked words in a frame do not directly represent the values of physical quantities. We are given a prescription or mapping of how to obtain the physical quantities from the unpacked words in a frame. This mapping of unpacked frame words into physical quantities consists of two steps:

1. specification of what physical quantity corresponds to what word of the frame,
2. operating on the frame word to obtain the corresponding physical quantity.

The words in a frame are stored in the array AW(I).

The physical quantities that must be constructed from a frame are:

1. pressure PP
2. current of both beams BBI(J,K)
3. outputs of all photocounters PPC(J,K)
4. Outputs of all photometers PPM(J,K).

The specification of the correspondence between frame words and physical quantities is done in terms of word key arrays. For example, the word key array JKWPC(J,K) (JKWPM(J,K)) is the word number that corresponds to the J'th photocounter (photometer) of beam K. These word key arrays are printed out.

How the frame word is operated on to obtain the physical quantity depends on the physical quantity in question. In the case of photometers, the operation is specified as follows:

```
CONV      = 5.0/2047
AWW(I)    = CONV * AW(I)
JK        = JKPM(J,K)
PPM(J,K)  = 10.0 **(0.8*AWW(JK) - 9.0)
```

Having discussed the construction of the physical quantities, we shall next consider the smoothing of the physical data.

C.4 Smoothing of Physical Data

Once the physical quantities have been constructed for a frame, we then wish to average these physical quantities over all the frames in a file. Let Q_{ij} be a certain physical quantity from the i'th frame of the j'th file. The smoothed (running average) physical quantity $\overline{Q}_j$ over the j'th file is defined as:

$$\overline{Q}_j = \frac{1}{N_j} \sum_{i=1}^{N_j} Q_{ij}$$

The number of frames in the j'th file is N_j. In the event that the physical quantity Q_{ij} is a photocount, then the smoothed photocount over the j'th file is defined as the sum of the photocounts over all frames rather than a running average.

It is impossible to hold the physical data from all frames in a file in the computer at once. Therefore, only the sums of the physical quantities over the frames in a file up to the frame currently being processed are stored in the computer. These sums are:

P(J,K) - pressure

BI(J,K) - beam current

PC(J,K) - photocount

PM(J,K) - photometer output

After a file has been processed, all the above sums except the photocounts are divided by the number of frames in the file. The resulting smoothed physical data for the I'th file are stored in the following arrays:

AP(I,K) - pressure

ABI(I,J,K) - beam current

APC(I,J,K) - photocount

APM(I,J,K) - photometer output

These smoothed arrays are printed out.

C.5 Suppression of Bad Physical Data and Reordering

If the smoothed beam current ABI(I, 1, 1) of the first beam of the I'th file is too low (less than CURTHR), then the corresponding outputs APC(I, J, K) of the photocounters and the outputs APM(I, J, K) of the photometers are to be rejected. This rejection is accomplished by reindexing the file index I of the smoothed arrays so that the rejected elements do not appear. The smoothed arrays are then reindexed (reordered) a second time in accordance to increasing pressure. The smoothed arrays are printed out after suppression and reordering.

C.6 Reduction of Smoothed Physical Data

The photo-device output depends not only on pressure but on beam current as well. We are only interested on the dependence of photo-device output on pressure. The reduction process consists in operating on the data to make it independent of beam current. The reduction process is essentially achieved by dividing the smoothed photo-device output for a file by the corresponding smoothed beam current. A more detailed description of the reduction process has already been given (section B.3.3).

The reduction of smoothed physical data is done in subroutine REDUCE. Subroutine REDUCE generates from the smoothed arrays the following corresponding reduced arrays:

ARP(I, J, K) - pressure

ARBI(I, J, K) - current

ARPC(I, J, K) - photocounter

ARPM(I, J, K) - photometer

The reduced arrays are printed out.

Having considered the reduction of smoothed physical data, the linear regression statistics based upon this reduced data are considered next.

C.7 Linear Regression Statistics

The linear regression statistics are computed based on the reduced physical data. The linear regression statistics consist of the following items for each photo-device:

1. the average
2. the standard deviation
3. the correlation
4. the regression coefficient
5. the regression intercept
6. sum of the squares of deviation from regression SSDR
7. the standard error of estimate
8. the standard deviation in the regression coefficient
9. the F-value
10. the t-value

The t-value is useful in determining whether or not pressure and photo-device output are independent (see section B.4.3). The F-value is useful in testing the hypothesis that both the regression coefficient and the regression intercept vanish.

The linear regression statistics are computed in the subroutine STAT. Subroutine STAT generates the following statistics arrays:

ASTATC(L, J, K)

ASTATM(L, J, K)

The array element ASTATC(L, J, K) is the L'th linear regression statistic for the J'th photocounter of beam K. The array ASTATM(L, J, K) is the L'th linear regression statistic for the J'th photometer of beam K.

These statistics were generated with the aid of the following IBM subroutines:

1. subroutine CORRE - (primarily generates correlation matrices)
2. subroutine MULTR - (uses information generated by CORRE to generate regression statistics)

The statistics arrays ASTATC and ASTATM are printed out.

REFERENCES

1. Mood, A., "Introduction to the Theory of Statistics," McGraw Hill Book Company, New York, 1950.

2. Subroutine (RD316-FM) Honeywell H-316-FM Unpack, AFCRL Analysis and Simulation Branch Account No. 4508/13, Project No. 6688-06-01, 17 February, 1974.

VIII. REFLECTION FROM AN IDEALIZED ATMOSPHERIC WAVE

A. Introduction

Program PPATH simulates radar echo reflections from traveling ionospheric acoustic-gravity waves. Quantities calculated as functions of time include reflection point locus, path length, doppler-shift and receiver ray azimuth.

The reflection point equations

$$F_1(\bar{x}, \bar{y}) = 0$$

$$F_2(\bar{x}, \bar{y}) = 0$$

have been derived in earlier work, where it was noted that the Newton-Raphson Method either may fail to converge or may converge in a limited region[1]. These difficulties may be overcome via Branin's algorithm[2].

B. Branin's Algorithm

Branin's algorithm for solving a system of nonlinear equations

$$\vec{F}(\vec{r}) = 0$$

where $\vec{r} = (x, y)$

and $\vec{F} = \left(F_1(r), F_2(r)\right)$

is a modification of Newton's method wherein a vanishing of the Jacobian determinant or an arrival at a solution point does not limit the region of convergence. This latter feature enables the determination of multiple solutions one after the other.

Newton's method is based on the recursion relation

$$\vec{r}_{j+1} = \vec{r}_j - h_j J^{-1}(\vec{r}_j) \cdot \vec{F}(\vec{r}_j) \quad ,$$

where h_j is a step size which may be varied from unity,

J^{-1} is the Jacobian inverse matrix

$$J^{-1} = \text{adj } J/\det J \quad ,$$

J is the Jacobian matrix

$$J = \begin{bmatrix} \partial_x F_1 & \partial_y F_1 \\ \partial_x F_2 & \partial_y F_2 \end{bmatrix} \quad ,$$

adj J is the Jacobian adjoint matrix

$$\text{adj } J = \begin{bmatrix} \partial_y F_2 & -\partial_y F_1 \\ -\partial_x F_2 & \partial_x F_1 \end{bmatrix} \quad ,$$

and det J is the Jacobian determinant

$$\det J = \left(\partial_x F_1\right)\left(\partial_y F_2\right) - \left(\partial_x F_2\right)\left(\partial_y F_1\right) \quad .$$

There are two difficulties with Newton's method: (1) the algorithm fails to proceed at an impasse where J becomes singular such that det $J = 0$ and (2) the region of convergence is limited by the initial guess $\vec{r}_o$. Consequently, multiple solutions cannot be found unless some extraneous technique such as a time-consuming winding-number calculation is invoked in order to obtain a set of $\vec{r}_o$'s with non-intersecting regions of convergence.

Branin's algorithm, which was designed to overcome both of these difficulties, is based on the recursion relation

$$\vec{r}_{j+1} = \vec{r}_j \mp h_j \frac{(\text{adj } J)\cdot\vec{F}}{\det J} \quad ,$$

where $\mp$ indicates that the sign of the predicator step vector $J^{-1}\cdot\vec{F}$ is to be altered whenever a sign change occurs in det J.

Suppose that the minus were initially chosen. The locus of points $\{\vec{r}_0, \vec{r}_1, \ldots, \vec{r}_j\}$ would then describe some trajectory in the x, y -plane. Because of the finite predicotr step size $J^{-1} \cdot \vec{F}$, this trajectory could change from a condition det $J > 0$ to det $J < 0$ without actually going through det $J = 0$ at a singularity in J. Thus, the predicted point may fall backwards along the trajectory. Subsequent iterations of the recursion relation would merely produce alternating reversals in the trajectory. Nevertheless, it would be possible to proceed through this impasse if the sign of the predictor step were altered. The implementation of this sign change is combined with additional computational techniques in Branin's algorithm as follows.

B.1. Step-size Normalization

Since $J^{-1} \cdot \vec{F}$ may vary widely in magnitude, it is normalized such that

$$\vec{r}_{j+1} = \vec{r}_j + h_j \frac{(\text{adj } J) \cdot \vec{F}}{(\text{adj } J) \cdot \vec{F}}$$

where the Euclidean norm

$$\| (\text{adj } J) \cdot \vec{F} \| = [\vec{F}^t \cdot (\text{adj } J)^t (\text{adj } J) \cdot \vec{F}]^{1/2} .$$

The superscript t denotes the matrix transpose operation. The resulting reduced step size enables better control of the computations such that roots are not accidentally missed. Also the sign of det J is of no practical consequence since det J does not appear explicitly.

B.2. Corrector-step "steering"

A second means of not missing a root values the application of a corrector step which "steers" the trajectory towards this root. Let

$$k = \left(\vec{F}^t(\vec{r}_{j+1}) \cdot \vec{F}(\vec{r}_0)\right) / \left(\vec{F}^t(\vec{r}_0) \cdot \vec{F}(\vec{r}_0)\right)$$

represent the component of $\vec{F}(\vec{r}_{j+1})$ orthogonal to $F(\vec{r}_o)$. Then

$$\delta\vec{r} = J^{-1} \cdot \vec{v}$$

represents a first order annihilation of $\vec{v}$ via Newton's method. By analogy with the theory of differential equations, the image vector $\vec{F}(\vec{r}_{j+1})$ should be made to lie parallel to the initial image vector $\vec{F}(\vec{r}_o)$. Therefore, the point $\vec{v}_{j+1}$ is steered towards the "true" trajectory on which

$$\vec{r}'_{j+1} = \gamma_{j+1} + \delta_{\vec{r}}$$

B.3. Recovery from Divergence of the Algorithm

Near some singular regions the foregoing corrector step may oversteer the predictor vector such that the trajectory may reverse itself. In these cases, it is advisable either to suppress the corrector step temporarily or to select another $\vec{r}_o$ and begin anew in the hope that the singular region thereby would be avoided.

B.4. Detection of Roots

A trajectory reversal also occurs at a root where $\vec{F}(\vec{r}_{j+1}) \simeq 0$. This event may be distinguished from a reversal associated with det $J = 0$ as follows. The trajectory is temporarily halted and a test for convergence is made via the unmodified Newton's method. If this calculation were to have converged, then the root would be recorded, the sign of (adj J)$\cdot \vec{F}$ would be altered and the trajectory would be allowed to proceed towards the next root. On the other hand, if convergence were not possible, then the trajectory would be halted. The user may begin anew with a different $\vec{r}_o$.

B.5. Termination of the Algorithm

The algorithm is terminated after an arbitrary number of iterations have elapsed without the detection of a new root.

REFERENCES

1. Woolf, S., O'Brien, J.V., Cohen, E., Hsiung, J., Tichovolsky, E.J., Development of Mathematical Models and Statistical Analysis Techniques as Applied to the Digital Processing of Signals and the Description of Other Physical Systems. ARCON Corporation, Scientific Report No. 1, AFCRL Contract No.

2. Branin, F.H. Jr. (1972) "Widely Convergent Method for Finding Multiple Solutions of Simultaneous Nonlinear Equations", IBM J. Res. Develop., 504-522.

IX. SPEECH PROCESSING

A. Introduction

A.1 Summary of Work Performed

This report describes work done for the Speech Research Laboratory (DCWL) of the Electronic Systems Division, U.S. Air Force Systems Command. Two primary tasks were to be performed:

(a) Production of a realtime computer program (TRIVOC) for speech bandwidth compression; this program was to run in a new minicomputer, the Digital Voice Terminal (DVT), being developed concurrently by Lincoln Laboratory of Massachusetts Institute of Technology.

(b) Production of a DVT monitoring program (DVTMON), to run in a PDP-11 computer, that would load programs into the DVT and possibly provide other services as well.

Both of these tasks were completed during the contract period. DVTMON became a working tool for the development of TRIVOC and thus received extensive checkout. It works as advertised (Sec. F). TRIVOC, in tests conducted at the Defense Communications Engineering Center in Reston, Virginia, was successfully demonstrated to provide voice communication between two DVT's connected by voice-grade lines as much as 8,000 miles in length.

In order to perform the primary tasks, it was necessary to write several ancillary programs and to expand the capabilities of DVTMON:

(a) An assembler (Sec. G) for DVT code was constructed by making use of the "macro" feature of a standard PDP-11 assembler.

AD-A040 378 ARCON CORP WAKEFIELD MASS F/G 12/1
INTERACTIVE MATH MODELING.(U)
FEB 77 S WOOLF, J V O'BRIEN, E COHEN, D BAKER F19628-74-C-0049
UNCLASSIFIED RADC-TR-77-86 NL

3 OF 3
AD
A040 378

END
DATE FILMED
6-77

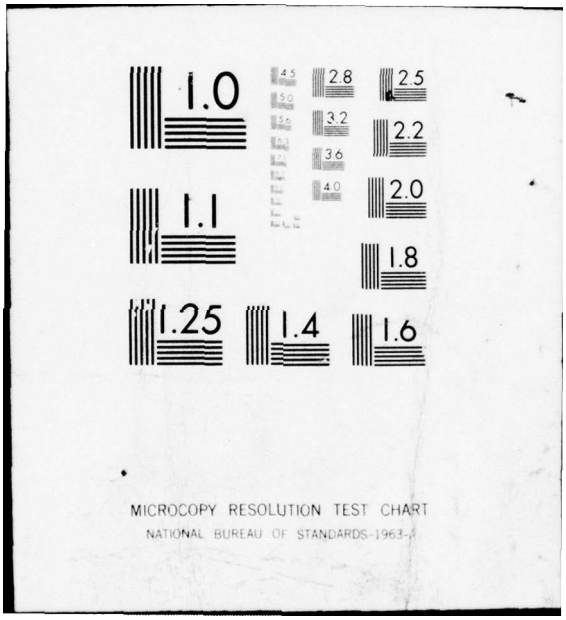
1.0
1.1
1.25
1.4
1.6
1.8
2.0
2.2
2.5
2.8
3.2
3.6
4.0
4.5
5.0
5.6
MICROCOPY RESOLUTION TEST CHART
NATIONAL BUREAU OF STANDARDS-1963-A

(b) A set of DVT programs was written to test I/O between the DVT and the PDP-11, and to dump the DVT data memory to the PDP-11 for subsequent printout.

(c) Several test modes were added to TRIVOC to enable the program to run without using the full complement of peripheral hardware. Two of these are simulation modes in which the PDP-11 plays the role of the A/D and D/A converters and/or that of the S/P and P/S converters.

(d) A data-logging mode was established for TRIVOC in which certain coefficients computed by the program are passed to the PDP-11 for statistical analysis in real time.

(e) DVTMON was extended (Secs. F.4 and F.5) to support the programs and modes described in (b)-(d) above.

A.2 Acknowledgments

Most of the mathematical analysis underlying the TRIVOC program was performed by MITRE Corporation personnel assigned to the Speech Research Laboratory. They developed an LPC algorithm[1] and a version of TRIVOC[2] that were tested on the CSP-30 computer at the laboratory. In addition, they wrote the digital-filter[3] and pitch-extractor portions of the DVT TRIVOC. Their assistance in this latter regard was essential to the timely completion of the program.

Lincoln Laboratory provided the physical facilities for most of the development of the DVT programs, since the DVT itself was undergoing construction, debugging, and modification at Lincoln concurrently with the programming effort. The authors of this report enjoyed unrestricted access to the Laboratory and benefitted from many conversations with Lincoln personnel who were engaged in the development of the machine

and in its application to the speech bandwidth compression problem.[4] TRIVOC subroutines OLAY (overlay) and DIVF (divide fraction) are adaptations of routines kindly supplied by P. E. Blankenship and E. M. Hofstetter, respectively.

B. Speech Bandwidth Compression

B.1 Principles

A voice-grade telephone line is built to pass frequencies up to ~3000 Hz in order that speech waveforms may be transmitted with acceptable fidelity. According to communication theory, such a line is capable of conveying information at a rate of ~30000 bits per second (bps), proportional to its channel bandwidth of 3000 Hz. By contrast, the information rate in ordinary speech is less than 50 bps, if we take the information to be merely the words and ignore the vocal properties of pitch, voice quality, expression, etc.[5]

Awareness of this disparity has led to the development and use of speech signal representations that, with some loss of fidelity, convey even the vocal properties at much lower bit rates than the 30000 bps required by the waveform representation. The alternate representations can be transmitted on channels of proportionately narrower bandwidth, so their use is called "speech bandwidth compression." Today, these representations are always transmitted by pulse-code modulation.

The success of various compression schemes implies that there is a large amount of redundancy in the natural speech signal and in its waveform representation. The redundancy arises in part from the fact that speech consists of a succession of individually recognizable sounds, each of which may last for tens or hundreds of milliseconds with little change in pitch, intensity, or quality. Consequently, it is feasible to analyze a sound and transmit a brief description of it instead of transmitting the

sound (i.e., waveform) itself. A clever receiver can then use the description to synthesize a sound which is acceptably similar to the original sound. Bandwidth-compression systems which operate on this principle are known as analysis-synthesis systems.[5]

In practice, most speech analyzers make no attempt to locate the actual boundaries between sounds. Instead, they divide the incoming speech signal arbitrarily into consecutive "frames" of equal duration (typically 10-25 ms) and construct and transmit a concise description of the content of each frame in turn.

B.2 Methods

Various analysis-synthesis systems differ in the ways in which they describe the speech signal. A large class of such systems bases its descriptions on a two-component model of the natural speaking apparatus. One component is the transmission function representing the vocal tract. The other is the excitation function representing the time-dependent input to the vocal tract.[6] In this model, a single frame is synthesized by filtering an excitation function $x(t)$ with a transmission function H to yield a signal

$$y(t) = Hx(t)$$

which is the output speech waveform. The functional forms of H and $x(t)$ are built into the synthesizer, so only the parameters of these forms need be transmitted by the analyzer. These parameters then constitute the "description" of the frame. It is the task of the analyzer to determine parameter values such that the sound produced by $y(t)$ is perceived as similar to the input sound; it is not necessary that $y(t)$ be similar to the input speech waveform.

The parameters of x(t) are particularly simple. For voiced sounds, x(t) must be periodic (at the pitch frequency) to represent the regular vibration of the vocal cords. For unvoiced sounds, x(t) should be broad-band noise to represent the irregular excitation of the vocal tract by the passage of air through a constriction. Assuming that the synthesizer knows the forms of the periodic and noise functions, the only parameters to be transmitted by the analyzer are the amplitude and pitch period of the excitation. Each of these can be encoded in about 6 bits, so the excitation is completely described in ~12 bits. (A period of zero can indicate that the unvoiced excitation is to be used.)

The parameters of H depend upon the particular realization of the transmission function and vary from system to system. However, they always carry much more information about the sound than do the excitation parameters, and thus require many more bits for their specification. Typically 30 to 80 bits suffice.

B.3 Systems

The most widely used excitation-transmission system is the channel vocoder.[6] Its analyzer performs a spectral resolution of the input speech into a number of narrow frequency bands. Its synthesizer generates signals in corresponding bands, weights them with the amplitudes determined by the analyzer, and combines the results into a single output signal (see pars. D.1.3, D.2.3).

Another system in this class, one that has become popular only recently, uses linear predictive coding (LPC) to generate an output that depends on earlier values of the output as well as on the excitation.[7] Here the system function H describes a single recursive filter whose coefficients have been determined by the analyzer (see pars. D.1.2, D.2.2).

The TRIVOC system is a third member of this class. It was conceived

as a way of combining the strengths of LPC with those of the channel vocoder.[2] The vocoder, with a separate filter for each frequency band, does a good job of reproducing the energy distribution at the upper end of the speech spectrum, where there is not much structure. This portion of the spectrum is important for speech intelligibility, and the vocoder consequently achieves high intelligibility ratings. The low end of the spectrum, however, exhibits a pronounced structure for voiced sounds and the vocoder does not do so well here. Since this part of the spectrum is chiefly responsible for the naturalness and quality of voiced sounds, the vocoder scores poorly in these respects.

LPC exhibits characteristics that are just the reverse of those of the vocoder. It excels at the low end of the spectrum but does not model the high end very well.

The TRIVOC concept, then, is to divide the entire speech spectrum into two contiguous ranges, to process the lower range by LPC and the upper range by a channel vocoder, and to combine the results of the two processes to obtain the final output. The system must of course also perform the third process of determining the excitation (pitch, amplitude, and voiced/unvoiced decision), so it is aptly named "Triple-Function Voice Coder" and called "TRIVOC."

C. The TRIVOC Hardware System

The arrangement used for the Reston tests (Sec. A.1) is given in Fig. IX.C.1, which shows only one of the two terminals actually used. The dashed lines indicate the two boxes in which one DVT system is housed. Except for the filters in the signal conditioner, all of the hardware is digital. The lines entering and leaving the DVT are all 16-bit lines, accessed via the DVT's input channel or output channel.

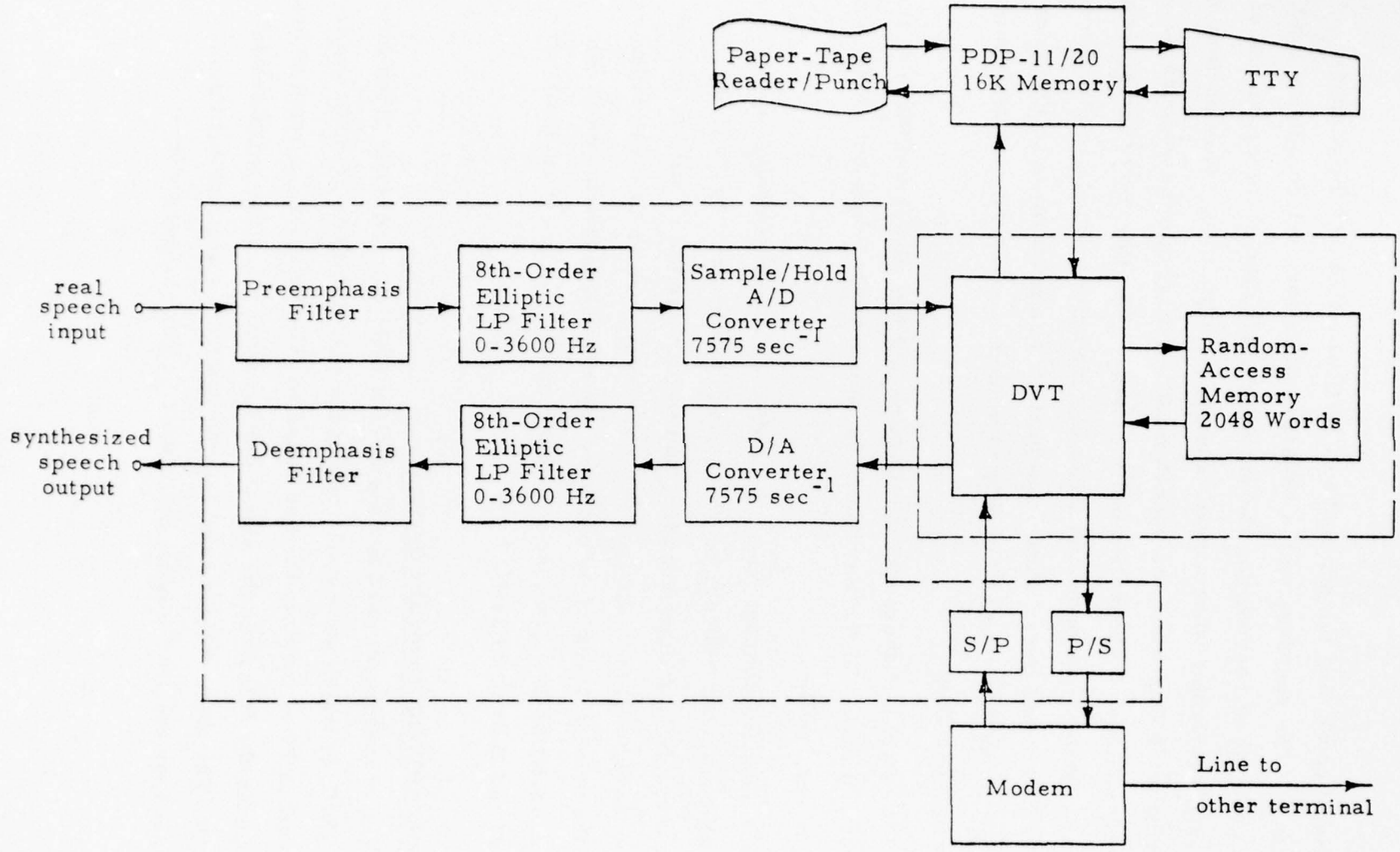

Fig. IX.C.1 One terminal of the TRIVOC hardware system.

S/P = serial-to-parallel converter, P/S = parallel-to-serial converter

C.1 The PDP-11 Subsystem

The PDP-11/20, running program DVTCOR (App. H.3), is normally used only to load the DVT with the TRIVOC realtime program and is not involved in the speech processing. It remains on line, however, and is always ready to accept a command from the teletypewriter keyboard or a memory dump from the DVT.

A larger, faster PDP-11 system was used for program development. It included a PDP-11/45 central processor, 64K words of memory, two disk-pack drives, and a line printer, as well as the paper-tape, TTY, and DVT facilities shown in the figure. This system supported TRIVOC assemblies (Sec. G) and the full capabilities of program DVTMON (Sec. F), including realtime simulation.

C.2 The DVT Subsystem

The DVT is an extremely fast 16-bit minicomputer developed specifically for speech-processing applications. Except for the design features[4] that give it its high speed (18 instructions per microsecond), it is a simple machine that provides few amenities to the user:

- 1 16-bit accumulator
- 1 16-bit index register, with limited arithmetic capability
- 1 16-bit input channel } each switchable among four
- 1 16-bit output channel } devices under program control
- 512 words of data memory (M_D)
- 1024 words of program memory (M_P)
- 2048 words of external memory (M_X), accessed like a peripheral
- no indirect addressing
- no hardware divide
- no double-word or rotary shift

These limitations, together with the high-speed, overlapped execution of instructions, lead to departures from "good programming practice" and

to sometimes esoteric coding. They may also affect the overall realtime structure of a program (see Sec. E.1). In practice, most users have found the small size of M_D and M_P to be the most nettlesome limitation, but one that is partly compensated by the speed with which M_X can be accessed (220 ns/word). Similarly, one can "code around" the other limitations, taking advantage of the high instruction speed, and still achieve a computation rate that is significantly higher than that of conventional machines.

The DVT instruction set is listed in Reference (4), along with a description of the machine and examples of its use by Lincoln Laboratory. A programming manual[8] and diagnostic-system manual[9] are in preparation.

C.3 The Signal-Conditioner Subsystem

The parameters of this subsystem may be adjusted by the user. The pre-emphasis/de-emphasis slope is controlled by a screwdriver adjustment, the low-pass filters are mounted on plug-in boards, and the sample period is selected by a 15-position switch.

For TRIVOC, 5 db/octave of pre-emphasis is used, 3600-Hz filters are plugged in, and a 132-μs sample period is selected.

The S/P and P/S converters are also quartered in the signal-conditioner box. For back-to-back testing of the analyzer and synthesizer in a single DVT, one can dispense with the modem. The P/S output is connected directly to the S/P input and an external oscillator and pulse-shaping circuit are used to provide simulated modem clock pulses.

D. The TRIVOC Software System

The overall system, resident in each DVT, consists of an analyzer portion and a synthesizer portion, each described in more detail below.

These two portions are completely independent of one another and both may operate during each frame, allowing full duplex communication. Each is driven by its respective modem clock and since the transmit and receive modems at one terminal may differ slightly in frequency, the analyzer and synthesizer frame rates may differ slightly in a given DVT (See par. E.3.2).

Two versions of TRIVOC exist, for operation at modem clock rates of 2400 and 3600 bps, respectively. Processing of the input speech is the same in both versions except for the difference in frame lengths. The frequency range below 1200 Hz is processed by the LPC section, while the range 1200-3600 Hz is handled by the channel vocoder. Other parameters of the system are summarized in Table IX. D. 1.

D. 1 The Analyzer

A block diagram of the analyzer is shown in Figure IX. D. 1. This is a functional diagram and is not to be construed as a diagram of the real-time program (RTP). Some of the functions are performed wholly in the RTP background, some wholly in the foreground (interrupt service), and some partly in each.

The input to the program consists of the sequence of speech samples issuing from the A/D converter at 7575 Hz. The arrival of each sample triggers a realtime interrupt that initiates the RTP foreground, which is mostly concerned with processing individual input and output (synthesized) samples. When the sample count reaches the predetermined number per frame (Table IX. D. 1), the foreground causes the background part of the analyzer to be initiated. The background performs once-per-frame tasks.

D. 1. 1 Pitch Extraction

TRIVOC uses the Gold-Rabiner method[10, 11] of determining the pitch of the speech signal. In this method, pitch period estimates are

TABLE IX. D. 1*

TRIVOC Parameters for the DVT

Parameter	2400 b/s	3600 b/s
Speech Sample Rate	7575 s/s (132 μsec)	7575 s/s (132 μsec)
Output (Frame) Rate	44.44 frames/sec	48 frames/sec
Samples/Frame (nominal)	170	158
LPC Sample Rate	2525 s/s	2525 s/s
LPC Samples/Frame	56	52
Reflection Coef. Coding (bits):		
RC #1	7	7
RC #2	6	6
RC #3	5	5
RC #4	4	4
Channel Level Coding (bits):		
C1	3	4
C2	3	3
C3	3	3
C4 through C13	1 each	3 each
Total Bits/Frame	54	75

*reproduced from Reference (3)

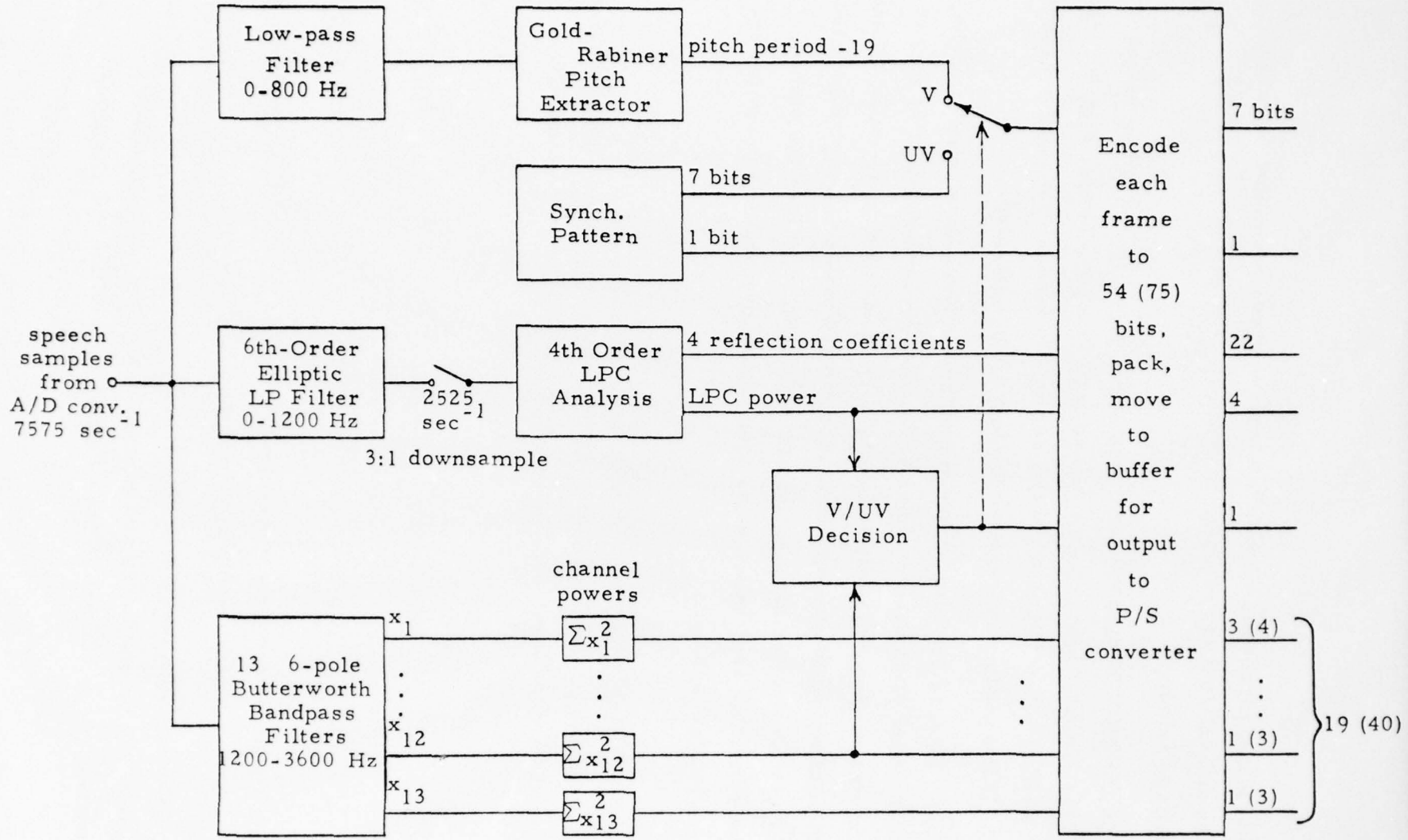

Fig. IX.D.1. TRIVOC Analyzer.

m (n) means m bits at 2400 bps, n bits at 3600 bps.

[adapted from Reference (3)]

based on measurements of time intervals between prominent features (peaks and valleys) of the signal landscape. The unit of time is the sampling period.

In the TRIVOC implementation of the method, the incoming speech samples are first low-pass filtered to ~800 Hz with a simple digital filter that yields as its output the moving average of the last 3 moving averages of the last 4 moving averages of the last 5 input samples.

The filtered samples are examined by the foreground portion of the Gold-Rabiner pitch extractor (GRAPE), whose output consists of recent estimates of the pitch period made by each of six pitch detectors. These estimates are updated every time a prominent peak or valley is detected. Once per frame, the background part of GRAPE examines the various pitch estimates and, by a complicated voting procedure, selects the one which is most popular.

D.1.2 Linear Predictive Coding

In LPC of order N, the next value of a discrete-time signal is estimated (predicted) by a linear combination of the N most recent actual values:[7]

$$\hat{s}_i = \sum_{j=1}^{N} a_j s_{i-j} \quad . \qquad (1)$$

This equation describes (approximately) the way the LPC synthesizer generates samples, using predictor coefficients a_j supplied by the analyzer.

Over a sufficiently short interval (a frame), the speech signal is assumed to be stationary and representable by a set of a_j which are constant. It is the task of the LPC analyzer to find the "best" values of

the a_j in the sense that the predicted $\hat{s}_i$ approximate most closely the actual s_i (which are, of course, known to the analyzer). The easiest criterion to use is the minimization of the total squared error over the entire frame,

$$E^2 = \sum_{i=1}^{M} (s_i - \hat{s}_i)^2 = \sum_{i=1}^{M} (s_i - \sum_{j=1}^{N} a_j s_{i-j})^2, \tag{2}$$

where we take $s_{i-j} = 0$ when $i-j \leq 0$ and where M is the number of samples per frame.

Setting to zero the partial derivatives of E^2 with respect to the a_j yields the set of N equations

$$\sum_{j=1}^{N} \left(\sum_{i=1}^{M} s_{i-k} s_{i-j} \right) a_j = \sum_{i=1}^{M} s_i s_{i-k}, \qquad k=1,2,\ldots,N \tag{3}$$

to be solved for the a_j. By taking $s_n = 0$ for $n > M$, we can write these equations as

$$\sum_{j=1}^{N} r_{|k-j|} a_j = r_k, \qquad k=1,2,\ldots,N \tag{4}$$

where both the coefficients of the a_j and the right-hand sides are members of the set of autocorrelation coefficients

$$r_k = \sum_{i=-\infty}^{\infty} s_i s_{i-k}, \qquad k=0,1,2,\ldots,N. \tag{5}$$

Because of this special property of the coefficients of the a_j (they constitute a finite Toeplitz matrix), Equations (4) may be solved by the following recursive procedure:[1]

$$
\left.
\begin{aligned}
& p_1^1 = q_1 = -r_1/r_0 \\
& \text{For} \quad i = 2, 3, \ldots, N: \\
& u = r_i + \sum_{j=1}^{i-1} r_j p_j^{i-1} \\
& v = r_0 + \sum_{j=1}^{i-1} r_j p_{i-j}^{i-1} \\
& p_1^i = q_i = -u/v \\
& p_{j+1}^i = p_j^{i-1} + q_i p_{i-j}^{i-1}, \qquad j = 1, 2, \ldots, i-1
\end{aligned}
\right\} \qquad (6)
$$

At the end of the recursion, we have the 2N quantities q_k and p_k^N, k=1, 2, ..., N. The q_k are called reflection coefficients and the quantities $a_j - p_{N-j+1}^N$ are the predictor coefficients we set out to find. However, the reflection coefficients, which are always <1 in magnitude, are a better conditioned set of parameters for transmission and it is these which are in fact transmitted.

The only input to the recursion is the set of correlation coefficients r_k, k=0, 1, 2, ..., N. In the TRIVOC program (foreground), the incoming speech is low-pass filtered and downsampled before being used to form the r_k. The filter is a 6th-order elliptic filter with a cutoff at 1200 Hz. Its output is taken only every third sample time, for an effective LPC input rate of 2525 samples/sec.

The correlation coefficient sums

$$r_k = \sum_{i=1}^{M} s_i s_{i-k}, \qquad k=0,1,\ldots,N \tag{7}$$

are computed in double precision and accumulated until the end of the frame, when they are scaled up and passed (in single precision) to the background (routine TOPLIZ) for use in the recursion (6). The sums are then cleared for the next frame.

The size of coefficient r_0 is proportional to the intensity (power) of the input signal. At the end of each frame, the number of left shifts required to normalize r_0 is determined and this shift count is transmitted as the intensity measure.

D.1.3 Channel Vocoder

While LPC involves analysis in the time domain, a channel vocoder performs analysis in the frequency domain. The incoming speech signal is applied in parallel to a bank of bandpass filters, which, taken together, span the frequency range to be analyzed. The output of each filter is a signal whose amplitude is proportional to that component of the input signal lying within the band (channel) passed by that filter. The square of each filter output is then proportional to the input power within the channel. This number (suitably encoded) is transmitted to the vocoder synthesizer for reconstruction of a power spectrum similar to that of the input speech.

TRIVOC receives audio input which has been low-pass filtered to 0-3600 Hz and then sampled and digitized 7575 times per second. Each sample is used as input to each of 13 digital third-order Butterworth

bandpass filters spanning the frequency range 1200-3600 Hz. For each input sample, an output number is produced by each of the 13 filters. Each output number is squared and added to a running sum which represents the power in the corresponding channel. At the end of each frame (as determined by the sample count), each sum of squares is logarithmically encoded for transmission and the sum is reset to zero for the next frame.

D.1.4 Voiced-Unvoiced Decision

This decision is based on the input signal powers in the LPC band (0-1200 Hz) and in the 12th channel (3000-3300 Hz) of the vocoder. If the LPC power is less than a certain limit, the decision "unvoiced" is declared. Otherwise, the LPC and vocoder powers are compared. If the LPC-to-vocoder ratio exceeds a certain limit, the "voiced" decision is made; otherwise, "unvoiced." The two limits involved in the decision have been determined empirically.

When the "voiced" decision is made, the current value of pitch period from the G-R pitch extractor is transmitted, if available, and the V/UV bit is set to zero. It sometimes happens that GRAPE has been unable to determine a pitch for the current frame; in this case, the most recent pitch is transmitted.

When the "unvoiced" decision is made, a 7-bit synchronization pattern is transmitted in place of the pitch period and the V/UV bit is set to 1.

D.2 The Synthesizer

Figure IX.D.2 shows a block diagram of the TRIVOC synthesizer. Again, this is a functional diagram, not the RTP diagram. The input data (left side of figure) are those obtained from the transmission line, via the receiving modem and serial-parallel converter. They have been

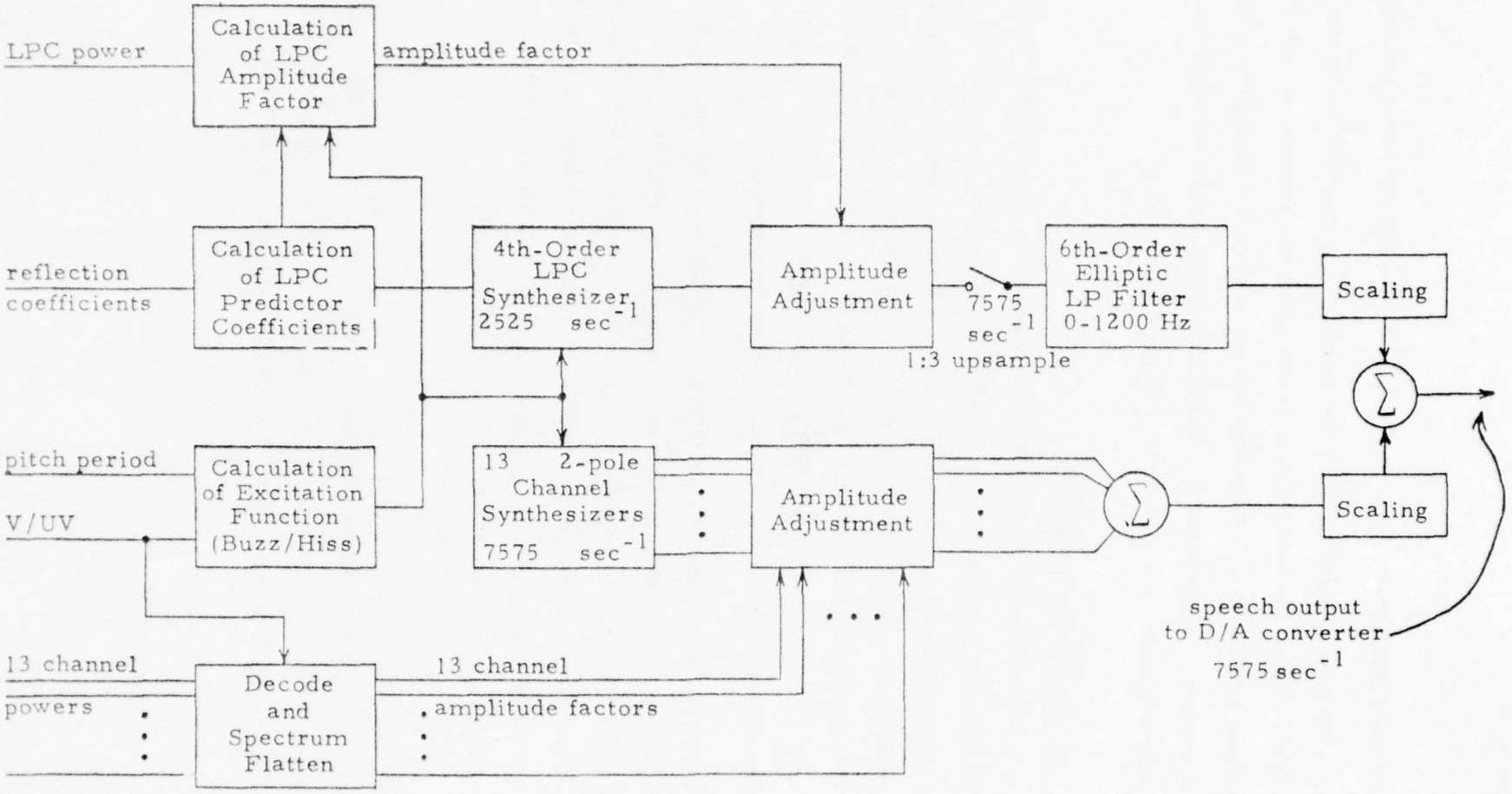

Fig. IX.D.2. TRIVOC Synthesizer.

[adapted from Reference (3)]

unpacked once per frame by a program section not shown in the figure.

The RTP foreground buffers the words from the S/P converter as they arrive. When the word count indicates that a frame's worth of bits (Table IX. D. 1) is on hand, the foreground causes the background part of the synthesizer to be initiated. The background performs once-per-frame tasks, starting with the unpacking referred to above.

D. 2. 1 Excitation Function

The V/UV decision determines the excitation function for both the LPC and vocoder synthesizers. Each synthesizer is a recursive filter with an external input (excitation). When a voiced sound is to be generated, the excitation is a single pulse at the start of each pitch period. For an unvoiced sound, the excitation consists of white noise applied throughout the frame. This is accomplished by inputting to the filter a signed pseudorandom number for each output sample generated.

The magnitude of the excitation is constant for a given synthesizer. It is chosen as large as possible (without causing overflow) in order to maximize the precision of the recursive filter calculations. Consequently, the raw samples generated by each filter must be adjusted in amplitude to cause the final output power to equal the input power seen by the corresponding filter in the analyzer.

D. 2. 2 LPC

A recursive procedure similar to that used in the analyzer serves to convert the reflection coefficients q_i to the predictor coefficients a_j that define the recursive filter for LPC synthesis (routine RCA):

$$
\left.
\begin{aligned}
& a_1^1 = -q_1 \\
& \text{For} \quad i = 2, 3, \cdots, N: \\
& \qquad a_i^i = -q_i \\
& \qquad a_j^i = a_j^{i-1} + q_i a_{i-j}^{i-1}, \qquad j = 1, 2, \cdots, i-1
\end{aligned}
\right\} \tag{8}
$$

The final values a_j^N are the desired coefficients a_j

Each LPC sample to be generated is then obtained by one operation of the recursive filter:

$$
s_i = \sum_{j=1}^{N} a_j S_{i-j} + g_i, \tag{9}
$$

where g_i is the excitation function described above.

By generating P samples (P = pitch period for voiced sounds or, arbitrarily, 16 for unvoiced sounds) and forming the sum of their squares, we find the output energy contained in one pitch period (routine RFSS):

$$
E_{out} = \sum_{i=1}^{P} s_i^2 . \tag{10}
$$

The mean output power (energy per sample) is then E_{out}/P. The desired output power, however, is E_{in}/M, where E_{in} is the energy figure determined by the analyzer for a full frame of M samples. Consequently, we derive the amplitude adjustment factor (routine RFADJ)

$$A = \sqrt{PE_{in}/ME_{out}} \tag{11}$$

which, when applied to the raw samples generated by the LPC recursive filter, yields samples whose mean power is equal to that of the input samples.

The above computations are made once per frame in the TRIVOC background. In the foreground, a sample is generated by Equation (9) once every third sample time and is adjusted in amplitude by applying factor (11). Samples of magnitude zero are generated the other two sample times.

The adjusted samples and zeroes are delayed by 15 sample times (to compensate an inherent delay in the vocoder output) and are then handed to a low-pass filter identical to the one used for the LPC input. The filter output is taken every sample time for combination with the vocoder output.

D.2.3 Channel Vocoder

The vocoder synthesizer comprises a bank of 13 two-pole recursive filters tuned to the same center frequencies as the corresponding filters in the analyzer. Equation (9), with N = 2, describes the operation of each filter. For unvoiced sounds, the g_i are pseudorandom numbers; for voiced sounds, the g_i are all zero except at the start of each pitch

period. Here the excitation pulse (par. D.2.1) alternates in sign from channel to channel to avoid overflow problems when the channels are combined.

The raw output of each channel is adjusted in amplitude (par. D.2.1) by applying three factors:

(a) Compensation for a pitch effect: the lower the pitch, the less often is the excitation pulse added to the filter and the smaller is the output power; the compensating factor increases linearly with pitch period and is the same for all channels;

(b) Compensation for channel-dependent effects in both the analog and digital filters; this factor equalizes the overall gains of all channels;

(c) A factor representing the square root of the speech input power in the channel; this factor is obtained from a table indexed by the logarithmic value transmitted by the analyzer (par. D.1.3).

D.2.4 Final Output

Each sample time, the adjusted outputs of all the channels are added together and formed into a weighted sum with the output of the LPC low-pass filter (par. D.2.2). The result is scaled up a bit, corrected for overflow (if it occurs), and finally output to the D/A converter.

E. The TRIVOC Realtime Program

E.1 Comments

The program structure is profoundly influenced by the DVT limitations enumerated in Sec. C.2:

(a) For lack of sufficient M_D, it is necessary to hold 78 vocoder filter coefficients (6 for each of 13 channels) in M_X and to read them into M_D every time an A/D sample arrives (every 132 μs).

(b) For lack of sufficient M_P, it is necessary to hold ~370 instruction words in M_X and to read them into M_P once every frame. They are divided into three overlays of roughly equal lengths. One overlay at a time occupies M_P; each overlay is a separate task.

(c) For lack of more than one I/O channel, it is impossible to initiate I/O and wait for interrupts from more than one device at a time. One would like to do exactly this with the A/D, S/P, and P/S converters. Instead, only the A/D interrupt is enabled and each time it occurs, the interrupt service polls the S/P and P/S converters. Each of these devices responds only once for every 34 (or more) times it is polled.

It should be clear that a good deal of real time is spent in the foregoing exercises; only the extreme speed of the DVT makes it possible to overcome the space and channel limitations in the ways described. In addition, a good deal of unreal time (that of the programmer) is spent in keeping track of common scratch storage in M_D. Almost every one of 47 common locations is used by four or more subprograms and is referred to by four different names. This overlapping is necessitated by the small size of M_D.

E.2 Program Loading and Initialization

The DVT contains a hardwired bootstrap which may be initiated by the CLEAR switch on its console or by an external interrupt from the PDP-11 host computer. The bootstrap loads M_P and M_D with the first 2762_8

words read from the host, then passes control to the first software routine, START. This routine reads 4000_8 more words and uses them to load M_X with the filter coefficients and program overlays referred to above. (Unused words are transmitted as zeroes by the host.) START then self-destructs by causing itself to be overlaid with Task GRAPE, read from M_X. The overlaying is done by subroutine OLAY, which finishes its work by enabling the input interrupt from the A/D converter and returning to the start of the background main loop. At this moment, the RTP is off and running.

E.3 Structure of the RTP

The RTP is made up of separate foreground and background components. The foreground is the interrupt service routine for the A/D converter and is entered regularly every 132 μs. The background is an endless loop (Fig. IX.E.1) that runs continuously whenever the foreground is not running. Within this loop, switches LFLAG and CFLAG are set by the foreground once every frame (~22 ms) to call the background analyzer and synthesizer, respectively. Each of these routines clears its own switch.

E.3.1 The RTP Foreground

The gross structure of the A/D interrupt service is shown in Fig. IX.E.2, which emphasizes the realtime communication between foreground and background (via switches) and between the DVT and its peripheral devices.

Switch LFLAG is set whenever a frame's worth (M samples) of input speech has been received and digested. Switch CFLAG is set whenever a frame's worth of coded data has been received from the line. Switch GIRDY is set by the background when it has prepared new input data for the foreground synthesizer.

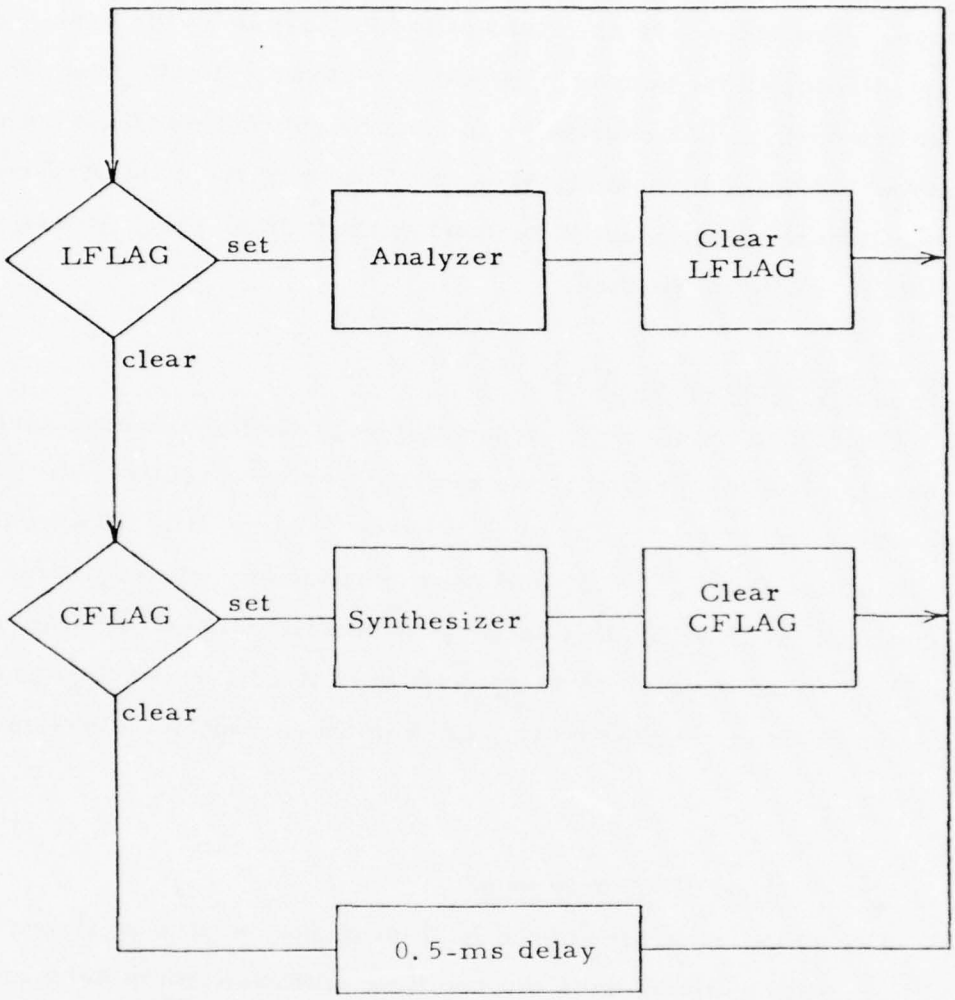

Fig. IX.E.1. TRIVOC RTP Background

The vocoder analysis filters are updated at the very start of the routine because they need to use the DVT's input channel to read coefficients from M_X. This use of the channel must be completed before the input from the S/P converter can be initiated, since the latter request remains in effect until almost the end of the routine.

Input sample analysis starts with the parallel filtering of the sample by the 13 channel filters (see above) and by the low-pass filters for the pitch detector and LPC. The LPC filter output is used every third time to update the double-precision correlation coefficient sums in Eq. (7). The other filter outputs are used every time to update the pitch estimates and channel powers.

End-of-frame actions are performed only for the channel vocoder and the LPC. The autocorrelation coefficient r_0 is normalized and the number of left shifts required is saved for encoding by the background. Then all the correlation coefficients are scaled up by the amount required to normalize r_0, truncated to single precision, and moved, along with the channel powers, to background buffers.

The foreground synthesizer tests switch GIRDY only when a sample counter indicates that a synthesized pitch period has just ended. Thus the synthesizer parameters are never changed during a pitch period, and there is no relation between pitch period boundaries and frame boundaries. Synthesizer operation has been discussed in Sec. D.2.

E.3.2 The RTP Background

In Fig. IX.E.1, note that the analyzer and the synthesizer are called independently. It is thus possible (indeed, it is the rule) that the execution frequencies of the two programs will differ (see Sec. D, first paragraph). When neither program is required, a .5-ms delay loop is executed.

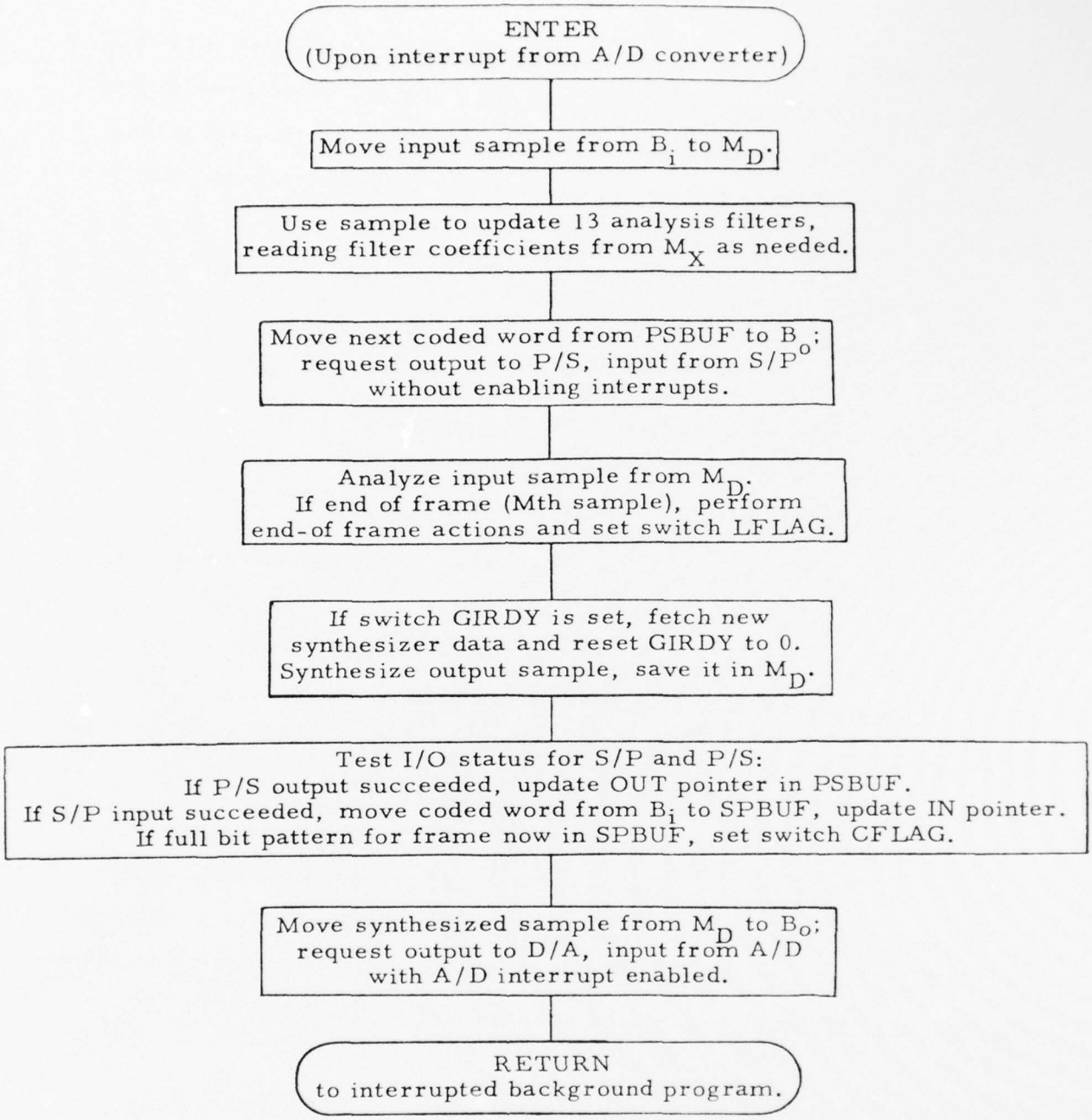

Fig. IX. E. 2. TRIVOC RTP foreground.

B_i = input register, B_o = output register

The analyzer program is composed of three tasks, GRAPE, TOPLIZ, and CODER, each of which exits by causing itself to be overlaid with the next task in the (cyclical) sequence. GRAPE is the Gold-Rabiner pitch extractor (Sec. D.1.1). TOPLIZ finds the LPC reflection coefficients (Sec. D.1.2). CODER encodes and packs the pitch, energy, LPC, and channel-vocoder data, then deposits the resulting bit pattern in circular buffer PSBUF, where the foreground will find it and send it to the P/S converter. Before CODER exits, it clears switch LFLAG.

The encoding scheme is shown in Table IX.D.1. At 2400 bps, each of the first three channel powers is logarithmically encoded to 3 bits; the remaining 10 channels are delta-encoded to 1 bit each. At 3600 bps, the first channel is log-encoded to 4 bits and the rest are delta-encoded to 3 bits each. LPC power is log-encoded to 4 bits; 7 bits are used for pitch period less 19; 1 bit for "unvoiced"; and 1 bit for framing.

CODER performs one further duty that is crucial to the realtime operation of the analyzer: it adjusts the analyzer frame length (number of samples per frame, M) so as to insure that the analyzer runs just often enough to supply data to PSBUF at exactly the same average rate that data are removed from PSBUF by the foreground. This rate is determined (via the P/S converter) by the clock in the transmitting modem, which is independent of the A/D clock. No fixed value of M will equalize the two rates, since the two clock periods are generally incommensurable and are, moreover, subject to drift. However, a rounded nominal value MNOM (Table IX.D.1) may be computed from the nominal clock periods and the length of the bit pattern for one frame. CODER sets the working value of M to MNOM + 1 if PSBUF is tending to fill up or to MNOM - 1 if the buffer is tending to run dry. This range of variation has proven to be sufficient in practice.

The background synthesizer consists of four routines: CRAKER, RCA, RFSS, and RFADJ. CRAKER performs the initial synchronization of the

receiving synthesizer with the sending analyzer by searching for the pattern transmitted in place of pitch when the speech is unvoiced (or silent); thereafter, it verifies synchronization on every unvoiced frame and automatically reenters the search if it fails to detect the pattern in 16 consecutive unvoiced frames. CRAKER also unpacks and decodes the whole bit pattern for the frame (taken from buffer SPBUF) and leaves its results in working storage for access by the succeeding routines.

RCA converts reflection coefficients to LPC predictor coefficients, RFSS generates one pitch period of LPC output to determine the raw power therein, and RFADJ finds the amplitude adjustment factor required to convert the raw power to the desired output level. These operations have been discussed in Par. D.2.2.

E.4 Performance

Extensive testing with speech input from handset or tape has demonstrated the soundness of the RTP structures. Synchronization of the two DVT's is achieved automatically within a second or so after program loading and is thereafter maintained. Although the program contains four realtime-violation halts, it can process speech* for hours without encountering any of them.

However, qualitative and quantitative listening tests (including those at Reston) have shown that the intelligibility and quality of the synthesized speech are lower than had been obtained with the CSP-30 (Sec. A.2). Further work on TRIVOC will address these problems.

---

*It has recently been discovered that a high-frequency sinusoidal input can cause the program to halt. It is suspected at this writing that this behavior results from an extra burden put upon the foreground part of GRAPE, which thinks it is detecting a very rapid succession of short pitch periods. Under these conditions, the foreground could use up so much of each 132 μs interval that the background would fall behind.

F. The DVT Monitor

F.1 The Monitor Program

The DVT Monitor (DVTMON) is a set of program modules written in Macro-11 assembly language on the PDP-11 under the RSX-11M operating system. It is designed to control a DVT through the DR11-C interface. The various source modules are assembled and then task built using the overlay descriptor file, DVTMOO.ODL (see App. H.2). If DVTMON runs on a mapped system, a common must be built over the I/O page. DVTMON can run concurrently with other tasks.

At startup, DVTMON tests to see if request A or B (input or output) of the DR11-C is enabled. If the result is positive, the warning message follows,

REQUEST A AND/OR B IS(ARE) ENABLED

Whether the result is positive or negative, the message

DO YOU WANT DR11-C INTERRUPTS ENABLED?
(Y) OR (N)

is output. A (Y)es answer allows the DVT to interrupt DVTMON to initiate communication.

If the above warning message was printed and (Y)es was typed, an immediate interrupt will occur. If DVTMON recognizes a legitimate request from the DVT, it will act upon it, otherwise the following messages

UNDEFINED FUNCTION FROM DVT
DDDDDD
TYPE "R" TO RESTART OR (CR) TO CONT

are output. DDDDDD is the octal contents of the received word. The second message indicates that the user can restart the program and perhaps not enable interrupts, or continue the program with interrupts enabled. If the user chooses to continue rather than restart, and if another word with an undefined function is received, some action must be taken on the DVT side

to lower Request A and/or B. Otherwise, the cycle will continue. There are two common reasons why undefined functions occur from the DVT. One is that the DVT is attempting to write to the PDP-11 and either the function code (See Section F-3) is incorrect or the PDP-11 has missed the function code word. The second common reason is that the DVT is disconnected from the DR11-C interface. Both requests A and B remain high (float).

If (N)o was typed and/or neither request A or B is enabled, then DVTMON prompts with

DVT>

DVTMON is now ready to accept keyboard commands and if DVT interrupts are enabled, requests from the DVT. All keyboard commands are two character commands. Characters following the first two characters are ignored until a space or (CR) is encountered. Spaces are generally used to separate arguments and (CR) always is the terminator. Optional arguments are enclosed in [BRACKETS]. All numerical arguments are considered to be octal unless otherwise noted. To exit, type ↑Z (depress CONTROL key and type Z).

The functions BA, BO, RP, PP, and PR (if outputing to the line printer) can be terminated by typing (CR). Typing a space plus (CR) will restart DVTMON. Output to the terminal can be turned off by typing ↑O.

F.2 DVTMON Keyboard Commands

LOAD

LO [SEGNUM] FILESPEC

Load a DVT image into segment, SEGNUM, where $0 \leq$ SEGNUM $\leq 13(8)$. The DVT image must be a file either assembled using the DVT assembler (See Section G) or a file that is a result of a previously saved (see SA) segment. If SEGNUM is not specified, the segment number used in the SEG directive is used. FILESPEC is any proper RSX-11 Files-11 file specification. Appendix H.4 contains a discussion of segments.

Examples:

1. LO 3 DK1: [200,200] LPC.OBJ;4

   This example means- load into segment 3 the file, LPC.OBJ;4, on RK-05 disk 1 under the UIC, [200,200].

2. LO LPC.OBJ

   Load into the segment indicated by the SEG directive, the highest numbered version of the file LPC.OBJ on the system disk under the terminal's UIC. If the program was assembled with segment number equal 3; if the system disk is RK-05 disk 1; if the terminal UIC is [200,200], and if the highest version number of LPC.OBJ is 4, then the two examples are equivalent.

BOOT

BO [SEGNUM]

Transmit the indicated segment to the DVT in the boot format. Segment 0 is the default. The boot format loads a segment from the end to the beginning (backwards), and the segment must be 2762(8) words long. This length represents the number of words the DVT hardware bootstrap routine must receive before giving up control (of Sec. E.2).

First the DVT is interrupted and forced into its boot routine by the setting of CSR0 in the DR11-C interface. The program memory is loaded first, then the data memory. The proper length falls short of 3000(8) (DM+ PM = 3000) because the bootstrap resides at the bottom of program memory, so only 2762 words are loaded. If timeout (ET) is enabled, and one second elapses without the transmission completing, the boot attempt is aborted and the timeout message is output.

BOOT ALL

BA [SEGNUM]

Same as BO except the segment length must be 6762(8) words. The additional 4000(8) words must be loaded by DVT software and are placed into extra memory. By agreement this is also loaded backwards.

Note: (CR) only acts as either a BO 0 or BA 0.

PRINT

PR SEGNUM [FILESPEC]

Write in ASCII to FILESPEC the segment, SEGNUM. SEGNUM is any segment and FILESPEC is any Files-11 specification. The line printer, LP0:, is used if FILESPEC is not specified. Eight words of memory are printed per line. The default format is unsigned octal integer (see FO).

SAVE

SA SEGNUM FILESPEC

Write an image copy of SEGNUM to FILESPEC. The default device, if none is specified in FILESPEC, is the system device, SY0:. The first record written into the file contains the segment number and information indicating that it is a saved file. The rest of the file is the binary image of the segment in 80. byte records.

FORMAT

FO [NEWFOR]

Set the numeric print (PR) format for ASCII files. The default (no argument) is octal magnitude (OM). There are six possible choices for the format (NEWFOR).

1. OM - Octal magnitude
2. OS - Octal signed
3. DM - Decimal magnitude
4. DS - Decimal signed
5. OF - Octal fraction - Sixteen bit word considered
6. DF - Decimal fraction to be 2's complement fraction.

PATCH

PA SEGNUM SEGLOC

Open and display contents of indicated segment and location. Example:

```
PA    2    321
321   000200 /L659
```

The user types the first line, DVTMON prints the second line up to the "/". At this point, the user can (1) terminate patch mode by typing (CR), (2) modify contents of location 321 by typing a new value, in which case the next location 322 is opened and displayed or (3) as shown in the example type L immediately followed by the address of the new location to be opened. The PA command may be used to open any segment location. There are two cases when it must be used. They are:

(1) When examining data memory (MD) and the segment is 2762 words in length.

(2) When examining extra memory (MX) and the segment is 6762 words in length.

MEMORY, PROGRAM

MP SEGNUM PMEMLOC

Similar to PA command except valid only when segment is either 2762 or 6762 words in length and has been assembled to be loaded by the DVT hardware bootstrap. PMEMLOC is the relative program memory location. The "L" command differs in that the new location is with respect to program memory and not the beginning of the segment.

MEMORY, DATA

MD SEGNUM DMEMLOC

Similar to the MP command but is valid only for a 6762 word segment and operates on data memory.

DELETE

DE SEGNUM

Delete the indicated segment ($0 \leq$ SEGNUM ≤ 13). See Appendix H.4.

FREE BUFFER SPACE

FR

Print the number of octal words of free buffer space.

READ PAPER TAPE

RP SEGNUM

Read paper tape from high speed reader (PC-11) into segment, SEGNUM. The tape must be a previously punched segment.

PUNCH PAPER TAPE

PP SEGNUM

Punch segment, SEGNUM, in binary image on to paper tape. The format of the tape is (1) a byte containing a one, (2) a blank byte, (3) two bytes containing the length, (4) the binary image of the segment, (5) a two byte checksum.

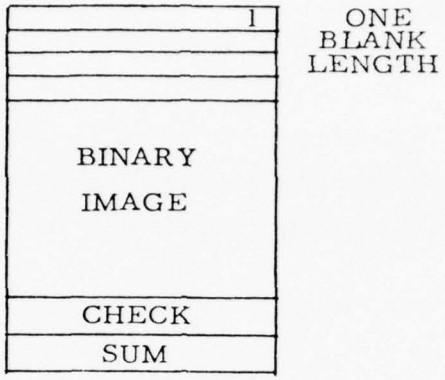

SELECT OUTPUT FILE

SO FILESPEC

Create and open an output file for dumps and simulations. When a dump finishes the dumped data is written into this file. See Section F.4 for a discussion of the simulations. This file remains open until closed by the CO command or by exiting from DVTMON.

CLOSE OUTPUT FILE

CO

If SO command has been executed, this command is mandatory before a SA or PR command can be issued.

ENABLE INTERRUPTS

EI

Allows the DVT to interrupt DVTMON for segment requests, dumps, etc. See Section F.3.

DISABLE INTERRUPTS

DI

Prevents DVT from initiating communication with DVTMON.

TRANSFER SEGMENT

TR OLDSEG>NEWSEG

Sets segment NEWSEG's pointer equal to OLDSEG's pointer. No data is transfered, hence both segment pointers point to the same data. To obtain two copies of the same program in memory, do a SA followed by a LO into a different segment.

LIST SEGMENTS

LS

Lists the segments resident and their lengths in octal words. In addition, segments 7, 10, 11, 12 and 13 have special significance in dumps and simulations. If one of these segments is resident, an auxiliary message is printed indicating its special meaning. See Section F.3.

Segment	Auxiliary Message
7	COMPR DATA
10	INDEX DATA
11	SIMUL DATA
12	RECVD DATA
13	DUMP DATA

ENABLE TIMEOUT

ET

Any communication initiated between PDP-11 and the DVT must be completed within one second or it is aborted. This is the default condition at startup.

DISABLE TIMEOUT

DT

Any communication between the PDP-11 and the DVT not terminating normally must be aborted by typing (CR).

TEST DIAGNOSTICS

TD [UNIT: [UIC]]

After issuance of this command, the DVT diagnostics sub-monitor will print

DIA>

See Reference (9) for a description of the diagnostic commands and the DVT diagnostics themselves. The diagnostics sub-monitor is a separate segment overlay of DVTMON and can be task built with or without all of DVTMON. The unit and UIC must be specified if the actual DVT diagnostic routines are stored on a unit other than the system device and/or a UIC other than the terminal UIC.

F.3 DVT-Initiated Functions

The DVT can initiate communication with DVTMON. To do this, PDP-11 interrupts must be enabled. There are presently four functions which the DVT can initiate. The first function is a boot. Pressing the CLEAR switch on the DVT console puts the DVT into its hardware bootstrap and sets output request high (on the PDP-11 side) in the DR11-C. If interrupts are enabled, DVTMON will boot Segment 0 to the DVT. Just as with the keyboard boot commands, the length of the segment must be 2762 or 6762 words long.

The other three functions which the DVT can initiate set the input request high and therefore, besides interrupting DVTMON, present a 16 bit word to DVTMON. The high order 4 bits contain the function code and the low order 12 bits contain auxiliary information dependent on the function.

1. System Simulation - This is one of the simulation routines and is discussed in Section F.4.
2. Segment Request - The low order 12 bits contain the segment number. The segment is transmitted to the DVT from first word through the last word (not the boot format).
3. Dump - A dump can be initiated by the DVT by running the DVT dump routine (Sec. A.1). The low order 12 bits of the first word contain the length of the dump that is to follow. Because of a DVT interface problem, the first word (function code + length) is sent twice. If only the second word is received, the message

MISSED FIRST DUMP REQUEST

is output although the dump will continue. The next word transmitted contains the data memory address of the first word of the dump. This is followed by the dump data and is written into segment 13. If there is an output file open (see SO), the dump data is also written into the opened file. In either case, the message

DUMP FINI

is output to the console.

F.4 Simulation Routines

A set of simulation routines were written to help test development of the TRIVOC software on the DVT. These routines are of a specialized nature and are tailored to the checkout of various parts of TRIVOC.

The first two routines, SI and EC, were used to test the DVT-PDP-11 software-hardware interface.

SIMULATE

SI

Segment 11 must be pre-loaded with data that is to be sent to the DVT and segment 7 with a copy of the data that is to be received. This routine simultaneously sends the data from segment 11 and receives data into segment 12. It continues to send and receive data, by testing the request bits, until all of segment 11 is transmitted and the number of words received is equal to the number in segment 7. When finished, a word for word comparison is made of segments 7 and 12. Pathological cases such as no data being sent or no data being received are allowed. A series of messages describe the results of the simulation.

ECHO

EC

Same as SI except the data received (segment 12) is compared with the data sent (segment 11).

SIMULATE SYSTEM

SS RSS

RSS is the receive segment (segment 12) size in octal words. This routine simulates the four peripherals of the DVT in real time. Segment 11 must be pre-loaded with one frame's worth of A to D samples and LPC reflection coefficients. Segment 10 must contain an index buffer whose function is to indicate when reflection coefficients should be transmitted to and received from the DVT.

The sample loop nominally takes 154 μs (the time for an A to D sample) on the PDP-11/45 and can be varied from about 40 μs upwards by using the CL command. The argument in this command can be varied from zero up. A value of 56 causes the loop to take the nominal 154 μs. Fill code is used to insure that each loop takes the same amount of time no matter what takes place on a particular loop. On every loop, one A to D sample is transmitted to the DVT and one D to A sample is received (Segment 12) from the DVT. Depending on the index buffer, a coefficient may or may not be sent or received. See Figure IX.F.1. Hence, the DVT by addressing the DR11-C can simulate the real-time system (A to D, D to A, P to S, S to P). The simulation terminates when the receive buffer (Segment 12) is full. If an output file is open (SO) the data is written into the file. After a simulation, a dump can be taken and then another simulation started, etc.

SIMULATE P TO S AND S TO P CONVERTERS

SP SAMPCO[C] DIFFCO DELAY BUFSIZ[S]

SAMPCO is the number of A to D samples between P to S words. DIFFCO is the initial difference between the number of samples for a PS and SP word. The value of DIFFCO is added to SAMPCO and this is the initial number of A to D samples per SP word. DELAY is the number of PS words to receive before transmitting the first SP word. BUFSIZ is the size of Segment 12 in words(8). All other numerical arguments are decimal. The optional "C" and "S" arguments are explained in the following paragraph.

This simulation runs in real time and works as follows - the DVT receives an A to D interrupt. It immediately notifies DVTMON. A count is kept of these notifications and when it equals SAMPCO, a PS word is read from the DVT and stored in Segment 12. If DIFFCO is zero and DELAY is zero, then each PS word received is immediately transmitted. If DELAY is non-zero and DIFFCO is zero, then the first SP word is not transmitted until the number of PS words received is equal DELAY. If DIFFCO is non-zero and DELAY is zero, then initially the PS rate is greater and the PS pointer will eventually catch the SP pointer. When this happens, and if the optional argument "C" has been typed, the SP rate is immediately changed from

1/(SAMPCO+DIFFCO) to 1/(SAMPCO-DIFFCO). Each rate will alternate between these two values as each catches the other. If "C" was not typed, then the rates are never altered; hence, periodically the PS pointer will move past the SP pointer. The second optional argument "S" is used to indicate whether the simulation should stop when the PS pointer reaches the end of the buffer, i.e., when the buffer is full. Otherwise, the pointer is reset to the beginning of the buffer as is the SP pointer when it reaches the end of the buffer.

This simulation tested the capability of the DVT real-time software to handle unequal PS and SP data rates (see discussion of CODER in par. E.3.2). Only one DVT was available during the program-checkout period, so it was operated in the back-to-back mode (Sec. C.3) in which the PS and SP rates were necessarily identical. The PDP-11 simulation provided the only proof that the TRIVOC analyzer and synthesizer could indeed operate at different frame rates (Sec. D, first paragraph).

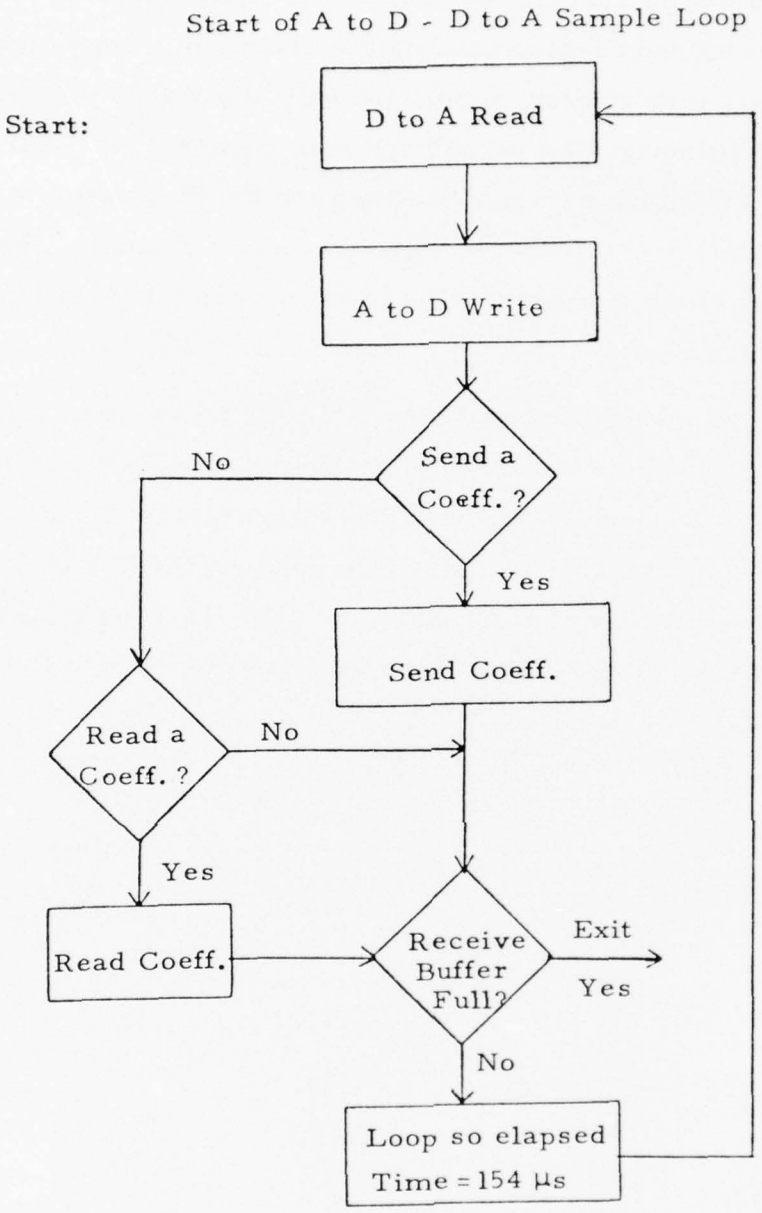

Figure IX. F. 1

Flow Diagram of System Simulation (SS) Routine

F.5 Data Analysis Routines

READ DATA

RD [Alphanumeric Character]

This routine reads 4 LPC reflection coefficients for each frame from the DVT and builds a frequency of occurrence table (FOOT) in Segment 12; records the number of frames received in Segment 11, and stores an optional raw data buffer in Segment 13. The FOOT is structured as follows: Rowone (first coefficient) and Rowtwo are each given a granularity of 64 possible values (words). The value 0 goes into slot 33, the most negative value into slot 1, and the largest positive value into slot 64. Rowthree has 32 slots and Rowfour has 16. The coefficients are truncated to fit into the table. The first 3 words of segment 11 contain the total number of frames, the number of silent frames and the number of non-silent frames, respectively. If the raw data buffer option is chosen, by typing any character as the argument, the routine will stop when the buffer fills up (all of free buffer space). Otherwise, it continues to run until terminated by a (CR).

GET SAMPLES

GS

Each DVT word received (normally the A to D sample) is stored sequentially in Segment 12 until free buffer space is full or until terminated by a (CR).

PUT SAMPLES

PS

Each sequential word in Segment 12 is sent to the DVT, when it indicates it is ready, until terminated by (CR). If the pointer reaches the bottom of the buffer, it is reset to the top.

G. The DVT Assembler

G.1 The Assembler Program

Programs that are loaded by DVTMON into the DVT are assembled using the RSX-11M Macro Assembler (see Appendix H.5) with the prefix file DIVOS.MAC. This file contains the macro definitions for the DVT instruction set and various directives that are needed.

Besides the different instruction set and the additional directives, the major differences between the Macro Assembler and the DVT Assembler (i.e., DIVOS.MAC plus the Macro-11 Assembler) are the following:

(1) The DVT Assembler allows only one operand per instruction (IOS the exception) since the DVT is limited to one operand address field. The method of addressing is generally equivalent to the PDP-11's absolute (@ #) mode with a few instructions using the operand itself as data; equivalent to the PDP-11 immediate (#) mode. The IOS instruction takes six operands. Otherwise, the syntax of the two assemblers is the same. See Reference (8) for a description of the DVT and its instruction set.

(2) Because the DVT is not byte oriented, the location counter is incremented by only one in moving from one word to the next word. This difference is transparent to the programer. However, due o this, the Macro-11 directives .WORD and .=. + DELOC must not be used. The DC directive is used to store data. The LOC and BL directives store zeroes, and the ORG and ALC change the location counter.

(3) Both a segment (SEG) and a memory (MD, MP, or MX) directive must be issued before any code is generated. The three memory directives may be in any order and issued more than once. Example: MP, MD, MP, MX, MD. Program and data memories would appear twice in the listing. Only one segment is allowed per assembly.

(4) The DVT Assembler maintains two counters for each memory. The first counter is the location counter (LC), designated by MD$, MP$, or MX$, and it is used to calculate the value of a symbol when it appears in the label field. It is also the value printed in the listing. The second counter is the word counter (WC) and is a count of the number of words of code or data that has been generated. These are designated by NMD$, NMP$, and NMX$. As long as neither the ORG nor the ALC directive has been utilized, the two counters (for a particular memory) are equal. These two directives change the location counter, but do not generate code or data. The LOC and BL directives and all the instruction set increment both counters equally. This slight complexity allows for overlays which are assembled in one address area of MX memory to be loaded (by a DVT program) into a different address area of MD or MP.

(5) The Macro-11 Assembler object file consist of a set of variable length records. Informational (for the task builder or linker) and text records are mixed together since the assembler generates these records as the need arises. A text record contains as its first word the location counter of text (binary image) that is to follow. The macro directives contained in DIVOS.MAC can only generate text records. Hence, DVT code is contained in normal text records. A kind of pseudo informational record is generated by merely changing the location counter to a value which is out of range for the DVT location counter and then issuing one or more .WORD directives. Then the location counter is reset to its previous value. This is all transparent to the programer.

The DVTMON loader (LO command) when loading a program uses these text records with large location counters as informational records and uses text records with location counters within the normal range as actual DVT program code.

Additional Notes

(A) The last statement of a DVT assembly must be the Macro-11 .END directive. It is recommended that the END statement immediately precede the . END.

(B) The location counter and the contents of the memory word are printed one line below the statement.

(C) The LOC directive can be used with either ENDD=512, ENDP=1024, or ENDX=4096, to fill the rest of each of the memories. Because of the present Lincoln DVT hardware bootstrap, data and program memories must be full although the first 20_8 words of program memory contain the bootstrap loader.

It might be added that the user can easily modify the DVT Assembler since it only involves modifying the macro file, DIVOS.MAC, rather than the Macro-11 assembler.

G.2 DVT Assembler Directives

ALC	D	- Change location counter (LC) to LC + D. D may be negative.
BL	D	- Store zeros from word counter (WC) to WC + D. Also, change LC to LC+D.
MD		- Transfer assembly into data memory and reset word and location counters to NMD$ and MD$ respectively.
END		- List the number of words consumed for each of the 3 memories.
EVEN		- Set location counter to next even value if need be via a NOP.
LOC	A	- Store zeros from WC to A and set the new WC and LC to A. A must be $\geq$ LC and LC should be = WC.
ORG	A	- Set LC to A. A may be $\leq$ LC.
MP		- Transfer assembly into Program memory and reset word and location counters to NMP$ and MP$.
SEG	SN,[SA]	- Define the segment number, SN, and optionally a starting address, SA. The default starting address is 0. Segments can be numbered from 0 to 13(8). SEG must be issued at the beginning of the program and only one SEG directive is allowed per program.
MX		- Transfer assembly into extra memory and reset word and location counters to NMX$ and MX$.

Special DVT Assembler Op Codes

CLX	- Clear X register (YIX0)
CLA	- Clear A register (LDAYP 0)
NOP	- No Operation (STA 0)

G.3 DVT Assembler Messages

ERROR MESSAGES

LOC ARG BAD - Present word counter is larger than value of operand in LOC directive.

NO MEMORY DEFINED - A memory (MD, MP, or MX) directive has not been issued before the first word of code or data is generated.

NO SEGMENT DEFINED - A segment (SEG) directive has not been issued before the first word of code or data is generated.

NOTE: All three of the above errors are considered to be fatal by DVTMON when loading a program.

INFORMATIONAL MESSAGES

DATA MEMORY - Indicates MD directive has been issued.

PROGRAM MEMORY - Indicates MP directive has been issued.

EXTRA MEMORY - Indicates MX directive has been issued.

```
.PRINT      NMD$      ;MD WORDS
.PRINT      NMP$      ;MP WORDS
.PRINT      NMX$      ;MX WORDS
```

- Printout, as a result of END directive, of the number of words generated in each memory.

H. Appendices

H.1 DVTMON Informational and Error Messages

BAD (1)DUMP STARTING ADDR AND/OR LENGTH

The length in words of the indicated dump is < 0 or > 512., and/or the starting address is < 0 or > 512., and/or the starting address plus the length exceed 512.

BAD FILE FORMAT

An attempt to load a file (program) that was (1) assembled with the DVT assembler in which a fatal assembly error was detected or (2) not the result of a DVT assembly or a SA command.

BAD FILE SPECIFICATION

A syntactical or semantic error has been detected in a Files-11 file specification.

BAD PATCH

Invalid syntax or semantics on command issued after location had been opened by a PA, MP, or MX command.

BAD TAPE FORMAT

Error in reading a paper tape due to (1) tape not punched by DVTMON or (2) tape inserted in reader incorrectly or (3) checksum error detected.

CLOSE FILE FAILURE

Hardware error detected in attempting to close a file.

DR11-C TIMEOUT

Time (≈1sec) has expired without DVT— PDP-11 communication completing.

DUMP OUTPUT FILE IS OPEN

Attempt to execute a SA or PR command while an output file is open for simulation or dumping. Solution: issue CO command first.

DUMP FINI

A dump initiated from the DVT has completed, and if there is an output file specified, the file has been written into.

DUMP OUTPUT FILE NOT SELECTED

Not an error message, just a notification. Dump still completes.

DVT LOADED

A segment has been successfully written to the DVT either as the result of a boot or a segment request.

DVT MONITOR EXITED

Indicates all open files have been closed and DVTMON has exited. Result of a ↑Z being typed.

FILE OPEN FAILURE

There has been (1) a hardware failure or (2) for an existing file, an invalid file specification; incorrect disk UIC, file name or version number or (3) for a new file, the disk or UIC does not exist.

FILE READ ERROR - Either a hardware error has occurred or a file record is larger than the input buffer.

FILE WRITE ERROR - Hardware error.

ILLEGAL COMMAND

Illegal syntax or semantics. More specifically, the first two letters typed were not a valid command.

INVALID SEGMENT ADDRESS

A memory address specified in a patch (PA, MP, MD, L) command is out of range, or has bad syntax or semantics.

MISSED FIRST DUMP REQUEST

User is notified that first dump request word was missed; however, dump continues.

PUNCH OFF LINE, TYPE (CR) WHEN READY

Either punch is out of paper tape or not powered up. If condition is corrected, type (CR) to resume or type any character plus (CR) to abort punch mode.

READER OFF LINE, TYPE (CR) WHEN READY

Paper tape reader switch is not in on position or it is not powered up. Type (CR) if condition is corrected or any character plus (CR) to abort read mode.

SEGMENT LENGTH IS IMPROPER

A boot (BA, BO, or CR) or a MP or MD command on a segment with an improper length has been issued.

SEGMENT LONGER THAN FREE BUFFER SPACE

Attempt to load too long a segment from disk or paper tape.

SEGMENT NOT EMPTY

An attempt to load a segment as a result of a LO, or RP command or a DVT request.

SEGMENT NOT RESIDENT

An attempt to output a segment due to a BO, BA, SA, PP, PR, or a DVT request.

UNDEFINED FUNCTION FROM DVT

Interrupts are enabled and a word received from the DVT contains an illegal function code (upper 4 bits). See Section F.1.

H.2 DVTMON Overlay Structure

DVTMON consists essentially of a set of independent functions with little interaction between them. Hence, it is written in a modular fashion allowing an overlay structure to be used. Overlaying enables one to increase the size of the buffer area. The file DVTMOO1.ODL contains the overlay structure outlined in the Figure IX.H.1. The file DVTMNO1.ODL contains a structure which lays out the modules (i.e. no overlaying) and is useful for debugging. The difference in program size using these two structures is almost 3K (7K vs. 4K). A more complex overlay structure using multiple trees could be implemented to make the program smaller.

In the figure, DVTROOT is the root segment and is always resident in memory. This segment contains the DR11-C driver, various data structures, common routines and the initialization code.

NONFCS contains all the DVTMON commands which do not use the file system, including the keyboard command dispatcher.

FCS contains all the commands which use the file system. FCS and NONFCS reside in the same area of memory. The six segments above FCS occupy the same area of memory since they are called serially by FCS. COSTIN contains the routines to check the syntax and semantics of a file specification. PARSE and OFNB open a file; GETS and PUTS read from and write to a file, and CLOSE closes a file. The rest of the partition is used for buffer space.

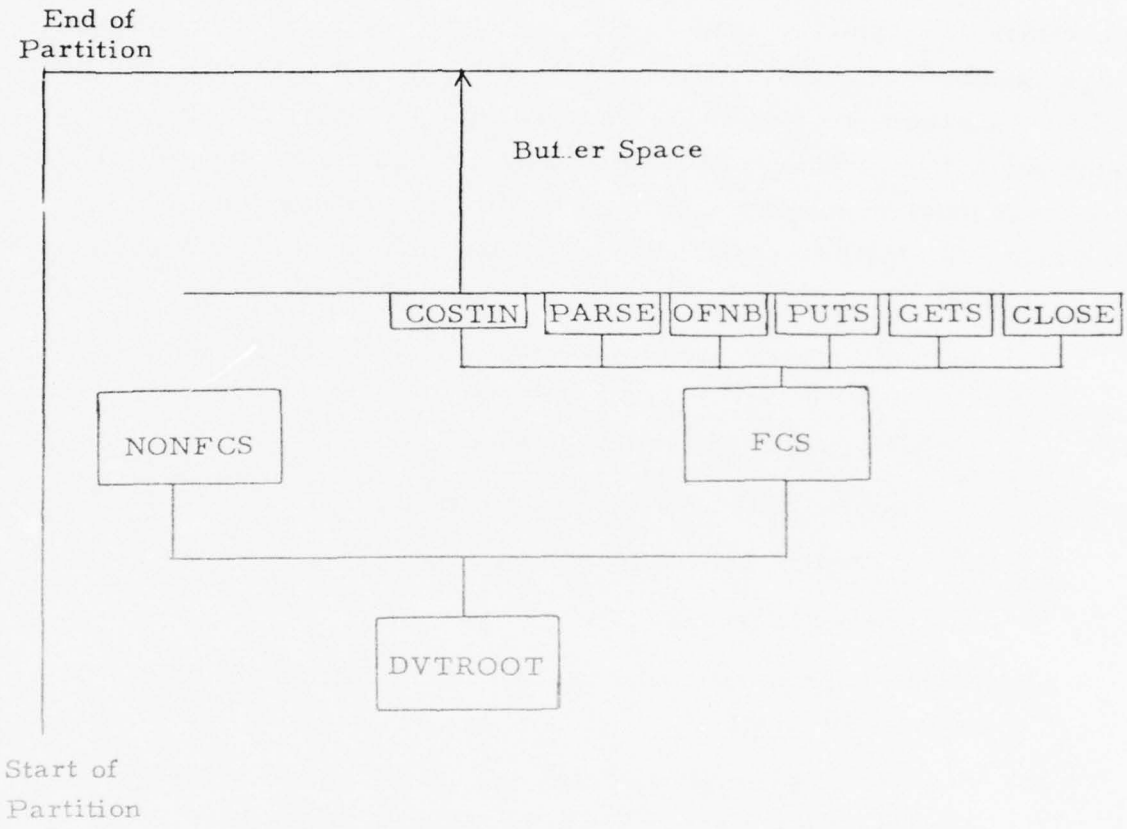

Figure IX. H. 1

DVTMON Overlay Structure

H.3 DVT Core-Only Monitor

A core-only stand-alone version (DVTCOR) of DVTMON was written for the tests in Reston, Virginia (Sec. A.1). DVTCOR is a stripped, modified version of DVTMON with access to the disk, the line printer and all simulations eliminated. IOX is assembled with DVTCOR to handle terminal I/O. The two PDP-11's have 16 K of memory, a terminal and a high speed readerpunch (PC-11). DVTCOR must be assembled and linked (Base Address = 0) using DOS, since Version 1 of RSX-11M does not support paper tape. It must be loaded using the absolute loader. After it is loaded it must be started at SA = 1000. It will immediately halt. Press the continue switch to restart it. It will then commence a dialogue similar to DVTMON.

The main differences between DVTCOR and DVTMON are:

(1) DVTCOR has no simulation modes.

(2) PR automatically goes to the terminal.

(3) The LO and SA commands do not exist.

(4) SO selects the terminal.

(5) Terminal printout can be broken into by typing ↑P. This restarts DVTCOR.

(6) There is no timeout capability (no clock). After sufficient elapsed time (≈2 sec) when attempting DVTCOR-DVT communication, type (CR) to abort.

H.4 DVTMON Segments

One of the initialization steps after DVTMON is loaded, is to determine the amount of free buffer space. This is the area from the end of the program proper to the end of the partition. This buffer area can contain up to 12 pieces (segments) of data. These segments can be of any length and loaded in any order. There is a segment directory that contains a pointer and the length for each segment. The first segment loaded starts at the first word of the free buffer space. The next segment loaded, whatever number, is loaded contiguous to the first loaded segment, etc. If a segment is deleted (DE), the pointer is zeroed and all segments which follow the deleted segment are moved to fill the hole left by the deleted segment. In other words, no holes are allowed between segments, and all of the free buffer space is contiguous and at the end of the partition.

H.5 How to Use the DVT Assembler and Start DVTMON

The user of the DVT Assembler and DVTMON should familiarize himself with the RSX-11M system; in particular the Line Text Editor, the MACRO-11 Assembler, and the Operator's Procedure. To use the DVT Assembler, type

```
MAC
```

The assembler will respond with

```
MAC>
```

and is ready for a command line. The command line to MAC should look similar to the following:

```
MAC> OBJECT, LP: =DIVOS, SOURCE
```

where OBJECT is the output object file which can be loaded by DVTMON, LP: is the line printer to which the listing is sent. DIVOS is the prefix file containing the DVT instruction set and directives, all written as MACRO-11 macros. SOURCE is the user's source file containing the DVT program.

To run DVTMON, just type

```
RUN DVTMON
```

DVTMON will start up with its initialization dialogue (Section F.1). To exit type ↑Z.

REFERENCES

1. Richard H. Wiggins, "Formation and Solution of the Linear Equations Used in Linear Predictive Coding", MITRE Technical Report MTR-2835, May 1974.

2. J.E. Roberts, C.P. Smith (ESD), and R.H. Wiggins, "Triple Function Voice Coder (TRIVOC)", MITRE Working Paper WP-20439, October 1975; also in J. Acoust. Soc. Am. 57, Supp. 1, 535 (1975).

3. John E. Roberts, "Design of Digital Filters for TRIVOC", MITRE Working Paper WP-20485, November 1975.

4. P.E. Blankenship, E.M. Hofstetter, A.H. Huntoon, M.L. Malpass, S. Seneff, and V.J. Sferrino, "The Lincoln Digital Voice Terminal System", Lincoln Laboratory Technical Note 1975-53, August 1975.

5. James L. Flanagan, Speech Analysis, Synthesis, and Perception, 2nd ed., secs. 1.2-1.4. Berlin: Springer-Verlag, 1972.

6. _____, chap. VIII.

7. B.S. Atal and S.L. Hanauer, "Speech Analysis and Synthesis by Linear Prediction of the Speech Wave", J. Acoust. Soc. Am. 50, 637 (1971).

8. R.I. Tucker, "The Lincoln DVT Programmers Manual", Lincoln Laboratory Manual LM-119, February 1976.

9. R.I. Tucker, "The Lincoln DVT Diagnostic System", Lincoln Laboratory Technical Note 1976-4, February 1976.

10. L.R. Rabiner and B. Gold, Theory and Application of Digital Signal Processing. Englewood Cliffs, N.J.: Prentice-Hall, 1975.

11. M.L. Malpass, "The Gold-Rabiner Pitch Detector in a Real-Time Environment", EASCON Proceedings, IEEE Electronics and Aerospace Systems Convention, p. 31-A (October, 1975).

X. LONG RANGE NAVIGATION--THE LORAN INTEGRAL EQUATION

A. Introduction

In the analysis which follows, we describe an algorithm developed for the numerical solution of the LORAN integral equation of the Volterra type. Long range navigation (LORAN) of an airplane may be achieved with the aid of radio stations. In this method a configuration of three radio stations, a master station M and two slave stations S_1 and S_2 emit radio waves at a given frequency ω. The airplane receives the radio waves from all three stations. The phase difference $\Delta\varphi_1$, $\Delta\varphi_2$ between the master station and each slave is noted. These phase differences may be converted into time delays Δt_1, Δt_2:

$$\Delta t_i = \omega \Delta \varphi_i \qquad i = 1, 2 \quad .$$

A certain time delay between master and slave implies a certain difference Δr_i in distance r_M between the slave and receiver and the distance r_i between master and receiver:

$$\Delta r_i = r_M - r_i = c\,\Delta t_i$$

The two range differences define two hyperbolas. A hyperbola is defined as the locus of points whose difference in distance from two given points (the focal points) is constant. In our case the focal points of the first (second) hyperbola are the master station and the first (second) slave. The constant difference in distance is Δr_1 (Δr_2). The intersection of these two hyperbolas is the location of the plane.

For each slave station, there is a family of hyperbolas corresponding to varying time delays. The superposition of both families of hyperbolas generates a grid system of intersection hyperbolas.

The preceding has been predicated on the assumption that there is no distortion of the radio waves due to the presence of the earth. In actual fact, the earth does cause a distortion in radio wave propagation. The grid system of hyperbolas is correspondingly distorted. The task to be accomplished is, therefore, that of computing radio wave propagation over irregular terrain.

The radio wave propagation is described by a Helmholz equation, subjected to boundary conditions imposed by the earth. This equation is converted to a two dimensional integral equation with the aid of Green's theorem. The integral equation incorporates the boundary conditions. This two dimensional integral equation is reduced to a one dimensional Volterra integral equation. Lastly, a method of solution is proposed for the Volterra integral equation.

B. The Wave Equation

Radio waves, being electromagnetic in character, may be described by a time dependent $\vec{A}$-field and φ-field (alternatively, an $\vec{E}$-field and $\vec{H}$-field), where $\vec{A}$, φ, $\vec{E}$, $\vec{H}$ are the vector and scalar potentials, electric and magnetic fields, respectively. The $\vec{A}$-field and φ-field satisfy inhomogeneous time dependent wave equations:

$$\nabla^2 \vec{A}(\vec{r}, t) - \frac{1}{c^2} \frac{\partial^2 A(\vec{r}, t)}{\partial t^2} = -4\pi \rho(\vec{r}, t), \qquad (1)$$

$$\nabla^2 \varphi(\vec{r}, t) - \frac{1}{c^2} \frac{\partial^2 \varphi(\vec{r}, t)}{\partial t^2} = -\frac{4\pi}{c} \vec{j}(\vec{r}, t), \tag{2}$$

where c = the velocity of light, ρ and $\vec{j}$ are the charge and current densities, respectively. The above equations (1, 2) may be derived from Maxwells equations. The above equations may be Fourier transformed to give the following equations:

$$\nabla^2 \varphi(\vec{r}, \omega) + k^2 \varphi(\vec{r}, \omega) = -4\pi \rho(\vec{r}, \omega) \quad , \tag{3}$$

$$\nabla^2 \vec{A}(\vec{r}, \omega) + k^2 \vec{A}(\vec{r}, \omega) = -\frac{4\pi}{c} \vec{j}(\vec{r}, \omega) \quad , \tag{4}$$

$$\omega/k = c \quad , \tag{5}$$

where ω is the angular frequency of the radiation and k is the wave number.

If only currents are present ($\varphi = 0$), then only the vector Helmholz equation (4) for the $\vec{A}$-field need be considered. The assumption of vanishing φ is usually valid for antennas. If $\varphi = 0$ then the directions of the $\vec{A}$-field and the $\vec{E}$-field coincide. If the direction (polarization) of the $\vec{A}$-field remains constant throughout space then the vector Helmholz equation (4) reduces to a scaler Helmholz equation:

$$\nabla^2 \psi + k^2 \psi = f(\vec{r}, \omega) \quad , \tag{6}$$

$$\psi = |\vec{A}| \quad , \tag{7}$$

where $f = -\frac{4\pi}{c}|\vec{j}|$. The homogeneous Green's function G(r) (G (r) vanishes at infinity) is

$$G(r) = \frac{e^{ikr}}{r}, \quad r = |\vec{r}|. \tag{8}$$

B.1 Boundary Conditions

Antennas can be designed to generate fields of a given polarization in free space. If the antenna generates a vertical (horizontal) field in the presence of the earth, the earth will not appreciably change the polarization. The vertical (horizontal) field is assumed to satisfy the following boundary (Leontovitch) conditions:

$$\frac{\partial \psi}{\partial n} = -ik\delta\psi \tag{9}$$

The surface impedance δ of the terrain depends on the field polarization at the terrain surface and the index of refraction n of the terrain. The refraction index n depends on the polarization. For vertical polarization the refraction index n is:

$$n = \eta/(\eta-1)^{1/2} \tag{10}$$

For horizontal polarization, the refraction index is:

$$n = (\eta-1)^{1/2} \tag{11}$$

In the long wavelength limit, the complex dielectric constant η

is given by:

$$\eta = \frac{\epsilon}{\epsilon_o} + i \frac{\sigma}{\epsilon_o \omega} \tag{12}$$

where ϵ is the dielectric constant, σ is the conductivity, and ω is the radio frequency.

C. The Helmholz Integral Equation

The conversion of the Helmholz differential equation (6) to an integral equation incorporating the boundary conditions (9) is accomplished with the aid of Green's theorem. Green's theorem relates a volume integral to a surface integral:

$$\int_V (\psi \nabla^2 \varphi - \varphi \nabla^2 \psi) \, dV = \int_{S^*} (\varphi \frac{\partial \psi}{\partial n} - \psi \frac{\partial \varphi}{\partial n} \, da \tag{13}$$

The functions φ and ψ are arbitrary differentiable functions. The surface S^* encloses the volume V. The surface S^* that we shall consider consists of three parts (see Fig. X.C.1): 1) the surface terrain S; 2) the surface Σ of a large hemisphere centered at the transmitter, 0; 3) the surface σ of a small hemisphere centered at the receiver P. The point Q is the variable point of integration. The function ψ is chosen to satisfy the Helmholz differential equation Eq. (6) together with the boundary condition Eq. (9).

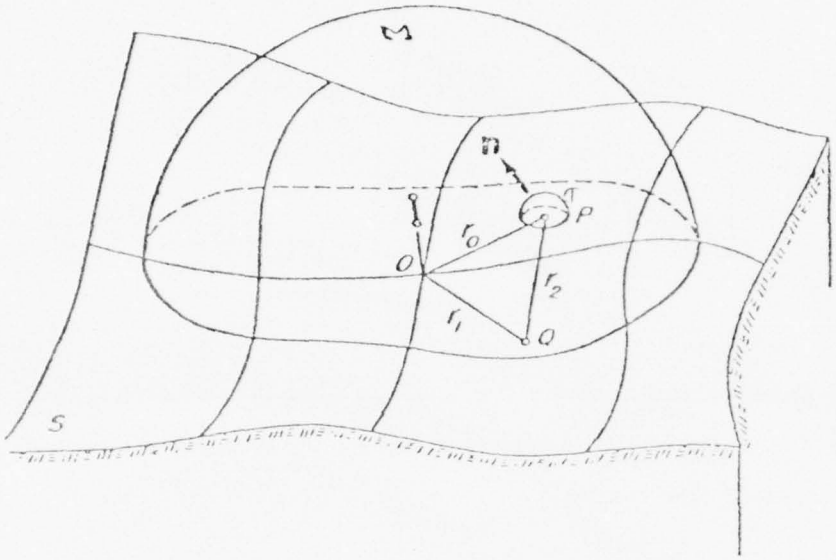

Fig. X.C.1 (From Ref. 1)

The LORAN Geometry

The function φ is chosen to be the Helmholz homogeneous Green's function.

With the aid of Green's theorem the integral equation finally arrived at is:

$$\psi(P) = 2\psi_o(P) + \frac{ik}{2\Pi} \int da\, \psi(Q) \frac{e^{ikr_2}}{r_2} \times \left[\delta + \left(1 + \frac{1}{ikr_2}\right) \frac{\partial r_2}{\partial n}\right] \quad . \tag{14}$$

The above integration is over the surface S of the terrain. The function $\psi_o(p)$ is the field in the absence of the earth. It may be assumed to be of the form:

$$\psi_o(P) = g(P)\, e^{ikr_o}/r_o \tag{15}$$

The function g(p) is the antenna pattern. The attenuation function f(p) is defined in terms of the field $\psi(p)$:

$$\psi(p) = 2\, f(p)\, e^{ikr_o}/r_o \tag{16}$$

Substituting Eqs. (15) and (16) into the Helmholz integral equation for the field $\psi(p)$, we obtain the Helmholz integral equation for the attenuation f(p):

$$f(P) = g(P) + \frac{ik}{2\Pi} \int_S f(Q) \exp\left[ik\,(r_1 + r_2 - r_o)\right] x$$

$$\frac{r_0}{r_1 r_2}\left[\delta + \left(1 - \frac{1}{ikr_2}\right)\frac{\partial r_2}{\partial n}\right] da \quad . \tag{17}$$

From the above Helmholz integral equation Eq. (17) for the attenuation, we see that the attenuation depends on the following four factors: 1) the topography of the terrain; 2) the surface impedence of the terrain; 3) the radio frequency; 4) the antenna gain.

D. Reduction of Helmholz Integral Equation to Hufford's Equation

The Helmholz integral equation Eq. (17) for the attenuation involves an integration over a surface. In general, this equation would be very difficult to solve. However, the Helmholz integral equation may be reduced to a one dimensional integral equation. In order to accomplish this reduction, everything is projected onto a horizontal plane (see Fig. X.D.1). The reduced one-dimensional integral equation (Hufford's equation) finally arrived at is:

$$f(x) = g(x) + \int_o^x K(x, s)\, f(s) \quad . \tag{18}$$

The projected distance between antenna and receiver is x. The kernel K(x, s) of Hufford's equation is singular at the endpoints o and x:

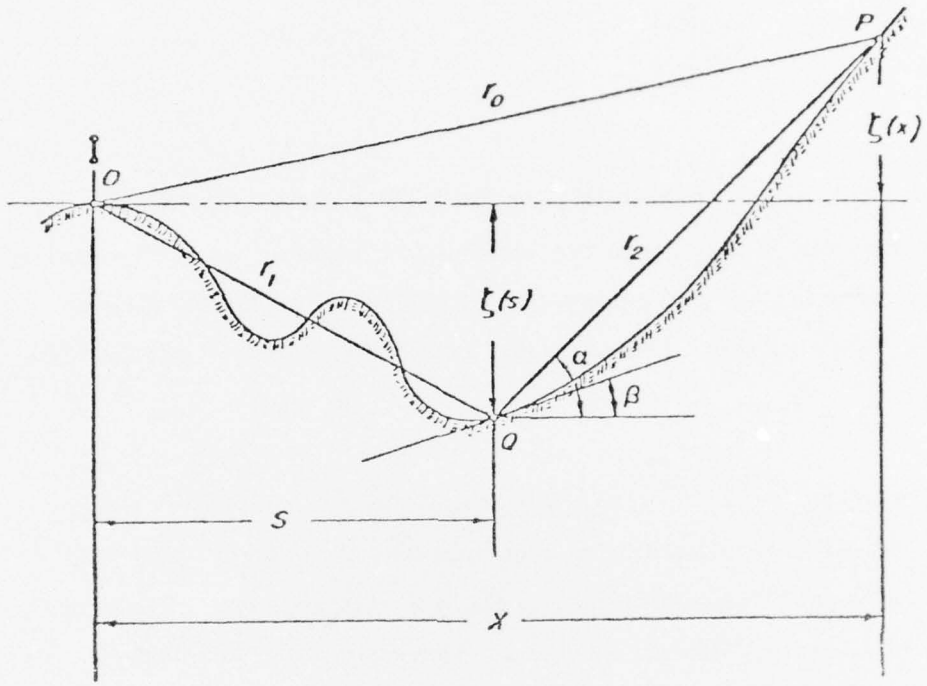

Fig. X.D.1 (From Ref. (1)

Horizontal Plane Projection

$$K(x, s) = F(x, s)/\sqrt{s(x-s)} \quad . \tag{19}$$

The function F(x, s) is given by:

$$F(x, s) = \left[\delta(s) + \left(1 + \frac{1}{ikr_2}\right)\frac{\partial r_2}{\partial n}\right] e^{i(k\epsilon - \Pi/4)} \tag{20}$$

where

$$r_2^2 = (x - s)^2 + (z(x) - z(s))^2 \quad , \tag{21}$$

$$\frac{\partial r_2}{\partial n} = \frac{(x-s)\frac{\partial z(s)}{\partial s} - (z(x) - z(s))}{r_2\sqrt{1 + \left(\frac{\partial z(s)}{\partial s}\right)^2}} \quad , \tag{22}$$

$$\epsilon = \frac{x\,s}{2(x - s)}\left[\frac{z(x)}{x} - \frac{z(s)}{s}\right]^2 \quad . \tag{23}$$

Using L' Hopital's rule, we have:

$$\lim_{s \to x} \frac{\partial r_2}{\partial n} = 0 \quad , \tag{24}$$

ARCON

$$\lim_{s \to x} \frac{1}{r_2} \frac{\partial r_2}{\partial n} = -\frac{1}{2} \frac{\frac{\partial^2 z(x)}{\partial s^2}}{\left[1 + \left(\frac{\partial z(x)}{\partial s}\right)^2\right]^{3/2}} \tag{25}$$

$$\lim_{s \to x} \epsilon = 0 \quad , \quad \epsilon(o) = \epsilon(x) = 0 \tag{26}$$

Hufford's equation, in general, must be solved numerically. However, Hufford's equation may be solved exactly in certain limiting cases. Two such cases are: 1) the plane earth case; 2) the cylindrical earth case. We shall only consider the limiting case of the plane earth.

By means of Laplace transforms, the plane earth solution is found to be:

$$W(x) = 1 + i \sqrt{\pi \rho}\ w(i \sqrt{\rho}) \tag{27}$$

Sommerfeld's complex numerical distance ρ is given by:

$$\rho = i k \delta^2/2 \tag{28}$$

The w-function w(z) is defined in terms of the complex error function erf(z):

$$w(z) = e^{-z^2} (1-\mathrm{erf}(z)) \quad , \tag{29}$$

where

$$\mathrm{erf}(z) = \frac{2}{\sqrt{\Pi}} \int_0^z e^{-t^2} dt \tag{30}$$

The w-function has a power series expansion:

$$w(z) = \sum_{n=0}^{\infty} \frac{(iz)^n}{\Gamma(\frac{n}{2} + 1)} \tag{31}$$

where the usual definition of the gamma function applies, i.e.

$$\Gamma(\tfrac{1}{2}) = \sqrt{\Pi}$$
$$\Gamma(z+1) = z\Gamma(z) \tag{32}$$

There exist subroutines for the evaluation of the w-function for arbitrary complex argument.

E_o Method for Numerical Solution of Hufford's Equation

The plane earth solution is primarily of interest as a check on the accuracy of the general numerical solution. The method of numerical solution of Hufford's equation is based on discretizing the following equation:

$$f_n = f(nh) = 1 + \sum_{m=0}^{n-1} \int_{mh}^{(m+1)h} K(nh, s)\, f(s)\, ds \tag{33}$$

Through a simple change of variables the above may be written as:

$$f_n = 1 + \sum_{m=0}^{n-1} \int_{0}^{h} f(s + mh)\, K(nh, s + mh)\, ds \tag{34}$$

The attenuation f(s) may be expanded in a set of basis functions $U_i(s)$:

$$f(s) = \sum_{i=1}^{N} \alpha_i\, U_i(s) \tag{35}$$

By evaluation the above expansion Eq. (35) at successive points we may generate a set of linear equations:

$$f_j = f(jh) = \sum_{i=1}^{N} U_{ji}\, \alpha_i \tag{36}$$

$$U_{ji} = U_i(jh) \tag{37}$$

The index j ranges through a block of N successive points.

The above set of linear equations Eq. (36) may be inverted to obtain:

$$\alpha_i = \sum_j B_{ij} f_j \quad , \qquad B = U^{-1} \tag{38}$$

The index j ranges through a block of N successive points. Substituting the expansion (38) into the discretized integral equation (34), we obtain:

$$f_n = 1 + \sum_j T_{nj} f_j \tag{39}$$

$$T_{nj} = \sum_{i=1}^{N} Q_{ni} B_{ij} \tag{40}$$

Both indexes n and j range through the same block of N successive points. The matrix of integrals Q_{ni} is given by:

$$Q_{ni} = \sum_{m=0}^{n-1} \int_0^h ds\, U_i (s + mh)\, K(nh,\ s + mh) \quad . \tag{41}$$

The total range of points may be partitioned into successive blocks of points. The above set of equations Eq. (39) may be solved for each block of N successive points. In this manner, the attenuation may be found for all points between antenna and receiver. The basis

functions $U_i(x)$ need not be the same for each block, nor do the number of points N in each block have to be the same.

The problem arises as to how to choose the basis functions. Perhaps the simplest basis functions to choose are powers of s. However, close to the origin, a better choice appears to be powers of $\sqrt{s}$. This is because the antenna is resting on flat ground. We know the flat earth solution Eq. (27) near the origin is a power series in $\sqrt{s}$. Therefore, near the origin, we shall assume a power series expansion:

$$f(s) = \alpha_o + \sum_{i=1}^{3} \alpha_i s^{i/2} \tag{42}$$

From Hufford's equation, it is simple to see that f(o) = 1. This implies that $\alpha_o = 1$. The matrix of integrals Eq. (41) becomes

$$Q_{ni} = \sum_{m=0}^{n-1} \int_o^h (s + mh)^{i/2} K(nh, s + mh)\, ds \tag{43}$$

where $i = 0, 1, 2, 3$

Farther away from the origin, an ordinary power series expansion appears to be adequate:

$$f(s) = \sum_{i=1}^{3} \alpha_i s^{(i-1)} \tag{44}$$

$$Q_{ni} = \sum_{m=0}^{n-1} \int_{o}^{h} (s + mh)^{i-1} K(nh, s + mh)\, ds \qquad (45)$$

where $i = 1, 2, 3$

From the above, we see that the integrals encountered are of the following form:

$$I(n, m, p) = \int_{o}^{h} \frac{(s + mh)^{p} F(nh, s + mh)}{\sqrt{(s + mh)((n-m)h - s)}}\, ds \qquad (46)$$

Depending on the values of n, m and p the above integral may or may not have singularities. There are three cases that may be encountered: 1) no singularity; 2) single singularity; 3) double singularity.

The case of single singularity arises if ($p > 0.5$ or $m > 1$) and ($n - m = 1$). In this case, the form of the integral is:

$$I(n, m, p) = \int_{o}^{h} \frac{g(s)}{\sqrt{h-s}}\, ds \qquad (47)$$

We propose to approximate the above integral using Gauss quadrature as follows:

$$I(n, m, p) = \sqrt{h} \sum_{i=1}^{N} w_i \, g(s_i) \tag{48}$$

$$s_i = h\, x_i \quad , \quad x_i = 1 - \xi_i^2$$

The i'th root of $P_{2N}(x)$ is ξ_i. The weights w_i depend on the Gaussian weights w_i^{2N} $\left(w_i = 2w_i^{2N}\right)$.

The case of double singularity is achieved if p = 0 and n = 1 and m = 0. In this case, the form of the integral is:

$$I(n, m, p) = \int_0^h \frac{g(r)}{\sqrt{s(h-s)}} \, ds \tag{49}$$

where $g(s) = F(h, s)$. We propose to approximate the above integral as follows:

$$I(n, m, p) = \sum_{i=1}^{N} w_i \, g(y_i) \quad , \tag{50}$$

where

$$y_i = \frac{1}{2} h (1 + x_i) \quad ,$$

$$x_i = \cos (2i - 1) \pi/(2N) \quad ,$$

$$w_i = \pi/N \quad .$$

If neither the condition for single or double singularity holds, then the integral I(n, m, p) has no singularities. In this case, the form of the integral is:

$$I(n, m, p) = \int_0^h g(s)\, ds \tag{51}$$

where $$g(s) = \frac{(s + mh)^P F(nh, s + mh)}{\sqrt{(s + mh)\,((n-m)\,h - s)}}$$

We would approximate the above integral by standard Gaussian quadrature:

$$I(n, m, p) = \sum_{i=1}^{N} w_i\, g(y_i) \quad , \tag{52}$$

where

$$y_i = \frac{1}{2} h\,(1 + x_i)$$

The i th root of $P_N(x)$ is x_i. The Gaussian weights are w_i.

F. Specification of Input Data

In order that a numerical solution of the LORAN integral equation be obtained, the input data must consist of the following items: 1) the radio frequency ω; 2) a table (z_i, x_i) of elevation

values z_i vs. position x_i; 3) a table (δ, x_i) of complex surface impedance values δ_i vs. position x_i.

The algorithm for the solution of Hufford's equation calls for the following: 1) an elevation table ($\bar{x}_n$, $\bar{z}_n$); 2) a derivative elevation table ($\bar{x}_n$, $\bar{z}'_n$); 3) a second derivative elevation table ($\bar{x}_n$, $\bar{z}''_n$); 4) an impedance table ($\bar{x}_n$, $\bar{\delta}_n$).

The input elevation table ($\bar{x}_n$, $\bar{z}_n$) may be different from the algorithm elevation table (x_n, z_n). Similarly, the input impedence table ($\bar{x}_n$, $\bar{\delta}_n$) may be different from the algorithm impedence table (x_n, δ_n). Because the input tables may differ from the corresponding tables needed in the algorithm, we are faced with the task of interpolating the input tables to produce the algorithm tables.

F.1 Trapezoidal Interpolation

Perhaps the simplest method of interpolation is the linear (trapozoidal) method. Indeed, this method may be adequate to generate of the algorithm impedence table (x_n, δ_n) from the input impedence table ($\bar{x}_n$, $\bar{\delta}_n$). However, in the case of the input elevation table ($\bar{x}_n$, $\bar{z}_n$), we not only wish to generate the algorithm elevation table (x_n, z_n), but the derivative tables (x_n, z'_n) and (x_n, z''_n) as well. If linear interpolation were used, the elevation derivatives would be discontinuous. An alternative interpolation method is the method of splines. The method of splines produces smooth elevation derivatives.

F.2 Spline Interpolation

In the method of splines, the problem we are faced with is the problem of interpolating between n given data points (x_i, z_i)

$(i = 1, 2 \ldots n)$ by means of the smoothest function $g(x)$ which has continuous derivatives of orders $1, 2 \ldots k$, $k < n$. The smoothest function is defined in the sense that $\sigma = \int_a^b [g^k(x)]^2 dx$ is as small as possible. For $k > n$, the problem does not have a unique solution. For $k = n$ the Lagrangian interpolation polynomial is the unique solution. For $k < n$, there is again a unique solution, the spline function, which is a piecewise function given in any interval $\left[x_i, x_{i+1} \right]$ by a polynomial.

X. REFERENCES

1. Hufford, G. A. (1952) Quart. J. Appl. Math., 9, 391.

2. Ott, R. H. (1971) Radio Science, 6, 4, 429.

MISSION
of
Rome Air Development Center

RADC plans and conducts research, exploratory and advanced development programs in command, control, and communications (C^3) activities, and in the C^3 areas of information sciences and intelligence. The principal technical mission areas are communications, electromagnetic guidance and control, surveillance of ground and aerospace objects, intelligence data collection and handling, information system technology, ionospheric propagation, solid state sciences, microwave physics and electronic reliability, maintainability and compatibility.